
Light propagation in confined photonic structures: modeling and experiments

Stefano Biasi

Ph.D. thesis submitted to University of Trento

**Light propagation in confined photonic
structures: modeling and experiments**
Thesis

Stefano Biasi

A dissertation submitted to the
Department of Physics
University of Trento

In fulfilment of the requirements for the Degree of
Philosophiæ Doctor in Physics

Under the Supervision of
Prof. Lorenzo Pavesi

Ph.D. School
22th April 2020

Supervisor:

Prof. Lorenzo Pavesi

Members of the committee:

Prof. Claudio Conti

Prof. Capmany José

Prof. Philipp Hans Juergen Hauke

to my unborn daughter

Acknowledgment

Looking back, at the end of my doctorate, I want to be grateful for the help and friendship I have received from various people, which have allowed me to face the difficulties encountered during these enriching years of research. First of all, I would like to express my sincere gratitude to my supervisor, professor Lorenzo Pavesi. He has guided me along this path of learning: valuing my personal inclinations, he gave me the opportunity to move on scientific research in the freest possible way, providing me with instrumental and moral support and always encouraging me to give my best. Besides my supervisor, I would like to thank the members of the committee for the insights and suggestions received. Special thanks goes then to Fernando Ramiro Manzano, not only for the countless fruitful scientific discussions, but also for his contagious enthusiasm, a colleague of great value and above all a true friend. Thank you also to Iacopo Carusotto: I have often knocked on his door full of theoretical doubts, in any case he has always been available and the discussions have always brought different ways to deal the problems. His passion in facing research gives relief and charge.

I would also like to thank all the members of my laboratory group: the NanoLab. In particular, the historical part, Alessandro Trenti and Massimo Borghi, friends and colleagues of both adventures and misfortunes during the Physics 2 exercises and in daily life in the Laboratories. Thank you also to Pierre Guilleme, not only for having put up with me as an office mate, but above all for the scientific discussions followed by the numerous blackboards. His patience and his meticulous way of dealing with research have often re-dimensioned me and guided to the real goal. A special thanks goes to my historical canteen mates: Claudio Castellan, Chiara Piotto, Maddalena Bertolla, Paolo Bettotti, Sara Piccione and Stefano Signorini because you can progress in research even by discussing with colleagues in your everyday life, over a hot meal and/or a cold beer. I wish to thank the old levers of the laboratory and who has returned: Santanu Manna, Stefano Tondini, Tatevik and Astghik Chalyan, Zahra Bisadi and Mattia Mancinelli. Thank you also to the new generation mates in particular to Nicolò Leone for the enjoyable hours spent in the laboratory and to Riccardo Franchi for the fruitful scientific discussions. A special acknowledgment goes also to Mher Ghulinyan, Martino Bernard and to all the technical staff who supported me in the realization of the measurement equipment, in particular Giorgio Fontana, Enrico Moser, and all the components of the electronic and mechanical service and of the didactic laboratories.

Last but not least, I would like to warm thank my wife Marta, who has patiently supported me during my journey, encouraging me in difficult moments, and my family: my parents Germano and Emanuela who have allowed me to undertake these studies, and, with my brother Andrea, have supported and

Acknowledgment

confided in me along the way.

Contents

Acknowledgment	iii
Contents	v
1 Introduction	1
I Theory and Simulations	9
2 Hermitian and non-Hermitian systems	11
2.1 Theoretical background: from diabolic points to exceptional points	12
2.2 Backscattering	18
2.3 Theoretical model	20
2.4 Helmholtz equation and the reflection of waves	52
2.5 From the backscattering to the Fano lineshape	59
3 Time response of Hermitian and non-Hermitian systems	73
3.1 Theoretical model	74
3.2 Numerical simulation and temporal output response	78
3.3 Backscattering	89
4 Nonlinear response: the Bogoliubov like dispersion and the Thermo Optic Coefficient	93
4.1 Towards nonlinear optics	94
4.2 Pulse propagation: the dissipative Gross-Pitaevskii equation	96
4.3 A degenerate four wave mixing in the language of the Bogoliubov's theory	98
4.4 Nonlinear response in a microresonator	121
II Experiments and Results	129
5 Complex field characterization in integrated Hermitian and non-Hermitian optical devices	131
5.1 The optical setup	132
5.2 Characterization of the <i>SiON</i> platform	144
5.3 Backscattering measurements	152
5.4 The inter-modal interaction measurements	157

Contents

6	Unidirectional reflection and time characterization	163
6.1	Transmitted and reflected intensity response	163
6.2	Time response measurements of an integrated microresonator	170
6.3	From integrated devices to macroscopic cavities	174
7	Conclusion	181
	Appendices	185
A	A simple model of a Mach-Zhender interferometer	187
	Bibliography	191

Chapter 1

Introduction

Photonics is emerging as a pervasive technology, which enables the knowledge society of these days. It has led to the realization of several devices that have become part of everyday life as well as factory and research. For instance, in vision correction, health monitoring, surgery, spectroscopy, information and material processing. The most important development in photonics has been the rise of integrated photonics circuits with unprecedented computation power and functionalities. One of the key building blocks of integrated photonics is represented by the microresonators [1]. Indeed, they are essential devices to develop several applications ranging from sensing [2, 3] to optical communication [4, 5] and to metrology [6, 7]. Their strength lies in a striking spectral response which enables dense wavelength division multiplexing applications and in an easy storage of high field intensity, which boosts light-matter interaction. This dramatically enhances both classical and quantum optical phenomena such as slow light transmission [8], frequency comb generation [9] or entanglement generation [10]. Although the physics of optical microresonators has been widely studied during the years, some aspects of their fundamental properties can generate peculiar and unexpected experimental outcomes. One example is the well-known backscattering phenomenon linked to the surface wall roughness. Here, the back-scattered light excites a counter-propagating optical mode which is degenerate in frequency with the propagating one. As a result of the repeated back-scattering processes, stationary super-modes are formed between the co-propagating and the counter-propagating modes with a sizeable energy splitting [11, 12, 13]. In an ideal microresonator, this gives rise to a symmetric transmission doublet and, therefore, to a Hermitian back-coupling [11, 14, 15]. However, measurements show an asymmetry between the split resonances in unperturbed resonators [12, 16, 17]. Experimentally, the asymmetry is observed as different intensities associated to the split peaks. These observations may be explained by theoretical studies maintaining the postulate of the Hermitian nature of the collective back-coupling. It has been suggested that the asymmetry might be caused by the interaction of the back-reflections at the bus-waveguide/microresonator coupling region [12], or by the nonlinear Kerr-effect [17]. Nevertheless, in a multimode microresonator vertically coupled to a bus waveguide, with a relative high quality factor ($\sim 10^5$) the simple Hermitian coupling is not enough to explain its physics. Thus, the broadly known temporal coupled mode equations should be generalized by introducing non-Hermitian (i.e. dissipative) coupling coefficients taking advantage of the equivalence between the Schroedinger's and the Helmholtz's equations. This allows studying in detail the exchange of energy between the counter-propagating modes paving the way to explore the unintuitive physics of the non-Hermitian systems in the field of microresonators. Actually

1. Introduction

non-Hermitian photonics [18] is a field of growing interest since it opens the avenues of the exceptional points [19] to the topological photonics [20]. The study of the degeneracies associated to these exceptional points, where not only the eigenvalues but also the eigenvectors coalesce, have brought the demonstration of non-trivial effects on photonics structures such as non-reciprocal light propagation [21] and chiral modes [22]. In addition, the introduction of active materials into topological photonic structures have brought to the realization of unidirectional light emission under the time-reversal symmetry breaking [20, 23]. The link between the non-Hermitian and the topological photonics arises from the isomorphism between the Schroedinger equation in quantum mechanics and the wave equation in optics [24]. These results show that a generalization of techniques which have been used for other fields can revive topics in photonics as well. A remarkable example arises from the bosonic nature of the photons and, therefore, from the parallelism with the boson atoms. This allows extend the study of quantum fluid physics to nonlinear optics giving rise to the field of quantum fluid of light [25]. Indeed, in the presence of a spatial confinement of the light and of a nonlinear medium, the light-matter interaction can give rise to photon-like particles which exhibit, unlike photons in vacuum, a sizable effective mass and a mutual interaction [25, 26, 27]. In this way, a many-photon system can behave collectively as a quantum fluid introducing, out of equilibrium, novel outcomes such as the superfluid flow around a defect [28] or the formation of vortices [29]. Within this thesis, we tried to develop on this photon-cold atom analogy to verify whether a sizable effect can be measured on an optical platform made of a simple channel waveguide which shows a third order nonlinear susceptibility.

This thesis analyzes the modeling of interacting modes inside waveguide/microresonator systems and studies a stimulated degenerate four wave mixing process exploiting the parallelism between photons and cold boson atoms. Specifically, the description of linear systems is reported taking advantage of the isomorphism between Schrodinger's equation and Helmholtz's equation. The backscattering phenomenon due to the surface wall roughness of a microresonator is addressed by adding to the usual conservative (Hermitian) coupling coefficient, a dissipative (non-Hermitian) term. This allows explaining the experimental measurements of a multimodal microresonator, which exhibits an asymmetrical resonance splitting characterized by a difference in the peak depths of the transmission spectra. It is shown theoretically, numerically and experimentally that the stochastic nature of the roughness along with the inter-modal dissipative coupling could give rise to a different exchange of energy between the co-propagating and the counter-propagating mode. The realization of an optical setup based on a Mach-Zehnder interferometer, which exploits some particular techniques of data acquisition, allows obtaining a full knowledge of the complex electric field of a propagating mode. In this way, the spectrum of a wedge microresonator vertically coupled to a bus waveguide is explained using analysis methods based on parametric phasors and inverse complex representations.

The non-Hermitian nature of the coupling between optical modes introduces important implications in their optical responses. Indeed, in a dissipative

scenario, whereas the Lorentz reciprocity enforces equal transmission in both directions of excitation, the reflection can be completely different. To show this phenomenology, the non-Hermitian model of backscattering is forced to work on an exceptional point thanks to a particular geometry. This gives rise to a counterintuitive behavior and then to an unidirectional reflection device which allows avoiding backscattering inside the optical cavity. In addition, the knowledge acquired studying the backscattering phenomena is extended, in the analogy of a three-level system, to the case of multi-modal microresonators where the interaction between modes can originate Fano line shape in the transmission spectra. Finally, the energy exchange between the co-propagating and counter-propagating modes is studied from a temporal point of view by extrapolating a simple model based on the Green function. In this way, it is discussed the analytical temporal response of a microring resonator excited through a bus waveguide by an optical rectangular pulse. Here, it is shown theoretically and experimentally, how the temporal response leads to the characterization of the coupling regime from the simple knowledge of the electric field intensity.

In this work, the isomorphism between the Schroedinger's equation and the Helmholtz wave equation is also analyzed in the nonlinear case. Considering a bulk nonlinear medium of the Kerr type, the complex amplitude of the optical field is a slowly varying function of space and time, which satisfies a nonlinear Schroedinger equation. When we neglect the losses and we exchange the role of the time and of the propagation coordinate in the Schroedinger equation, we obtain a relation which is mathematically identical to the Gross-Pitaevskii equation of dilute atomic Bose Einstein Condensate. Exploiting such analogy, the well-known nonlinear optical phenomenon of stimulated degenerate four wave mixing is reformulated in the language of the Bogoliubov theory. This parallelism between photons and cold atoms allows showing that the phase of the signal assumes a peculiar sound-like dispersion under proper assumptions. At the end, for the sake of completeness, the nonlinear response of a waveguide/microresonator system is studied paving new ways to exploit the different energy distribution inside the microresonator.

During my PhD I had the opportunity to explore different facets of research ranging from theoretical studies to experimental measurements. The problems were addressed starting from the realization of simple theoretical models which are able to reproduce the behavior of the phenomena and, therefore, to show reasonable physical interpretations in the most intuitive scenarios. Typically, these outcomes were first verified through finite element methods or finite difference time domain simulations. Finally, the opportunity to work in laboratory allowed me to face the real world by building optical setups and realizing acquisition methods of measurements capable to analyze the problems. The possibility of comparing the experimental results with the theoretical predictions allowed me investigating different techniques of analysis and data representations. This path of study leads me to divide my thesis into two parts:

- Theory and Simulations.
- Experiments and Results.

1. Introduction

The first one introduces the theoretical models capable of understanding the physics that governs the problems, providing a first validation of the deductions obtained by numerical simulations. The second one, is focused on the experimental part. In particular, it reports the optical setups built to analyze the phenomena introduced in the theoretical part, and the results obtained from the measurements.

This work is based on the main results and ideas developed in the following manuscripts, which are listed in chronological order, separating them into peer-reviewed papers, papers in preparation and proceedings.

Peer-reviewed papers

- a S. Manna, M. Bernard, S. Biasi, F. Ramiro-Manzano, M. Mancinelli, M. Ghulinyan, G. Pucker and L. Pavesi, “Stimulated degenerate four-wave mixing in Si nanocrystal waveguides” in *Journal of Optics*, v. 18, n. 7 (2016), p. 075801. - DOI: 10.1088/2040-8978/18/7/075801;
- b P.-E. Larré, S. Biasi, F. Ramiro-Manzano, L. Pavesi and I. Carusotto, “Pump-and-probe optical transmission phase shift as a quantitative probe of the Bogoliubov dispersion relation in a nonlinear channel waveguide” in *the European Physical Journal. D, Atomic, Molecular, Optical and Plasma physics*, v. 71, n. 6 (2017), p. 146.1-146.17, - DOI: 10.1140/epjd/e2017-80208-5;
- c F. Turri, S. Biasi, F. R. Manzano, and L. Pavesi, “A Free-Space Interferometer for Phase-Delay Measurements in Integrated Optical Devices in Degenerate Pump-and-Probe Experiments” in *IEEE Transactions on Instrumentation and Measurement*, v. 2018, 67, n. 12 (2018), p. 2863-2871, - DOI: 10.1109/TIM.2018.2830845;
- d A. Trenti, M. Borghi, S. Biasi, M. Ghulinyan, F. Ramiro-Manzano, G. Pucker, and L. Pavesi, “Thermo-optic coefficient and nonlinear refractive index of silicon oxynitride waveguides” in *Aip Advances*, v. 8, (2018), p. 025311, - DOI: 10.1063/1.5018016;
- e S. Biasi, F. Ramiro-Manzano, F. Turri, P.-E. Larré, M. Ghulinyan, I. Carusotto and L. Pavesi, “Hermitian and Non-Hermitian mode coupling in a micro-disk resonator due to stochastic surface roughness scattering” in *IEEE Photonics Journal*, v. 11, n. 2 (2019), p. 1-14, - DOI: 10.1109/JPHOT.2018.2880281;
- f C. Castellan, R. Franchi, S. Biasi, M. Bernard, M. Ghulinyan and L. Pavesi, “Field-Induced Nonlinearities in Silicon Waveguides Embedded in Lateral p-n Junctions” in *Frontiers in Physics*, v. 7, (2019). - DOI: 10.3389/fphy.2019.00104;

-
- g S. Biasi, P. Guilleme, A. Volpini, G. Fontana and L. Pavesi, “Time response of a microring resonator to a rectangular pulse in different coupling regimes” in *Journal of Lightwave Technology*, vol. 37, no. 19, pp. 5091-5099, 1 Oct, (2019). -DOI: 10.1109/JLT.2019.2928640.

In preparation

- h A. Calabrese, F. Ramiro-Manzano, H. Price, M. Bernard, S. Biasi, M. Ghulinyan, I. Carusotto and L. Pavesi, “Unidirectional reflection from an integrated “taiji” microresonator ”;
- i S. Biasi, F. Ramiro-Manzano, C. Castellan, M. Ghulinyan, I. Carusotto and L. Pavesi, “Photonic Lamb-shift induced in the transmission and phase Fano spectra of a multi-modal microresonator”.

Proceedings

- j F. Ramiro-Manzano, S. Biasi, M. Bernard, M. Mancinelli, T. Chalyan, F. Turri, M. Ghulinyan, M. Borghi, A. Samusenko, D. Gandolfi, R. Guider, A. Trenti, P.E. Larré, L. Pasquardini, I. Carusotto, G. Pucker, and L. Pavesi, “Microring Resonators and Silicon Photonics” in *MRS Advances*, Volume 1, Issue 48 (Electronics and Photonics), Cambridge: Cambridge University Press, 2016, p. 3281-3293. Proceedings of: MRS Spring meeting, Phoenix, Arizona, USA, 28 March - 1 April, (2016), -DOI: 10.1557/adv.2016.393;
- k S. Biasi, F. Ramiro Manzano, M. Ghulinyan, I. Carusotto and L. Pavesi, Lorenzo, “From the Backscattering to the reactive coupling” in *Integrated Photonics Research, Silicon and Nanophotonics in Proceedings OSA Advanced Photonics Congress (AP) 2019* (IPR, Networks, NOMA, SPPCom, PVLED), Burlingame, California United States 29 July–1 August 2019: OSA Technical Digest (Optical Society of America), (2019).

The outline of my thesis is the following: chapter 2 contains the study in the frequency domain of the coupling between counter-propagating modes and the extension of our analysis to the case of two co-propagating modes. This chapter is based on the work contained in article (e). Here, in collaboration with Dr. I. Carusotto I realized the theoretical model of backscattering that includes Hermitian and non-Hermitian coupling terms. I studied the complex visualization of the transmission and phase response by employing the parametric phasor diagrams and the inverse complex representations. In addition, I collaborated with Dr. F. Ramiro Manzano on the numerical simulations of the ring resonators, which present a non-negligible surface roughness. Finally, with Dr. F. Ramiro Manzano and Dr. F. Turri I worked on the experimental measurements of the transmission and phase response of the wedge microresonator. The notions acquired in this analysis have been extended to the case of a multimodal microdisk resonator, see articles (i), (k). In section 2.5, I reformulated the theoretical model of two

1. Introduction

interacting modes by studying the modal interference in the form of a Lorentzian shape perturbed by an interaction term. With Dr. C. Castellan I worked on the numerical simulations and I measured the experimental results with the help of Dr. F. Ramiro Manzano. The end of chapter 2 shows that the backscattering coefficients can be forced in order to select the clockwise or counterclockwise mode by modifying the geometry of the microresonator/waveguide system. This result find a connection with the taiji microresonator work reported in (h).

The main experimental results which support the theory of chapter 2 are presented in chapter 5. Here the novel optical setup reported in article (c) is described. In this work, I collaborated with Dr. F. Ramiro Manzano by building the optical setup and by writing the LabView code to remote control the apparatus. With Dr. F. Turri I performed the characterization measurements shown in manuscript (c). Chapter 5 also contains a section related to the study of the *SiON* platform based on the work (d). Here, I used our Mach-Zehnder interferometer to measure the transmission and phase responses of the racetrack microresonators by estimating the intrinsic and extrinsic coefficients.

The work presented in chapter 3, contains the results obtained by studying the temporal response of a microresonator/waveguide system. The central body is based on article (g). Here, with Dr. P. Guilleme, I derived the theoretical model and participated in numerical simulations. The experimental results of this work are contained in chapter 6. In this case, I collaborated to the realization of the experimental setup and the measurement of the temporal response with Dr. G. Fontana and Mr. A. Volpini. In addition, with Dr. M. Ghulinyan and Miss. C. Vecchi I extended the optical setup to the case of a macroscopic cavity and, finally, performed the Cavity ring down measurements. In addition, this experimental chapter contains the response measurements of the taiji microresonators studied in the theoretical chapter 2.

Chapter 4 presents the propagation of a light beam in materials that exhibit nonlinear properties. The first part is the result of a collaboration with the Bose-Einstein condensate group of the University of Trento. As mentioned, we exploit the analogy between the nonlinear Schrödinger equation of a propagating impulse and the Gross-Pitaevskii equation of a condensate. Thus, a nonlinear process of the third order was studied using the mathematical methods of the field of cold atoms. This part is based on work (b). As we will see, in the reformulation of the process, the parallelism between photons and cold atoms allows introducing the concept of superfluid of light. The model developed is well structured since it is based on two processes well-known in two different fields, i.e. photons and cold atoms. Unfortunately, from the experimental point of view, this chapter does not find a conclusion within this thesis. In fact, the limit in the fabrication of waveguides combined with the maximum accuracy of our optical setup have not yet allowed measuring the characteristic linear dispersion of the fluid of light. Within this work, with Dr. Pierre I participated in the first part of the theoretical derivation, in particular in the parallelism between the degenerate four wave mixing process and the Bogoliubov spectrum. With Dr. Pierre, Dr. Fernando and Dr. I. Carusotto, I worked in the extrapolation of the observable to be measured as well as in the design of the optical setup. In

addition, with Dr. Fernando Ramiro-Manzano I collaborated to the numerical simulation of the waveguides. This experimental setup is based on the extension of the Mach-Zhender interferometer to pump and probe measurements. It refers to the work (c) and is reported in the chapter 5. For the sake of completeness, the last part of chapter 4 considers the study of the nonlinear response of a waveguide/microresonator system. This section introduces the thermo optic coefficient comparing its effect with the Kerr nonlinearity. Precisely, it shows how the energy stored inside the cavity can strongly modify the transmitted intensity of a microrisonator bringing to a bistability behavior. This opens future perspectives for using a different energy distribution between counter-propagating mode in order to break the Lorentz reciprocity theorem. All the integrated photonics circuits studied in this thesis have been made by Dr. Georg Pucker, Dr M. Ghulinyan and their collaborators in the Fondazione Bruno Kessler (FBK) processing facility.

Part I

Theory and Simulations

Chapter 2

Hermitian and non-Hermitian systems

The energy conservation is a fundamental concept which underlies our understanding of the nature. In physics and chemistry, the total energy of an isolated system remains constant over the time. From a theoretical point of view, this can be proved by using the Noether's theorem because of the validity of the temporal translation symmetry [30]. Therefore, the energy conservation is a direct consequence of the fact that the laws of physics do not change over time [31]. In other words, this means that the laws of nature do not change by changing the time of an experiment. Such property is generally called time invariance.

In quantum physics, the energy conservation demands that a closed system exhibits real-valued eigenvalues [32]. For this reason, the physical models have been based on the mathematical Hermiticity of the systems. These models require the description of the physical system as a whole by means of a Hermitian Hamiltonian. Thus, they are based on the assumption of a complete isolation of the system from its surrounding environment [33]. However, the reality often demands a description of a part of a system. In these cases, the energy can be exchanged between the specific subsystem and its environment. This leads to the introduction of non-conservative elements and, then, of a non-Hermitian Hamiltonian. By nature, optics is ruled by non-Hermitian Hamiltonian. In fact, the dissipation is everywhere in optics, it arises from the material absorption as well as from the radiation to the environment [19]. Therefore, in optics the non-Hermitian Hamiltonians have a direct meaning, they represent systems with loss and/or gain.

Typically, the non-Hermitian models have been introduced as a perturbation to Hermitian ones where the physical behavior of the system is not affected a part for an exponential decay [34, 35]. A simple example is the propagation of a beam through a crystal, where the refractive index is a complex quantity. Here, the material response is described by a real term (dispersion) and an imaginary term (losses or gain). Generally, non-Hermitian matrices exhibit complex eigenvalues. However, in 1998 Carl Bender and Stefan Boettcher [36] showed that it does exist a large class of dissipative Hamiltonian that exhibits entirely real eigenvalues. These non-Hermitian matrices commute with the parity-time (PT) operator. Such operator describes the PT symmetry, which demands that the physics is equivalent for a system and its mirror image (parity symmetry P) and even when the time is running backwards (time reversal T) [33].

The radically difference between the non-hermiticity and the hermiticity arises in the presence of degeneracies, i.e. when the eigenvalues coalesce [35]. Let

us consider the Hermitian matrices that are real symmetric because they describe a conservative physics with time-reversal symmetry. In these cases, the three-dimensional space of eigenvalues, as a function of two dependent parameters, forms a double-cone topology (a diaboloid) where the cones touch each other at their apex creating a diabolic point (DP) [19, 33, 35]. Here, approaching the degeneracy, the eigenvectors remain orthogonal. The non-Hermitian matrices exhibit a complex topology of two intersecting Riemann sheets centered on the degeneracies in the three-dimensional space of eigenvalue with respect to two parameters [19, 33, 35]. Such degeneracies are referred to as exceptional points (EPs). Contrary to the Hermitian matrices, approaching the degeneracy, not only the eigenvalues but also the eigenvectors coalesce. The appearance of the EPs is associated with the PT symmetry breaking which causes the eigenvalues to change from being real valued to be complex valued [33].

The EPs and the PT-symmetry breaking find in optics a fertile ground in which they can be fruitfully studied. In fact, the realization of optical structures working close to the EPs have brought to the demonstration of non-trivial effects such as unidirectional invisibility [37, 38, 39], loss-induced transparency [40], non-reciprocal light propagation [21], chiral modes [41], directional emission [22] and PT-symmetric lasers [42].

In this chapter, starting from a general model, we describe the mathematical framework of the Hermitian and non-Hermitian physics. The isomorphism between Schrodinger's equation -describing the temporal evolution of a quantum particle in a potential- and the Helmholtz wave equation -describing the spatial evolution of the electric field envelope- allows depicting a parallelism between quantum mechanics and classical waves. Thus, we will use definitions typically introduced in the context of quantum mechanics because they naturally extend to the classical waves. The attention is focused on the two different degeneracies: DPs and EPs. In particular, we show how the presence of the EPs changes the optical response of a microresonator subject to the backscattering due to the surface wall roughness.

2.1 Theoretical background: from diabolic points to exceptional points

Let us study the DPs and EPs by considering a generic two-level system. From a theoretical point of view, the dynamics of these structures can be described by the temporal coupled mode theory (TCMT) as [43]:

$$\frac{d}{dt} \begin{pmatrix} \alpha_1 \\ \alpha_2 \end{pmatrix} = i \begin{pmatrix} \omega_1 + i\rho_1 & i\beta_{12} \\ i\beta_{21} & \omega_2 + i\rho_2 \end{pmatrix} \begin{pmatrix} \alpha_1 \\ \alpha_2 \end{pmatrix}, \quad (2.1)$$

where $\alpha_{1,2}$ and $\omega_{1,2}$ are the amplitudes and the resonant frequencies of the two coupled modes respectively. $\rho_{1,2}$ ($\beta_{12,21}$) are the damping rate (complex coupling coefficient) of the two modal amplitudes. As shown in figure 2.1, this Hamiltonian, depending on the matrix values, describes a large class of devices relevant in photonics. In particular, it describes the coupling of two single

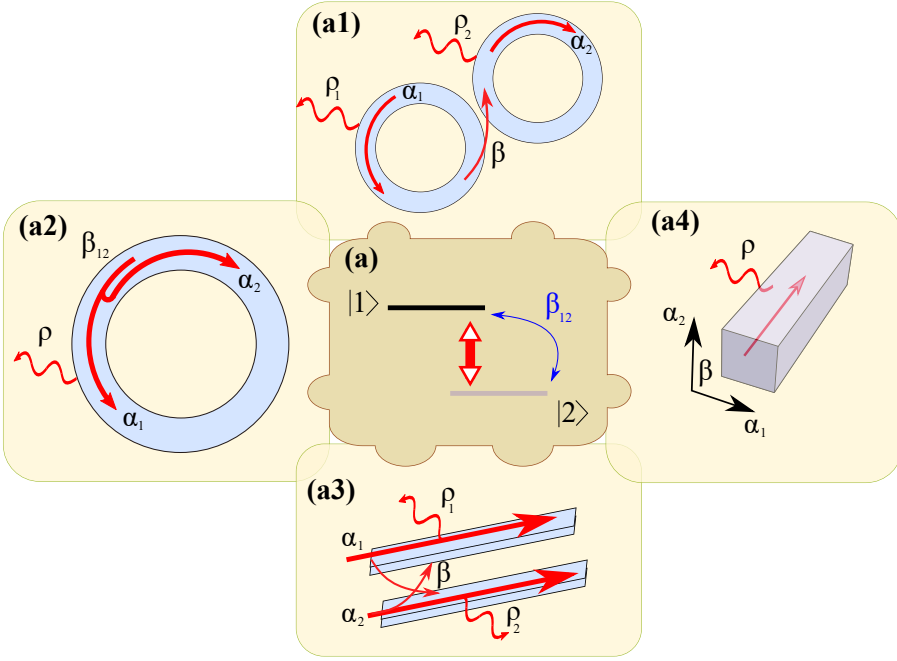


Figure 2.1: Mathematical framework of a two-level system in optics. (a) Sketch of a two-level $|1\rangle$ and $|2\rangle$ coupled via the coefficient β_{12} , (a1) two single-mode resonant cavities coupled via their evanescent field, (a2) a resonant cavity which exhibits backscattering due to the surface wall roughness, (a3) evanescent coupling between two straight waveguides, (a4) coupling between the two orthogonal polarization states inside a waveguide.

mode resonant cavities or waveguides (figure 2.1 (a1) and (a3) respectively), coupling of co-propagating and counter-propagating modes inside a resonator due to the backscattering (figure 2.1 (a2)), the variation of the polarization states inside an optical waveguide (figure 2.1 (a4)) and the wave mixing in nonlinear crystals. In the following, without losing generality, we will reformulate the 2×2 Hamiltonian of equation 2.1 as the sum of two matrices. In this way, varying the matrix elements, we can investigate when the system is Hermitian, PT-symmetric and PT-non-symmetric non-Hermitian. Defining $\chi_+ = (\rho_1 + \rho_2)/2$ and $\chi_- = (\rho_2 - \rho_1)/2$ as an overall damping rate, one can write the equations system 2.1 as:

$$\frac{d}{dt} \begin{pmatrix} \alpha_1 \\ \alpha_2 \end{pmatrix} = i \left[\begin{pmatrix} \omega_1 - i\chi_- & i\beta_{12} \\ i\beta_{21} & \omega_2 + i\chi_- \end{pmatrix} + \begin{pmatrix} i\chi_+ & 0 \\ 0 & i\chi_+ \end{pmatrix} \right] \begin{pmatrix} \alpha_1 \\ \alpha_2 \end{pmatrix}. \quad (2.2)$$

2. Hermitian and non-Hermitian systems

The first matrix of the right side of this equation presents, in the diagonal elements, the same magnitude of loss and gain ($\mp\chi_-$)¹. Let us define the complex off-diagonal coupling coefficients as: $i\beta_{12} = (a + \delta a_1) - i(b + \delta b_1)$ and $i\beta_{21} = (a + \delta a_2) + i(b + \delta b_2)$. Thus, the previous Hamiltonian can be reformulated in the following form:

$$\begin{pmatrix} \omega_1 - i\chi_- & a - ib \\ a + ib & \omega_2 + i\chi_- \end{pmatrix} + \begin{pmatrix} i\chi_+ & \delta a_1 - i\delta b_1 \\ \delta a_2 + i\delta b_2 & i\chi_+ \end{pmatrix} = H_0 + H_1, \quad (2.3)$$

where the two off-diagonal coupling coefficients of H_0 have the same and opposite real and imaginary part, respectively.

2.1.1 Hermitian systems and DPs

Following the definition of the quantum mechanics, the Hamiltonian H_0 of equation 2.3 is Hermitian when $H_0 = H_0^\dagger$. The subscript \dagger is defined as the matrix operation of transposition plus complex conjugation. Such requirement ensures real eigenvalues and consequently a unitary time evolution for which the system is non-dissipative [32]. The Hamiltonian H_0 is Hermitian, if and only if $\chi_- = 0$ and, then, $\rho_1 = \rho_2$. In this case, the system can be considered as a whole and it is conservative with no loss and gain. It is worth noticing that the off-diagonal elements have been written in the form of equation 2.3 in order to satisfy the Hermitian matrix definition. In summary, the Hamiltonian H_0 reduces to:

$$H_0 = \begin{pmatrix} \omega_1 & a - ib \\ a + ib & \omega_2 \end{pmatrix}. \quad (2.4)$$

Assuming harmonic solutions, the eigenvalues of this Hermitian matrix are:

$$\lambda_{\pm} = \Omega_{\pm} \pm \sqrt{\Omega_{-}^2 + (a^2 + b^2)} \quad (2.5)$$

where $\Omega_{\pm} = \frac{1}{2}(\omega_1 \pm \omega_2)$ are the overall frequencies of the system. As expected, the eigenvalues are real for whatever frequencies and/or coupling coefficients of the two modes. As we will see in the backscattering chapter 2.2, the coefficients a and b give rise to the same non-dissipative coupling between the mode amplitudes. Without loss of generality, we can assume one of the two terms equal to zero ($a = 0$ or $b = 0$). Furthermore, if both the a and b coefficients are different from zero, the two eigenvalues cannot be degenerate.

Figure 2.2 shows the eigenvalue of equation 2.5 as function of the frequency detuning Ω_- and the off-diagonal coefficient a , fixing $b = 0$. As shown in the 3D plot of figure 2.2 (a), varying the frequency detuning (Ω_-) and the coupling strength (a) the eigenvalues form a double-cone topology with a DP degeneracy

¹It is worth noticing that the second matrix of the equations system 2.2 introduces just an overall damping term. In fact, considering the transformation $\begin{pmatrix} \alpha_1 \\ \alpha_2 \end{pmatrix} = e^{-\chi_+ t} \begin{pmatrix} \alpha'_1 \\ \alpha'_2 \end{pmatrix}$, the equations 2.2 reduce to: $\frac{d}{dt} \begin{pmatrix} \alpha'_1 \\ \alpha'_2 \end{pmatrix} = i \begin{pmatrix} \omega_1 - i\chi_- & i\beta_{12} \\ i\beta_{21} & \omega_2 + i\chi_- \end{pmatrix} \begin{pmatrix} \alpha'_1 \\ \alpha'_2 \end{pmatrix}$.

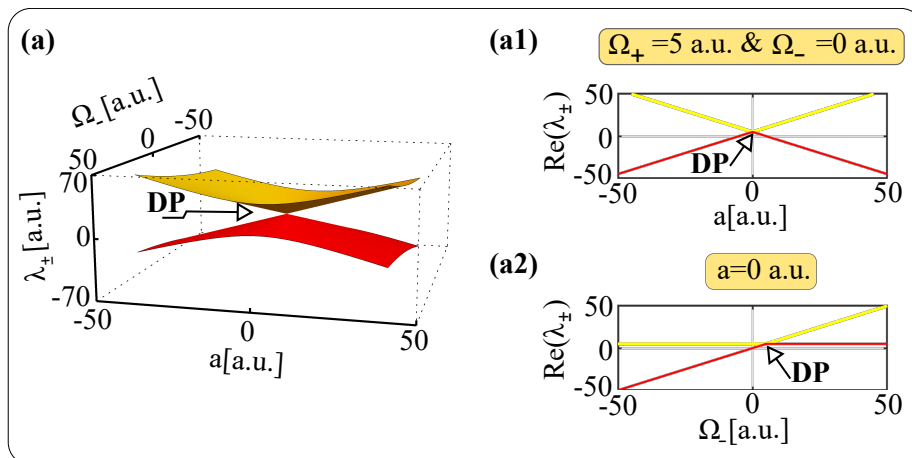


Figure 2.2: Eigenvalues as a function of the frequency detuning Ω_{-} and the coupling coefficient a . (a) Double-cone topology of the Hermitian degeneracy; the yellow and red surfaces show the two eigenvalues of equation 2.5. Panels (a1) and (a2) are drawing sections of the figure (a) when: $\Omega_{+} = 5$ a.u. with $\Omega_{-} = 0$ a.u. and $a = 0$ a.u. respectively. The black arrows highlight the *DP* points.

on their apex when $\Omega_{-} = a = 0$ (i.e. $\omega_1 = \omega_2$ and $a = 0$). In these systems, around a DP, the resulting eigenvalues splitting is linearly proportional to the coupling coefficients keeping $\Omega_{-} = 0$ (see figure 2.2 (a1)) or to the frequency detuning fixing $a = 0$ (see figure 2.2 (a2)). The Hermitian Hamiltonian is characterized by eigenvectors that are mutually orthogonal for each value of the matrix elements. Here, they can be expressed with respect to the frequency detuning and coupling strength as $\bar{v}_{\pm} = \left(\frac{\Omega_{-}}{a} \pm \sqrt{\left(\frac{\Omega_{-}}{a}\right)^2 + 1}, 1 \right)$. It is worth noticing that they are orthogonal also in the diabolic degeneracy.

A simple and didactic experimental demonstration of the diabolical degeneracies and double-cone topology of eigenvalues was proposed by M.V. Berry in ref. [44]. In this work is introduced a structure consisting of two squares of polaroid sheet that contain, like a sandwich, a square of overhead-projector plastic transparency foil. Looking at the transmission of diffused light over a range of directions it is possible to see the diabolic degeneracy as interference fringes that form a bull's-eye. Examples of photonic structures that fall into this category are: two cavities with the same resonant frequencies and intrinsic losses coupled via non-dissipative terms, a resonant cavity that exhibits a conservative coupling between the co-propagating and the counter-propagating modes.

2.1.2 PT-symmetric non-Hermitian systems and EPs

The PT-symmetry was first proposed in quantum mechanics [45]. Thanks to the analogy between the Schroedinger and Helmholtz wave equations, the PT-symmetry can be extended to the context of optics. The parity P operator corresponds to the Pauli operator $\sigma_x = \begin{pmatrix} 0 & 1 \\ 1 & 0 \end{pmatrix}$ while the time reversal one coincides with the complex conjugation. The matrix H_0 is PT-symmetric when it commutates with the PT operator (i.e. $[H_0, PT] = 0$). Making use of this relation and considering the properties of the parity and time operator (unitary $TT = T^2 = I$, $PP = P^2 = I$ and $T = T^{-1}$, $P = P^{-1}$) one obtains that the matrix H_0 satisfies the PT-symmetry when $H_0 = PH_0^*P$. This happens if and only if the frequency detuning Ω_- reduces to zero, then $\omega_1 = \omega_2 = \omega_0$:

$$\begin{aligned} \begin{pmatrix} \omega_0 - i\chi_- & a - ib \\ a + ib & \omega_0 + i\chi_- \end{pmatrix} &= \begin{pmatrix} 0 & 1 \\ 1 & 0 \end{pmatrix} \begin{pmatrix} \omega_0 + i\chi_- & a + ib \\ a - ib & \omega_0 - i\chi_- \end{pmatrix} \begin{pmatrix} 0 & 1 \\ 1 & 0 \end{pmatrix} \\ &= \begin{pmatrix} 0 & 1 \\ 1 & 0 \end{pmatrix} \begin{pmatrix} a + ib & \omega_0 + i\chi_- \\ \omega_0 - i\chi_- & a - ib \end{pmatrix} \\ &= \begin{pmatrix} \omega_0 - i\chi_- & a - ib \\ a + bi & \omega_0 + i\chi_- \end{pmatrix}. \end{aligned} \tag{2.6}$$

Assuming harmonic solutions, the eigenvalues of this non-Hermitian matrix are:

$$\lambda_{\pm} = \omega_0 \pm \sqrt{a^2 + b^2 - \chi_-^2} \tag{2.7}$$

As in the previous paragraph, without losing generality, we can study the equation of the eigenvalues 2.7 by assuming $b = 0$. In this case, the system has real (complex) eigenvalues when the condition $a \geq \chi_-$ ($a < \chi_-$) is satisfied. It is worth noticing that contrary to the Hermitian system showed in the previous subsection, in this case it is possible to obtain a degeneration of the eigenvalues even if both the coefficients a and b are different from zero. Figures 2.3 (a) and (b) show the three-dimensional plot of the real and the imaginary parts of the eigenvalues as a function of the overall damping rate χ_- and the coupling strength. The topology of the eigenvalues displays two intersecting Riemann sheets centered around the degeneracies. These degeneracies occur when $a = \chi_-$ (see equation 2.7) and are knew as EPs. Figures 2.3 (a1) and (a2) display a drawing section of figure 2.3 (a) when $\chi_- = 50 a.u.$ and $a = 50 a.u.$, respectively. The imaginary part is highlighted in figures 2.3 (b1) and (b2) by the drawing section of figure 2.3 (b) when $\chi_- = 50 a.u.$ and $a = 50 a.u.$, respectively. As expected, around an EP, the eigenvalue splitting scales as the square root of the perturbation magnitude. The eigenvector of this Hamiltonian can be formulated as $\bar{v}_{\pm} = \left(\frac{i\chi_-}{a} \pm \sqrt{1 - \left(\frac{\chi_-}{a}\right)^2}, 1 \right)$. Contrary to the Hermitian case, at the EP not only the two eigenvalues but also the two eigenvectors coincide (i.e. $\bar{v}_{\pm} = (i, 1)$). Furthermore, as we will see in the next paragraphs, introducing a perturbation

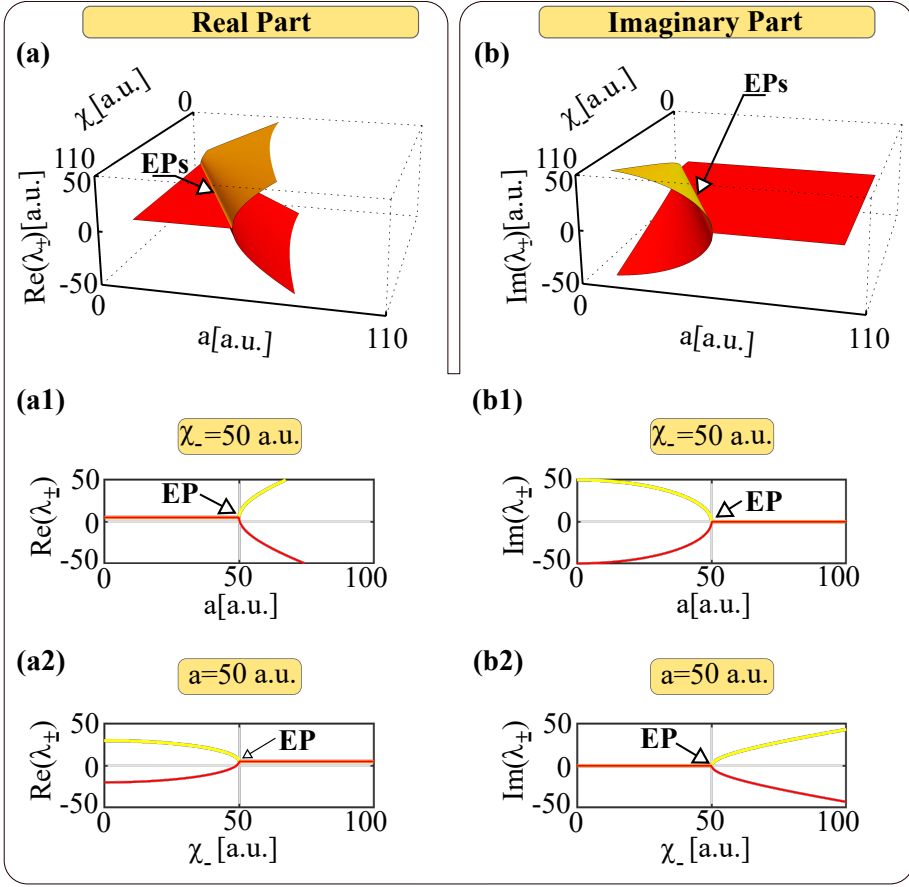


Figure 2.3: Real and imaginary part of the eigenvalues as a function of the overall damping rate χ_{-} and the coupling coefficient a . Panels (a) and (b) are the topology of the non-Hermitian degeneracies in the real and in the imaginary space, respectively. The yellow and red surfaces display the two eigenvalues of equation 2.7. Images (a1), (a2) and (b1), (b2) are the drawing sections of figure (a) and (b) when $\chi_{-} = 50$ a.u. and $a = 50$ a.u..

of this Hamiltonian it is possible to break the PT-symmetry. As a result, one can induce a phase transition in which the symmetry of the eigenvectors is spontaneously broken and the transition threshold occurs precisely at an EP. In photonics, this can give rise to counterintuitive optical phenomena such as unidirectional reflection [39].

Example of optical devices that can be described by this formalism are two identical coupled structures in which one exhibits optical gain and the other loss of equal magnitude. This configuration can be achieved by considering

two coupled waveguide or resonant cavities. Such structures satisfy the PT-symmetry: the parity operator interchanges the two elements while the time operator changes loss to gain and gain to loss. Not only systems with gain - called active - fall into this category but also passive structures where gain is not involved [34]. In equation 2.3 we have seen that a non-Hermitian Hamiltonian can be formulated as a PT-symmetric matrix plus the sum of two matrices, one for the uncoupled and the other for the coupled loss. Therefore, the dynamics of loss-loss systems can be treated as those of loss-gain structures except from a global exponential decay and amplification. Examples of passive devices that fulfill this mathematical framework are two cavities with the same resonant frequency and different intrinsic losses coupled via non-dissipative terms, a resonant cavity subjected to the non-conservative backscattering, and optical systems composed by layers with different imaginary parts of the refractive index.

2.1.3 Excitation and response measurement: a three-level system

The optical devices that fall within the mathematical description of a two-level system are partially limited from a practical point of view. In fact, in order to study these structures, it is necessary to excite them and measure their responses. The excitation and measurement of the response simply consist in coupling a beam of light to the input of the sample, and measuring its intensity at the output. There are different ways of excitation depending on the structure under investigation. For example, in integrated optical circuits, the evanescent field coupling approach is typically used where a waveguide is placed near to the optical system [46]. On the other hand, in bulk systems, excitation consists in coupling the beam of light in free-space and, then, coupling the light through the incident field [46, 47]. Generally, it is possible to include the excitation and the optical response in the mathematical framework of a two-level system using a three-level system with a λ -shape (see figure 2.4 (b)). The figures 2.4 (a1), (a2) and (a3) show three examples of optical structures excited through a bus waveguide that can be treated as a three-level system. In particular, a resonant cavity, which exhibits backscattering due to surface roughness (a1), two coupled cavities (a2), and a two-mode resonator vertically coupled to a single mode waveguide (a3).

2.2 Backscattering

One of the limiting factors of microresonators with high and ultra-high quality factor is the backscattering of the propagating modes [48]. This phenomenon is generated by the surface wall roughness and it is characterized by a wave that propagates in the opposite direction with respect to the input one. Typically, the stochastic nature of the surface roughness leads to a simple statistical approach resulting in a Hermitian description of the coupling coefficients. The Hermitian

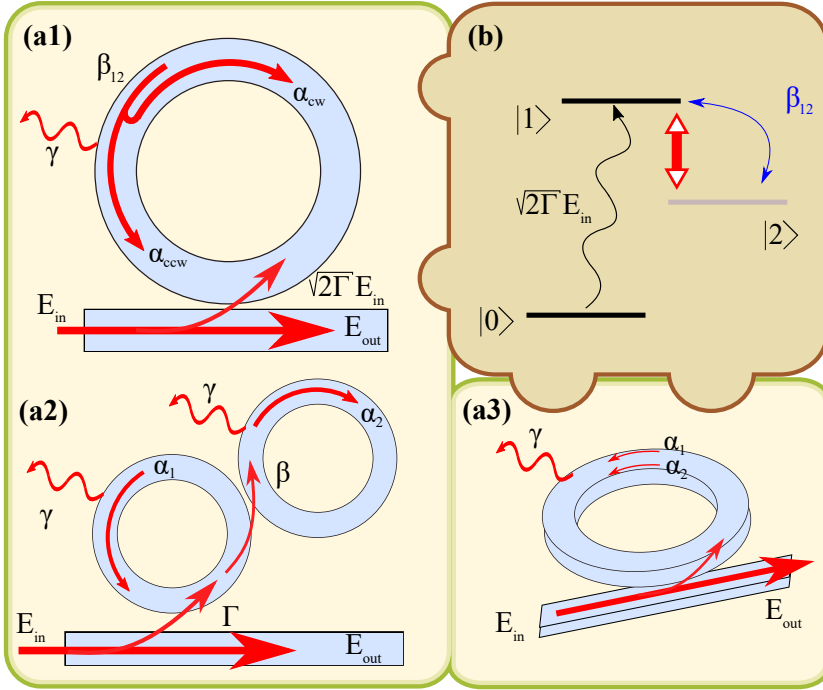


Figure 2.4: Mathematical framework of a three-level system in optics. Panel (a): sketch of a three-level system, the background $|0\rangle$ state and the excited $|1\rangle$, $|2\rangle$ states coupled via the coefficient β . Panel (a1): resonant cavity which exhibits backscattering due to the surface wall roughness coupled to a bus waveguide. Panel (a2): two single-mode resonant cavities coupled via evanescent field excited by a waveguide. Panel (a3): two-mode resonator vertically coupled to a single mode waveguide.

coupling, directly linked to a conservative exchange of energy between the co-propagating and the counter-propagating waves, leads to a symmetrical resonance splitting in the transmission spectra [11, 14, 15]. Furthermore, the Hermiticity of the coupling with the Lorentz's theorem enforces to have the same reflection in both directions of excitation.

In a recent work [16], we have showed that, in the case of multimodal microresonators, the transmission may exhibit asymmetrical resonance splitting. This asymmetry is characterized by a difference in the peak depths of the transmission doublets. We have defined this asymmetrical response as unbalance doublet. Such unbalance can be explained by considering non-Hermitian coupling coefficients. The basic idea is that the symmetrical losses, depending on the propagation direction of the beam, could be differently distributed between conservative and dissipative couplings. Therefore, in the presence of multimodal

2. Hermitian and non-Hermitian systems

microresonators, the interplay between the stochastic roughness and the inter-modal dissipative coupling could originate a collective non-symmetrical behavior. The non-Hermitian description introduces important implications in the optical responses. In fact, a non-Hermitian system may exhibit a different reflection for forward or backward propagating modes.

In this section, we will discuss the tree-level system response to stationary excitation. Focusing on the general case of backscattering in a resonator (see figure 2.4 (a1)), we will show how the presence of the excitation waveguide introduces three different coupling regimes. In addition, we will explain how the complex electric field can be characterized by the measurements of the transmission intensity and of the phase. We will start with the case in which the surface roughness gives rise to a conservative coupling between the co-propagating and counter-propagating modes (i.e. Hermitian coupling). Then, we will extend the model to the scenario where the presence of multimode inside the resonator induces a dissipative term passing to a non-Hermitian coupling description. We will demonstrate how the presence of this non-Hermitian coupling coefficient modifies the response of a waveguide/microresonator system giving rise to a non-reciprocal reflection in the limit case. Finally, we will introduce a structure exploiting this dissipative coefficient in order to create an unidirectional reflection device and, then, to avoid the backscattering.

2.3 Theoretical model

Let us consider the simplest case of a bus waveguide coupled to a resonator of resonant frequency ω_0 and define the counterclockwise (α_{ccw}) and the clockwise (α_{cw}) amplitude fields (see figure 2.4 (a1)). The dynamic of this structure can be described with the mathematical framework of a three-level system considering the TCMT:

$$\frac{d}{dt} \begin{pmatrix} \alpha_{ccw} \\ \alpha_{cw} \end{pmatrix} = i \begin{pmatrix} \omega_0 + i\rho & i\beta_{12} \\ i\beta_{21} & \omega_0 + i\rho \end{pmatrix} \begin{pmatrix} \alpha_{ccw} \\ \alpha_{cw} \end{pmatrix} + i\sqrt{2\Gamma} \mathbf{E}_{in}^T, \quad (2.8)$$

where $\rho = (\Gamma + \gamma)$ is the sum of the intrinsic and the extrinsic damping rate and $\beta_{12/21}$ are the complex coupling parameters. The difference between these coupled differential equations and those of the two-level system (equation 2.1) is connected to the last term ($i\sqrt{2\Gamma} \mathbf{E}_{in}^T$). This takes into account the coupling between the bus waveguide and the resonator. In fact, \mathbf{E}_{in} is a two column vector whose elements are the amplitudes of the electric field injected into the bus waveguide. In particular and referring to figure 2.4 (a1), the input vector can be $(E_{in}, 0)$ or $(0, E_{in})$ for an excitation that propagates from left to right or from right to left, respectively. The extrinsic coefficient (Γ) is related to the exchange of energy between the waveguide and the resonator. Instead, the intrinsic parameter (γ) describes the losses in the resonator which are due to intrinsic factors such as material absorption, and bending losses. The input and output ports, depending on the direction of the incident field, are connected by $E_{out} = E_{in} + i\sqrt{2\Gamma}\alpha_{ccw}$ for an excitation from left to right and $E_{out} = E_{in} + i\sqrt{2\Gamma}\alpha_{cw}$ for an excitation

from right to left. Instead, the reflection field amplitude is $E_{ref} = i\sqrt{2\Gamma}\alpha_{cw}$ for an excitation from left to right and $E_{ref} = i\sqrt{2\Gamma}\alpha_{ccw}$ for a right-left excitation.

As reported in [16], this system of differential equations has been determined by assuming some hypothesis that will be justified in the next simulation section and experimental part. In particular, we neglect the back-reflections from the bus-waveguide/resonator coupling and the coupling of the incident field to the oppositely circulating modes. Moreover, in the absence of the roughness, the counterclockwise and the clockwise propagating modes are related by specular symmetry, so they have the same resonant frequency, they are subject to the same intrinsic losses, due to material absorption, and they are identically coupled to the corresponding incident field. When the surface wall roughness is relevant, the physics changes. The coupling coefficients β_{12} and β_{21} can have fully independent values, their Hermitian and non-Hermitian parts are generally fully independent from each other.

2.3.1 Transmission and reflection

Let us analyze the transmission and reflection response of our system in the frequency domain. The stationary solution of the differential equations 2.8 is obtained by considering a monochromatic input field $E_{in} = E_{in0} e^{i\omega t}$. In this way, one can obtain, for the two different directions of excitation (i.e. $(E_{in}, 0)$ and $(0, E_{in})$), the same analytical expression of the field amplitude transmission $t = E_{out}/E_{in}$:

$$t = 1 - \frac{2\Gamma (i\Delta\omega + \gamma + \Gamma)}{(i\Delta\omega + \gamma + \Gamma)^2 - (\beta_{12}\beta_{21})}, \quad (2.9)$$

where we have defined the frequency detuning as $\Delta\omega = \omega - \omega_0$. As expected, in according with the Lorentz's theorem, the transmission from left to right is equal to that from right to left ($t_{r-l} = t_{l-r} = t$). A different behavior arises in the case of the reflection amplitude. Since the off-diagonal coupling elements of the matrix 2.8 (β_{12} and β_{21}) may be different, the reflection amplitudes, swapping the input with the output port, can be different:

$$r_{l-r} = \frac{2\Gamma \beta_{21}}{(i\Delta\omega + \gamma + \Gamma)^2 - (\beta_{12}\beta_{21})} \quad (2.10)$$

and

$$r_{r-l} = \frac{2\Gamma \beta_{12}}{(i\Delta\omega + \gamma + \Gamma)^2 - (\beta_{12}\beta_{21})}. \quad (2.11)$$

2.3.2 No surface wall roughness

Considering a surface wall with no roughness, the off-diagonal coupling elements reduce to zero. Consequently, the two reflections tend to zero according to the hypothesis of no backscattered wave in the coupling region. In this case, the transmission amplitude assumes the simple shape:

$$t = 1 - \frac{2\Gamma}{i\Delta\omega + \gamma + \Gamma}. \quad (2.12)$$

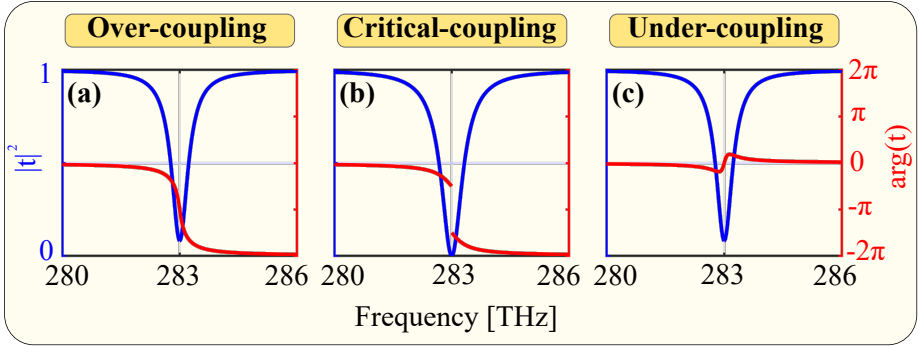


Figure 2.5: Intensity and phase of the output transmission response as a function of the frequency. Panels (a), (b) and (c) show the over-, critical- and under-coupling, respectively. The resonant frequency is $\omega_0 = 283 \text{ THz}$. The intrinsic and extrinsic damping rate used in the over-coupling (under-coupling) case are $\gamma(\Gamma) = 90 \text{ GHz}$ and $\Gamma(\gamma) = 162 \text{ GHz}$. The Critical coupling of panels (b) is obtained fixing $\gamma = \Gamma = 162 \text{ GHz}$.

The square modulus of this expression is the transmitted intensity and it assumes the conventional shape of a DC component minus a symmetric Lorentzian shape:

$$|t|^2 = 1 - \frac{4\gamma\Gamma}{(\gamma + \Gamma)} \frac{(\gamma + \Gamma)}{\Delta\omega^2 + (\gamma + \Gamma)^2}. \quad (2.13)$$

The Lorentzian function is the typical frequency response of a resonant system. Here, the full width at half maximum (FWHM) is given by $2(\gamma + \Gamma)$. Focusing the attention on equation 2.13, we can introduce the quality factor (Q) exploiting its definition via the bandwidth [49]:

$$Q = \frac{\omega_0}{FWHM} = \frac{\omega_0}{2(\Gamma + \gamma)}. \quad (2.14)$$

The quality factor determines the figure of merit of a resonator and describes the efficiency with which a resonator traps the light. As we will see in chapter 3, the previous definition is equivalent to the more intuitive quality factor definition via the stored energy. At this point, it should be noted that the introduction of the excitation bus waveguide changes the response of the system. As previously mentioned, the coefficient Γ takes into account the rate of energy exchange between the waveguide and the resonator, while γ considers the dissipations arising from the material absorption and/or the radiation to the environment. Depending on the values of the extrinsic Γ and the intrinsic coefficients, three different coupling regimes can be identified: critical- ($\Gamma = \gamma$), under- ($\Gamma < \gamma$) and over-coupling ($\Gamma > \gamma$).

Figures 2.5 (a), (b) and (c) show the transmitted intensity ($|t|^2$) and the phase ($\arg(t)$) as a function of the input field frequency for the three different

regimes: over-, critical- and under-coupling, respectively. At the critical-coupling $\Gamma = \gamma$ and the transmission goes to zero at resonance (see panel (b)). The Lorentzian of the under-coupling regime of figure (c) is obtained by exchanging the extrinsic and intrinsic coefficients of the over-coupling case (panel (a)). It is worth noticing that the transmitted intensities so determined are identical. In fact, the equation 2.13 is unaffected by changing the value of Γ with γ . Therefore, it is not possible to discriminate in figures 2.5 (a) and (c) the two regimes of under- and over-coupling by only knowing the transmission in the frequency domain. On the contrary, as shown in figures 2.5 (a) and (c), the phase allows discriminating between the different regimes.

From a physical point of view, this can be understood by studying the expression of the transmission amplitude 2.12. This relation is determined by the interference between the field coming out of the resonator (the Lorentzian component) and the field which goes through the bus waveguide (the DC component). As will be explained in more details in the time domain section (chapter 3), the difference in phase between these two fields is crucial to understand the coupling regime of the system. In fact, due to the energy conservation and the resonance condition, on resonance, the phase difference between the field coming out of the resonator and the field which goes through the waveguide is equal to π . Consequently, as shown in figure 2.5, the phase shift of the transmitted field on resonance is π and 0 in over- and under-coupling regimes, respectively. This can be understood intuitively by the destructive interference between the two fields. In particular, when the system is in the under-coupling regime, the intrinsic coefficient is greater than the extrinsic one. As a result, the exchange of energy between the waveguide and the resonator is not efficient and the phase of the output field is determined by the input field. On the contrary, in the over-coupling regime, the extrinsic coefficient is greater than the intrinsic one and, therefore, the energy is efficiently exchanged between the resonator and the bus waveguide. The phase shift of the output field is, then, determined by the field coming out of the resonator and is equal to π .

2.3.3 Complex visualization: phasor and inverse complex graph

As we have seen in the previous sections, the transmitted field is a complex quantity and so, it is completely characterized by the knowledge of its module (i.e. intensity $|E|^2$) and its argument (i.e. phase $arg(E)$). These informations can be condensed into a single representation by considering separately the real and imaginary part of the field: $Re[E] = |E| \cos[arg(E)]$ and $Im[E] = |E| \sin[arg(E)]$. Plotting together the real and imaginary parts as a function of an independent variable, one obtains a two-dimensional graph, which is typically called parametric phasor plot. This representation has been widely used in electronics as a method of analysis, but has not found comparable attention in optics [14, 50]. As reported in [16], the parametric phasor plot is an useful tool to study interference phenomena such as the backscattering or the interaction between different modes.

2. Hermitian and non-Hermitian systems

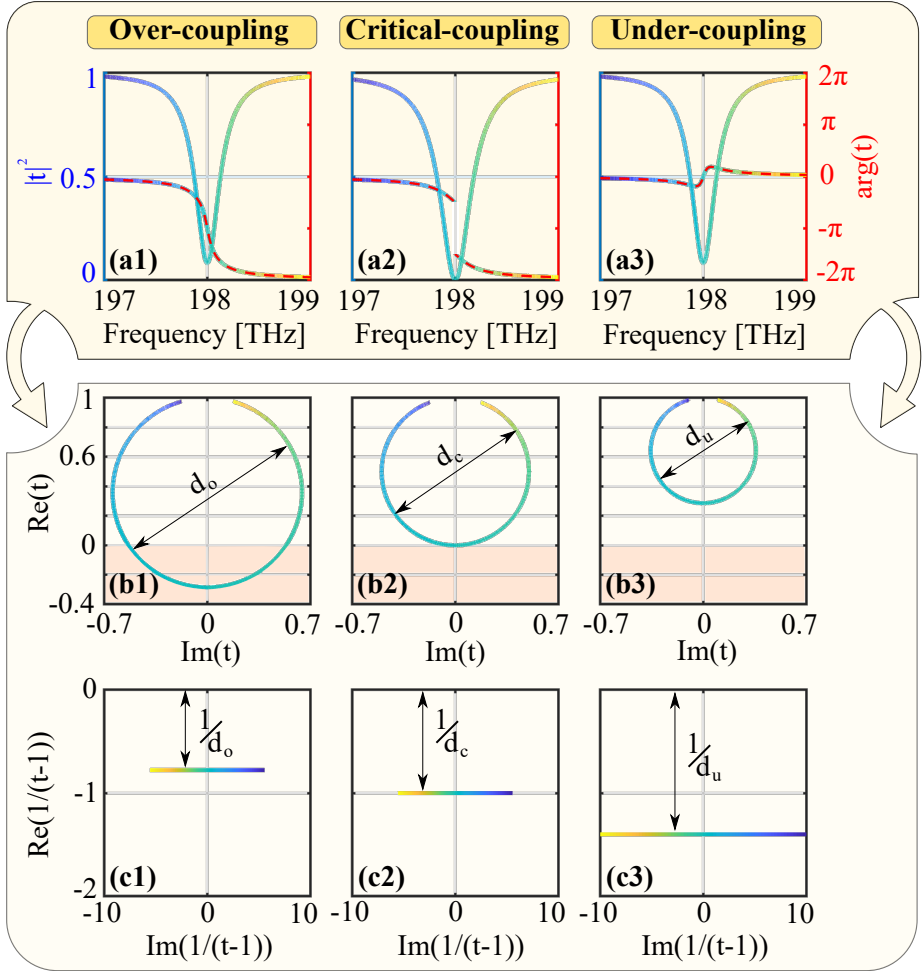


Figure 2.6: (a1-a3) Transmission intensity ($|t|^2$) and phase ($arg(t)$) as a function of the incident frequency for over-, critical- and under-coupling respectively. The red dashed lines highlight the phase response. Panels (b1-b3) and (c1-c3) show parametric phasor plot and inverse complex representation of the graphs (a1-a3). The rainbow colors show the frequency values and they allow relating the panels on the same column. The parameters used are $\omega_0 = 198 THz$, $\gamma = 50 GHz$ ($\gamma = 90 GHz$) and $\Gamma = 90 GHz$ ($\Gamma = 50 GHz$) for over-coupling (under-coupling). The critical-coupling regime is obtained by fixing $\gamma = \Gamma = 90 GHz$.

Let us start considering the simplest case of a single mode resonator with a field amplitude transmission described by equation 2.12. We use the frequency of the input field (ω) as independent variable for the parametric plot. Figures

2.6 (a1-a3) show the graphs of the square module and argument of the field amplitude transmission as a function of the frequency for the different coupling regimes. In particular, the panels (a1), (a2) and (a3) represent over-, critical- and under-coupling regimes. In the figures 2.6 (b1-b3) the phase and intensity are put together in a phasor representation. The rainbow colors represent the values of the different frequencies and they allow relating the graphs displayed on the same column. As you can see in the phasor plots (panels (b1), (b2) and (b3)), the Lorentzian transmission and its peculiar phase shape translates into a perfect circle. From an intuitive point of view, this perfect circle can be understood by analyzing the real and imaginary part of the transmitted field amplitude:

$$Re[t] = 1 - \frac{2\Gamma(\gamma + \Gamma)}{\Delta\omega^2 + (\gamma + \Gamma)^2} \quad \text{and} \quad Im[t] = \frac{2\Gamma\Delta\omega}{\Delta\omega^2 + (\gamma + \Gamma)^2}. \quad (2.15)$$

As we will see in the section dealing with the temporal response of the resonator, these two expressions are nothing more than the inverse Fourier transform of the real ($E_{out}[t] \cos(\omega_0 t)$) and imaginary ($E_{out}[t] \sin(\omega_0 t)$) components of the temporal output field, obtained by a stationary excitation $E_{in} = E_{in0} e^{i\omega t}$. Since the phasor condenses phase and transmission, the diameter of the circle is directly connected to the coupling regime of the system. In particular, the real part of the transmission on the resonant frequency ($\Delta\omega = 0$) can be reformulated as:

$$Re[t] = 1 - \frac{2}{(1 + \frac{\gamma}{\Gamma})}. \quad (2.16)$$

From this expression it is easy to see that, when the resonator is in the critical-coupling regime ($\gamma = \Gamma$), the real part reduces to 0. Interestingly, when the resonator is under (over)-coupling regime the real part is positive (negative). This behavior is confirmed by the panels (b1), (b2) and (b3) of figure 2.6. Using the equation 2.16, it is possible to formulate the real and imaginary parts in the more common equation of a circle, such as $x^2 + y^2 = r^2$:

$$\left(\frac{1}{1 + \frac{\gamma}{\Gamma}} - \frac{2\Gamma(\gamma + \Gamma)}{(\gamma + \Gamma)^2 + \Delta\omega^2} \right)^2 + \left(\frac{2\Gamma\Delta\omega}{\Delta\omega^2 + (\gamma + \Gamma)^2} \right)^2 = \left(\frac{1}{1 + \frac{\gamma}{\Gamma}} \right)^2. \quad (2.17)$$

As expected, the radius depends on the coupling regime, in particular, the diameter ($d = 2r$) is $d > 1$, $d = 1$ and $d < 1$ for the regime of over-, critical- and under-coupling, respectively.

In addition, it is possible to exploit these perfect circles by using the properties of the complex plane. By performing the complex inversion, a circle, which passes through the origin of the phasor plot, maps a straight line into the complex plane [51]. Let us define the complex inverse by mapping the data into the complex plane ($Re[1/(t-1)]$, $Im[1/(t-1)]$)- as shown in figure 2.6 (c1-c3). Precisely, figures 2.6 (c1-c3) show the inverse complex graph of panels (b1-b3). The straight line in the inverse complex graph can be understood by formulating the real and imaginary parts of the inverse complex as:

$$Re\left[\frac{1}{t-1}\right] = -\frac{\gamma + \Gamma}{2\Gamma} = -d^{-1} \quad \text{and} \quad Im\left[\frac{1}{t-1}\right] = -\frac{\Delta\omega}{2\Gamma}. \quad (2.18)$$

2. Hermitian and non-Hermitian systems

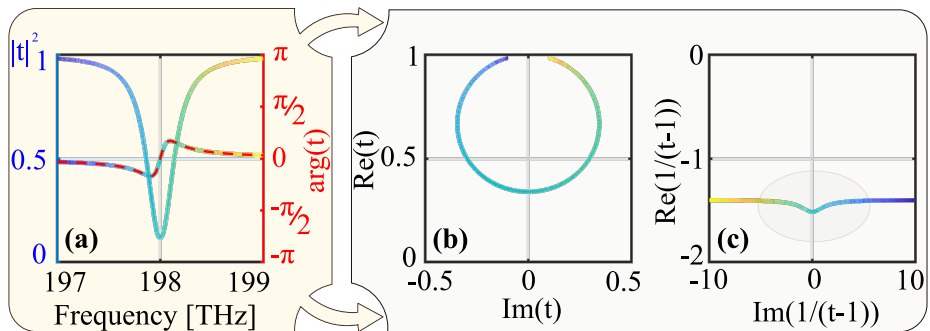


Figure 2.7: (a) Transmitted intensity and phase as a function of the incident frequency. Panels (b) and (c): parametric phasor diagram and inverse complex of figure (a). The color code (rainbow curves) represents the data as a function of the frequency (the color allows to relate the different panels on the same row). The used parameters are those of figure 2.6 (a3) with a small backcoupling coefficient $\beta_{12} = -\beta_{21}$, where $\beta_{12}/(\Gamma + \gamma) = 0.29$.

As expected, the imaginary part is a linear function of the frequency detuning while the real part is a constant. This constant is determined by the extrinsic and the intrinsic coefficient and its amplitude is the inverse of the phasor diameter.

The complex inverse graph represents a strong tool for visualizing any variation of a simple Lorentzian response. In fact, we can treat the presence of the coupling terms as a perturbation of the simple response of an uncoupled single mode system. In general, in the case of the linear optics, it is possible to formulate the response of a generic coupled system as a Lorentzian with a perturbative term η :

$$t = 1 - \frac{2\Gamma}{i\Delta\omega + \gamma + \Gamma - \eta}. \quad (2.19)$$

Considering the backscattering and, then, the transmission amplitude of equation 2.9, the short hand interaction is given by: $\eta = \frac{\beta_{12}\beta_{21}}{i\Delta\omega + \gamma + \Gamma}$. In this case, η depends on the coupling coefficients β_{12} and β_{21} . In the absence of backscattering, η reduces to zero and the transmission assumes the typical form of equation 2.12. As we will see in the following paragraphs, the presence of the off-diagonal elements of matrix 2.8 substantially modifies the system response.

Figures 2.7 (a), (b) and (c) show the modulus and phase of the transmission amplitude, their phasor graph and the inverse complex representation as a function of the incident frequency. In this case, the $\beta_{12,21}$ are small and they yield an indiscernible perturbation of the symmetric Lorentzian in transmission or of the perfect circle in the phasor representation. On the contrary, they produce a noticeable peak in the single line of the inverse complex. The strong sensitivity to deformations makes this representation a valuable tool to reveal information which are masked in the conventional resonance analysis [16]. Therefore, this

method could be applied in various other fields, such as metrology or sensing, to enhance the sensitivity of devices. Moreover, the complex inverse allows separating the real and imaginary part of the perturbation η , namely:

$$Re\left[\frac{1}{t-1}\right] = -\frac{\gamma + \Gamma - Re[\eta]}{2\Gamma} \quad \text{and} \quad Im\left[\frac{1}{t-1}\right] = -\frac{\Delta\omega - Im[\eta]}{2\Gamma}. \quad (2.20)$$

The knowledge of both the intensity and the phase of the transmitted field permits to use these complex representations and, as we will see in section 2.5, to study a precise element of the coupling matrix.

2.3.4 Hermitian coupling with conservative coefficients

In this subsection we see how the presence of the coupling terms modifies the system response. Initially, we focus the attention on the Hermitian coupling and then on the non-Hermitian one. Following the notation used in the previous chapters, we write the coupling coefficients as: $i\beta_{12} = a - ib$ and $i\beta_{21} = a + ib$. In this way, following the derivation of section 2.1 the system of differential equations 2.8 can be reformulated as:

$$\frac{d}{dt} \begin{pmatrix} \alpha_{ccw} \\ \alpha_{cw} \end{pmatrix} = i \left[\begin{pmatrix} \omega_0 & a - ib \\ a + ib & \omega_0 \end{pmatrix} + \begin{pmatrix} i\rho & 0 \\ 0 & i\rho \end{pmatrix} \right] \begin{pmatrix} \alpha_{ccw} \\ \alpha_{cw} \end{pmatrix} + i\sqrt{2\Gamma} \mathbf{E}_{in}^T. \quad (2.21)$$

The coupling between the co-propagating and counter-propagating waves can be seen as the sum of a Hermitian and a perturbation matrix. This allows us to treat the passive non-Hermitian system by considering the physical behavior of its Hermitian counterpart attenuated by an exponential decay.

It should be noted, that the coefficients β_{12} and β_{21} so defined, are consistent with the notation of the Hermitian and non-Hermitian coupling terms introduced in [16]:

$$h = i\frac{\beta_{12} - \beta_{21}^*}{2} = a - ib \quad \text{and} \quad n = i\frac{\beta_{12} + \beta_{21}^*}{2} = 0. \quad (2.22)$$

In fact, in this scenario, the Hermitian part (h) is given by $a + ib$ while the non-Hermitian one (n) is reduced to zero. The presence of this Hermitian coefficient characterizes the response of the transmitted and reflected field intensities in the two directions of excitation. The real and imaginary coupling coefficients (b and a) give rise to the same behavior of the transmitted and reflected intensity.

Figure 2.8 (a1) shows the intensity of the transmitted field as a function of frequency. The Hermitian coupling coefficient generates a splitting of the transmitted intensity. There is no longer a simple Lorentzian but a doublet. In this case, as indicated by the horizontal black dotted line, the doublet exhibits the same depth of the peaks. In our work [16], we have defined the response of the Hermitian system as a balanced doublet. The same depth of the peaks is highlighted in figure 2.8 (b1) where the argument of the transmission is drawn as a function of frequency. In fact, the phase shows the same trend and the same amplitude close to the peaks. Figure 2.8 (c1) displays the parametric phasor plot of panels (a1), (b1). In the presence of resonance splitting, the

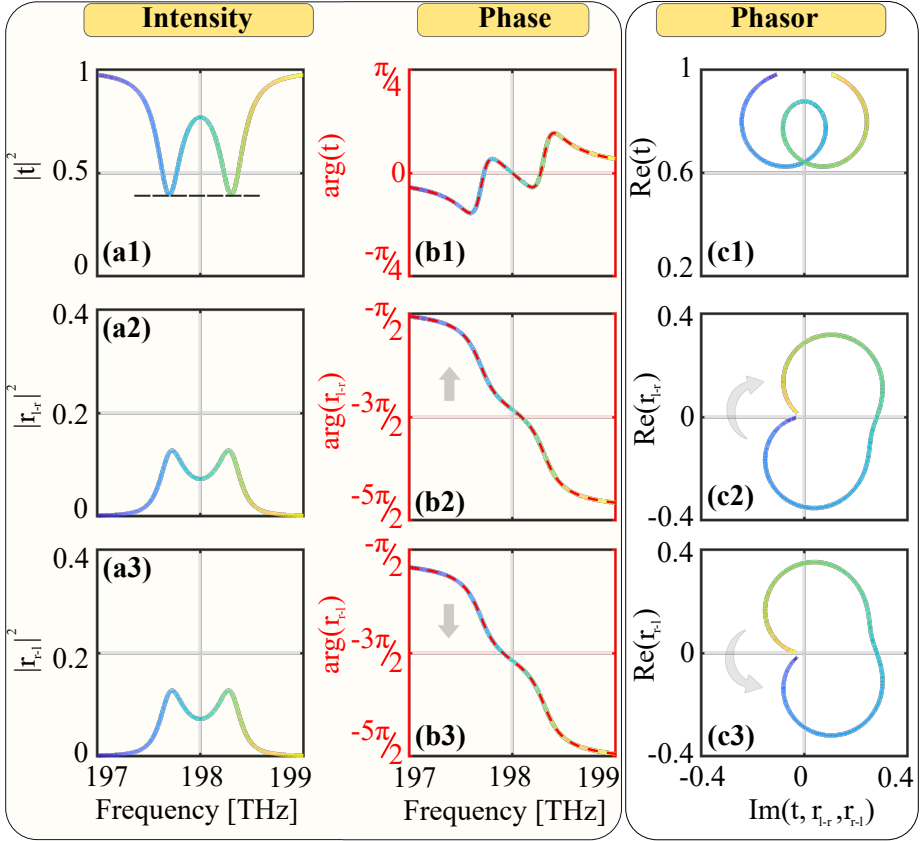


Figure 2.8: (a1),(b1) and (c1) ((a2, b2 and c2)) Transmitted and reflected intensities (phase) as a function of the frequency for the two directions of excitation. (a3), (b3) and (c3) parametric phasor plot of panels (a1)-(b1), (a2)-(b2) and (a3)-(b3), respectively. The rainbow color code represents the data as a function of frequency. The dashed black line highlights the balance doublet response. The resonant frequency, intrinsic and extrinsic parameters are those used in figure 2.7. The backcoupling parameters are: $a = 300 \text{ GHz}$ and $b = 70 \text{ GHz}$.

circle in the phasor representation is significantly deformed. The phasor is no more a simple circle but has two lobes. Particularly, in the case of a balanced doublet, the phasor corresponds to a pair of symmetric lobes. Increasing the value of the Hermitian coupling coefficients yields, as a consequence, an increase of the splitting, i.e. the distance between the two peaks. The magnitude of the frequency splitting is connected to the eigenvalues and in this scenario, as we have seen in the chapter 2.1.1, fixing one of the two terms equal to zero (i.e. $a = 0$ or $b = 0$) it depends linearly on the strength of the coupling coefficient. In

fact, defined $b = 0$, the eigenvalues and the eigenvectors are: $\lambda_{\pm} = \omega_0 \pm a$ and $\bar{v}_{\pm} = (\pm 1, 1)$, respectively. In this way, $a = 0$ is a diabolic point: precisely the eigenvalues coalesce, so that the transmission is no more a doublet, while the eigenvectors remain orthogonal.

In order to have a first intuitive physical explanation of this balanced response it is useful to study the behavior of the reflection in the two directions of excitation (see equations 2.10 and 2.11). Figures 2.8 (a2), (a3) and (b2), (b3) show the intensity and phase of the reflected field as a function of frequency, for an excitation from left to right and from right to left, respectively. Panels (c2) and (c3) show the parametric phasor of figures 2.8 (a2), (a3) and (b2), (b3). The presence of the coupling coefficient means that the reflection is different from zero. In particular, as can be seen by comparing the panels (a2) and (a3), the presence of a Hermitian term makes the intensity of the field reflected equal in the two excitation directions. Since, in this model, the reflection is directly connected to the transfer of energy between the co-propagating and counter-propagating modes, we have that a Hermitian coupling gives rise to the exchange of the same energy between the two modes. In fact, this coupling is known as conservative coupling.

Contrary to the intensity of the transmitted field, the phase given by an excitation of the system from right to left is shifted upwards with respect to that of the excitation from left to right (compare panel 2.8 (b2) with (b3)). This is more evident in the phasor graph, where the two lobes are rotated clockwise in panel (c2) and counterclockwise in (c3), as indicated by the grey arrows. This behavior is due to the backcoupling coefficient b . In fact, considering separately the two contributions, a and b , as far as the intensity of the transmitted and reflected field is concerned, the response of the system does not change. On the contrary, in the case of the phase, the real coefficient b (imaginary a) introduces a π (0) phase shift between left-right and right-left reflection amplitudes. Thus, the presence of an imaginary term together with a real coefficient rotates the phasor of the two reflections in opposite directions.

Summarizing, when $\beta_{12} = -\beta_{21}$ with $\beta_{12}, \beta_{21} \in \mathbb{R}$ the reflection amplitudes are different $r_{l-r} \neq r_{r-l}$ but the intensities are equal $|r_{l-r}| = |r_{r-l}|$. While, when $\beta_{12} = \beta_{21}$ with $\beta_{12}, \beta_{21} \in \mathbb{C}$ also the reflection amplitudes for the two excitations are equal: $r_{l-r} = r_{r-l}$. This can be explained taking into account the symmetry of the backcoupling coefficients, which gives rise to the same response in the two directions of excitation. It is worth noticing that the case in which $\beta_{12} = \beta_{21}$, with only the backcoupling coefficient b , does not fall within the classification of Hermitian coupling coefficients and does not give rise to a splitting of the resonance.

As we will see in more detail in the following sections, generally the stochastic nature of the surface walls roughness gives rise to an exchange of the same energy between co-propagating and counter-propagating modes and therefore, as in this case, to the same intensity of the reflections in the two excitation directions. In fact, on the ideal condition of a single mode high Q microresonator, the stochastic nature of the roughness leads to a simple statistical approach. This neglects the non-Hermitian terms and therefore just a balanced doublet appears in the

2. Hermitian and non-Hermitian systems

transmission response [11, 14, 15]. Therefore, TCMT with an energy-conserving reactive coupling (i.e. Hermitian coefficient) between the counter-propagating modes describes the ideal case [16].

2.3.5 Non-Hermitian coupling with dissipative coefficients

Let us consider the presence of a dissipative term in the coupling coefficient. In this case, the system of differential equations can be reformulated as:

$$\frac{d}{dt} \begin{pmatrix} \alpha_{ccw} \\ \alpha_{cw} \end{pmatrix} = i \left[\begin{pmatrix} \omega_0 & a - ib \\ a + ib & \omega_0 \end{pmatrix} + \begin{pmatrix} i\rho & \delta a_1 + i\delta b_1 \\ \delta a_2 + i\delta b_2 & i\rho \end{pmatrix} \right] \begin{pmatrix} \alpha_{ccw} \\ \alpha_{cw} \end{pmatrix} + i\sqrt{2\Gamma} \mathbf{E}_{in}^T, \quad (2.23)$$

where the off-diagonal coupling coefficients exhibit a non-Hermitian component. The introduction of these non-Hermitian coupling coefficients can strongly modify the optical response of the system. Figures 2.9 (a1)-(a3) ((b1)-(b3)) show the intensity (phase) of the transmitted and reflected fields in the two directions of excitation as a function of frequency. In this scenario, the resonance splitting exhibits a couple of peaks with an appreciable difference in height (see arrow in panel (a1)). In ref. [16] we have defined these features as unbalanced doublets. This unbalance in amplitude between the peaks is even more evident in the figures 2.9 (c1)-(c3). These figures show the parametric phasor plot of the graphs (a1)-(b1), (a2)-(b2) and (a3)-(b3). As in the previous figures, the rainbow color code allows relating graphs on the same row in term of frequency. In panel 2.9 (c1) the unbalance of the transmission response results in two lobes of different sizes. As we have seen in the Hermitian case, in our model, the reflection is closely connected to the surface roughness and allows us to make a first estimate of the energy exchange between the co-propagating and counter-propagating modes. The presence of dissipative terms makes the intensity of the reflection for an excitation from left to right different from the intensity of the reflection for an excitation from right to left (compare panel (a2) with panel (a3)). This gives rise to a different exchange of energy between the co-propagating and counter-propagating modes which results in an unbalanced resonance splitting in the transmission response. Summarizing, the introduction of non-Hermitian coefficients can cause a different behavior of both intensity and phase of the reflection fields in the two directions of excitation (i.e. $|r_{l-r}| \neq |r_{r-l}|$, and $r_{l-r} \neq r_{r-l}$). This can be seen by comparing the phasor diagrams in the panels 2.9 (c2) and (c3). In fact, they exhibit different dimensions and orientations. As we will see in more detail in the following sections, these terms can be connected to the multimodal nature of the microresonator. The physical mechanism, that yields the non-Hermitian coefficient, is the interplay between scattering and dissipative coupling which, on average, gives rise to an asymmetrical scattering. Therefore, the waves propagating in opposite directions interact with the surface defects in a different way.

The wide range of values that the backcoupling coefficients can assume, makes difficult to classify the different responses in transmission and reflection. In the Hermitian case we have established a relationship between the two coefficients

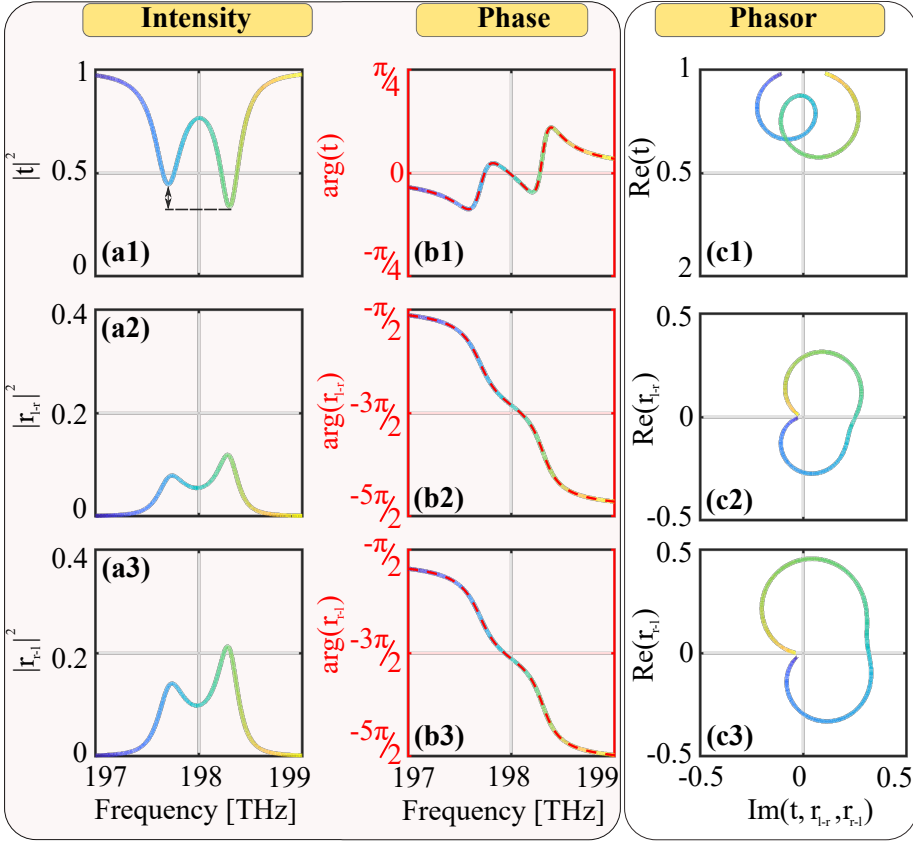


Figure 2.9: (a1),(b1) and (c1) ((a2, b2 and c2)) Transmitted and reflected intensity (phase) as a function of the frequency for the two directions of excitation. Panels (a3), (b3) and (c3) are parametric phasor plot of panels (a1)-(b1), (a2)-(b2) and (a3)-(b3), respectively. The rainbow color code represents the data as a function of frequency. The dashed black line in (a1) highlights the unbalance doublet response. The resonant frequency, the intrinsic and extrinsic parameters are those used in figure 2.7. The backcoupling parameters are: $a = 250 \text{ GHz}$, $b = 30 \text{ GHz}$, $\delta a_1 = 90 \text{ GHz}$, $\delta a_2 = 10 \text{ GHz}$, $\delta b_1 = 60 \text{ GHz}$ and $\delta b_2 = 10 \text{ GHz}$.

(i.e. $\beta_{12} = -\beta_{21}^*$) by considering the energy conservation. At this point, it is good to open a parenthesis on the existence of a possible connection between the coefficients β_{12} and β_{21} even in the case of Non-Hermitian coupling. For this purpose, let us use the Hermitian and non-Hermitian coefficient relations of equation 2.23 and let us formulate them as $h = |h|e^{i\theta}$ and $n = |n|e^{i\phi}$. Their origin can be easily understood in the simplest case of counter-propagating modes $e^{\pm i\ell\varphi}$ perturbatively coupled by a single localized scatterer located at

2. Hermitian and non-Hermitian systems

an angle φ_0 along the ring resonator and of complex potential V_0 , whose real (imaginary) part is reactive (dissipative). In this case, the couplings β_{12} (β_{21}) are proportional to $V_0 e^{2il\varphi_0}$ (and $V_0 e^{-2il\varphi_0}$). The complex-valued Hermitian and non-Hermitian components $h \propto \text{Re}[V_0] e^{2il\varphi_0}$ and $n \propto \text{Im}[V_0] e^{2il\varphi_0}$ are related to the reactive and dissipative effects of the potential. Since the contribution of many scatterers adds up, it is immediate to see that no special relation holds between β_{12} and β_{21} , which can then attain arbitrary and independent values [16].

2.3.6 Transmission and reflection field response classification by Hermitian and non-Hermitian coefficients

The lack of a relationship between the backcoupling coefficient β_{12} and β_{21} leads to a wide spectrum of responses of the transmitted and reflected fields. To give an idea of the variety of the possible behaviors, a tentative classification of the system response can be given by considering the normalized difference between the r-l and l-r reflections. In fact, this depends only on the scatterers inside the microresonator and can be written as [16]:

$$\frac{|\max(|r_{l-r}|^2) - \max(|r_{r-l}|^2)|}{\max(|r_{l-r}|^2, |r_{r-l}|^2)} = \frac{1}{\frac{|h|^2 + |n|^2}{4|h|n \sin(\Delta\Theta)} + \frac{1}{2}}, \quad (2.24)$$

where $\Delta\Theta = \phi - \theta$. While this angle vanishes for a single scatterer, it can attain any value for more complex configurations with assemblies of scatterers. As reported in [16], a classification of the system response can be the following one:

- $\Delta\Theta = m\pi$ where $m \in \mathbb{Z}$: The reflection l-r is equal to the r-l one (i.e. Eq.2.24 vanishes) but the transmission spectra can assume different doublet shapes depending on the relative values of the Hermitian and non-Hermitian coefficients $|h|$ and $|n|$. In particular, for a purely reactive coupling, we have $|n| = 0$ so that the intra-cavity coefficient satisfies $\beta_{12} = -\beta_{21}^*$ and the doublet is perfectly balanced.
- $\Delta\Theta = (m + 1/2)\pi$ where $m \in \mathbb{Z}$: the reflection spectra between the l-r and r-l excitations are different but a perfectly balanced doublet exists in the transmission response. In the limiting case $|h| = |n|$ one of the two β_{12}, β_{21} vanishes. Reflection then occurs in only one direction and transmission recovers a simple Lorentzian. In the $|n| = 0$ limit, this case reduces to the previous one with $\beta_{12} = -\beta_{21}^*$.
- $\Delta\Theta \neq m\pi$ and $\neq (m + 1/2)\pi$ with $m \in \mathbb{Z}$: both the transmission spectra display an unbalanced doublet and the reflections responses l-r and r-l are different.

In all cases the non-Hermitian coefficient $|n|$ is constrained by the intrinsic term γ , which takes into account the total losses of a propagating mode inside the microresonator. Both the material absorption and the inter-modal mediated

coupling losses contribute to the intrinsic parameter. While the Hermitian coefficient induces the mode splitting giving rise to a continuous exchange of the same energy between the co-propagating and counter-propagating modes, the presence of n introduces a different balance between the reflection and inter-modal mediated coupling losses. Thus, $|n|$ has to be less than or equal to the intrinsic coefficient (i.e. $|n| \leq \gamma$) in order to avoid gain of the system.

2.3.7 Numerical Simulations of the backscattering

In order to have a first validation of the theoretical model and a support of the assumption made during its derivation, we have performed numerical simulations. These simulations are based on the finite elements method (FEM) engine by Comsol Multiphysics controlled by the mathematical programming environment of Matlab. In particular, we have studied a two-dimensional and a three-dimensional model. The first one is a simplified 2D model including a ring resonator coupled to a waveguide, while the second one is a 3D model of a microresonator coupled to a bus waveguide with a particular geometry (see figure 2.10 (a) and (b), respectively). This consists of a cavity formed by a wedge microdisk resonator vertically coupled to a bus-waveguide. As we will see in the experimental part, the choice of this geometry is justified by the manufacturing methods that allows to reach a high quality factor of about $2 \cdot 10^5$ in a monolithic-integrated optical system [26].

At first, let us deal with the case of the 2D model of figure 2.10 (a) and let us see how the presence of roughness and the mono or multimodal nature of the system can influence the optical response. As reported in [16], in contrast to the overwhelming computational cost of the 3D calculations, this simplified 2D model allows performing large scale statistical studies (with up to 10^4 simulations) of highly detailed geometries containing nanometric-size surface roughness. The microring geometry has been chosen to select different radial modes, allowing for single-(multi-)mode operation for a waveguide width of $0.53 \mu\text{m}$ ($0.7 \mu\text{m}$). As material parameters, we have used a silicon nitride/silica ($\text{Si}_3\text{N}_4/\text{SiO}_2$) platform with refractive indexes equal to 2, 2 and 1.45 for the resonator, bus-waveguide and surrounding media. The large radius of curvature of $25 \mu\text{m}$ allows neglecting bending losses as well as back-reflections from the bus-waveguide/resonator coupling area. For the configuration under examination, the back-scattered intensity (S_{sc}) with respect to the forward scattered intensity ($S_{forward}$) amounts to $S_{sc}/S_{forward} \approx 2 \times 10^{-8}$ or 10^{-6} , for single- or multi-mode resonators, respectively. Therefore, this 2D simulations are based on the assumption that the back-scattering process responsible for the coupling between the counter-propagating modes and, then, for the balanced or unbalanced doublets is the roughness on the ring edges. This assumption is in accordance with the theoretical model presented in the previous paragraphs. It is valid if the back-reflections from the bus-waveguide/resonator coupling area are negligible with respect to the backcoupling due to the surface wall roughness. This assumption will be confirmed by the simulations based on the 3D model and, as we will see, from the experimental observations in chapter 5. The roughness on the ring

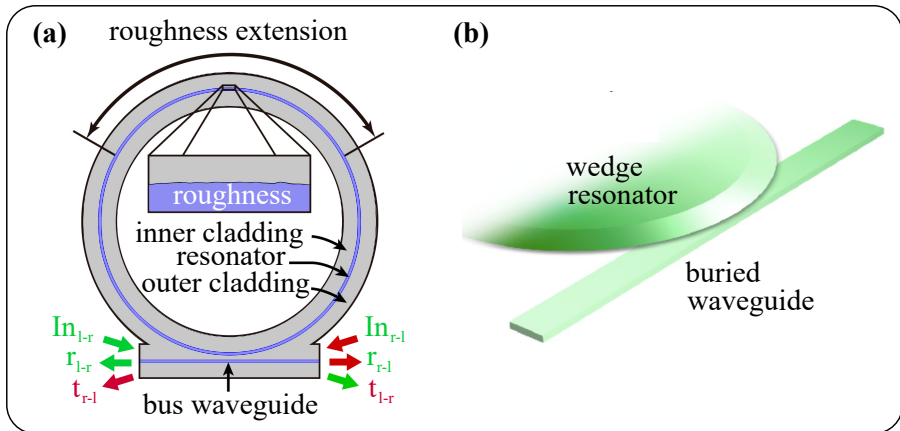


Figure 2.10: (a) 2D model of the bus-waveguide/resonator system. The arrows labelled by in, r and t represents the inserted, reflected and transmitted signals, respectively. The labels l-r and r-l refer to the two situations where the input signal light is inserted on the left and propagates from left-to-right (l-r, green arrows) or is inserted on the right and propagates from right-to-left (r-l, red arrows). (b) Sketch of the ring-shaped wedge microresonator device vertically coupled to the bus waveguide.

edges has been simulated in the 2D model as a disorder in the waveguide width of the ring with a Gaussian statistics (root mean square amplitude ranging from 4 to 8.5 nm, and a correlation length of 0.1 μm). As shown in figure 2.10 (a), the scatterers are distributed over one third of the external rim in the opposite region of the bus-waveguide/ring coupling. In this way, the coupling region remains isolated from any possible back-scattering source. The roughness determines the intrinsic coefficient (γ) of the device while the gap between the resonator and the waveguide allows changing the extrinsic coefficient (Γ) and imposing a critical coupling condition.

The histograms in figure 2.11(a)-(c) show a statistical study of about 400 realizations of the disorder (~ 100 simulations per studied case). These characterize the effect on the mode splitting and on the peak unbalance of different values of the Q-factor and different mono-/multi-radial-modal scenarios. Here, the unbalance is defined as the ratio between the difference in height of the doublet dips and the minimum of the transmittivity. For each choice of parameters, the amount of the splitting and of the unbalance changes stochastically for each realization of the disorder. In particular, the histograms (a1)-(c1) of the unbalance show a symmetry around the origin (confirmed by a very small mean value of about 10^{-3}). On the other hand, the mode splitting exhibits a net non-zero average value.

Panels (a1-a2) show the effect of increasing the waveguide width in the

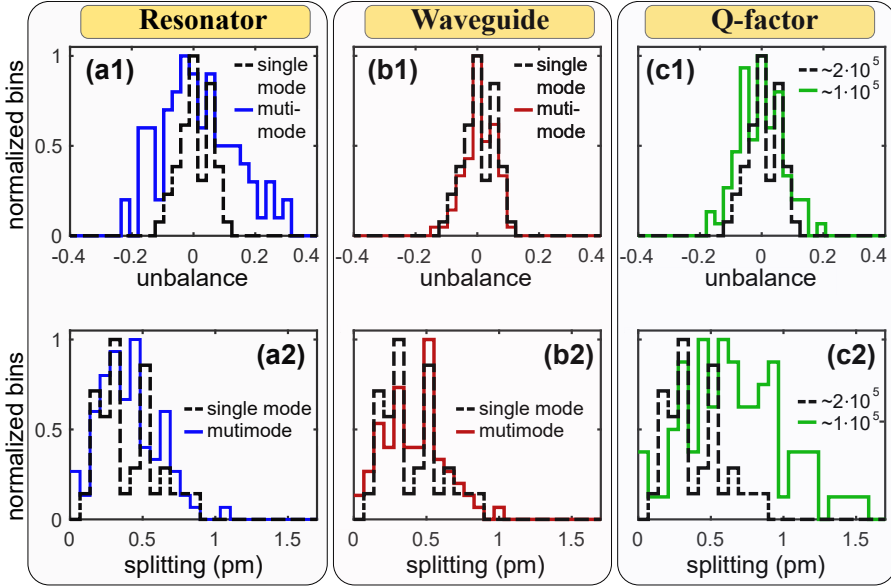


Figure 2.11: Panels (a-c): Normalised histograms of the peak unbalance (a1-c1) and of the mode splitting (a2-c2) in different cases: when the resonator (a) or the waveguide (b) are changed from single- to multi-mode (black dashed and coloured solid lines, respectively), and when the Q-factor of the single-mode resonator is halved (black dashed line $Q=2 \times 10^5$, green solid line $Q=1 \times 10^5$).

ring from $w = 0.53 \mu\text{m}$ to $w = 0.7 \mu\text{m}$, passing from a single-mode (SM) to a multi-mode (MM) configuration while preserving the Q-factor ($Q \approx 2 \times 10^5$) via an increased amplitude of the roughness. Similar values of the mode splitting are observed ($\overline{m\bar{s}}_{(MM)}/\overline{m\bar{s}}_{(SM)} \simeq 1.02$ and $\sigma_{(MM)}/\sigma_{(SM)} \simeq 1.05$, where $\overline{m\bar{s}}_{(XX)}$ is the average of the distribution of the data for the XX case and $\sigma_{(XX)}$ is its standard deviation), which can be explained by the similar value of the total losses. On the other hand, the magnitude of the unbalance is strongly increased ($\sigma_{(MM)}/\sigma_{(SM)} \simeq 2.4$) by the presence of more channels for back-reflection and absorption in the multimode resonators.

Panels (b1-b2) represent the same study for an increasing size of the bus-waveguide width, while the gap is reduced to maintain the same Q-factor for the resonator. This allows investigating the role of the back-reflections in the bus-waveguide/resonator coupling area: as expected from previous calculations, the almost-identical results obtained for the single- and multi-modal waveguide case (for both the unbalance $\sigma_{(MM)}/\sigma_{(SM)} \simeq 0.96$ and the mode splitting $\overline{m\bar{s}}_{(MM)}/\overline{m\bar{s}}_{(SM)} \simeq 1.04$, $\sigma_{(MM)}/\sigma_{(SM)} \simeq 1.06$) give a confirmation that the waveguide coupling is not the source of the unbalance in our system.

Panels (c1-c2) represent the effect of an increased roughness amplitude, which

2. Hermitian and non-Hermitian systems

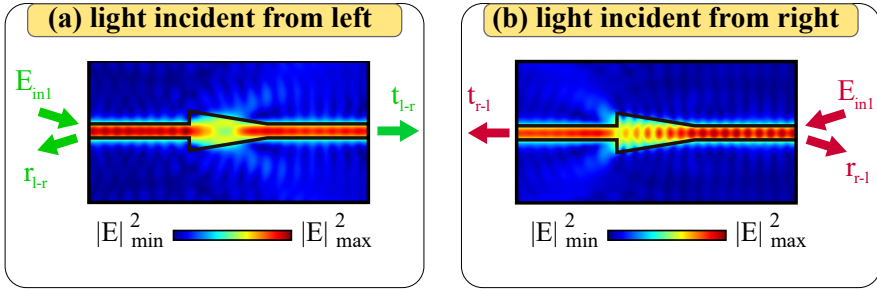


Figure 2.12: Simulation of a non-symmetrical scatterer device inside a single-mode waveguide for light incident: (a) from the left (l-r) or (b) from the right (r-l). Both cases show the same transmission ($T = 84.48\%$) but different reflections ($R_{l-r} = 6.7 \times 10^{-2}\%$, $R_{r-l} = 0.674\%$).

reduces the Q-factor from $Q \approx 2 \times 10^5$ to its half value $Q \approx 1 \times 10^5$. As expected, the increased disorder reinforces the backscattering phenomena visible in the amount of unbalance (with a standard deviation ratio of $\sigma_{(Low-Q)}/\sigma_{(High-Q)} \simeq 1.43$) and mode splitting (of mean value of $\overline{m\bar{s}}_{(Low-Q)}/\overline{m\bar{s}}_{(High-Q)} \simeq 1.77$ and standard deviation of $\sigma_{(Low-Q)}/\sigma_{(High-Q)} \simeq 1.74$).

In summary, these simulations indicate that the unbalance is negligible in high/ultra-high Q-factor or single-mode resonators, in agreement with the previous literature [11, 14, 15]. On the other hand, the amount of unbalance is increased in multi-mode resonators. The physical mechanism which yields the unbalance is the interplay between scattering and dissipative coupling which, on average, gives rise to an asymmetrical scattering, so that waves propagating in opposite directions interact with the surface defects in a different way. This can be demonstrated by a simple simulation of a scatterer which has a specific asymmetric shape (figure 2.12). In a simple model, we simulate an arrow-like waveguide. Here, the scattering is due to the non adiabatic waveguide width increase and to the asymmetry of the abrupt width reduction. The two panels (a) and (b) show the electric field distribution for light incident from different directions: when the input port is swapped, the reflectance R exhibits a marked difference of about one order of magnitude ($R_{l-r} = 6.7 \times 10^{-2}$ vs $R_{r-l} = 0.67\%$, where the index l-r refers to light that travels from left to right and is reflected back to the left, the index r-l to the opposite situation). This difference in reflectivity is of course compatible with Lorentz reciprocity theorem, which only imposes that the transmittance is the same in the two directions (simulations yield a similar value of $T = 84.48\%$). The reflectance difference is due to the power loss caused by the light scattering out of the propagating waveguide mode. Note that such an asymmetry can not occur in purely reactive single mode resonators where the transmission and reflection are related by energy conservation and the symmetry of the former is imposed by the Lorentz reciprocity theorem. The numerically observed asymmetry of panels (a-b) therefore involves a non-

Hermitian process. These findings help to understand our theoretical model. Since the two peaks in the doublet originate from a repeated exchange of energy between waves propagating in opposite directions due to reflection, we expect that the average asymmetric reflection, similar to that shown in panels (a-b), bears a close relation with the non-Hermitian coefficient which generates the unbalance.

To better understand this link, we have extended our numerical simulations to look directly at the reflected intensity by the ring resonator. The results are shown in the different panels of figure 2.13. In particular, in the central and right columns we have compared the reflectivity for light injected on the left (l-r) or on the right (r-l) for different realizations of the disorder which yield different balance in the doublets. As a check of our numerical simulations, we have controlled that in all cases the transmission does not change with the incidence direction, in agreement with the Lorentz reciprocity theorem.

In the absence of any surface roughness, according to the theoretical model, the reflectivity vanishes independently of the excitation direction. In the presence of a sizable roughness, reflection acquires a marked asymmetry, typically in association with a marked unbalance in the transmission doublet. Panels (a1-a3) illustrate a case with an almost balanced doublet, where l-r and r-l reflections are very close. Panels (b1-b3) show the case of a markedly unbalanced doublet in the transmission response (b1), which is associated to very different reflection spectra in the two directions (b2-b3). Interestingly, the simulation is also able to correctly model the presence of a small backcoupling coefficient as reported in the theoretical model in figure 2.7. In ref. [16], we have defined this case as hidden doublet. Panels (c1-c3) show that the doublet is completely hidden in the transmission spectra (c1) while the reflectivity is strongly quenched in one direction (c3) and is significant in the other (c2). While the phasor plot, shown in panel (c4), still resembles to the typical circle of a single Lorentzian resonance, the deviation of its inverse (shown in panel (c5)) from a straight line is a clear signature of the back-scattering process.

A first validation of our analytical model comes from the comparison with the numerical simulations. A stringent test in this direction can be performed as follows. The doublets in the transmission (figure 2.13 (a1)-(c1)) and l-r reflection (figure 2.13(a2)-(c2)) spectra are simultaneously fitted by using the Eqs.2.9-2.10 (red lines). Then, the fit parameters obtained in this way are inserted in Eq.2.11 to get a prediction for the r-l reflectivity (green lines in figure 2.13 (a3)-(c3)). The perfect match of this prediction with the numerical data is a strong evidence that the analytical model is capturing the main points of the physics. In particular, it turns out that figure 2.13 (a) corresponds to an almost balanced doublet with a slight difference in the l-r and r-l reflections. This behavior corresponds to intra-cavity parameters resembling the second case of our classification with $|n|/|h| = 1 \cdot 10^{-2}$, $\Delta\Theta = -90$ degrees and $\phi = 90$ degrees and $\Gamma/\gamma = 0.82$. On the other hand, the simulation results of figure 2.13(b)-(c) belong to the third case with $|n|/|h| = 0.41$, $\Delta\Theta = -64.93$ degrees and $\phi = 114.19$ degrees and $\Gamma/\gamma = 0.59$ in the former case; $|n|/|h| = 0.87$, $\Delta\Theta = 247.42$ degrees and $\phi = 136.48$ degrees and $\Gamma/\gamma = 0.74$ in the latter case.

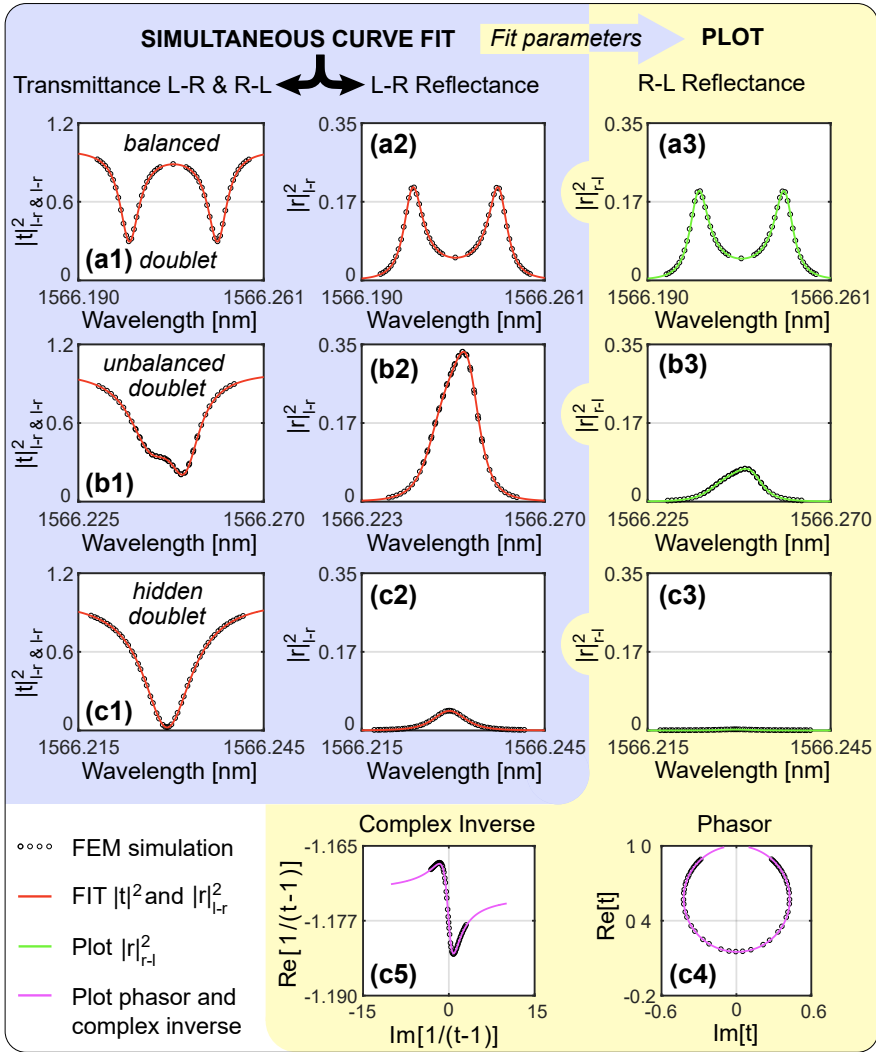


Figure 2.13: Transmission (a1-c1), l-r (a2-c2) and r-l (a3-c3) reflection for different realizations of the disorder which yield a balanced doublet (1), an unbalanced doublet (2) and a hidden doublet (3). The black circles are the simulation values while the red line is the fit with the theoretical model. For each case, the green curves are obtained by plotting the Eq.2.11 for the r-l excitation using the parameters fitted from the l-r ones. While almost invisible in the transmission, the hidden doublet of panel (c1) can be revealed in the complex inverse (c5) of the phasor diagram (c4). This figure is taken from [16].

These results support our initial guess that the unbalance is closely related to an asymmetric coupling between the two propagating modes induced by the roughness scattering. Note that such an asymmetric coupling has already been seen in a microdisk with two nanoparticles close to its external rim [52]. In this case, the strength of the backscattering can be different depending on the propagating direction: from clockwise (CW) to counter-clockwise (CCW) or from CCW to CW. In our case, the stochastic nature of the roughness should introduce a statistical approach which leads, on average, to a symmetric backscattering as shown in [11, 14, 15]. However, the repeated back-scattering processes on the surface roughness in a multi-modal resonator is not enough to neglect the possible asymmetric behavior of several scatterers. This means that the collective action of the scatterers, instead of canceling the phase contribution, could intrinsically lead to the unbalance. One could easily reproduce this behavior following the receipts shown in the histograms (figure 2.11) and, therefore, without forcing extreme conditions.

At this point, we have an open question about the backcoupling reflections related to the coupling between the resonator and the bus waveguide. In order to understand this, we made use of a full 3D model of the device to study the back-reflections connected to the vertical coupling between the bus-waveguide and the wedge shaped microdisk. As shown in figure 2.14 (a), almost all the coupled light propagates in the forward direction inside the resonator and the back-reflections into oppositely propagating modes have an almost negligible amplitude. This is due to the fact that the light entering the coupling area experiences a smooth growth of the wedge profile (7 degrees), so it progressively couples to the resonator with almost no reflections. Quantitatively, the back-scattered intensity (S_{sc}) with respect to the forward scattered intensity ($S_{forward}$) amounts to $S_{sc}/S_{forward} = 2 \times 10^{-3}$ distributed over all the supported modes. This result gives a further justification of the assumption that the change of energy

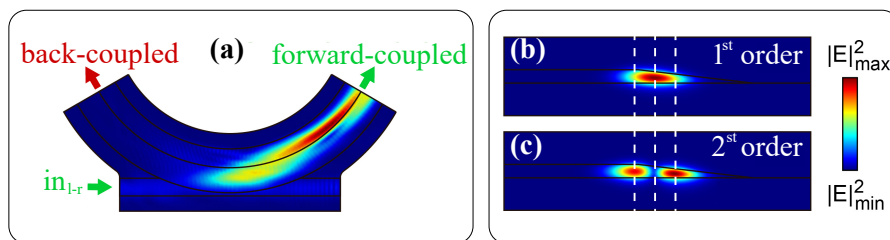


Figure 2.14: (a) 3D simulation of the light intensity in the vertical coupling region between the bus-waveguide and the wedge resonator. The field intensity inside the wedge portion reveals a beating pattern between the different radial modes of the wedge resonator [32], [33] that are excited by the forward coupling. The amount of back-scattered light is instead almost negligible. Panels (b)-(c): field profiles of the 1st and 2nd radial modes of the wedge resonator.

between the clockwise and the counterclockwise modes is strictly connected to the wall roughness of the microresonator. The figures 2.14 (b) and (c) show the profile of the first and second radial modes of the wedge resonator, respectively. As we will see in the experimental section 5, on the contrary of the in-plane coupling, the vertical coupling allows to properly excite not only the first radial mode but also the other radial ones.

2.3.8 Unidirectional reflection at the exceptional point

Let us consider the eigenvalues and the eigenvectors in the case of non-Hermitian coefficients. For simplicity, let us formulate the coupling coefficients as $i\beta_{12} = a + \delta a_1 + i(-b + \delta b_1) = a_{12} + ib_{12}$ and $i\beta_{21} = a + \delta a_2 + i(b + \delta b_2) = a_{21} + ib_{21}$. By neglecting the bus waveguide, one obtains a Hamiltonian, describing a two-level system as in subsection 2.1.2. In this case, the eigenvalues and the eigenvectors can be written as: $\lambda_{\pm} = \omega_0 \pm \sqrt{(a_{12} + ib_{12})(a_{21} + ib_{21})} = \omega_0 \pm i\sqrt{\beta_{12}\beta_{21}}$ and $\bar{v}_{\pm} = \left(\pm \frac{a_{12} + ib_{12}}{\sqrt{(a_{12} + ib_{12})(a_{21} + ib_{21})}}, 1 \right) = \left(\pm \sqrt{\frac{\beta_{12}}{\beta_{21}}}, 1 \right)$, respectively. The eigenvalues depend on the square root of the coupling coefficients product. The lack of a relationship between β_{12} and β_{21} means that a curious boundary case may occur. Precisely, when β_{12} reduces to zero an EP occurs. In fact, approaching the degeneracy, i.e. decreasing β_{12} , not only the eigenvalues but also the eigenvectors coalesce. This has important implications in the optical response of the system. Figures 2.15 (a), (b) and (c) show the intensity of the transmission and of the reflection as a function of $\Delta\omega$ and of β_{12} . In panel (a), as we have seen in the previous chapters, the presence of backcoupling coefficients gives rise to a resonant splitting in the transmission spectrum. This translates into a doublet in the reflected intensities: $|r_{l-r}|^2$ and $|r_{r-l}|^2$. Fixing the coefficient β_{21} and decreasing β_{12} we approach the degeneracy. In this way, the splitting in transmission and reflection decreases and the difference between the reflected intensities increases (compare panel 2.15 (b) and (c)). At the exceptional point, i.e. when β_{12} reduces to zero, the transmission does not exhibit a doublet but a typical Lorentzian shape and the contrast in reflection amplitudes is maximized. In particular, for one direction the reflection becomes zero (i.e. $|r_{l-r}| = 0$) and for the other can be very large. Therefore, in this extreme condition the system can behave as an unidirectional reflection device.

As we have seen, when $\beta_{12} = 0$, the transmission does not exhibit a doublet but a typical Lorentzian shape. By perturbing the system, and therefore changing the coupling terms, a resonant splitting can occur. The magnitude of the frequency splitting is connected to the eigenvalues of the system and, then, depends on the square root of the perturbation. This particular variation is used to enhance the sensing in an optical microcavity [53]. Due to the complex-square-root topology near an exceptional point, the frequency splitting scales as the square root of the perturbation instead of scaling as the linear variation as in the diabolic topology case [54]. Therefore, for sufficiently small perturbations, the exceptional points enhance the typical sensor sensitivity [55].

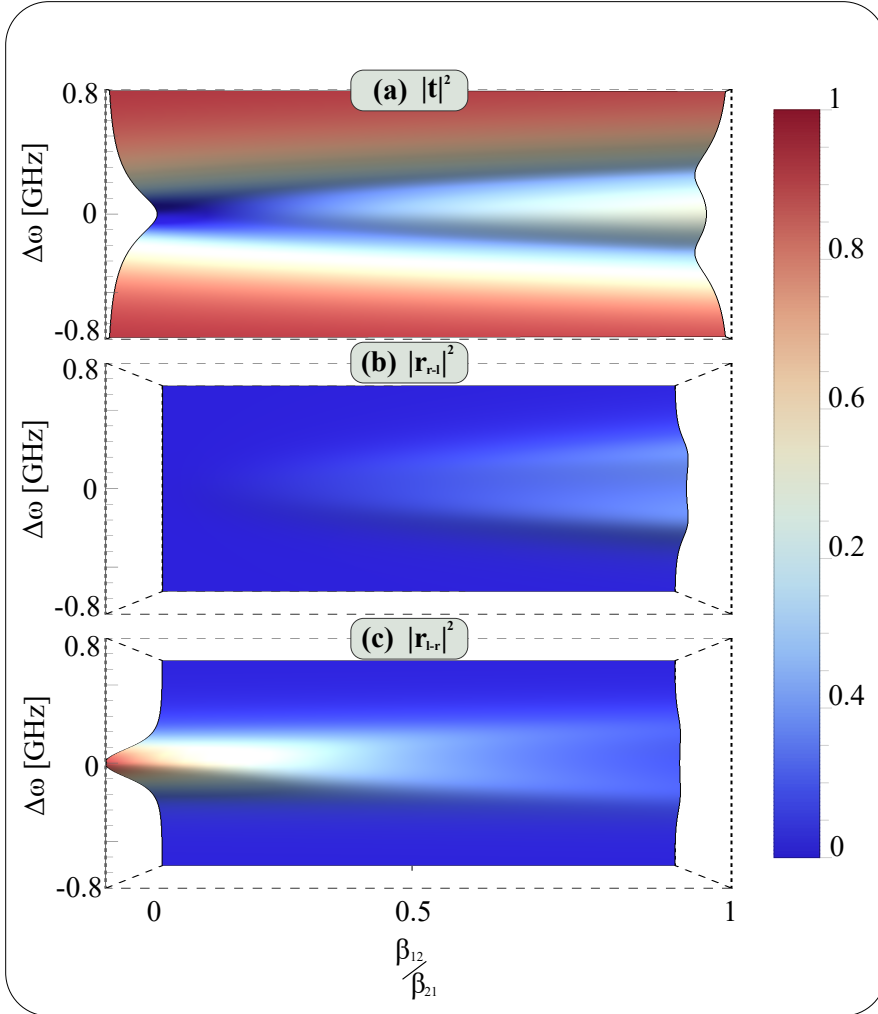


Figure 2.15: Intensity of the field transmitted (a), reflected by left-right (b) and right-left (c) excitation as a function of the detuning ($\Delta\omega$) and the coupling coefficient (β_{12}). The intrinsic γ , extrinsic Γ parameters and the coupling coefficient β_{21} are 140 MHz , 70 MHz and $i0.3\text{ GHz}$ respectively.

2.3.9 A microresonator as unidirectional reflection device

We have seen that the energy exchange between the CCW and CW modes regulates the system response. The conservative and dissipative coupling coefficients can be tuned to avoid the presence of the backscattering. Since these parameters are connected to the surface wall roughness and to the multimodal nature of the resonator (see figure 2.16 (a)), the control of the optical response is prohibitive. In fact, the roughness is a stochastic process due to a manufacturing limit and, therefore, difficult to control. However, it is possible to introduce new geometries capable of controlling the exchange of energy. As seen previously, the requirement is that only one of the two off-diagonal elements of the two-level Hamiltonian has to be zero. This can be achieved by introducing a non-reciprocal loss inside the cavity thanks to a S-shaped waveguide as in figure 2.16 (b) and (c). Such a peculiar geometry resembles the taiji symbol and allows exploiting the non-Hermitian nature of the system, obtaining an on-chip unidirectional reflector. In the taiji microresonator of figure 2.16 (b), the equations that govern the propagation of the light are:

$$\frac{d}{dt} \begin{pmatrix} \alpha_{ccw} \\ \alpha_{cw} \end{pmatrix} = i \begin{pmatrix} \omega_0 + i\rho & i\beta_{12} \\ 0 & \omega_0 + i\rho \end{pmatrix} \begin{pmatrix} \alpha_{ccw} \\ \alpha_{cw} \end{pmatrix} + i\sqrt{2\Gamma} \mathbf{E}_{in}^T, \quad (2.25)$$

where the coupling coefficient is present only in the CCW mode (i.e. $\beta_{21} = 0$). The energy exchange is so forced in one direction and this gives rise to the analogous limit scenario seen in figure 2.15, when $\beta_{12} = 0$. Thus, even when $\beta_{21} = 0$, there is no longer the splitting of the resonance, and the reflection is maximum for one direction of excitation and zero for the other. In particular, as shown in figure 2.16 (b) the reflection $l - r$ reduces to zero. The system works on

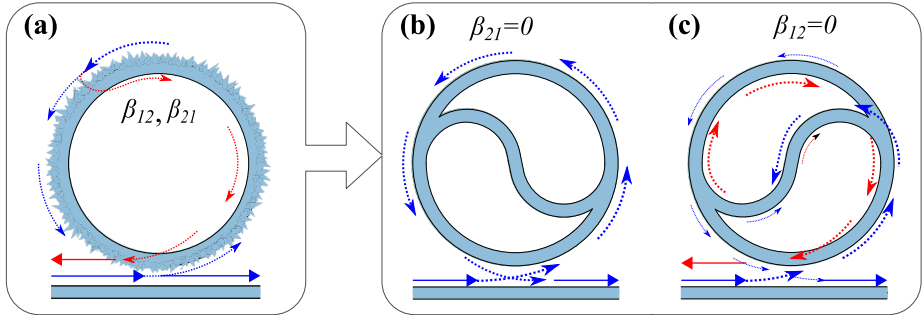


Figure 2.16: (a) Sketch of the backscattering process due to the surface wall roughness. Panels (b) and (c): S-shape waveguide inscribed into a circular microresonator which resembles the taiji symbol. In particular, panel (c) is obtained mirroring the S-shape of panel (b). Considering an excitation from left to right, the configuration (b) ((c)) presents a $l - r$ reflection equal (different) to zero.

an exceptional point and presents both degenerate eigenvalues and eigenvectors (i.e. ω_0 and $\bar{v}_\pm = (1, 0)$). It is worth noticing that mirroring the S (see figure 2.16 (c)) a forced energy exchange takes place from the CCW to the CW mode, and leads exactly to the limit case seen in figure 2.15, where $\beta_{12} = 0$ and the eigenvalues and eigenvectors are ω_0 and $\bar{v}_\pm = (0, 1)$, respectively. Here, the reflection $l - r$ is maximized, while the reflection $r - l$ is equal to zero. Therefore, embedding S-shaped waveguide element in the microring selectively couples the counter-propagating modes in a particular propagation direction.

Similar systems are known in the literature under different names, such as “spectacles-shaped ring resonator” [56], “yin-yang cavities”[57] and “theta cavities”[58]. As far as we known, an analogous system was first introduced in order to achieve an unidirectional lasing in a circular Y-junction ring diode laser [59]. In addition, these systems were used to build unidirectional fiber lasers [60], to prompt electromagnetically induced transparency (EIT) [61] and to control light velocity in monolithic microfiber [62]. Recently, they have been used to build an array of cavities for topological laser operations [23]. Even though light transmission at linear regime remains reciprocal, the intrinsic nonlinearity of laser operation combined with the breaking of the left-right symmetry by the S-shaped branch are responsible for an efficient unidirectional laser operation [63].

As far as we know, despite their successful use in unidirectional lasing and in topological system, a detailed study of the transmission and reflection properties in a microresonator/waveguide system is lacking. In order to understand the counterintuitive behavior of the $l - r$ and $r - l$ optical response, it is useful to proceed with the derivation of the scattering matrix of the whole system. This analytical derivation was obtained in the works [63, 64], and is based on the equations that govern the different coupling regions of the system. These equations allow obtaining the optical response connecting the intrinsic and extrinsic coefficients to the dimensions and material of the taiji microresonator.

Let us consider the taiji scheme of figure 2.16 (b) and let us assume an excitation of the system from right to left, defining E_{in}^R as the amplitude of the input field. The excitation process is shown in figure 2.17 (a), where the different coupling regions are indicated by the grey squares. The amplitudes of the fields that excite these regions are defined as E_n where n is an integer number ranging from 1 to 16. E_{e_j} with $j = 1, 2$ indicates the signal amplitudes lost as radiation modes at the S-shaped branch ends (see black arrows in figure 2.16). z_j is the distance that separates the different coupling regions and, then, the perimeter of the ring circumference is defined as $p = z_1 + z_2 + z_3$. The different coupling regions are treated as beamsplitters, so that k_i, t_i are real terms which represent the coupling and transmission amplitudes at the i -th beamsplitter. In this way the different signal amplitudes are related by the following equations [63]:

$$\begin{aligned} E_{out}^L &= t_1 E_{in}^R + i\kappa_1 E_{15} & E_{out}^R &= i\kappa_1 E_2 \\ E_{e1} &= t_2 E_{14} + i\kappa_2 E_{12} & E_{e2} &= t_3 E_8 + i\kappa_3 E_6 \end{aligned}$$

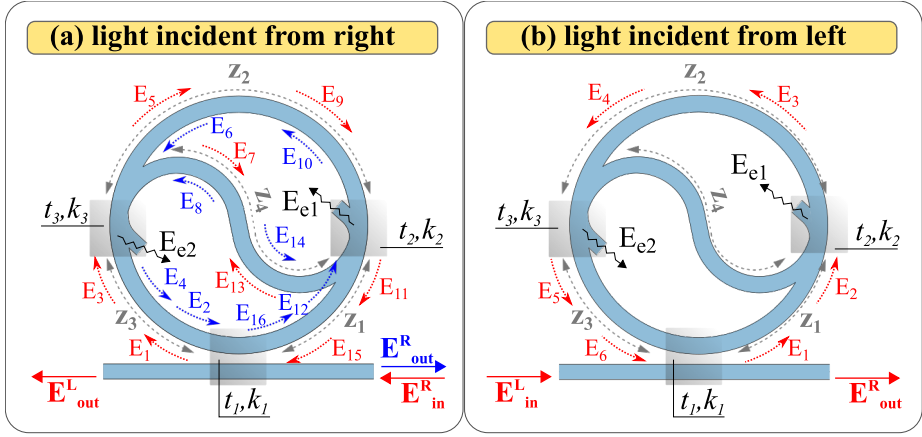


Figure 2.17: (a), (b) Sketch of the taiji microresonator. In particular, (a) ((b)) shows an excitation from the right (left). The gray square highlights the i -th beamsplitter while the arrows map the complex electric field amplitudes. Precisely, the blue (red) arrows label the CW (CCW) propagation. E_j with $j = 1, \dots, 16$ stands for the complex amplitudes of the guided modes, E_{en} with $n = 1, 2$ indicates the evanescent modes. z_m with $m = 1, 4$ labels the distance travelled by the light between the beamsplitters. The transmission and coupling amplitudes of the i -th beamsplitter are indicated as t_i and k_i , respectively.

$$\begin{aligned}
 E_1 &= i\kappa_1 E_{in}^R + t_1 E_{15} & E_2 &= e^{i\gamma_1 z_3} E_4 \\
 E_3 &= e^{i\gamma_1 z_3} E_1 & E_4 &= i\kappa_3 E_8 + t_3 E_6 \\
 E_5 &= t_3 E_3 & E_6 &= e^{i\gamma_1 z_2} E_{10} \\
 E_7 &= i\kappa_3 E_3 & E_8 &= e^{i\gamma_1 z_4} E_{13} \\
 E_9 &= e^{i\gamma_1 z_2} E_5 & E_{10} &= i\kappa_2 E_{14} + t_2 E_{12} \\
 E_{11} &= t_2 E_9 & E_{12} &= e^{i\gamma_1 z_1} E_{16} \\
 E_{13} &= i\kappa_2 E_9 & E_{14} &= e^{i\gamma_1 z_4} E_7 \\
 E_{15} &= e^{i\gamma_1 z_1} E_{11} & E_{16} &= t_1 E_2
 \end{aligned}$$

where the energy conservation is satisfied: $k_i^2 + t_i^2 = 1$. γ_l takes into account the propagation along the segments separating the different beamsplitters. This propagation leads to a phase shift proportional to the optical path and to an amplitude attenuation. The shift is related to the propagation constant β , while the amplitude attenuation per length unit is indicated with α and is related to the material and/or bending losses. Thus, we can define $\gamma_l = \beta + i\alpha$. The previous system of equations has a unique solution for the transmitted E_{out}^L and

reflected E_{out}^R field amplitude:

$$\begin{aligned} E_{out}^L &= \left(t_1 - \frac{\kappa_1^2 t_2 t_3 e^{i\gamma_1 p}}{1 - t_1 t_2 t_3 e^{i\gamma_1 p}} \right); \quad E_{in}^R = \frac{t_1 - t_2 t_3 e^{i\gamma_1 p}}{1 - t_1 t_2 t_3 e^{i\gamma_1 p}} E_{in}^R; \\ E_{out}^R &= \frac{2\kappa_1^2 \kappa_2 \kappa_3 t_3 e^{i\gamma_1(z_2+2z_3+z_4)}}{(1 - t_1 t_2 t_3 e^{i\gamma_1 p})^2} E_{in}^R. \end{aligned} \quad (2.26)$$

In the same way, considering the diagram in figure 2.17 (b), we can treat an excitation from left to right. In this case, the amplitudes of the field are related by the following equations:

$$\begin{aligned} E_{out}^R &= t_1 E_{in}^L + i\kappa_1 E_6 & E_{e1} &= i\kappa_2 E_2 & E_{e2} &= i\kappa_3 E_4 \\ E_1 &= i\kappa_1 E_{in}^L + t_1 E_6 & E_2 &= e^{i\gamma_1 z_1} E_1 & E_3 &= t_2 E_2 \\ E_4 &= e^{i\gamma_1 z_2} E_3 & E_5 &= t_3 E_4 & E_6 &= e^{i\gamma_1 z_3} E_5, \end{aligned}$$

also in this case there is only one solution for the transmitted E_{out}^R and the reflected E_{out}^L field amplitude:

$$\begin{aligned} E_{out}^R &= \left(t_1 - \frac{\kappa_1^2 t_2 t_3 e^{i\gamma_1 p}}{1 - t_1 t_2 t_3 e^{i\gamma_1 p}} \right); \quad E_{in}^L = \frac{t_1 - t_2 t_3 e^{i\gamma_1 p}}{1 - t_1 t_2 t_3 e^{i\gamma_1 p}} E_{in}^L; \\ E_{out}^L &= 0. \end{aligned} \quad (2.27)$$

The transmission and reflection amplitudes to the left (right) of the taiji can be defined as $t_{taiji}^L = E_{out}^R/E_{in}^L$ ($t_{taiji}^R = E_{out}^L/E_{in}^R$) and $r_{taiji}^L = E_{out}^L/E_{in}^L$ ($r_{taiji}^R = E_{out}^R/E_{in}^R$). They have a direct physical meaning and they can be condensed as elements of the scattering matrix:

$$\mathbf{S}_{taiji} = \begin{pmatrix} r_{taiji}^L & t_{taiji}^R \\ t_{taiji}^L & r_{taiji}^R \end{pmatrix} = \begin{pmatrix} 0 & \frac{t_1 - t_2 t_3 e^{i\gamma_1 p}}{1 - t_1 t_2 t_3 e^{i\gamma_1 p}} \\ \frac{t_1 - t_2 t_3 e^{i\gamma_1 p}}{1 - t_1 t_2 t_3 e^{i\gamma_1 p}} & \frac{2\kappa_1^2 \kappa_2 \kappa_3 t_3 e^{i\gamma_1(z_2+2z_3+z_4)}}{(1 - t_1 t_2 t_3 e^{i\gamma_1 p})^2} \end{pmatrix}. \quad (2.28)$$

Thus, this matrix connects the output and input field amplitudes:

$$\begin{pmatrix} E_{out}^L \\ E_{out}^R \end{pmatrix} = \mathbf{S}_{taiji} \begin{pmatrix} E_{in}^L \\ E_{in}^R \end{pmatrix}. \quad (2.29)$$

As expected, the scattering matrix of the taiji microresonator respects the Lorentz reciprocity theorem and, therefore, the transmission is equivalent in the two directions of excitation. On the contrary, the two diagonal elements are different. In fact, the reflection depends on the direction of excitation and, in particular, it is zero for an excitation from left to right. This leads us to say that the taiji microresonator behaves as an unidirectional reflector. It is worth noticing, as we will also see in section 2.4, that the reciprocity of the system in the transmission response is a concept that goes beyond the time reversal symmetry. In fact, the scattering matrix \mathbf{S}_{taiji} is not unitary. The reciprocity of the transmission response combined with the different reflection responses, implies that the energy must be compensated by another process. This process is linked to the radiative loss due to unguided modes in the cladding that occur at the end of the S-shaped branch.

2.3.10 Numerical simulations of the taiji

The predictions of the analytical model reported in the previous section, were tested through FEM simulations engine by Comsol Multiphysics. These results are taken from [63, 64] and assumed a two-dimensional geometry. The taiji microresonator is built by a circular ring, with an embedded S-shaped waveguide, coupled to a bus waveguide (see figure 2.18 (a) and (b)). This microresonator is made of silicon oxynitride (SiO_xN_y) embedded in air. The refractive indices are 1.83 and 1 at the wavelength of $\lambda = 1.55 \mu m$, for SiO_xN_y and air, respectively. The coupling between the ring resonator and the bus waveguide is set to work in the critical coupling regime by fixing $t_1 = 0.9$. While the S-branch shape ends are evanescently coupled to the ring by a point-like coupling. The gap between the S waveguide and the ring is chosen to obtain $t_2 = t_3 = 0.9$. In this numerical model, there is no power dissipation so that $\alpha = 0$.

Figures 2.18 (a) and (b) show the square modulus of the electric field amplitudes when the taiji is excited from right and from left, respectively. The frequency of the input field is fixed equal to the resonant frequency of the taiji.

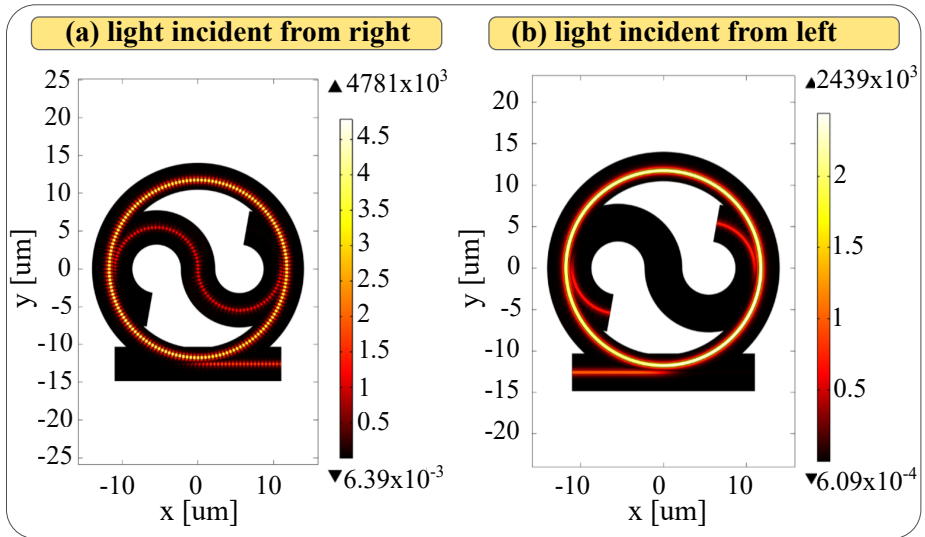


Figure 2.18: (a) and (b) Numerical simulations for a resonant input signal injected from right and from left, respectively. The taiji is designed to work in the critical coupling. The colors map the electric field intensity in the stationary regime and highlight the non-symmetrical behavior of the reflection. When the signal is injected from right (a), the light travels in the S-branch and both counter-propagating modes are excited. Thus all input power is reflected. In (b), the left excitation causes only the propagation of the CCW modes, so that the reflection is null, and all the power is lost into the cladding.

Since the model works in the critical coupling regime, both panel (a) and (b) exhibit null transmitted field. This is in agreement with the Lorentz reciprocity theorem and confirmed by the theoretical model. Figure 2.18 (a) shows the response to the signal at the resonant frequency injected from the right. As predicted by the analytical model, the CW mode travels into the S-branch and excites the CCW mode. In this way, both the CCW and CW modes are excited and the interference causes the field distribution showed in panel (a). Thus, the S-branch excites the CCW mode by changing the propagation direction to the CW one, and causes the reflection of the whole input power. In panel 2.18 (b), when the system is fed from left, the injected power satisfies the resonant condition and travels into the ring resonator. It is worth noticing that a part of the power is coupled to the S-branch and flows to the ends of it, from where it is transmitted to the cladding. In this case, only the CCW mode is excited and the reflection $r - l$ is null.

Figures 2.19 (a) and (b) show the transmitted (blue dots) and reflected (yellow and green dots) intensity for an incident field injected from left and from right, respectively. The intensities are extrapolated from the numerical simulation and they are plotted as a function of the incident wavelength. The red lines display the fit by using the analytical model of subsection 2.3.9. Precisely, we have used the on-diagonal and off-diagonal elements of the scattering matrix 2.28 to

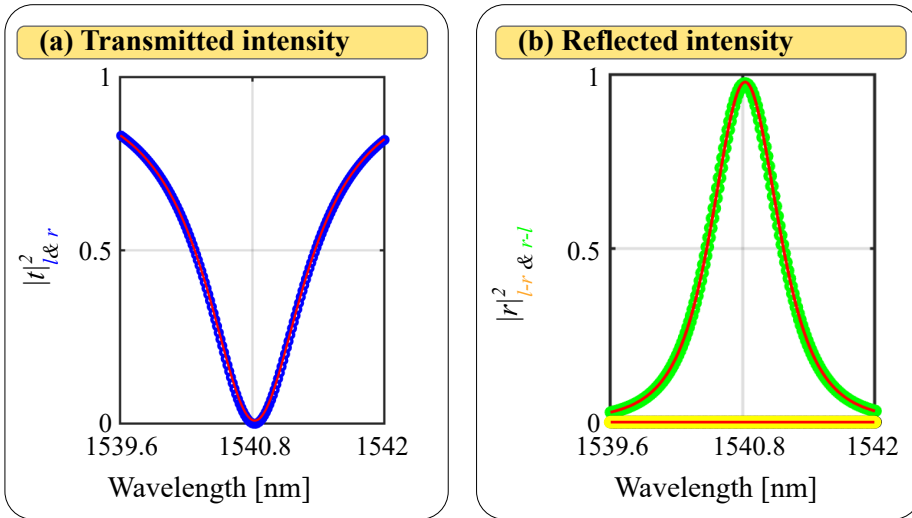


Figure 2.19: (a) and (b): numerical results of the transmitted (blue dots) and reflected (green and yellow dots) intensity as a function of the incident wavelength for an input signal injected from right and from left, respectively. At the resonant frequency, the transmitted intensity reduces to 0 while the reflected $r - l$ and $l - r$ intensity is 1 and 0.

reproduce the transmitted and reflected $r - l$ and $l - r$ intensities, respectively. The three sets of data were simultaneously fit in order to remove the mutual dependency of the shared parameters among the various equations. The fit parameters fixed are the geometric sizes of the taiji model and the effective index of the material. The perfect agreement between the numerical simulation and the analytical model gives a first validation of the previous predictions.

2.3.11 The Fabry-Perot and the transfer matrix approach

As we will see in detail in the experimental section, the incident light is butt-coupled to the sample. Due to the index difference between the external medium (air) and the sample (SiO_xN_y), a Fabry-Perot cavity is created on the facets. In this way, part of the light that propagates in the bus waveguide is reflected by the output and input facets. These continuous reflections give rise to oscillations in the frequency spectrum. Since we consider single mode waveguides, the system's response is modified by a background which exhibits a fast oscillation with a clear carrier frequency. This frequency depends on the geometry of the system and the material of the sample. The transfer matrix approach can be used to model the whole system. In this way, the fields at the input facet are related to the fields at the output facet as follows [63]:

$$\begin{pmatrix} E_{in}^L \\ E_{out}^L \end{pmatrix} = \mathbf{M} \begin{pmatrix} E_{out}^R \\ E_{in}^R \end{pmatrix}, \quad (2.30)$$

where \mathbf{M} is the matrix product of different contributions:

$$\mathbf{M} = \mathbf{M}_{FL} \mathbf{M}_{PL} \mathbf{M}_{taiji} \mathbf{M}_{PR} \mathbf{M}_{FR}. \quad (2.31)$$

Precisely, \mathbf{M}_{FR} and \mathbf{M}_{FL} are associated with the right and left facets of the system and are given by:

$$\mathbf{M}_{FR} = \frac{1}{\tau_R} \begin{pmatrix} 1 & \rho_R \\ \rho_R & 1 \end{pmatrix} \quad \mathbf{M}_{FL} = \frac{1}{\tau_L} \begin{pmatrix} 1 & -\rho_L \\ -\rho_L & 1 \end{pmatrix}, \quad (2.32)$$

where τ_j and ρ_j are the transmission and reflection from the $j = R, L$ facet (see sketch of figure 2.20 (a)). The different sign in reflection between the two matrices means that the interfaces are opposite. \mathbf{M}_{PR} and \mathbf{M}_{PL} are associated with the propagation along the length between the taiji and the right and left facet, respectively. These take the following form:

$$\mathbf{M}_{Pj} = \begin{pmatrix} e^{-i\theta_j} & 0 \\ 0 & e^{i\theta_j} \end{pmatrix}, \quad (2.33)$$

where we have introduced the notation $\theta_j = (\beta + i\alpha)l_j$ to denote the phase shift and attenuation accumulated over the length l_j (see figure 2.20 (a)). \mathbf{M}_{taiji} is the transfer matrix of the taiji microresonator. Considering the equation 2.30 and 2.29, the transfer matrix can be defined through the scattering matrix as:

$$\mathbf{M}_{taiji} = \frac{1}{t_{taiji}^L} \begin{pmatrix} 1 & -r_{taiji}^R \\ r_{taiji}^L & -\det[\mathbf{S}] \end{pmatrix}. \quad (2.34)$$

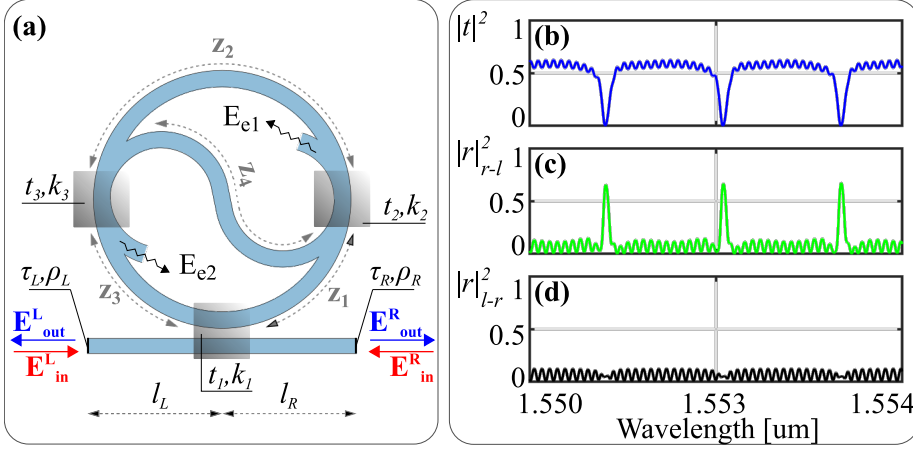


Figure 2.20: (a) Sketch of the taiji microresonator, where l_L (l_R) is the distance between the left (right) facet and the coupling region. Panels (b), (c) and (d) represent transmitted intensity, reflected intensity from left and right as a function of the incident wavelength. Out of resonances, the Fabry-Perot oscillations due to the input and output facets are clearly observed.

In this way, by formulating explicitly the single elements of the transfer matrix we obtain:

$$\mathbf{M}_{taiji} = \begin{pmatrix} A_1 & A_2 \\ A_3 & A_4 \end{pmatrix} = \begin{pmatrix} \frac{1-t_1 t_2 t_3 e^{i\gamma_{LP}}}{t_1 - t_2 t_3 e^{i\gamma_{LP}}} & -\frac{2\kappa_1^2 \kappa_2 \kappa_3 t_3 e^{i\gamma_1(z_2+2z_3+z_4)}}{(1-t_1 t_2 t_3 e^{i\gamma_{LP}})(t_1 - t_2 t_3 e^{i\gamma_{LP}})} \\ 0 & \frac{t_1 - t_2 t_3 e^{i\gamma_{LP}}}{1 - t_1 t_2 t_3 e^{i\gamma_{LP}}} \end{pmatrix}. \quad (2.35)$$

From equation 2.30, we can derive the transmission amplitude of the whole system in both directions (i.e. light incident from left or from right) as $t = E_{out}^R/E_{in}^L = E_{out}^L/E_{in}^R = \frac{1}{M_{11}} = \frac{\det[\mathbf{M}]}{M_{11}}$:

$$t = \frac{\tau_{RTL}}{A_1 e^{-i\Theta^+} - \rho_R \rho_L A_4 e^{i\Theta^+} + \rho_R A_2 e^{i\Theta^-} - \rho_L A_3 e^{-i\Theta^-}}, \quad (2.36)$$

where $\Theta^+ = \theta_R + \theta_L$ and $\Theta^- = \theta_R - \theta_L$. As expected from the Lorentz reciprocity theorem, the transmission in both directions is the same. On the other hand, the reflection amplitude from light incident from the left (right) is defined as $r_L = E_{out}^L/E_{in}^L = M_{21}/M_{11}$ ($r_R = E_{out}^R/E_{in}^R = -M_{12}/M_{11}$):

$$r_L = \frac{\rho_R A_4 e^{i\Theta^+} - \rho_L A_1 e^{-i\Theta^+} - \rho_R \rho_L A_2 e^{i\Theta^-} + A_3 e^{-i\Theta^-}}{A_1 e^{-i\Theta^+} - \rho_R \rho_L A_4 e^{i\Theta^+} + \rho_R A_2 e^{i\Theta^-} - \rho_L A_3 e^{-i\Theta^-}}, \quad (2.37)$$

and

$$r_R = -\frac{\rho_R A_1 e^{-i\Theta^+} - \rho_L A_4 e^{i\Theta^+} + A_2 e^{i\Theta^-} - \rho_L \rho_R A_3 e^{-i\Theta^-}}{A_1 e^{-i\Theta^+} - \rho_R \rho_L A_4 e^{i\Theta^+} + \rho_R A_2 e^{i\Theta^-} - \rho_L A_3 e^{-i\Theta^-}}. \quad (2.38)$$

2. Hermitian and non-Hermitian systems

The transmission and reflection amplitudes for left and right excitation have inside the Fabry-Perot oscillations. Figure 2.20 (b), (c) and (d) show the transmission, reflection from right and left, plotted by using equation 2.36, 2.38 and 2.37, as a function of the incident wavelength. In all three panels the presence of the Fabry-Perot oscillations connected to the input and output facets are evident. The typical response of the taiji microresonator does not change. In fact, the reflection for an excitation from right is different from zero and exhibits clear peaks. While the reflection for an excitation from left vanishes into the Fabry-Perot oscillation.

Neglecting the Fabry-Perot of the bus waveguide ($\tau_R = \tau_L = 1$ and $\rho_R = \rho_L = 0$) the equations 2.36, 2.37 and 2.38 reduce to the transmission and reflection amplitude seen in the scattering matrix 2.28. In addition, the amplitudes of transmission and reflection formulated in 2.36, 2.37 and 2.38 can be reduced to the simple case of a resonator butt-coupled through a bus waveguide, by imposing $t_2 = t_3 = 1$. This condition prevents light traveling through the S-branch and, therefore, reduces the coupling coefficients k_1, k_2 to zero. The taiji transfer matrix 2.35 reduces to the usual transfer matrix of a single mode resonator [65]:

$$\mathbf{M}_r = \begin{pmatrix} A_1 & A_2 \\ A_3 & A_4 \end{pmatrix} = \begin{pmatrix} \frac{1-t_1 e^{i\gamma p}}{t_1 - e^{i\gamma p}} & 0 \\ 0 & \frac{t_1 - e^{i\gamma p}}{1-t_1 e^{i\gamma p}} \end{pmatrix}. \quad (2.39)$$

In this scenario, the reflection amplitude from left and right is only connected to the reflections of the Fabry-Perot. We can reformulate the equations 2.36, 2.37 and 2.38 as:

$$r_L = \frac{\rho_R A_4 e^{i\Theta^+} - \rho_L A_1 e^{-i\Theta^+}}{A_1 e^{-i\Theta^+} - \rho_R \rho_L A_4 e^{i\Theta^+}}, \quad (2.40)$$

$$r_R = -\frac{\rho_R A_1 e^{-i\Theta^+} - \rho_L A_4 e^{i\Theta^+}}{A_1 e^{-i\Theta^+} - \rho_R \rho_L A_4 e^{i\Theta^+}}. \quad (2.41)$$

and

$$t = \frac{\tau_R \tau_L}{A_1 e^{-i\Theta^+} - \rho_R \rho_L A_4 e^{i\Theta^+}}. \quad (2.42)$$

The equation 2.42 can be used to fit the experimental spectrum and to extract the characteristic parameters of a resonator coupled to a bus waveguide as in [66]. Neglecting the resonator (i.e. imposing $t_1 = 1$), A_1 and A_4 are equal to 1 and the previous equations reduce to the usual response of a Fabry-Perot cavity:

$$r_L = \frac{\rho_R e^{i\Theta^+} - \rho_L e^{-i\Theta^+}}{e^{-i\Theta^+} - \rho_R \rho_L e^{i\Theta^+}}, \quad (2.43)$$

$$r_R = -\frac{\rho_R e^{-i\Theta^+} - \rho_L e^{i\Theta^+}}{e^{-i\Theta^+} - \rho_R \rho_L e^{i\Theta^+}}. \quad (2.44)$$

and

$$t = \frac{\tau_R \tau_L e^{i\Theta^+}}{1 - \rho_R \rho_L e^{2i\Theta^+}}. \quad (2.45)$$

Similarly, neglecting the Fabry-Perot induced by the facets (i.e. $\tau_L = \tau_R = 1$, $\rho_L = \rho_R = 0$ and $\Theta^+ = \Theta^- = 0$), we obtain the transmission amplitude of a single mode resonator:

$$t = \frac{t_1 - e^{i\gamma p}}{1 - t_1 e^{i\gamma p}} = \frac{t_1 - \sigma e^{i\beta p}}{1 - t_1 \gamma e^{i\beta p}}, \quad (2.46)$$

where $\sigma = e^{-\alpha p}$. Since the reflection, without the S-branch, is only connected to the facets of the bus waveguide, the reflection amplitudes r_L and r_R reduce to zero. As we have seen in the theoretical model, β is the propagation constant and can be defined as $\beta = \frac{n_{eff}}{c} \omega$, where n_{eff} is the effective index. Therefore, the transfer function exhibits a set of symmetric Lorentzians when the resonance condition $n_{eff} p = m \frac{2\pi c}{\omega}$ is satisfied, where m is an integer number and c is the vacuum speed of light. In this scenario, depending on t_1 and σ , the different coupling regimes of the resonator can be identified: under-coupling ($t_1 > \sigma$), critical-coupling ($t_1 = \sigma$) and over-coupling ($t_1 < \sigma$).

The equation in 2.46 can be reduced to the Lorentzian of a three-level system seen in section 2.2 by the relation 2.12. For this purpose, it is good to pay attention to the meaning of the intrinsic and extrinsic coefficients. In equation 2.46, σ is a dimensionless coefficient that quantifies how much field amplitude remains into the resonator. Similarly, t_1 and k_1 are dimensionless terms that quantify how much field amplitude travels unperturbed along the bus waveguide and couples into the resonator, respectively. In contrast, the intrinsic Lorentzian coefficient of equation 2.12, γ , provides the damping rate of losses within the resonator for a round trip and has the dimension of an inverse of time (Hz). While the extrinsic coefficient Γ provides the damping rate of excitation and is related to how much energy we put into the resonator per round trip. It is also measured in Hz . In order to connect the equation 2.46 with 2.12 we define $g^2 + \sigma^2 = 1$, where g is a dimensionless coefficient that quantifies how much field is lost into the resonator. This expression is nothing more than the energy conservation, in fact the sum of the lost g^2 and the remaining σ^2 intensity must be equal to 1. At this point, it is better to reformulate equation 2.46 as:

$$t = t_1 - \frac{k_1^2 \sigma}{e^{-i \frac{n_{eff}}{c} p \omega} - t_1 \sigma}. \quad (2.47)$$

By focusing our attention on a single resonance (ω_0), we can write the previous equation as:

$$t = t_1 - \frac{k_1^2 \sigma}{e^{-i \frac{n_{eff}}{c} p (\omega_0 - \omega)} - t_1 \sigma} = t_1 - \frac{k_1^2 \sigma}{e^{i \frac{n_{eff}}{c} p \Delta \omega} - t_1 \sigma}, \quad (2.48)$$

where, in agreement with the definition of section 2.2, $\Delta \omega = \omega - \omega_0$. At this point, we must introduce some assumptions. First, we develop the equation 2.48 around the resonance ω_0 (i.e. $\omega \rightarrow \omega_0$) and, then, we suppose a high Q-factor. This hypothesis allows fixing $t_1 \rightarrow 1$ (i.e. $k_1 \rightarrow 0$) and $\sigma \rightarrow 1$ (i.e. $g \rightarrow 0$), and

2. Hermitian and non-Hermitian systems

writing:

$$t \approx 1 - \frac{k_1^2}{1 + i \frac{n_{eff}}{c} p \Delta\omega - \sqrt{1 - k_1^2} \sqrt{1 - g^2}} \approx 1 - \frac{k_1^2}{i \frac{n_{eff}}{c} p \Delta\omega + \frac{k_1^2}{2} + \frac{g^2}{2}}. \quad (2.49)$$

Finally, by multiplying and dividing by $\frac{c}{n_{eff} p}$, we can compare this expressions with equation 2.12:

$$t \approx 1 - \frac{2 \frac{k_1^2 c}{2n_{eff} p}}{i \Delta\omega + \frac{g^2 c}{2n_{eff} p} + \frac{k_1^2 c}{2n_{eff} p}} \equiv 1 - \frac{2\Gamma}{i\Delta\omega + \gamma + \Gamma}. \quad (2.50)$$

Therefore, we obtain that $\Gamma = \frac{k_1^2 c}{2n_{eff} p}$ and $\gamma = \frac{g^2 c}{2n_{eff} p}$. As we have previously mentioned, Γ (γ) is connected to how much energy is transferred (lost) into the resonator per round trip.

2.4 Helmholtz equation and the reflection of waves

For the sake of completeness, in this section we will deal with transmission and reflection in the two directions of excitation considering the propagation of a monochromatic wave within a medium which has an inhomogeneous permittivity. This derivation does not consider the TCMT or the coupled mode theory, as in the previous discussion, but focuses on the solution of the typical Helmholtz equation. We will use the analogy between the time-dependent Schroedinger equation for a generic complex potential and the one-dimensional Helmholtz equation. We will take as reference the articles reported in [67, 68, 69], and we will see how the symmetry of the dielectric medium, absorptive/emissive or non-absorptive/non-emissive, determines the reflection for the two directions of excitation.

Let us consider a monochromatic electromagnetic wave of frequency ω that propagates in the x direction within a material with an inhomogeneous permittivity $\epsilon_r[x]$. For simplicity, let us consider a transverse electric field (TE) polarization and, then, formulate the electric field along z as $\vec{E}[x] = E_z[x] \hat{z} e^{i\omega t}$. $E_z[x]$ is the x -dependent electric field amplitude which satisfies the one-dimensional Helmholtz equation [70]:

$$\frac{d^2 E_z[x]}{dx^2} + \mu_0 \mu_r \epsilon_0 \epsilon_r[x] \omega^2 E_z[x] = \frac{\mu_r'}{\mu_r} \frac{dE_z[x]}{dx}, \quad (2.51)$$

where μ is the permeability and $'$ indicates the first derivative with respect to x . Assuming a permeability given by $\mu_r = 1$ and writing the permittivity as $\epsilon_r[x] = 1 + \epsilon_R[x] + i \epsilon_I[x]$ the Helmholtz equation reduces to:

$$\frac{d^2 E_z[x]}{dx^2} + V[x] E_z[x] = 0. \quad (2.52)$$

where $V[x] = \left(\frac{\omega}{c}\right)^2 (1 + \epsilon_R[x] + i \epsilon_I[x])$ is, in the analogy with the Schroedinger equation, the complex potential for an incident particle of mass m .

Let us assume that the dielectric region is within the range $[-d, d]$ and that $\epsilon_R[x]$ and $\epsilon_L[x]$ are only appreciable in that range. In the following, we consider the two cases: light injected from the left and light injected from the right. In the case of incident light which propagates from left to right, the electric field in the spatial range of $x < -d$ assumes the following form:

$$E_z[x < -d] = A_{l-r} e^{i k (x+d)} + B_{l-r} e^{-i k (x+d)}, \quad (2.53)$$

where $k = \frac{\omega}{c}$ is the wavevector and the equation is written as the sum of the incident and the reflected wave. While for $x > d$ the electric field has only one component that propagates in the direction of the injected light and assumes the following expression:

$$E_z[x > d] = C_{l-r} e^{i k (x-d)}. \quad (2.54)$$

With regard to the region of space inside the dielectric material $[-d, d]$, the electric field is fixed by the solution of the differential equation 2.52. In order to determine the behavior of the transmission and reflection it is useful to determine the Wronskian function (W) [71]. Assuming that u and v are linearly independent solutions of equation 2.52, the electric field can be formulated as:

$$E_z[-d \leq x \leq d] = \alpha u[x] + \beta v[x], \quad (2.55)$$

where α and β are constant coefficients. The solutions u and v are such that $u[0] = 1$, $u'[0] = 0$ and $v[0] = 0$, $v'[0] = 1$. The Wronskian functions, are defined by reformulating the linear differential equation in vector form as:

$$\tilde{E}'_z[x] = \tilde{A}[x] \tilde{E}_z[x] \quad (2.56)$$

where $\tilde{E}_z = (E_z, E'_z)^T$ and \tilde{A} is the matrix:

$$\tilde{A} = \begin{pmatrix} 0 & 1 \\ -V[x] & 0 \end{pmatrix}. \quad (2.57)$$

If u and v are solutions of the equation 2.52, then the following matrix:

$$\tilde{\phi}[x] = \begin{pmatrix} u[x] & v[x] \\ u'[x] & v'[x] \end{pmatrix}, \quad (2.58)$$

is solution of the matrix equation 2.56. This is called the fundamental solution, and this matrix satisfies the following differential equation:

$$\tilde{\phi}[x]' = \tilde{A}[x] \tilde{\phi}[x]. \quad (2.59)$$

The determinant of this matrix is a function of the spatial coordinates and is called the Wronskian of the linear differential equation:

$$W[x] = \det(\tilde{\phi}[x]) = u v' - u' v. \quad (2.60)$$

2. Hermitian and non-Hermitian systems

Taking advantage of the equation 2.59 and the definition of W it is trivial to see that, in our case, W is constant with respect to the spatial coordinate ($\frac{dW}{dx} = 0$). In particular, W is equal to 1 along the dielectric material. The transmission and reflection amplitude can be determined as: $t_{l-r} = C_{l-r}/A_{l-r}$ and $r_{l-r} = B_{l-r}/A_{l-r}$. These coefficients can be found by matching the electric field and its derivative at the boundary $x = \pm d$. In this way, one obtains:

$$r_{l-r} = -\frac{u'_d v'_{-d} - u'_{-d} v'_d + ik(v_d u'_{-d} + u_{-d} v'_d) - ik(u_d v'_{-d} + v_{-d} u'_d) + k^2(u_{-d} v_d - u_d v_{-d})}{u'_d v'_{-d} - u'_{-d} v'_d + ik(v_d u'_{-d} - u_{-d} v'_d) - ik(u_d v'_{-d} - v_{-d} u'_d) - k^2(u_{-d} v_d - u_d v_{-d})} \quad (2.61)$$

and

$$t_{l-r} = \frac{-2ik(u_d v'_d - v_d u'_d)}{u'_d v'_{-d} - u'_{-d} v'_d + ik(v_d u'_{-d} - u_{-d} v'_d) - ik(u_d v'_{-d} - v_{-d} u'_d) - k^2(u_{-d} v_d - u_d v_{-d})}, \quad (2.62)$$

where we use the subscript "-d" and "d" to denote the value of the function at $x = -d$ and $x = d$ respectively.

Let us consider the case where the light is injected from the right. Here, the wave propagates from right to left and the electric field can be written as:

$$E_z[x < -d] = C_{r-l} e^{-ik(x+d)}, \quad (2.63)$$

$$E_z[x > d] = A_{r-l} e^{-ik(x-d)} + B_{r-l} e^{ik(x-d)}, \quad (2.64)$$

and

$$E_z[-d \leq x \leq d] = \delta u[x] + \gamma v[x]. \quad (2.65)$$

As we have done above it is possible to compute the transmission and reflection amplitude as $t_{r-l} = C_{r-l}/A_{r-l}$ and $r_{r-l} = B_{r-l}/A_{r-l}$:

$$r_{r-l} = -\frac{u'_d v'_{-d} - u'_{-d} v'_d + ik(v_{-d} u'_d + u_d v'_{-d}) - ik(u_{-d} v'_d + v_d u'_{-d}) + k^2(u_{-d} v_d - u_d v_{-d})}{u'_d v'_{-d} - u'_{-d} v'_d + ik(v_{-d} u'_d - u_d v'_{-d}) - ik(u_{-d} v'_d - v_d u'_{-d}) - k^2(u_{-d} v_d - u_d v_{-d})} \quad (2.66)$$

and

$$t_{r-l} = \frac{-2ik(u_{-d} v'_d - u'_{-d} v_d)}{u'_d v'_{-d} - u'_{-d} v'_d + ik(u'_{-d} v_d - u_{-d} v'_d) - ik(u_d v'_{-d} - v_{-d} u'_d) - k^2(u_{-d} v_d - u_d v_{-d})}. \quad (2.67)$$

As we have seen, the Wronskian function is constant during the light propagation, then $W_{-d} = W_d$. This means that the transmission amplitudes in the equations 2.62 and 2.67 are equal. It should be noted that this result is valid for any potential, in fact the dielectric constant can be real, complex, symmetric and non-symmetric. This result is in agreement with the case of the backscattering and, with a real potential, it is strictly connected to the time reversal symmetry of the system. It is worth noticing that in the case of a complex permittivity the time-reversal symmetry is broken and, therefore, the unitarity is no longer assured (we can have the presence of absorption and/or gain). Then, the invariance of the transmission amplitude goes beyond the time-reversal symmetry and, as we will see, allows a dependence of the reflection amplitude on the excitation direction.

Obviously, when the spatial dependence of the permittivity is equal to zero (i.e. $\epsilon_R[x] = \epsilon_I[x] = 0$), the transmission and reflection amplitude in both directions of excitation are equal to 1 and 0 respectively. On the other hand, depending on the permittivity of the material (i.e. of the potential $V[x]$), we can identify three different cases (each scenario contains a table with the transmission and reflection amplitudes computed by fixing $k = 1 a.u.$, $d = 1 a.u.$ and choosing a particular potential $V[x]$):

- when the permittivity is symmetric (i.e. $\epsilon_r[x] = \epsilon_r[-x]$) real or complex. In this case, the function $u[x]$ is even, while the function $v[x]$ is odd [72], so we have that $u_d = u_{-d}$, $v_d = -v_{-d}$ and $u'_d = -u'_{-d}$, $v'_d = v'_{-d}$. The reflection amplitudes 2.61 and 2.66 become equal and consequently $r_{l-r} = r_{r-l}$. Then, a real or complex symmetric potential makes both $r_{l-r} = r_{r-l}$ and $|r_{l-r}| = |r_{r-l}|$ satisfied. We have seen that in the case of backscattering there is a similar scenario when $\beta_{12} = \beta_{21}$ whether they are real or complex;

$\epsilon_R = 4x^2 \ \& \ \epsilon_I = 0$			
t_{l-r}	t_{r-l}	r_{l-r}	r_{r-l}
$-0.857 - i 0.129$	$-0.857 - i 0.129$	$-0.0743 + i 0.493$	$-0.0743 + i 0.493$
$ t_{l-r} ^2$	$ t_{r-l} ^2$	$ r_{l-r} ^2$	$ r_{r-l} ^2$
0.752	0.752	0.248	0.248
$\epsilon_R = 0 \ \& \ \epsilon_I = x^2$			
t_{l-r}	t_{r-l}	r_{l-r}	r_{r-l}
$-0.308 + i 0.651$	$-0.308 + i 0.651$	$-0.03 - i 0.027$	$-0.03 - i 0.027$
$ t_{l-r} ^2$	$ t_{r-l} ^2$	$ r_{l-r} ^2$	$ r_{r-l} ^2$
0.518	0.518	0.002	0.002

Table 2.1: Values computed from the equations 2.61, 2.62, 2.66 and 2.67 for a symmetrical potential of the type ax^2 real or complex. As required by the parity of the function u and v , both relations are satisfied: $r_{l-r} = r_{r-l}$ and then $|r_{l-r}| = |r_{r-l}|$. As expected, the two transmission amplitudes are equal: $t_{l-r} = t_{r-l}$.

- when the permittivity is real and non-symmetric, all terms within round brackets of equation 2.61 and 2.66 are real [72] and we have that $r_{l-r} \neq r_{r-l}$ but the intensity reflected in the two directions of excitation is the same $|r_{l-r}| = |r_{r-l}|$. This corresponds to the case of backscattering with a Hermitian coupling coefficient $\beta_{12} = -\beta_{21}^*$;

2. Hermitian and non-Hermitian systems

$\epsilon_R = x \ \& \ \epsilon_I = 0$			
t_{l-r}	t_{r-l}	r_{l-r}	r_{r-l}
$-0.375 + i 0.833$	$-0.375 + i 0.833$	$0.080 - i 0.399$	$-0.245 - i 0.325$
$ t_{l-r} ^2$	$ t_{r-l} ^2$	$ r_{l-r} ^2$	$ r_{r-l} ^2$
0.834	0.834	0.166	0.166

Table 2.2: Values computed from the equations 2.61, 2.62, 2.66 and 2.67 for a real and non-symmetric potential of the type x . As expected from the trend of the functions u and v the following relations are satisfied: $r_{l-r} \neq r_{r-l}$ and $|r_{l-r}| = |r_{r-l}|$; while $t_{l-r} = t_{r-l}$ is still valid.

- when the permittivity is complex and non-symmetric, the terms in the round parentheses of the equation 2.61 and 2.66 are complex quantities [72] and consequently the module is different $|r_{l-r}| \neq |r_{r-l}|$. In the case of backscattering, this corresponds to the non-Hermitian scenario (i.e. with dissipative terms): $\beta_{12} \neq -\beta_{21}^*$ and $\beta_{12} \neq \beta_{21}$.

$\epsilon_R = 2x \ \& \ \epsilon_I = 0.2$			
t_{l-r}	t_{r-l}	r_{l-r}	r_{r-l}
$-0.265 + i 0.568$	$-0.265 + i 0.568$	$-0.034 - i 0.653$	$-0.400 + i 0.364$
$ t_{l-r} ^2$	$ t_{r-l} ^2$	$ r_{l-r} ^2$	$ r_{r-l} ^2$
0.393	0.393	0.427	0.293

Table 2.3: Values calculated from the equations 2.61, 2.62, 2.66 and 2.67 for a complex non-symmetric potential of the type $2x - i 0.2$. In this case, the intensities reflected in the two directions of excitation are different and then also the amplitudes are diverse, i.e $|r_{l-r}| \neq |r_{r-l}|$ and then $r_{l-r} \neq r_{r-l}$; while the transmission amplitudes are always equal: $t_{l-r} = t_{r-l}$.

It is worth noticing that a non-homogeneous material, which exhibits a real permittivity, has the reflection amplitudes constrained by the conservation of the energy. In fact, the sum of the intensities transmitted and reflected must be equal to the intensity of the incident beam. Multiplying the Helmholtz equation 2.52 by the complex conjugate electric field E_z^* and subtracting the complex conjugate of the equation so obtained, one get the following conservation law:

$$\frac{d}{dx}(\text{Im}[E_z^* \frac{d}{dx} E_z]) = -\text{Im}[V]|E_z|^2. \quad (2.68)$$

When the imaginary part of the potential reduces to zero (i.e. $\epsilon_I = 0$), the $\text{Im}[E_z^* \frac{d}{dx} E_z]$ does not depend on the spatial coordinate x . Replacing the solutions of the differential equations (equations 2.53, 2.54, 2.63 and 2.64), in this conservation law and then considering both sides of excitation, one obtains the following relations:

$$|t_{l-r}|^2 + |r_{l-r}|^2 = 1, \quad (2.69)$$

$$|t_{r-l}|^2 + |r_{r-l}|^2 = 1. \quad (2.70)$$

If the permittivity of the material is real, then the reciprocity of the system, i.e. the same value of the transmission amplitudes $t_{l-r} = t_{r-l}$, causes that the intensities reflected in the two directions of excitation are equal $|r_{l-r}|^2 = |r_{r-l}|^2$.

Summarizing, the propagation of a monochromatic wave within a material with a non-homogeneous permittivity gives rise to a different intensity of the reflected field in the two directions of excitation if and only if the permittivity is non-symmetric and complex (i.e. with the presence of gain or absorption term). This is in agreement with the case of the backscattering due to the surface wall roughness inside a microresonator, where a different intensity of the field, reflected in the two directions of excitation, can be obtained if and only if the two coupling coefficients are different and complex. This generates a different energy exchange between the clockwise and the counterclockwise mode due to a different interplay between the absorption and back-reflection in the two directions of excitation.

A particular function that makes the system reflectionless is based on the hyperbolic secant. In the field of quantum mechanics, it is remarkable and even amazing that this potential makes the system reflectionless for a quantum particle at any energy when A assumes some specific values [73, 74]. In fact, there are families of potentials based on the hyperbolic secant that make the system non-reflecting for both directions of excitation (see figure 2.21 (a)). These dielectric functions were first considered by Epstein [75]. Fixing the imaginary part of the permittivity equal to zero ($\epsilon_I = 0$) and the real one in the following way:

$$\epsilon_R[x] = n(n+1) \operatorname{sech}[x]^2, \quad (2.71)$$

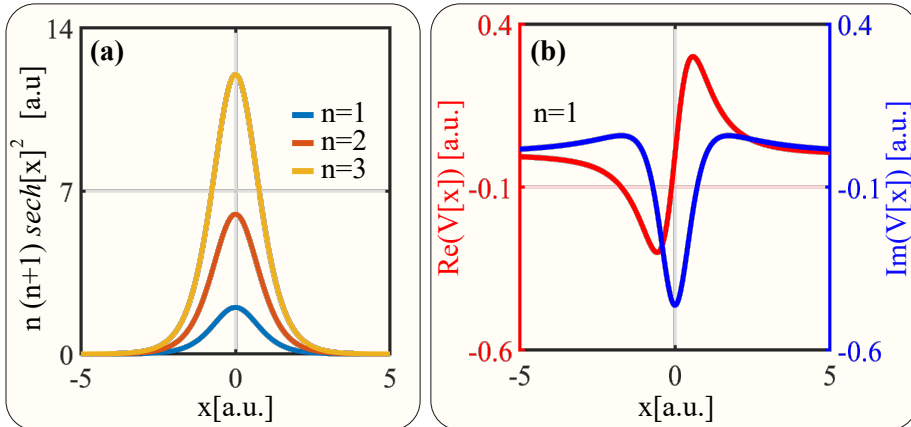


Figure 2.21: (a) The hyperbolic secant potential as a function on the spatial coordinate x for $n = 1, 2, 3$. (b) Real (red line) and imaginary (blue line) parts of a potential, which satisfies the Kramer-Kronig relation, as a function of x .

2. Hermitian and non-Hermitian systems

one gets that the system is reflectionless for any integer value of n . In other words, an inhomogeneous material that presents this spatial dependence of the permittivity is a perfectly transparent medium. As mentioned above, this potential is symmetrical and real, so the reflection amplitudes are equal. By setting the wavevector and the dielectric region as $k = 1 \text{ a.u.}$, $d = 6 \text{ a.u.}$ and using the potential in equation 2.71, one obtains: $t_{l-r} = t_{r-l} = 1$ and $r_{l-r} = r_{r-l} = 0$ for $n = 1, 2, 3, \dots, n \in \mathbb{Z}$. The zeros are in the order of the computer's accuracy ($\approx 0.1 \cdot 10^{-11}$). It should be noted that by increasing n the potential expands within the dielectric region and it is therefore necessary to increase the value of d .

A possible way to obtain no reflection in only one direction of excitation was introduced in ref. [68]. In this work, it is shown that an inhomogeneous dielectric material does not scatter light from one side if the complex dielectric permittivity is such that its real part is spatially related to the imaginary one by Kramers-Kronig. In this case, the potential $V[x]$ satisfies the following relations:

$$\text{Re}[V[x]] = \frac{1}{\pi} \mathbf{P} \int_{-\infty}^{+\infty} \frac{\text{Im}[V[s]]}{s-x} ds, \quad (2.72)$$

$$\text{Im}[V[x]] = -\frac{1}{\pi} \mathbf{P} \int_{-\infty}^{+\infty} \frac{\text{Re}[V[s]]}{s-x} ds, \quad (2.73)$$

where P indicates the main part of the integral. Typically, in optics, the Kramers-Kronig relations connect the real and imaginary part of the complex susceptibility of a material in the frequency domain. For a wide class of linear systems, the causality introduces the Kramer-Kronig relation between the real and imaginary part of the Fourier transform of the response function. Therefore, the origin of this relation in the frequency domain is based on the fact that the response of the material to an applied electric field can only depend on the past of such electric field [70]. A family of functions, which satisfies the Kramer-Kronig relations (equation 2.72 and 2.73), is:

$$V[x] = e^{\pi/2(n+1)} \frac{A i}{(x + i/\xi)^{(n+1)}}, \quad (2.74)$$

where A , ξ and $n = 1, 2, 3, \dots, n \in \mathbb{N}$ are constants. In particular, A fixes the amplitude while ξ defines the spatial scale. When ξ reduces to zero, the potential V tends to 0. The real and imaginary part of this family obtained fixing $n = 1$ is shown in figure 2.21 (b). Substituting these potentials into 2.72 and 2.73 one can prove that they satisfy the Kramers-Kronig relation.

Fixing $A = 1/50 \text{ a.u.}$ and $\xi = 1 \text{ a.u.}$ we obtain from equations 2.61, 2.62, 2.66 and 2.67: $|t_{l-r}|^2 = |t_{r-l}|^2 = 1.074$ ($|t_{l-r}|^2 = |t_{r-l}|^2 = 0.994$) $|r_{l-r}|^2 = 0.23$ ($|r_{l-r}|^2 = 0.857$) and $|r_{r-l}|^2 = 0$ ($|r_{r-l}|^2 = 0$) with $n = 0$ ($n = 1$). Therefore, solving the Helmholtz equation for any integer n value, we get zero reflection by exciting the system from right to left. In our case we have seen this result by solving the one-dimensional Helmholtz equation and considering a perpendicular excitation, thus neglecting the angle of the incidence beam. This result can be

easily extended for any angle of incidence, and therefore, lossy media obeying the Kramers-Kronig relations in space will not reflect radiation for any angle of incidence [68].

2.5 From the backscattering to the Fano lineshape

In section 2.2, the knowledge of the complex field allows studying the coupling dynamics between the co-propagating and counter-propagating modes. Precisely, we have seen how the presence of Hermitian and non-Hermitian coupling coefficients, regulates the optical response of a microring resonator subjected to the backscattering. The theoretical model used, is based on the TCMT in analogy with a λ three-level system. This simple model can be generalized to structures where the coupling between two co-propagating modes leads to electromagnetically induced transparency, Fano interference or Autler-Townes splitting [76].

In this section, we study the optical response of a multimodal microresonator coupled to a single mode waveguide, in which the interplay of resonant modes could give rise to asymmetric Fano lineshape. The Fano lineshape is characterized by a sharp asymmetry in the response spectrum of a system because of the interaction between a discrete localized state and a continuum of states [77]. In integrated photonics, these phenomena could be revealed by the coupling between narrow and broad resonances from two resonators coupled through feedback waveguides. Fundamental phenomena, such as electromagnetic induced transparency (EIT)[78], subwavelength topological photonics [79], Borrmann and Kerker effect [80], yield Fano-like resonances. Moreover, these peculiar resonances have been exploited in many applications such as ultra-small lasers [81], enhanced all-optical switching [82] and ultra-sensitive spectroscopy [83].

In a previous work in ref. [84], the authors have studied Fano lineshape in a single microresonator vertically coupled to a bus waveguide. The asymmetrical response is obtained as a consequence of the coupling between different radial modes through the buried waveguide. Additionally, in ref. [85], it is proved the possibility to locally tune the relative spectral position between modes by modifying their overlap. This is particularly important for multi-mode optical devices, which are used in optical communication and signal processing [86]. As an example, the addition of a multi-modal operation in a single device could yield a new synthetic dimension [87], that is similar to the mapping of a single resonator to an array of operating devices. This analogy gives rise to multi-dimensional photonics and opens new avenues in the optical topological field [88].

It is well known that the resonant frequency in a resonator can be shifted by means of a non-linear process [65]. In a linear regime, the overlap between the resonances governs the interaction and introduces a complex or reactive inter-mode coupling that manifests in a self-shift of the resonant frequencies [40]. In ref. [84], this phenomenon is described as an analogy to the electronic Lamb-shift.

2. Hermitian and non-Hermitian systems

Since the observation of Fano lineshapes implies the presence of two resonances, multiple parameters are needed to model the system by a closed set of equations [40, 84]. In some cases, the only modeling and characterization of the transmitted intensity could give rise to indeterminate parameters since the modeling yields different fitting solutions. Therefore, this limits the reliability of the extracted coefficients. In the following, we reduce the mutual dependencies of the parameters by analyzing both the phase and the intensity of the transmitted signal. The knowledge of the complex nature of the transmitted electric field allows the use of an inverse complex representation. As we will see, this permits to fit simultaneously three different quantities represented by two sets of data (intensity and phase) and one strategical transformation (inverse complex-representation) in order to extract the relevant coefficients. Precisely we will focus the attention on the role of the coupling parameter that gives rise to a self shift of the resonances, defined as Δ .

2.5.1 Theoretical model

Let us consider a two-mode microresonator vertically coupled to a single mode waveguide. The light coming from the input port of the waveguide (E_{in}) couples with the two resonance modes of the resonator and, then, propagates to the waveguide output port. The dynamic behavior of the electromagnetic field amplitudes (α_1 and α_2) of the two resonance modes can be described by means of TCMT [43, 89, 90]. Following the work of ref. [84], the coupled time differential equations are:

$$\begin{cases} \frac{d\alpha_1}{dt} = -[i(\omega_1 + \Delta_{11}) + \frac{\gamma_1 + \Gamma_{11}^{rad}}{2}] \alpha_1 - (i\Delta_{12} + \frac{\Gamma_{12}^{rad}}{2}) \alpha_2 - i\bar{g}_1 E_{in} \\ \frac{d\alpha_2}{dt} = -[i(\omega_2 + \Delta_{22}) + \frac{\gamma_2 + \Gamma_{22}^{rad}}{2}] \alpha_2 - (i\Delta_{12} + \frac{\Gamma_{12}^{rad}}{2}) \alpha_1 - i\bar{g}_2 E_{in} \end{cases} \quad (2.75a)$$

where ω_1 and ω_2 (γ_1 and γ_2) are the bare frequencies (intrinsic losses inside the microresonator) of the two resonance modes α_1 and α_2 , respectively. Γ_{ij}^{rad} and Δ_{ij} are elements of two (2x2) Hermitian matrices and describe the dissipative and reactive effects due to the presence of the bus waveguide [84]. Their diagonal terms take into account the direct coupling between the waveguide and the microresonator, while the off-diagonal elements introduce an inter-mode interaction between the two microresonator modes. As a result, in the absence of the waveguide, the off-diagonal (Γ_{ij}^{rad} , Δ_{ij}) and the diagonal (Γ_{ii}^{rad} , Δ_{ii}) terms cancel. In this case, the two microresonator modes oscillate independently at the resonant frequencies ω_1 and ω_2 , with intrinsic decay rates γ_1 and γ_2 . In equation 2.75, E_{in} is the incident field that we consider monochromatic $E_{in} = E_{in} e^{-i\omega_{in} t}$ and \bar{g}_1 , \bar{g}_2 are the waveguide-resonator coupling coefficients which are different for the two modes since they depend on the overlap integral of the waveguide mode (incident field) with the specific resonator mode.

To calculate the system transmission we follow the reference [84]. We write the reactive matrix as a sum of two terms: $\Delta_{il} = \Delta_{il}^{rad} + \Delta_{il}^{other}$, where the

first term describes the contribution of the single propagating waveguide mode while the second one takes into account all the other possible waveguide modes. Assuming $\Delta_{12}^{other} \simeq 0$, we define $\omega_1^b = \omega_1 + \Delta_{11}^{other}$ and $\omega_2^b = \omega_2 + \Delta_{22}^{other}$. Then, the elements of the two Hermitian matrices (Δ_{il}^{rad} and Γ_{il}^{rad}) are written in terms of an overall radiative dissipation rate (Γ) and an overall frequency shift (Δ) by introducing two real relative weights (η_1 and η_2). These two coefficients take into account the coupling amplitude of the two resonator modes to the propagating waveguide mode, so that $\eta_1^2 + \eta_2^2 = 1$ and:

$$\Gamma_{il}^{rad} = \eta_i \eta_l \Gamma \quad (2.76)$$

$$\Delta_{il}^{rad} = \eta_i \eta_l \Delta. \quad (2.77)$$

The equations 2.76 and 2.77 are a direct consequence of the energy conservation [91]. The complex transmission, which is the quantity we are interested in, is then given by:

$$t = 1 - i\Gamma(\eta_1 \bar{\alpha}_1 + \eta_2 \bar{\alpha}_2) \quad (2.78)$$

where $\bar{\alpha}_1$ and $\bar{\alpha}_2$ are the stationary solutions of the temporal coupled mode equations. As usual, the square modulus of t is the transmission intensity and its argument ($\phi = \arg(t)$) is the phase of the transmitted field.

To make use of the analysis techniques seen in the subsection 2.3.3, we reformulate the transmission response as a Lorentzian shape perturbed by an interaction term. Introducing $\bar{\beta}_1 = \frac{\eta_1 \bar{\alpha}_1 + \eta_2 \bar{\alpha}_2}{2}$ and $\bar{\beta}_2 = \frac{\eta_1 \bar{\alpha}_1 - \eta_2 \bar{\alpha}_2}{2}$ as a new base, we rewrite the stationary coupled mode equations as:

$$\begin{pmatrix} \bar{\beta}_1 \\ \bar{\beta}_2 \end{pmatrix} = \frac{1}{AD - BC} \begin{pmatrix} D & -B \\ -C & A \end{pmatrix} \begin{pmatrix} i E_{in} \\ 0 \end{pmatrix} \quad (2.79)$$

with:

$$A = i(\Omega^+ + 2\Delta - 2\omega_{inc}) + \gamma^+ + \Gamma \quad (2.80)$$

$$B = i\Omega^- + \gamma^- \quad (2.81)$$

$$C = i(\Omega^- + \eta(\Omega^+ - 2\omega_{inc})) + \gamma^- + \eta\gamma^+ \quad (2.82)$$

$$D = i(\Omega^+ - 2\omega_{inc} + \eta\Omega^-) + \gamma^+ + \eta\gamma^- \quad (2.83)$$

where $\Omega^\pm = \omega_1^b \pm \omega_2^b$, $\gamma^\pm = \frac{\gamma_1 \pm \gamma_2}{2}$ and $\eta = \eta_2^2 - \eta_1^2$. Using equation 2.78, the complex transmission field can be written as follows:

$$t = 1 - \frac{2\Gamma}{i(\Omega^+ + 2\Delta - 2\omega_{inc}) + \gamma^+ + \Gamma - \Theta_{int}} \quad (2.84)$$

where we have used the short-hand notation for the interaction coefficient:

$$\Theta_{int} = \frac{[i(\Omega^- + \eta(\Omega^+ - 2\omega_{inc})) + \gamma^- + \eta\gamma^+][i\Omega^- + \gamma^-]}{i(\Omega^+ - 2\omega_{inc} + \eta\Omega^-) + \gamma^+ + \eta\gamma^-}. \quad (2.85)$$

2. Hermitian and non-Hermitian systems

The equation 2.84 is mathematically analogous to the transmission response seen in section 2.2 for a microresonator subjected to the backscattering. In that case, the interaction term was the intra-cavity backcoupling parameter η .

Equation 2.84 reduces to the known expression of the single-mode microresonator transmission, seen in equation 2.12, when the two resonant frequencies are equal (i.e. $\Omega^- = 0$ and $\gamma^- = 0$). In this limiting case, the interaction term (Θ_{int}) vanishes and equation 2.84 reduces to the typical Lorentzian form:

$$t = 1 - \frac{\Gamma}{i(\omega_1^b + \Delta - \omega_{inc}) + \frac{\gamma_1}{2} + \frac{\Gamma}{2}}, \quad (2.86)$$

where we can identify three coupling regimes: under ($\Gamma < \gamma_1$), over ($\Gamma > \gamma_1$) and critical ($\Gamma = \gamma_1$) coupling.

2.5.2 Complex representation and role of the overall frequency shift

Let us consider the parametric phasor graph as a tool for studying the physics of the system. As seen in detail in section 2.2, this basic graph plots the real and imaginary parts of the transmitted field for different values of the incident frequency [14, 16, 50]. Each point of the phasor graph is associated to a vector, whose modulus (phase angle) denotes the field amplitude (phase shift) of the transmission. In the presence of the interaction coefficient, the optical response is no more a simple Lorentzian but a doublet. Examples of the transmitted intensity and phase as a function of the incident frequency are shown in figure 2.22(a). In panels (a)-(c), we consider a system with $\Gamma_{11}/\gamma_1 = 0.23$, $\Gamma_{22}/\gamma_2 = 0.16$, $\eta_1 = 0.96$ and different values of the overall frequency shift Δ . As explained in section 2.2, when the system is described by an unperturbed Lorentzian ($\Theta_{int} = 0$), the shape of the phasor diagram is a perfect circle [16]. When a modal interaction is present (i.e. $\Theta_{int} \neq 0$), the circular shape divides into two connected loops corresponding to the two excited and interacting modes (see figure 2.22(b)). Their size is strictly connected to the coupling regimes of the mode. In particular, if the diameter is greater (smaller) than one, the excited mode is in over (under) coupling regime.

Another possibility to describe the physics of the system is by using the inverse complex diagram [16, 51]. As in section 2.2, we define the inverse complex of $(1-t)$ as $(\Im m(\frac{1}{1-t}), \Re e(\frac{1}{1-t}))$. We have seen that this representation is particularly effective to make any small perturbation to a Lorentzian lineshape clearly visible. In fact, a perfect circle in the phasor graph (unperturbed Lorentzian) maps into a straight line in the inverse complex diagram [51]. We know that the complex inverse allows separating the real and imaginary part of perturbative coefficient (see equations 2.20 in section 2.2). This is important to study the overall frequency shift Δ . Precisely, as shown in equation 2.84, Δ does not appear in the interaction term Θ_{int} . As a result, the real part of the complex inverse does not depend on Δ , while the imaginary part is just a linear function

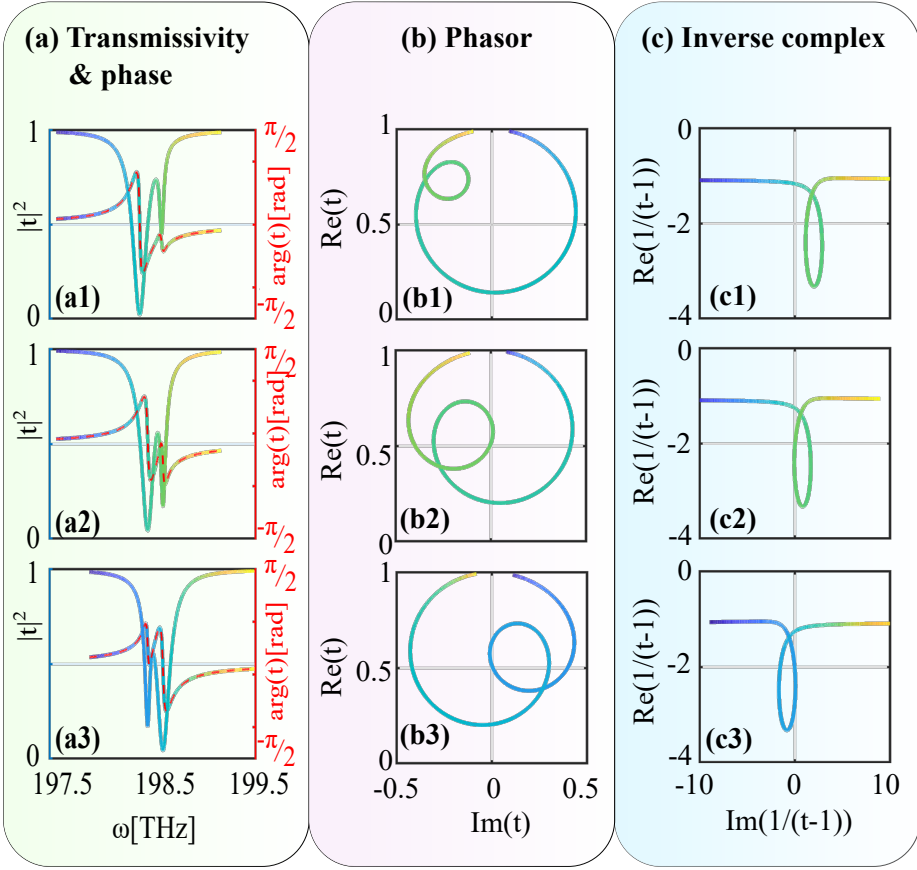


Figure 2.22: (a) Transmission intensity and phase as a function of the incident frequency. Panel (b): parametric phasor graph. Panel (c): inverse complex diagram. The overall frequency shifts are $\Delta = 1 \text{ GHz}$, $\Delta = 10 \text{ GHz}$ and $\Delta = -10 \text{ GHz}$ for (a1)-(c1), (a2)-(c2) and (a3)-(c3) respectively. The graphs (a3)-(c3) are the mirror images of (a2)-(c2) obtained by swapping the two bare frequencies and setting a negative Δ . The rainbow colours highlight the different frequency values.

of it:

$$\frac{\partial}{\partial \Delta} \Re e \left(\frac{1}{t-1} \right) = \frac{\partial}{\partial \Delta} \left(- \frac{\gamma^+ + \Gamma - \Re e(\Theta_{int})}{2\Gamma} \right) = 0 \quad (2.87)$$

$$\frac{\partial}{\partial \Delta} \Im m \left(\frac{1}{t-1} \right) = \frac{\partial}{\partial \Delta} \left(- \frac{\Omega^+ + 2\Delta - 2\omega - \Im m(\Theta_{int})}{2\Gamma} \right) = -\frac{1}{\Gamma}. \quad (2.88)$$

This allows to isolate the contribution of the overall frequency shift, which is

2. Hermitian and non-Hermitian systems

connected to the off-diagonal Lamb-shift, and to partially remove this parameter in the fitting process.

Figures 2.22(a1)-(c1), (a2)-(c2) and (a3)-(c3) report the results of equation 2.84 in the three representations and for three different values of the overall frequency shift: $\Delta = 1THz$, $\Delta = 10THz$ and $\Delta = -10THz$. The other parameters are not changed. Figures (a1)-(b1) and (a2)-(b2) show that Δ strongly affects the shape of the resonance doublet and the phasor diagram curve. As expected, the inverse complex exhibits a small shift of the imaginary part (see figure 2.22(c1) and (c2)). Moreover, from equation 2.87 and 2.88, it is clear that the role of Δ can not be played by the bare frequencies of the two modes. Noteworthy, increasing the mode frequency $\omega_{1,2}^b$ at the same rate, the overall frequency Ω^+ changes but its counterpart Ω^- remains fixed. In this case, the transmission and phase spectra exhibit a frequency shift maintaining the same shape and, consequently, the same phasor representation and the same complex inverse graph. Actually, Δ is connected to the mode interaction with the bus waveguide mode, which causes the shift of the bare resonances and the radiative coupling between the two orthogonal modes in the microresonator.

At this point, is good to open a parenthesis on the sign of the Δ coefficient. It is worth noting that the transmission of equation 2.84 is symmetric for an exchange of the modes. We define I as the function that swaps one mode with the other, i.e. $I := 1 \leftrightarrow 2$. By swapping the modes, Ω^+ and γ^+ remain unaffected (i.e. $I[\Omega^+] = \Omega^+$, $I[\gamma^+] = \gamma^+$), while the Ω^- , γ^- and η change their sign: $I[\Omega^-] = -\Omega^-$, $I[\gamma^-] = -\gamma^-$ and $I[\eta] = -\eta$. As a result, the interaction term of equation 2.85 is unaffected under the mode swap (i.e. $I[\Theta_{int}] = \Theta_{int}$) so that the transmission (equation 2.84) remains the same: $I[t] = t$. On the contrary, when the resonance frequency of one mode shifts due to a change in the mode properties and it crosses the resonance frequency of the other, the negative frequency Ω^- reverses its sign. This introduces a different value of the interaction term (Θ_{int}) and, consequently, a different shape of the doublet in transmission. However, it is possible to recover the situation where the swap of the modes yields a transmission which is a mirror image of the original transmission and which is in the same spectral position, as shown in figure 2.22 (a2) vs (a3). It suffices to reverse the overall frequency sign ($\Delta \rightarrow -\Delta$) and to subtract Δ to both mode frequencies ($w_1^b \rightarrow w_1^b - \Delta$ and $w_2^b \rightarrow w_2^b - \Delta$). Under this transformation the positive and negative overall frequencies become: $\Omega^+ \rightarrow \Omega^+ + 2|\Delta|$ and $\Omega^- \rightarrow \Omega^-$ respectively. Therefore, the intrinsic symmetric behaviour of the theoretical model needs both positive and negative overall frequency shift (Δ).

Summarizing, the inverse complex representation permits to focus the attention on the inter-mode coupling coefficient. In principle, both a positive and a negative reactive inter-mode coupling coefficient is allowed by the theoretical model. The knowledge of both phase and transmission allows to fit simultaneously the real part of the complex inverse, the transmission and phase response. This fit process partially removes the mutual dependency of the shared parameters among the equations.

2.5.3 Numerical simulations

Based on the results reported in the previous sections, we have performed numerical simulations in order to understand the sign of the overall frequency shift (Δ). These simulations were based on the FEM engine by Comsol Multiphysics and controlled by the mathematical programming environment of Matlab. The studied model consists of two single-mode ring resonators connected to a single-mode bus waveguide (see figure 2.23(a-b)). In this way, we have two optical modes coupled through a bus waveguide. Such a situation is similar to the previous one but with an additional advantage: we can independently define the single mode properties by changing the characteristics of each ring separately. In fact, the dynamic behavior of this model can be described by means of the same temporal coupled mode equations seen in the previous section. The flexibility of this system allows determining the unperturbed parameters of the modes such as the bare frequencies and intrinsic coefficients. The model is based on a *Si/SiO₂* platform with refractive index equal to 3.4, 3.4 and 1.45 for the ring resonator, bus waveguide and surrounding medium respectively.

As a first step, we have computed the transmission of the two single modes by considering the coupling between their relative resonator and the bus waveguide. The radius of the rings is chosen in order to fix a specific value of the bare frequencies (ω_1^b and ω_2^b). Playing with the absorption of the rings it is possible to set a proper coupling regime and, hence, to determine the intrinsic parameters of the resonators without changing their resonant frequencies.

The idea is to take a bare frequency of one mode as reference and to change the other one in order to obtain two symmetric configurations. For the sake of clarity we define *Sh* as the transformation in which the bare frequency of the first mode remains unaffected, while the second one changes as: $\omega_2^b = \omega_1^b + \delta\omega \rightarrow \omega_2^b = \omega_1^b - \delta\omega$ (see figure 2.23(c)). This can be obtained, without modification of the coupling parameters, slightly varying the radius ($r_0 \pm \delta r$) of the second ring resonator.

Let us consider a scenario where the modes have the same intrinsic coefficient (i.e. $\gamma_1 = \gamma_2 = \gamma$). The overall intrinsic parameters reduce to $\gamma^- = 0$ and $\gamma^+ = \gamma$, so that the interaction term of equation 2.85 becomes:

$$\Theta_{int} = \frac{[i(\Omega^- + \eta(\Omega^+ - 2\omega_{inc})) + \eta\gamma][i\Omega^-]}{i(\Omega^+ - 2\omega_{inc} + \eta\Omega^-) + \gamma}. \quad (2.89)$$

Moreover, we consider a symmetric system where the coupling regions of the two rings are the same (i.e. same distance between the bus waveguide and resonators). In this case, the relative weights become $\eta_1 = \eta_2 = 1/\sqrt{2} \rightarrow \eta = 0$, and the interaction term reduces to:

$$\Theta_{int} = \frac{[i\Omega^-]^2}{i(\Omega^+ - 2\omega_{inc}) + \gamma^+}. \quad (2.90)$$

Focusing the attention on the *Sh* transformation, the overall negative frequency reduces to $Sh[\Omega^-] = -\Omega^-$, while the positive exhibits a shift of $-2\delta\omega$ ($Sh[\Omega^+] = \Omega^+ - 2\delta\omega$). The symmetry of the system ensures that the transmitted field t

2. Hermitian and non-Hermitian systems

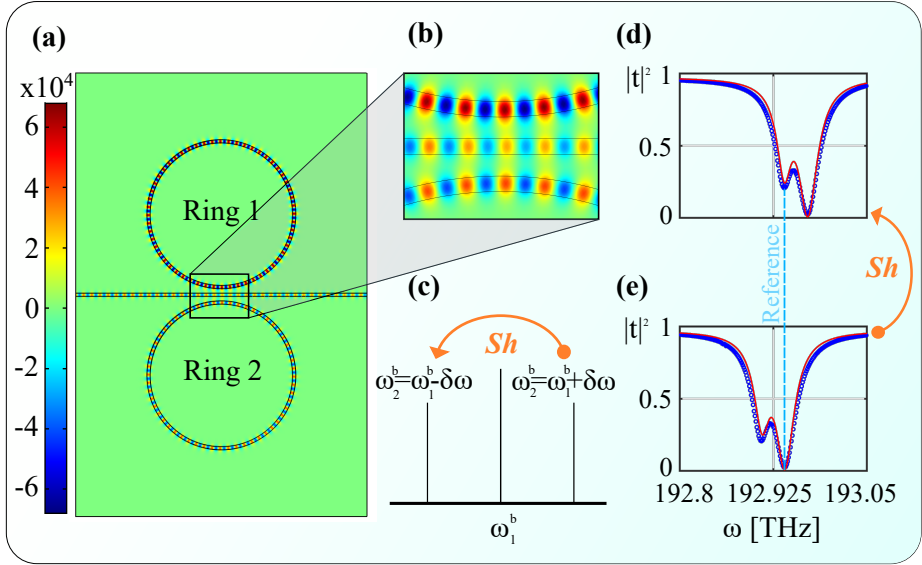


Figure 2.23: (a) Model of two single-mode ring resonators connected to a single-mode waveguide. Panel (b): zoom of the coupling region of figure (a). Panel (c): sketch of the *Sh* transformation: $\omega_2^b = \omega_1^b + \delta\omega \rightarrow \omega_2^b = \omega_1^b - \delta\omega$. Panels (d-e) are the transmissions as a function of the incident frequency of a simple case where the two rings have the same intrinsic coefficient and coupling regions (i.e. $\gamma_1 = \gamma_2 = \gamma$ and $\eta = 0$). Panel (e): doublet obtained under the *Sh* transformation. The blue circles are the numerical simulation values while the red line is the fit with the theoretical model of section 2.5.1. On panels (d-e) we specifically show the reference frequency (ω_1^b) through the light blue dashed line.

and $Sh[t]$ have the same lineshape apart from the expected frequency shift. This can happen if and only if $Sh[\Delta] = \Delta$.

Figure 2.23(d-e) shows the transmission responses of the two rings system, with the same intrinsic coefficient and coupling ($\gamma_1 = \gamma_2 = \gamma$ and $\eta = 0$), under the *Sh* transformation. In order to set $\gamma_1 = \gamma_2 = \gamma$ and $\eta = 0$, we imposed for the two rings the same extinction coefficient, $n_{i1} = n_{i2} = 1.9 \cdot 10^{-4}$ and gap 310 nm (i.e. distance between the ring and bus waveguide). The bus waveguide and rings width is 220 nm while the external radius of the first ring is $R_1 = 5 \mu\text{m}$. The radius of the second ring changes from $R_1 - 1 \text{ nm}$ to $R_1 + 1 \text{ nm}$ for the figure (d) and (e) respectively. As expected, the simulation for the two cases: $\omega_2^b = \omega_1^b - \delta\omega$ and $\omega_2^b = \omega_1^b + \delta\omega$ exhibits the same doublet with a frequency shift of $\delta\omega$. The knowledge of the bare frequencies and of the intrinsic parameters allows determining uniquely the overall frequency shift. These numerical results prove that $Sh[\Delta] = \Delta$ and define a positive sign of the Lamb shift parameter Δ . Therefore, in this scenario, the same behavior of the system under the *Sh*

transformation requires no reverse sign of Δ . On the other hand, as we have seen in previous sections, the same sign of Δ with different intrinsic terms, $\gamma_1 \neq \gamma_2$, means $t \neq Sh[t]$, i.e. a transmission different lineshape.

It is worth noticing that in this case, where $\gamma_1 = \gamma_2 = \gamma$ and $\eta = 0$, the overall frequency term plays a fundamental role in the definition of the doublet shape. In fact, if $\Delta = 0$, equation 2.84 reduces to the typical relation see in section 2.2 for an Hermitian backscattering process. Therefore, the difference between the bare frequencies gives rise to a symmetric transmission doublet (same intensities associated to the split peaks). Δ introduces a non-Hermitian term which means an asymmetric doublet in the transmission response.

Let us consider different values of the intrinsic coefficient (i.e. $\eta = 0$ and $\gamma_1 \neq \gamma_2$). The interaction term reduces to:

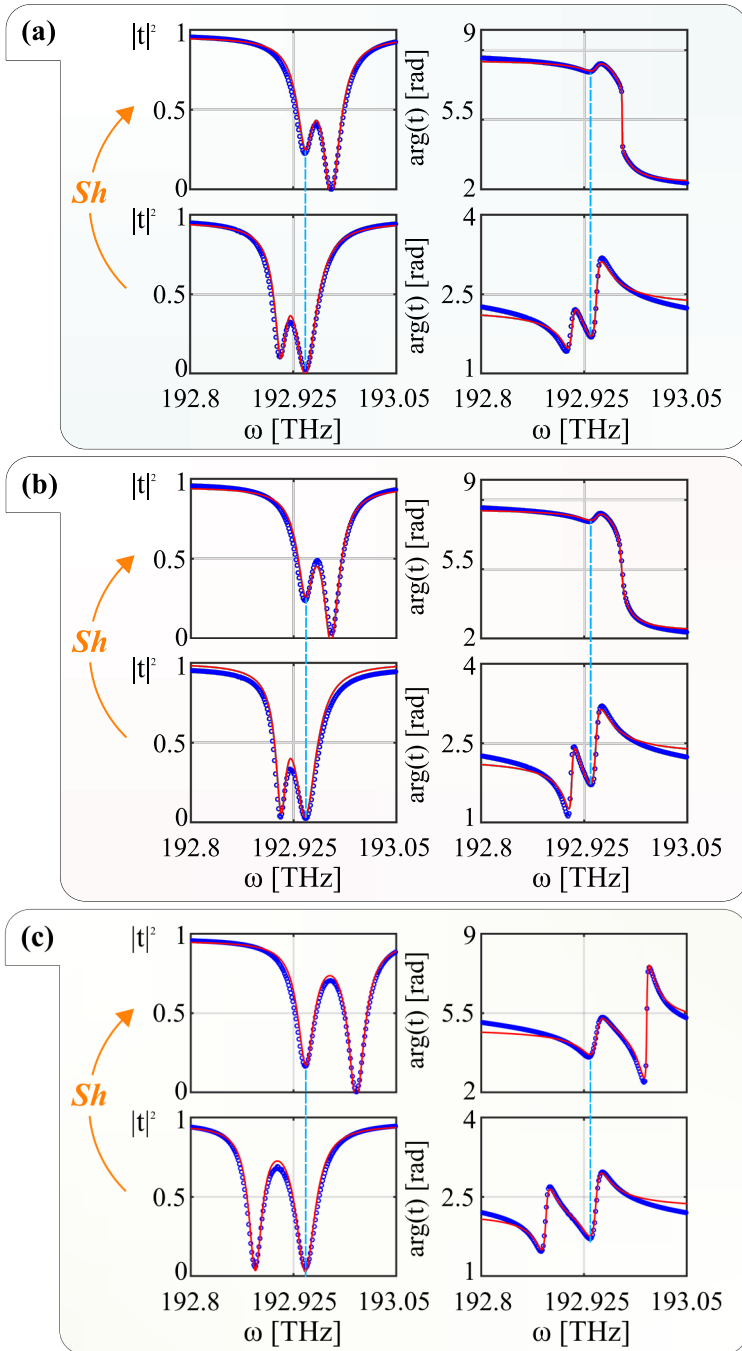
$$\Theta_{int} = \frac{[i\Omega^- + \gamma^-]^2}{i(\Omega^+ - 2\omega_{inc}) + \gamma}, \quad (2.91)$$

and it is different under the Sh transformation ($Sh[\Theta_{int}] \neq \Theta_{int}$). Figure 2.24 shows distinct transmission and phase doublets before and after the application of the Sh transformation. In each panel the coefficients of the first ring are fixed and the dashed blue line highlights the bare frequency ω_1^b . Panels (a)(b) and (c)(d) exhibit a frequency shift between the two bare frequencies of $\delta\omega$ and $2\delta\omega$ respectively. In particular, the panels (a) and (b) are obtained by setting $R_2 = R_1 \pm 1$ nm and $R_2 = R_1 \pm 2$ nm. Panels (a)(c) and (b)(d) show an extinction coefficient of the second ring of $n_{i1} = 1.3 \cdot 10^{-4}$ and $n_{i2} = 9 \cdot 10^{-5}$, respectively. Each panel displays clearly a distinct behavior under the Sh transformation. Changing the bare frequency of the second ring from $\omega_2^b = \omega_1^b + \delta\omega$ to $\omega_2^b = \omega_1^b - \delta\omega$ the interaction between the two modes mediated by the coupling waveguide changes. This is evident in the second column of panels (a-d), where the phase responses display a different coupling regime of the system. In all the analyzed cases, the overall frequency shift (Δ), obtained by fitting simultaneously the transmission and phase, exhibits a positive sign. This means an asymmetric behavior of the waveguide mediated coupling under the Sh transformation.

In order to test the robustness of this model, we consider the simplest case of just one ring coupled to the bus waveguide (see Figure 2.25(a)). Let us consider the behavior of the bare frequency as a function of the extinction coefficient n_i . Figure 2.25 (b) displays the transmission and phase for different values of the intrinsic parameter. The points are the numerical results while the red lines are the fit with the theoretical model imposing $\eta_2 = 0$. Figure 2.25 (c) shows that the resonant frequency of the resonator remains constant over the range of the intrinsic coefficient used in the previous numerical simulations.

In this simple scenario, there is just one mode and the overall frequency shift appears only in the resonance frequency (i.e. Δ_{11}). It is therefore possible to directly investigate the sign of the overall frequency shift. Figure 2.25 (d) exhibits the numerical results of the transmission for different values of the gap between the ring and the bus waveguide. In this graph, the waveguide width is 220 nm. As reported in Figure 2.25 (e), the overall frequency shift decreases

2. Hermitian and non-Hermitian systems



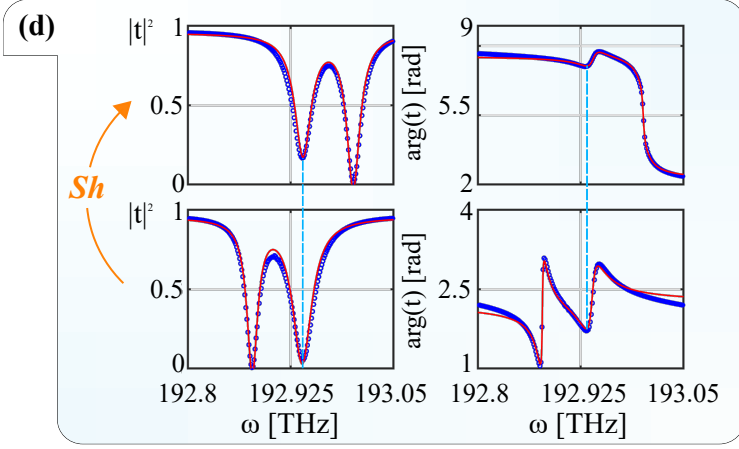


Figure 2.24: Panels (a-d) show transmission and phase response as a function of the incident frequency for different values of the intrinsic coefficient and bare frequency of the second ring (i.e. γ_2 and ω_2^b). Each panel displays a bare frequency of $\omega_2^b = \omega_1^b + \delta\omega$ and $\omega_2^b = \omega_1^b - \delta\omega$ in the first and second row respectively (i.e. before and after the application of the *Sh* transformation). In each panel the bare frequency and intrinsic coefficient of the first ring are fixed. The blue circles are the numerical values, while the red line is the fit with the analytical model of section 2.5.1. The blue dashed line highlights the reference frequency of the first ring (ω_1^b). In the Panels (a)(b) and (c)(d) the radius of the second ring is $R_2 = R_1 \pm 1$ nm and $R_2 = R_1 \pm 2$ nm respectively. Panels (a)(c) and (b)(d) display an extinction coefficient of about: $n_{i1} = 1.3 \cdot 10^{-4}$ and $n_{i2} = 9 \cdot 10^{-5}$, respectively.

with increasing the gap and shows positive sign. By changing the width of the bus waveguide (370 nm) the numerical simulation exhibits an opposite sign of the frequency shift (see figure 2.25 (e)). In panel (e) we have fixed as bare frequency the resonant frequency obtained with the largest gap. As expected, the magnitude of the frequency shift decreases with increasing the gap following an exponential function. This is due to the exponential tails of the interacting evanescent fields. An explanation of the sign of the frequency shift, i.e. of Δ , is not easy. Typically in the literature is reported that the presence of a dielectric, e.g. the bus waveguide, next to a microring, gives rise to a shift of the resonance frequency toward the red (i.e. a negative frequency shift). However, as reported in [92], a small positive refractive index perturbation can introduce positive or negative signs of the frequency shift. The sign depends on the contributions from effects beyond first-order index perturbation, including non-orthogonal cross-energy exchange between the resonant modes and the confined modes in nearby structures, and resonant-mode shape modification by the adjacent structures [92].

2. Hermitian and non-Hermitian systems

Summarizing, the sign of the overall frequency shift Δ depends on the details of the physical system under study. The numerical simulations confirm the presence of either a positive or negative reactive coupling Δ , excluding any possible change of sign attributed to the crossing of the resonant frequencies.

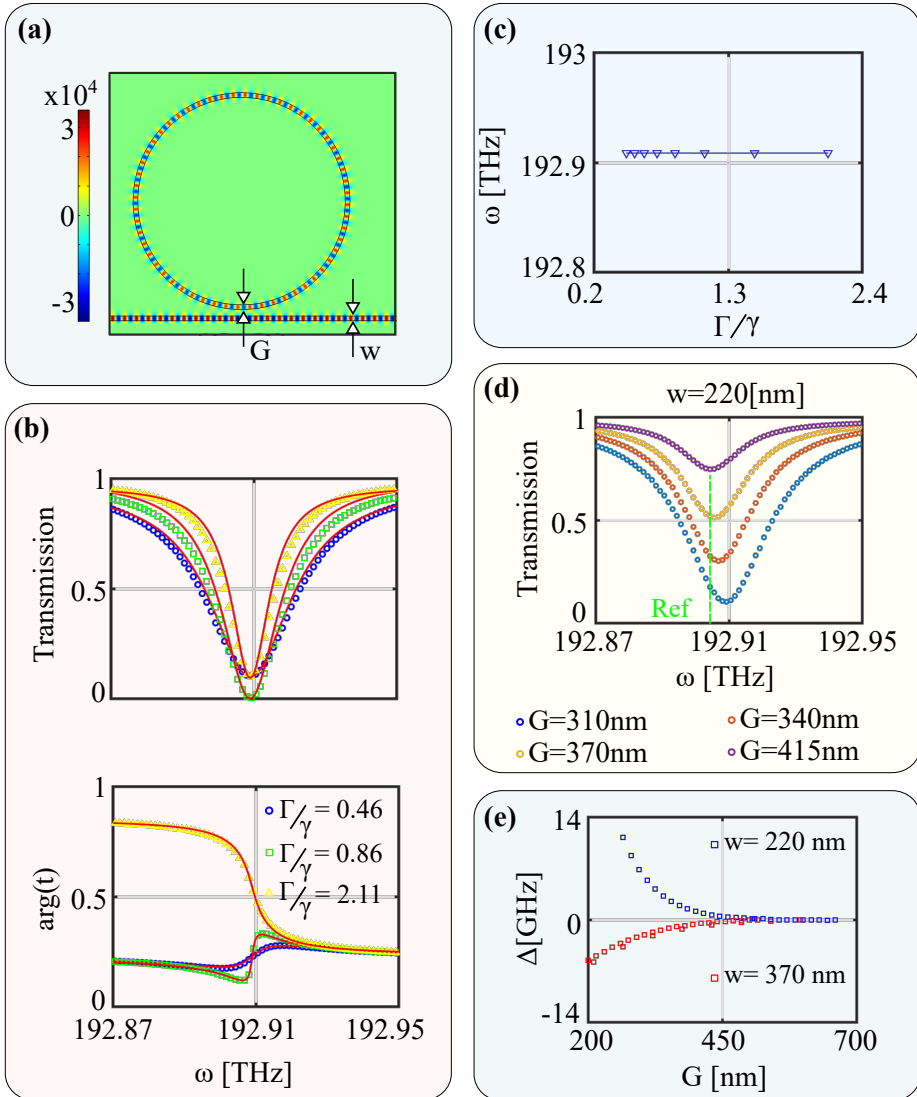


Figure 2.25: (a) The simplest system of a ring resonator coupled to a bus waveguide. Panel (b): numerical transmission and phase as a function of the incident frequency for different absorptions of the material (i.e. distinct intrinsic coefficients). The circle, triangle and square points are the simulation values while the red line is the fit with the theoretical model. Panel (c): graph of the resonant frequency with respect to the intrinsic coefficient. Panel (d): transmission as a function of the incident frequency for distinct values of the gap (G) between the ring and waveguide. Panel (e): Δ coefficient with respect to the gap for two different widths of the waveguide. In particular, the red (blue) square points are the simulation results for a bus waveguide of a width of 220 nm (370 nm).

Chapter 3

Time response of Hermitian and non-Hermitian systems

Up to now, we have focused on the optical response of Hermitian and non-Hermitian systems in stationary regime. We have therefore considered a dynamic equilibrium, ignoring the evolution in order to reach such state. In fact, we have described the optical response neglecting the temporal dependence of the amplitude field.

In this chapter, we will discuss the response of a microresonator excited through a bus waveguide with a rectangular pulse. Taking advantage of the three-level system previously introduced, we will first study the simplest case of a single mode microresonator, then by introducing the coupling coefficients, we will analyze the case of the backscattering. The analytical derivation of the temporal response will be supported by Finite Difference Time Domain (FDTD) simulations. These allow not only verifying the theoretical model but also understanding the meaning of different coupling regimes.

As we have seen in the previous chapter, the bus waveguide can be coupled to the microring in three characteristic regimes: under-coupled, over-coupled and critical-coupled. Among these, the critical coupling regime is characterized by the fact that no light is detected at the bus waveguide output when a resonant continuous signal is input at the bus waveguide. It is often said that all the light is coupled into the microresonator [93, 94]. Since the critical coupling is defined as the regime where the injected power exactly compensates the losses inside the resonator, and since these losses are relatively weak in microresonators, the fact that all the pump power enters into the resonator seems contradictory [95]. In this chapter, taking as reference [95], we will clarify this apparent contradiction by illustrating the propagation of a rectangular pulse of light in a resonator/waveguide system. In addition, we will see how the response of the system is determined by the interference at the coupling region between the light coupled to the resonator and that propagating in the bus waveguide. The different coupling regimes show different interference conditions which determine both the phase delay of the output light as well as the temporal line shape of the output pulse. Finally, we will propose an analytical complex expression for the single Lorentzian transmission response which can be used to fit the experimental data and, therefore, to extract the characteristic parameters of the system, e.g. the intrinsic (γ), the extrinsic (Γ) coefficients, and consequently, the Q-factor.

3.1 Theoretical model

Let us consider a resonator coupled to a bus waveguide as shown in figure 3.1. Precisely, we deal with a single mode resonator and a single mode bus waveguide. First, we suppose that there are no coefficients related to the surface roughness (i.e. $\beta_{12} = \beta_{21} = 0$).). Moreover, we consider an input amplitude field E_{in} injected into the bus waveguide from left to right. This field couples into the resonator and excites the cavity mode with an amplitude field α_{ccw} . For simplicity, we define the amplitude field of the resonator mode as $\alpha_{ccw} = \alpha$. In this way, the coupled equation system 2.8 of section 2.2, reduces to a simple differential equation of the type:

$$\frac{d\alpha}{dt} = (i\omega_0 - \gamma - \Gamma) \alpha[t] + i\sqrt{2\Gamma} E_{in}[t]. \quad (3.1)$$

As we have seen in section 2.2, ω_0 is the resonant frequency of the resonator and Γ (γ) is the usual extrinsic (intrinsic) damping rate. The output field of the whole system is given by the following equation:

$$E_{out}[t] = E_{in}[t] + i\sqrt{2\Gamma} \alpha[t], \quad (3.2)$$

where the interference between the amplitude of the incident field and of the field exiting the resonator determines the system response.

In general, the amplitude of the incident field depends on spatial variables and time (i.e. x , y and t). In the following derivation, we consider an input field of the form $E_{in}[t, x, y] = F_i[x, y] E_{in}[t]$ where $F_i[x, y]$, is the normalized profile of the eigenmode number i in the bus waveguide cross-section. By

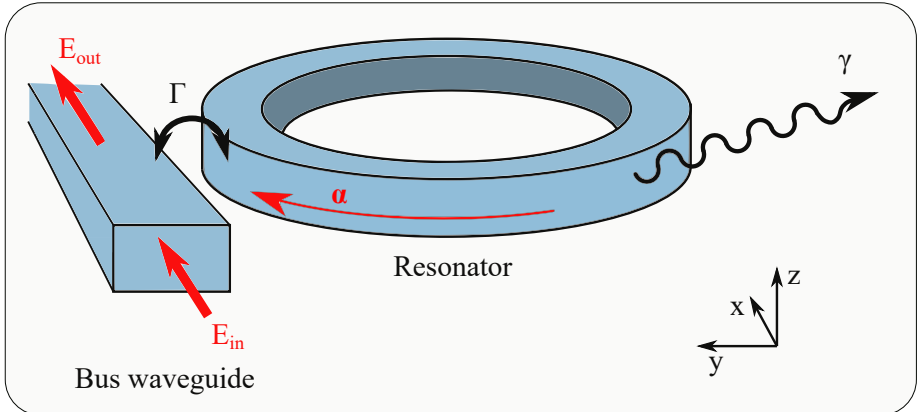


Figure 3.1: Sketch of a resonator coupled to a bus waveguide. E_{in} , E_{out} and α are the electric field amplitudes at the input of the waveguide, at its output and in the resonator respectively. The intrinsic and extrinsic damping rates are labeled by γ and Γ .

definition, this eigenmode profile $F_i[x, y]$ remains constant during the time evolution. This is in agreement with the TCMT which treats the system as dimensionless. It is worth noticing that, considering a monochromatic input field like $E_{in} = F_i[x, y] E_{in0}[\omega] e^{i\omega t}$, the transmission amplitude $t = E_{out}/E_{in}$ reduces to the stationary equation 2.12 of section 2.2.

In order to calculate the temporal response, it is necessary to solve the equation 3.1 for an impulse which exhibits a generic temporal dependence. This solution can be obtained by using the Green function $G[t]$. This is defined as the solution of the differential equation when its forcing equals a Dirac's function pulse $\delta[t]$ [96]. The general solution is, therefore, given by the convolution of the temporal Green function with the excitation function. Let us substitute an input field equal to $E_{in}[t] = \delta[t - t']$, and take the Fourier transform of the equation 3.2, so that it can be formulate as:

$$i\omega G[\omega] - (i\omega_0 - \gamma - \Gamma)G[\omega] = i \frac{\sqrt{2\Gamma}}{\sqrt{2\pi}} e^{i\omega t'}. \quad (3.3)$$

In this way, we can write the spectral Green function of the equation 3.1 as:

$$G[\omega] = \frac{1}{\sqrt{2\pi}} \frac{i\sqrt{2\Gamma}}{i(\omega - \omega_0) + \gamma + \Gamma} e^{i\omega t'}. \quad (3.4)$$

The inverse Fourier transform of spectral Green function leads to the temporal Green function:

$$G[t - t'] = i\sqrt{2\Gamma} e^{-(-i\omega_0 + \gamma + \Gamma)(t - t')} \Theta[t - t'], \quad (3.5)$$

where $\Theta[t]$ is the Heaviside function. Finally, the general solution of the equation 3.1 reads [95]:

$$\alpha[t] = \int_{-\infty}^{\infty} G[t - t'] E_{in}[t'] dt'. \quad (3.6)$$

Therefore, the general temporal response of the system composed of a resonator coupled to a bus waveguide is given by substituting the last expression in equation 3.2:

$$E_{out}[t] = E_{in}[t] + i\sqrt{2\Gamma} \int_{-\infty}^{\infty} G[t - t'] E_{in}[t'] dt'. \quad (3.7)$$

In this chapter, we will focus the attention on an input field given by a rectangular pulse. However, in order to test the versatility of the solution formulated in the last equation 3.7, let us first consider the well-known case of a Gaussian pulse excitation. The dynamics of such an excitation within a cavity is well described in literature and is needed to understand important applications such as cavity dumping [97] and high-speed optical communication [98]. Therefore, let us briefly consider the case where the system is resonantly excited through a Gaussian pulse of the form:

$$E_{in}[t] = \frac{A_0}{\sqrt{2\pi}\sigma} e^{-\frac{t^2}{2\sigma^2}} e^{i\omega_0 t}, \quad (3.8)$$

3. Time response of Hermitian and non-Hermitian systems

where A_0 is the amplitude of the field and 2.355σ is the full width at half maximum (FWHM) of the Gaussian pulse. As is well known, the Fourier transform of a Gaussian function is still a Gaussian with a FWHM inversely proportional to that of the original one. Hence, the envelope of the Gaussian excitation in the frequency domain reads:

$$\begin{aligned} E_{in0}[\omega] &= \frac{1}{\sqrt{2\pi}} \int_{-\infty}^{\infty} E_{in0}[t] e^{-i\omega t} \\ &\vdots \\ &= \frac{A_0}{\sqrt{2\pi}} e^{-\frac{1}{2}\sigma^2\omega^2}. \end{aligned} \quad (3.9)$$

Figure 3.2 (a) and (b) show the time dependent Gaussian pulse envelope and its Fourier transform. As one can see from the FWHM definition, by increasing the pulse duration the spectral width decreases.

Interestingly, substituting the time dependent Gaussian pulse into the the general solution 3.7 and using the Green's function, we obtain straightforwardly the response of the whole system:

$$\begin{aligned} E_{out}[t] &= A_0 e^{i\omega_0 t} \left\{ \frac{e^{-\frac{t^2}{2\sigma^2}}}{\sqrt{2\pi}\sigma} - e^{\frac{1}{2}(\gamma+\Gamma)(\sigma^2(\gamma+\Gamma)-2t)} \right. \\ &\quad \left. \times \Gamma \left(1 + \operatorname{erf} \left[\frac{t - \sigma^2(\gamma+\Gamma)}{\sqrt{2}\sigma} \right] \right) \right\}. \end{aligned} \quad (3.10)$$

where $\operatorname{erf}[z] = \frac{2}{\sqrt{\pi}} \int_0^z e^{-t^2} dt$ is the *error function*[99].

At this point, let us consider the temporal response by exciting the system with a rectangular pulse. This particular input field is an optimal example to explain the physics beyond the charge and discharge of a resonator. In addition, such an input field allows easily understanding the illustrations of the FDTD simulations. Let us assume that the resonator is excited by a continuous wave (CW) pulse of light of duration Δt and of angular frequency ω (see figure 3.2 (c)). Thus, the input field reads as:

$$E_{in}[t] = A_0 (\Theta[t] - \Theta[t - \Delta t]) e^{i\omega t}, \quad (3.11)$$

where A_0 is the amplitude and $\Theta[t]$ is the Heaviside step function. This is equal to 0 for negative arguments ($t < 0$) and 1 for positive one ($t \geq 0$). As shown in figure 3.2 (d), the Fourier transform of the excitation envelope $E_{in0}[t]$ is a cardinal sine (Sinc) response:

$$\begin{aligned} E_{in0}[\omega] &= \frac{1}{\sqrt{2\pi}} \int_{-\infty}^{\infty} E_{in0}[t] e^{-i\omega t} \\ &\vdots \\ &= \frac{iA_0(e^{-i\omega\Delta t} - 1)}{\sqrt{2\pi}\omega}. \end{aligned} \quad (3.12)$$

As expected, from the last equation one can see that by decreasing the duration of the pulse (Δt), the frequency bandwidth of the Sinc increases.

Substituting the expression 3.11 in equation 3.7 and using the Green's function 3.5 one obtains the response of the resonator:

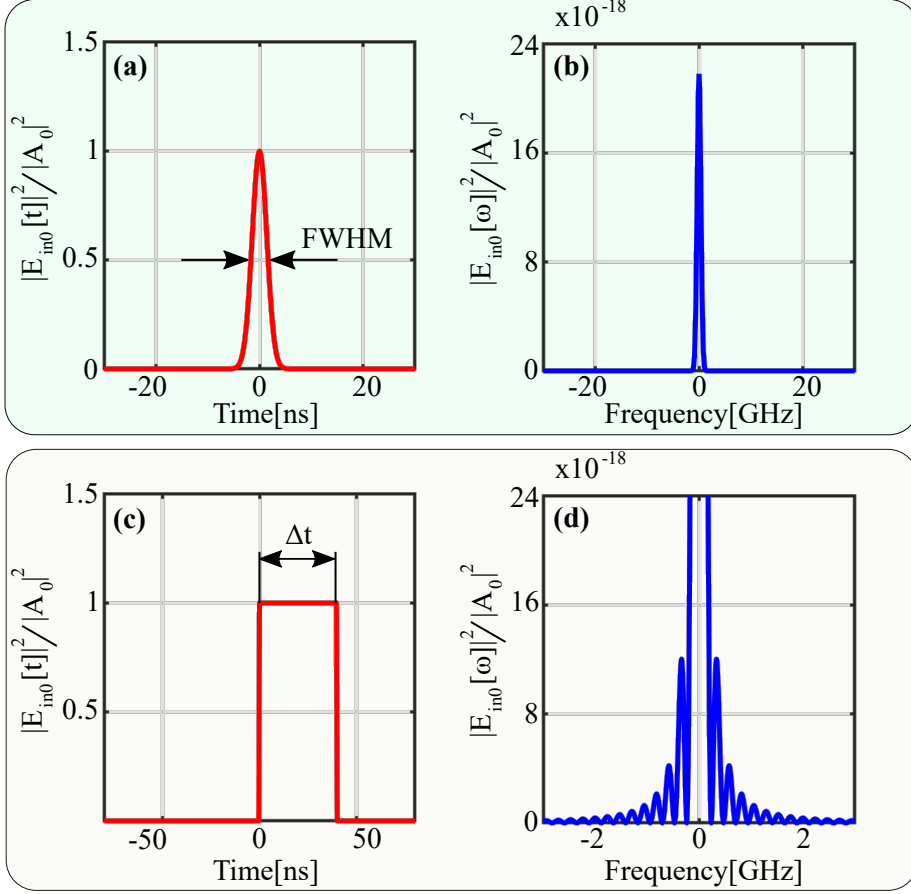


Figure 3.2: (a) and (b) Normalized input field as a function of time for a Gaussian and a Rectangular pulse respectively. Panels (b) and (d) show the Fourier transform of graph (a) and (b). The black arrows indicate the Full Width Half Maximum (FWHM) in panel (a) and the duration of the pulse (Δt) in panel (b).

$$\begin{aligned}
 E_{out}[t] = A_0 e^{i\omega t} \left\{ -\Theta[t] \left(\frac{-2\Gamma e^{-t(i\Delta\omega + \Gamma + \gamma)}}{i\Delta\omega + \Gamma + \gamma} \right. \right. \\
 + \frac{(\Gamma - \gamma) - i\Delta\omega}{i\Delta\omega + \Gamma + \gamma} \Big) + \Theta[t - \Delta t] \left(\frac{(\Gamma - \gamma)}{i\Delta\omega + \Gamma + \gamma} \right. \\
 \left. \left. - \frac{2\Gamma e^{-(t - \Delta t)(i\Delta\omega + \Gamma + \gamma) + i\Delta\omega}}{i\Delta\omega + \Gamma + \gamma} \right) \right\}. \quad (3.13)
 \end{aligned}$$

This equation depends on the characteristics of the incident field and of the resonator. In particular, from the amplitude A_0 and duration Δt of the rectangular pulse and from the intrinsic and extrinsic coefficient of the resonator. Let us fix

3. Time response of Hermitian and non-Hermitian systems

an input field with an amplitude $A_0 = 1 \text{ a.u.}$ and a duration $\Delta t = 30 \text{ ns}$ and plot the equation 3.13 as a function of time t and frequency detuning $\Delta\omega$. Figure 3.3 shows a 3D plot of the output electric field intensity (i.e. $|E_{out}[t]/A_0|^2$) for the three different regimes: over-, critical- and under-coupling (panel (a), (b) and (c) respectively). From these 3D graphs, it is rather difficult to fully understand the behavior of the system. As you one see in figure 3.3, in all three regimes, far from the resonance condition, the intensity oscillates damping to one as time increases. Moreover, when $\Delta\omega$ tends to zero (i.e. we approach the resonance), the signal decreases. In particular, on resonance, the intensity drops, until it reaches a stationary regime, and then it jumps when the source is turned off. At this point, the intensity gives rise to a peak that presents a maximum on resonance. In addition, we see a discharge part where the intensity fades over time. It is also evident that by switching from over- to under-coupling, the discharge peak decreases its height.

To give a physical explanation to the observations resulting from figure 3.3, it is better to consider a section of these graphs by fixing the frequency of the incident field. In this way, one can plot the intensity of the output field as a function of time. To illustrate the different temporal behavior, we will use a numerical model based on the FDTD simulation explained in the next subsection. As first case, we will consider the scenario in which the frequency of the incident field is equal to the resonance frequency of the resonator ω_0 . Here, the equation 3.13 is simplified and assumes the following formulation:

$$E_{out}[t] = A_0 e^{i\omega_0 t} \left\{ -\Theta[t] \left(\frac{-2\Gamma e^{-t(\Gamma+\gamma)} + (\Gamma-\gamma)}{\Gamma+\gamma} \right) + \Theta[t - \Delta t] \left(\frac{-2\Gamma e^{-(t-\Delta t)(\Gamma+\gamma)} + (\Gamma-\gamma)}{\Gamma+\gamma} \right) \right\}. \quad (3.14)$$

3.2 Numerical simulation and temporal output response

In order to illustrate the results given by the previous analytical model, we perform a FDTD simulation [100, 101], using Meep, an open-source software package [102]. As in the previous section, we study a straight waveguide coupled to a microring resonator. The characteristic parameters of the analyzed structures are shown in table 3.2. This reports two sets of values which produce the same physical behavior. The first (A) contains values that greatly reduce computational time but do not reflect the size and material used in the experimental measurements of chapter 6. While, the second (B) shows values comparable with the experimental waveguide/microrisonator system but that make the simulation expensive.

A preliminary step consists in computing a resonant frequency of the system. To do this, the microring is excited with a Gaussian source with a relatively large frequency span. Then, the function *harminv* determines the quality factors of different modes. Finally, to study the time-response of the resonator to a pulse of light, a continuous wave source with frequency f_{cen} , corresponding to the best quality factor, is inserted at the bus input at $t = 0$ and stopped at $t = 3000 \text{ a.u.}$

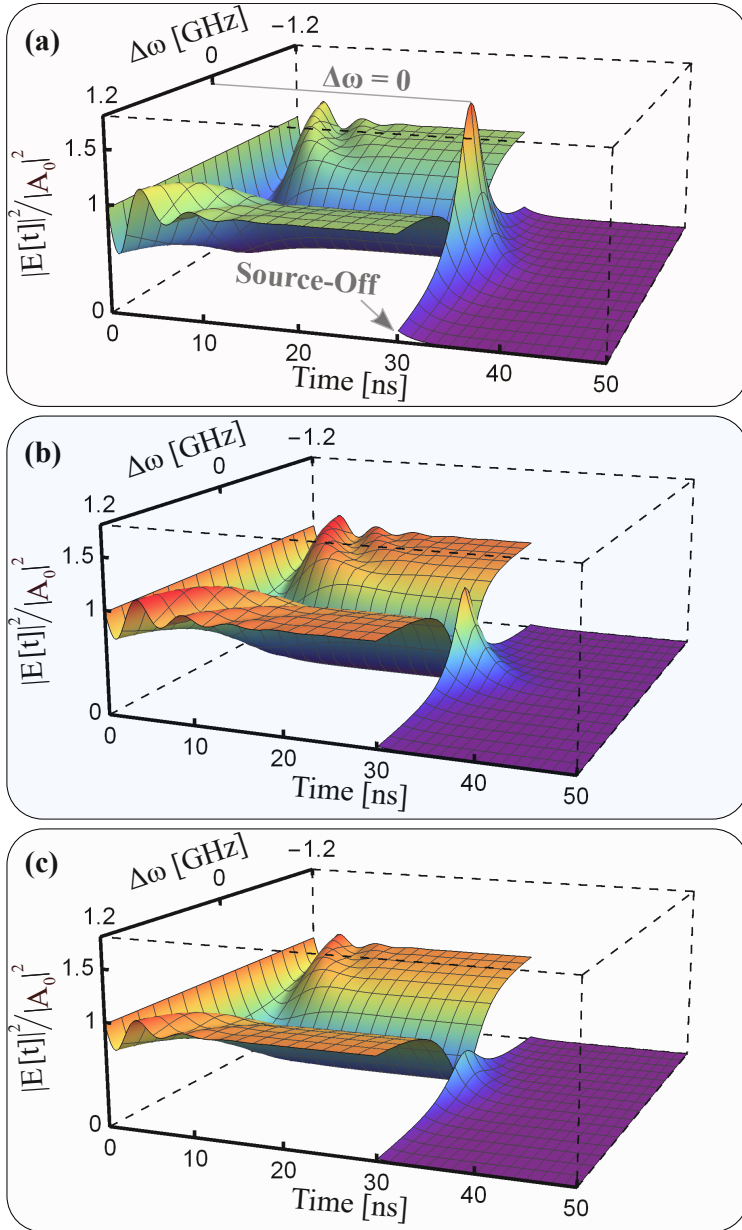


Figure 3.3: (a)-(c) Normalize electric field intensity as a function of time t and frequency detuning $\Delta\omega$. Panel (a) Over-, (b) critical- and (c) under-coupling regime.

3. Time response of Hermitian and non-Hermitian systems

Design parameters	A	B
Ring internal radius	5	10
Waveguide width	1	0.5
Ring width	1	0.5
Gap between ring and bus waveguide	0.8	0.58
Refractive index of the waveguide	2.9	1.72
Imaginary part of the permittivity ($\times 10^{-3}$)	35	0.05
Resonant frequency	0.15185	0.6431
PML thickness	1	
Distance between border and waveguide	4	
Frequency pulse width	0.1	
Resolution	10	

Table 3.1: Parameters used in the Meep simulations. The values are given in the internal Meep units, where $\epsilon_0 = \mu_0 = c = 1$ and where the characteristic length of the system is $1 = 1 \mu\text{m}$ (e.g. the set of parameters B corresponds to a Si_3N_4 waveguide with a width of 500 nm , describing a ring resonator with a radius of $10 \mu\text{m}$ and a gap of 580 nm ; an imaginary permittivity of 50μ means a linear loss of $\alpha = 5 \text{ dB/cm}$).

The different cases of the analytical study are reproduced by keeping the geometry constant and varying the imaginary part of the microring permittivity. Doing so, the extrinsic quality factor remains constant, whereas the intrinsic one is tuned to achieve the different coupling regimes. Table 3.2 reports the value of the imaginary part of the permittivity which yields a critical coupling regime. For example, by decreasing (increasing) the permittivity of the set A to 0.01 (0.07) we obtain an over-(under-)coupling regime.

3.2.1 Output intensity in the time domain

As reported in [95], let us discuss the output electric field as a function of time for the three coupling regimes over-, critical and under-coupling, considering the analytical model and the FDTD simulation described in the previous section. Here, we focus the attention on an excitation given by a continuous wave pulse of light of duration Δt and of angular frequency ω_0 . In this case of resonant excitation, the 3D graph of figure 3.3 reduces to a 2D plot which shows the norm of the electric field intensity as a function of time.

The three panels of figure 3.4 show the squared norm of the electric field at the bus output as a function of time for the three coupling regimes. Precisely, (a), (b) and (c) labels the output temporal response of over-, critical- and under-coupling respectively. In the first and last panel ((a) and (c)), are reported some images of the electric field z-component distribution obtained from the FDTD simulation. These images have been taken at different times, highlighted by pink pins in the temporal profiles. The same arbitrary units are used in order to allow

a direct comparison of the three regimes. It is worth noticing that the intensity of the temporal response exhibits a different trend in the three different coupling regimes.

Let us describe the temporal sequences in the over-coupling case (first panel of figure 3.4) by studying the diverse pins separately.

Time 1: After a small delay needed for the light to propagate along the bus waveguide, the power is detected at the output. Its value is equal to the value coming out of the source minus the part that has been coupled into the ring. The inset image number 1 shows the field leaving from the bus and the one that begins a round trip inside the microring. The light is coupled into the microring via evanescent coupling, so that the field in the second part of the bus is slightly weaker than the one in the first part. This evidence that a small amount of light is coupled into the microring.

Time 2: After three round-trips, the exiting power is given by the interferences between the field propagating in the bus and the one exiting from the ring. The inset image number 2 shows that these interferences destroy the field, hence the exiting power decreases after each round-trip as the field gets stronger and stronger in the resonator. As expected, the magnitude of the output electric field decreases for increasing time, following an exponential shape until the system reaches the time 3. This exponential behavior is given by the charge of the resonator.

Time 3: After four round-trips, the field trapped in the resonator is large enough to make the interferences able to completely destroy the exiting wave. This is apparent from the inset picture number 3 where no field appears after the coupling region.

Time 4: After a few more round-trips, the field inside the resonator becomes too large and the interferences are not balanced anymore. The wave exiting from the resonator prevails and a power is detected again at the output of the bus waveguide. We can also observe that the stationary regime is reached (corresponding to the minimum of the spectral Lorentzian seen in figure 2.5 (a) of section 2.2), which means that the power losses in the resonator are exactly balanced by the coupled power.

Time 5: Once the source has been turned off, the interferences can not take place anymore and the power detected at the output is directly the one coming from the resonator. Since the power trapped in the resonator is larger than the source's one, the power detected at the output is larger than the one detected at time 1. Clearly, the inset image number 5 shows no field before the coupling region. In addition, it exhibits a stronger field with respect to all the other field distribution images at the waveguide output.

Time 6: At each round-trip, the microring discharges the trapped power, thus, the exiting power fades away as time goes by. Then, the magnitude of the output electric field decreases by increasing the time, following the same exponential law of the charge case. This description of the time evolution of the electric field, in the particular case of the over-coupling regime, can also be found in [49].

3. Time response of Hermitian and non-Hermitian systems

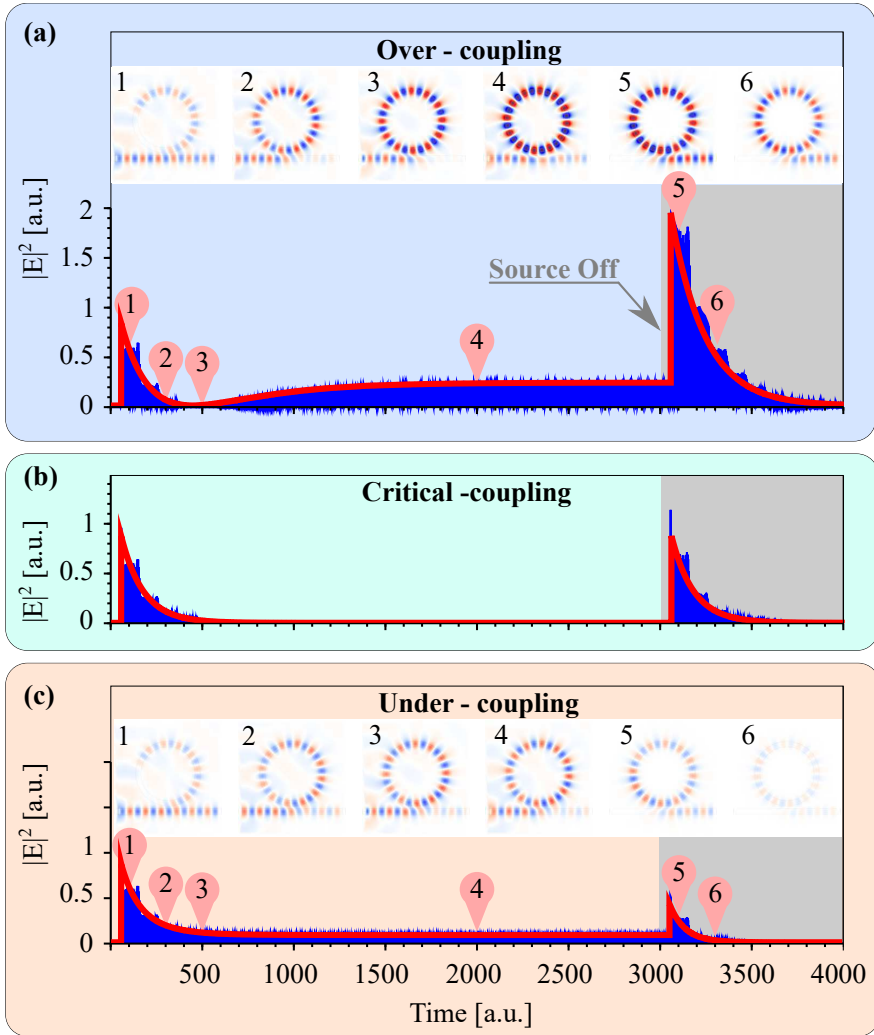


Figure 3.4: FDTD simulations of a microring coupled to a bus waveguide excited with a resonant CW source. The source is turned on at $t = 0$ and stopped at $t = 3000 a.u.$ After the shut down of the source, the discharge interval is represented with a gray background. The gap remains constant while the intrinsic losses are varied to reproduce the three coupling regimes. The plots show the squared electric field norm at the output of the waveguide during the time computed with the analytical model (red) and from the FDTD simulation (blue). The images represents the electric field z -component, E_z . The same arbitrary units are used in the three regimes to allow comparison. This image is taken from [95]

In the critical-coupling case (see figure 3.4 (b)), the stationary regime corresponds to the situation when the interference exactly destroys the exiting wave. Therefore, after a few round trips needed to charge the microresonator, no power is detected at the output anymore. It is worth noting that, the vanishing of the output power means that the amplitudes of the electric fields going through the bus and exiting from the resonator are equal. Meanwhile, it does not imply that the whole power coming from the source is coupled into the resonator.

On the other hand, in the under-coupling regime (see figure 3.4 (c)), the round-trip losses become equal to the coupled power before the power inside the resonator becomes large enough to observe the destructive interference. Thus, the stationary regime is reached without observing the canceling of the exiting power. This is apparent from the inset images of figure 3.4 (c) where the field never vanishes at the output of the bus waveguide. At time 5, when the source is turned-off, the exiting power is smaller than the one measured at time 1 because the power trapped into the microring is smaller than the source's one.

As expected, also in the critical- and under-coupling regime the charge and discharge of the resonator are characterized by a typical exponential trend. Interesting is the fact that just measuring the intensity of a resonance response of the waveguide/microring system as a function of the time, one can determine the coupling regime. As explained in section 2.2, this is not possible in the frequency domain.

Our simple analytical model can perfectly predict the simulation behavior observed. The red lines of figure 3.4 show the analytical fit of the numerical simulation by using equation 3.14. As the extrinsic coefficient is connected to the coupling between the bus waveguide and the resonator, it is equal to $\Gamma = 20800 \text{ a.u.}$ in all three cases. Instead, the intrinsic coefficient is about $\gamma = 6400 \text{ a.u.}$, $\gamma = 20800 \text{ a.u.}$ and $\gamma = 38800 \text{ a.u.}$ for over-, critical- and under-coupling regimes, respectively.

3.2.2 Phase shift

The dynamics of the charge and discharge of the resonator can be understood by looking at the output electric field. The phase is strictly connected to the interference between the two fields in the coupling region: the field exiting from the resonator and the one propagating in the bus waveguide. As a result, the phase contains information about the coupling regime of the system. This has been seen in section 2.2, where the phase response of a waveguide/microresonator system allows discriminating between the different coupling regimes. In particular, on resonance and in the stationary condition, the accumulated phase is 0 and π in under- and over-coupling regime, respectively.

This can also be deduced from the FDTD simulations. In figure 3.4, if we concentrate on the field image 4 we can note that the relative phases of the fields are different in the two regimes. Consider the sign of the field E_z given by the colors (blue negative, red positive). In the coupling region and in both cases, E_z propagating in the bus waveguide is positive while E_z exiting from the ring has suffered a π phase shift and therefore is negative. Since in the

3. Time response of Hermitian and non-Hermitian systems

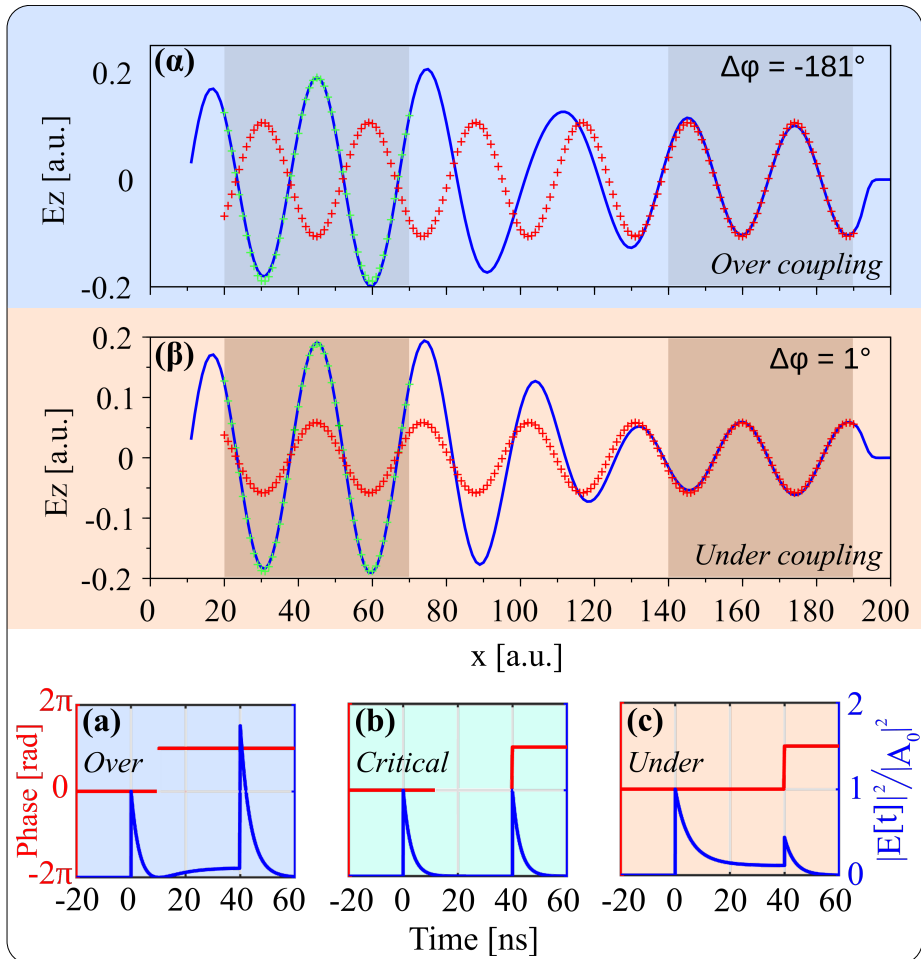


Figure 3.5: Electric field z -component along a cut-line in the middle of the bus waveguide simulated by FDTD at $t = 2000 a.u.$ corresponding to the stationary regime in the over- (α) and under-coupling (β) regimes. An harmonic fit at the input ($(20 < x < 70) a.u.$, green crosses in the dark area) and the output ($(140 < x < 190) a.u.$, red crosses in the dark area) allows to evaluate the phase shift $\Delta\phi$ of the output wave with respect to the input. Panels (a), (b) and (c) display the analytical intensity and phase of the output electric field norm as a function of the time in the different coupling regimes.

over-coupling regime, the field from the ring is dominating the interference, the field transmitted through the coupling region acquires a π phase shift. On the contrary, in the under-coupling regime, the field in the bus waveguide is dominating the interference and, therefore, the transmitted field has no phase

shift.

A more accurate illustration of the phase shift is given for the stationary regime in figure 3.5. The graphs (α) and (β) show the electric field z-component along a cut-line in the middle of the bus waveguide at $t = 2000 a.u.$ of the simulation (i.e. time 4 in figure 3.4) in the over- and under-coupling regime respectively. To determine the phase of the output wave with respect to the input, a sinusoidal fit was made on the left-hand side of the waveguide ($(20 < x < 70) a.u.$, green crosses in the gray area) and on the right-hand side ($(140 < x < 190) a.u.$, red crosses in the gray area). We can see that in the over-coupling regime the output wave has a π -phase shift whereas it is not the case in the under-coupling regime. The 1° difference between the theoretical and simulated phase shift is due to the size of the simulation cell. Its small extension forbids to select the fit interval further away from the resonator.

Interestingly, the analytical model is also able to correctly display the phase behavior. Figure 3.5(a)-(c) displays the typical intensity of the electric field and the phase as a function of time for the different regimes: over-, critical- and under-coupling (panels (a), (b) and (c), respectively). During the resonator discharge part, all the cases exhibit a phase shift of π (last exponential part of figure 3.5(a)-(c)). This is explained by the fact that only the field exiting from the resonator survives when the input field is turned off. This field has accumulated, due to the resonance condition and the energy conservation, a π shift with respect to the input electric field. In the under-coupling regime, the exciting (input) field is always dominant over the field which exits from the resonator so that the phase shift is 0 during the charge and in the stationary condition (see figure 3.5(c)). In the critical-coupling, the phase is 0 until the field reaches the stationary condition, where the amplitude of the field coming out of the resonator is equal to the exciting one and, therefore, no field is transmitted due to the complete destructive interference (see figure 3.5(b)). More interesting is the over-coupling regime. As shown in figure 3.5(a), during the resonator charging, the phase of the output field is 0. At some time, the system reaches the perfect destructive interference condition (see image 3 in figure 3.4). Thereafter, the field coming out of the resonator is dominant over the input one so that the accumulated phase is π and the system reaches the stationary condition.

3.2.3 Interpretation of the steps observed on the simulation

The FDTD results (blue curve in figure 3.4) exhibit steps which are not observed in the analytical model (red curve). This is due to the fact that the analytical model does not take into account the finite system size. On the other hand, in the FDTD simulation, the output power reaches a new value only when the signal wave coupled to the resonator has performed a complete round-trip which takes about $100 a.u.$

The sharp response in the FDTD simulation is also related to the temporal profile of the input signal. In the simulation we did, the source was a rectangular pulse, i.e. an abrupt switch-on/off of the signal. This causes the sharp steps. It is possible, instead, to use a trapezoidal pulse with a characteristic on-off

3. Time response of Hermitian and non-Hermitian systems

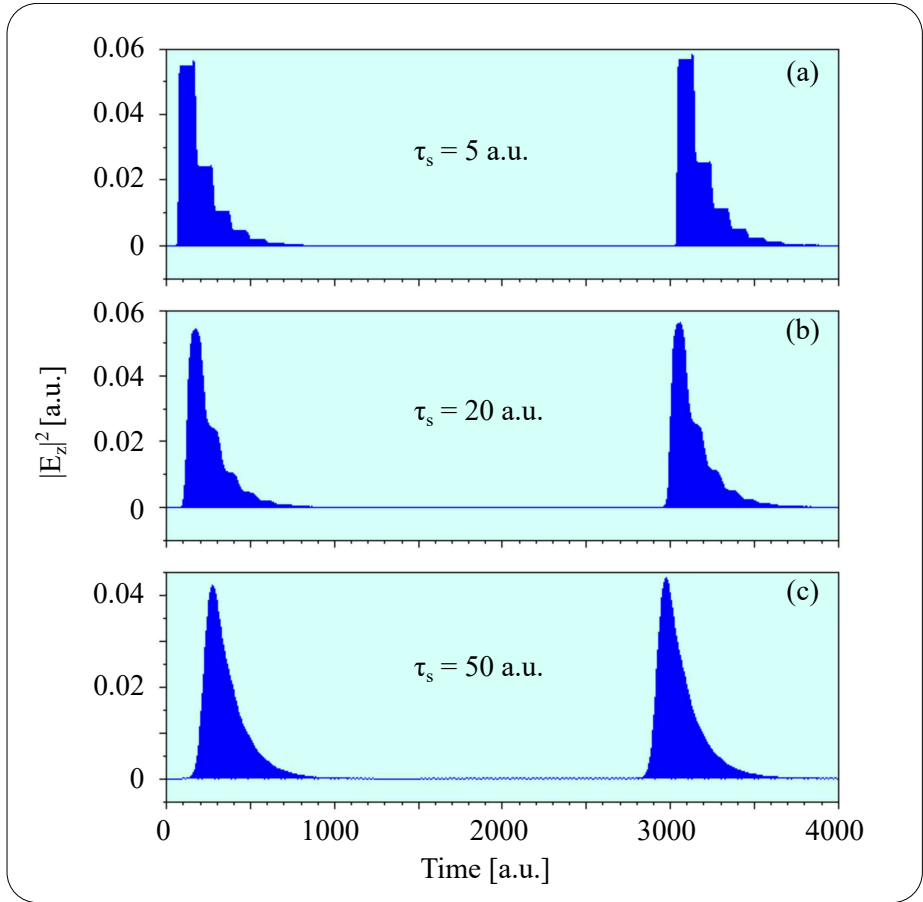


Figure 3.6: FDTD simulations in the critical coupling case. As in figure 3.4, the source is turned on at $t = 0$ and stopped at $t = 3000$ a.u. but, this time, the input pulse has a smooth exponential profile with the time constant τ_s . Panels (a), (b) and (c) show different values of the time constant: 5 a.u., 20 a.u. and 50 a.u. respectively.

exponential edge characterized by a time constant, τ_s . In this case the steps in the simulations are smoothed. Indeed Figure 3.6 (a) shows that, when τ_s is small, the steps due to the round-trip delay are clearly visible. As τ_s increases, the field decrease due to the onset of the destructive interference shows smoother or vanishing steps (see figure 3.6 (b) and (c)).

3.2.4 Interpretation of the intensity modulation far from resonance

At this point, we still have to analyze the oscillation of the temporal output response for a signal with a frequency far from the resonant frequency (ω_0). As we have seen in the 3D graph of figure 3.3, it shows an optical intensity modulation as a function of time, for frequencies far from the resonance. In these cases, the system is still stable but oscillates while approaching the steady-state value. As shown in figure 3.7, this behavior is confirmed by the numerical FDTD simulation, obtained by exciting the system with a rectangular pulse, whose frequency is not resonant. Looking at the field patterns we can explain these oscillations.

While in figure 3.4, the constructive interference inside the resonator reinforces the signal field coupled to the resonator at each round trip, here the destructive interference leads to periodic reinforcement and vanishing of the field inside the

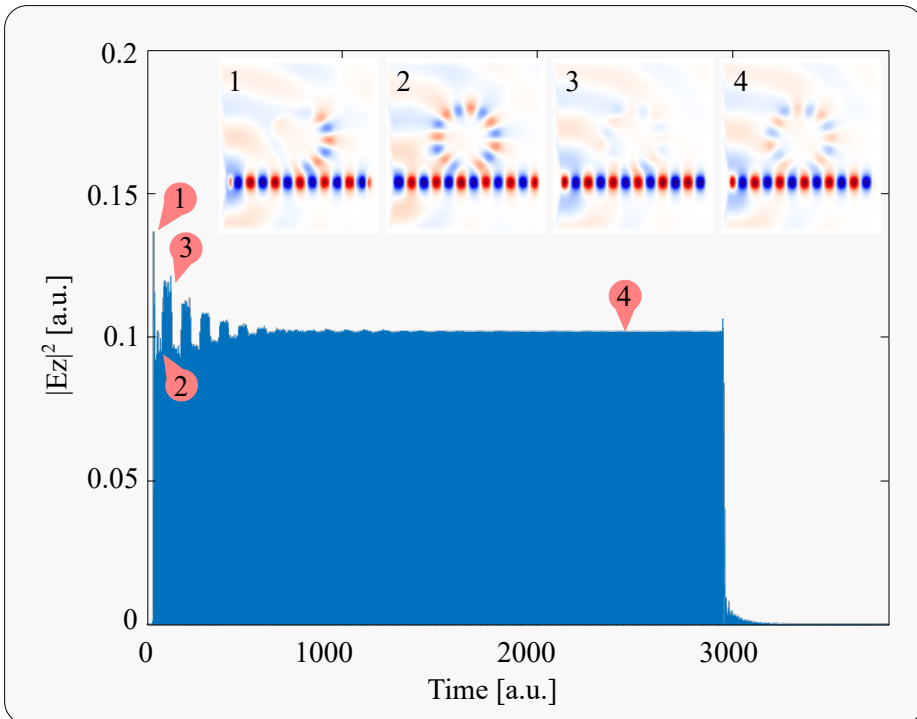


Figure 3.7: FDTD simulation of a microring coupled to a bus waveguide excited with a CW source of frequency different from the resonant one. The source is switched on at time $t = 0 \text{ a.u.}$ and off at time $t = 3000 \text{ a.u.}$. The images show the electric field z -component at the time indicated by the red pins.

3. Time response of Hermitian and non-Hermitian systems

resonator (see inset images 2,3 of figure 3.4). In turn, the interference in the coupling region between this internal beating wave and the input one induces oscillations in the output field. After several round trips, a stationary regime is reached where few light is coupled inside the cavity (see inset image 4 of figure 3.7).

3.2.5 Q-factor determination

Here, we will express the quality factor with respect to the characteristic parameters of the system (i.e. ω_0 , Γ and γ). Moreover, using the definition of the quality factor via the energy stored and the formulation of the temporal output field (see equation 3.14), we will proof the equation 2.14 of section 2.2. Such equation determines the quality factor via the resonance bandwidth as the ratio between the resonant frequency and the FWHM. The definition via the energy storage of the quality factor Q is [49, 70]:

$$Q = 2\pi \frac{\xi}{\Delta\xi}, \quad (3.15)$$

where ξ is the energy stored inside the resonator, while $\Delta\xi$ is the energy dissipated per each cycle. In all the three cases of figure 3.4, the exponential trend of the electric field, visible when the source is switched on/off, is connected to the quality factor of the system. Precisely, in equation 3.14, the discharge of the resonator is characterized by an electric field amplitude that assumes the following behavior:

$$E[t] = A_0 e^{i\omega_0 t} \frac{2\Gamma}{\Gamma + \gamma} e^{-t(\Gamma + \gamma)}. \quad (3.16)$$

The energy stored into the resonator as a function of time is connected to the square modulus of the electric field amplitude:

$$\xi[t] = \left(\frac{2A_0\Gamma}{\Gamma + \gamma} \right)^2 e^{-2t(\Gamma + \gamma)}, \quad (3.17)$$

in this way, the derivative of the energy with respect to the time assumes the following formulation:

$$\frac{d\xi[t]}{dt} = -2(\Gamma + \gamma)\xi[t]. \quad (3.18)$$

Using the previous equation we can define the energy lost per cycle as a function of the energy stored into the resonator. Precisely, the energy lost per cycle $\Delta\xi[t]$ is simply the product of equation 3.18 and the period $T = \frac{2\pi}{\omega_0}$:

$$\Delta\xi[t] = \frac{d\xi[t]}{dt} T = \frac{2\pi}{\omega_0} 2(\Gamma + \gamma)\xi[t] \quad (3.19)$$

Making use of the Q-factor definition seen in relation 3.15 we can reformulate the previous equation as:

$$2\pi \frac{\xi}{\Delta\xi} = \frac{\omega_0}{2(\Gamma + \gamma)} = Q. \quad (3.20)$$

This result is consistent with the definition of the quality factor via resonance bandwidth seen in section 2.2 and expressed by the equation 2.14. Therefore, we have proved the equivalence of the two Q-factor definitions: via the energy stored and via the resonance bandwidth.

3.3 Backscattering

For the sake of completeness, in this section we will discuss the temporal solution of the output field in the presence of the backscattering coefficients. As explained in detail in chapter 2.2, the roughness of the surface gives rise to an exchange of energy between the counter-propagating modes. The dynamics of a resonator coupled to a bus waveguide is then described by a system of two coupled equations (see equations 2.8). The previous derivation of the temporal response by means of the Green function can be extended to the case of coupled modes. For this purpose, it is necessary to consider the system excited by a Dirac pulse. In this way, exploiting the Fourier transform of the transmission amplitude (i.e. equation 2.9), it is possible to formulate the spectral Green function as:

$$G_{ccw}[\omega] = \left(1 - \frac{2\Gamma(i\Delta\omega + \rho)}{(i\Delta\omega + \rho)^2 - \beta_{12}\beta_{21}}\right) \frac{1}{\sqrt{2\pi}}, \quad (3.21)$$

where $\rho = (\Gamma + \gamma)$ and $1/\sqrt{2\pi}$ is introduced for normalization reason. The time-dependent Green Function is obtained by applying the inverse Fourier transform to equation 3.21:

$$G_{ccw}[t - t'] = \delta[t] - \frac{i\sqrt{2\Gamma}}{2} \left(e^{-(t-t')}(-i\omega_0 + \rho + \sqrt{\beta_{12}\beta_{21}}) + e^{-(t-t')}(-i\omega_0 + \rho - \sqrt{\beta_{12}\beta_{21}}) \right) \Theta[t - t'], \quad (3.22)$$

where the presence of the off-diagonal coupling terms is explicit by β_{12} and β_{21} . It is easy to see that the temporal Green function is reduced to the one of a single mode resonator (equation 3.5) plus a Dirac function when the walls roughness of the resonator is neglected (i.e. $\beta_{12}, \beta_{21} \rightarrow 0$). The Dirac's pulse takes into account the *DC* component of the field which is now intrinsically included in the Green function. Indeed, in the previous formulation we found the spectral Green function of equation 3.4 dealing only with the mode within the resonator. Only at a later stage we have formulated the total field as the sum of the mode coming out of the resonator and the *DC* component. The generic temporal response of our system is then given by the convolution of the temporal Green function for the amplitude of the incident field:

$$E_{out}[t] = \int_{-\infty}^{\infty} G[t - t'] E_{in}[t'] dt'. \quad (3.23)$$

Let us consider, as in the previous case, an excitation constituted by a CW signal of frequency ω and duration Δt (see figure 3.2 (c)). This scenario,

3. Time response of Hermitian and non-Hermitian systems

characterized by a rectangular impulse (see equation 3.11), represents a good didactic example to visualize the interaction between the counter-propagating modes. Substituting the input pulse of equation 3.11 in the relation 3.23, and calculating the convolution, we obtain the following temporal response:

$$\begin{aligned}
 E_{out}[t] = & \left\{ -\Theta[t] \left(-1 - \Gamma \left(\frac{e^{-t(i\Delta\omega + \rho - \sqrt{\beta_{12}\beta_{21}})} - 1}{i\Delta\omega + \rho - \sqrt{\beta_{12}\beta_{21}}} \right) \right. \right. \\
 & + \left. \left. \frac{e^{-t(i\Delta\omega + \rho + \sqrt{\beta_{12}\beta_{21}})} - 1}{i\Delta\omega + \rho + \sqrt{\beta_{12}\beta_{21}}} \right) \right) + \Theta[t - \Delta t] \left(-1 \right. \\
 & - \left. \Gamma \left(\frac{e^{-(t-\Delta t)(i\Delta\omega + \rho - \sqrt{\beta_{12}\beta_{21}})} - 1}{i\Delta\omega + \rho - \sqrt{\beta_{12}\beta_{21}}} \right) \right. \\
 & \left. \left. + \frac{e^{-(t-\Delta t)(i\Delta\omega + \rho + \sqrt{\beta_{12}\beta_{21}})} - 1}{i\Delta\omega + \rho + \sqrt{\beta_{12}\beta_{21}}} \right) \right) \right\} A_0 e^{i\omega t}. \tag{3.24}
 \end{aligned}$$

Also this last equation can be easily reduced to the temporal response of a single mode resonator (see equation 3.13) when $\beta_{12} = \beta_{21} = 0$. It shows that both resonator charging (the whole product with $\Theta[t]$) and discharging (the whole product with $\Theta[t - \Delta t]$) are characterized by damping oscillations. Indeed, the exponential terms exhibit in their arguments the square root of the coupling coefficients with positive and negative sign. The equation 3.24 allows having an idea about the exchange of energy between the two counter-propagating modes.

Figure 3.8 shows the square modulus of the output field amplitude as a function of time and frequency detuning. The intensity is represented in three different views: in a 3D perspective, from the top and in front. Panel (a) exhibits the case in which there are just Hermitian coefficients. While panel (b) shows the behavior of the transmitted intensity by considering non-Hermitian terms. The equation 3.24 is graphed using an impulse of duration $\Delta t = 30 \text{ ns}$. As in the case of no-roughness, out of resonance there are oscillations that are damped by approaching the stationary state (see the top views of figure 3.8). These are due to the light that couples in the resonator via evanescent field, but that does not fully satisfy the resonance condition. They can be interpreted with the same explanation given in subsection 3.2.4. In both cases Hermitian and non-Hermitian, the charging of the resonator is not a simple exponential trend. In fact, there is an exchange of energy between the counter-propagating modes that gives rise to a splitting of the resonance. In both cases, the system reaches the characteristic stationary state seen in chapter 2.2. Indeed, in panel (a), the presence of Hermitian coefficients characterizes the optical response through a balanced doublet (see front view of figure 3.8). On the other hand, in figure (b), the presence of dissipative terms gives rise to an unbalanced doublet. As we have seen in section 2.2, the stationary state is formed by two peaks that have the minimum at a frequency equal to the eigenvalues of the system. When the source of the input field is turned off, the resonator discharges. Interestingly, two distinct peaks are present at the same frequency of the two transmission peaks depth. The resonator discharge exhibits a modulation that tend to damp around a decreasing exponential. As can be seen in figure 3.8 (a), in the case of a balanced doublet, the two discharge peaks show the same intensity and trend. This means the same exchange of energy between the two eigenstate. On the

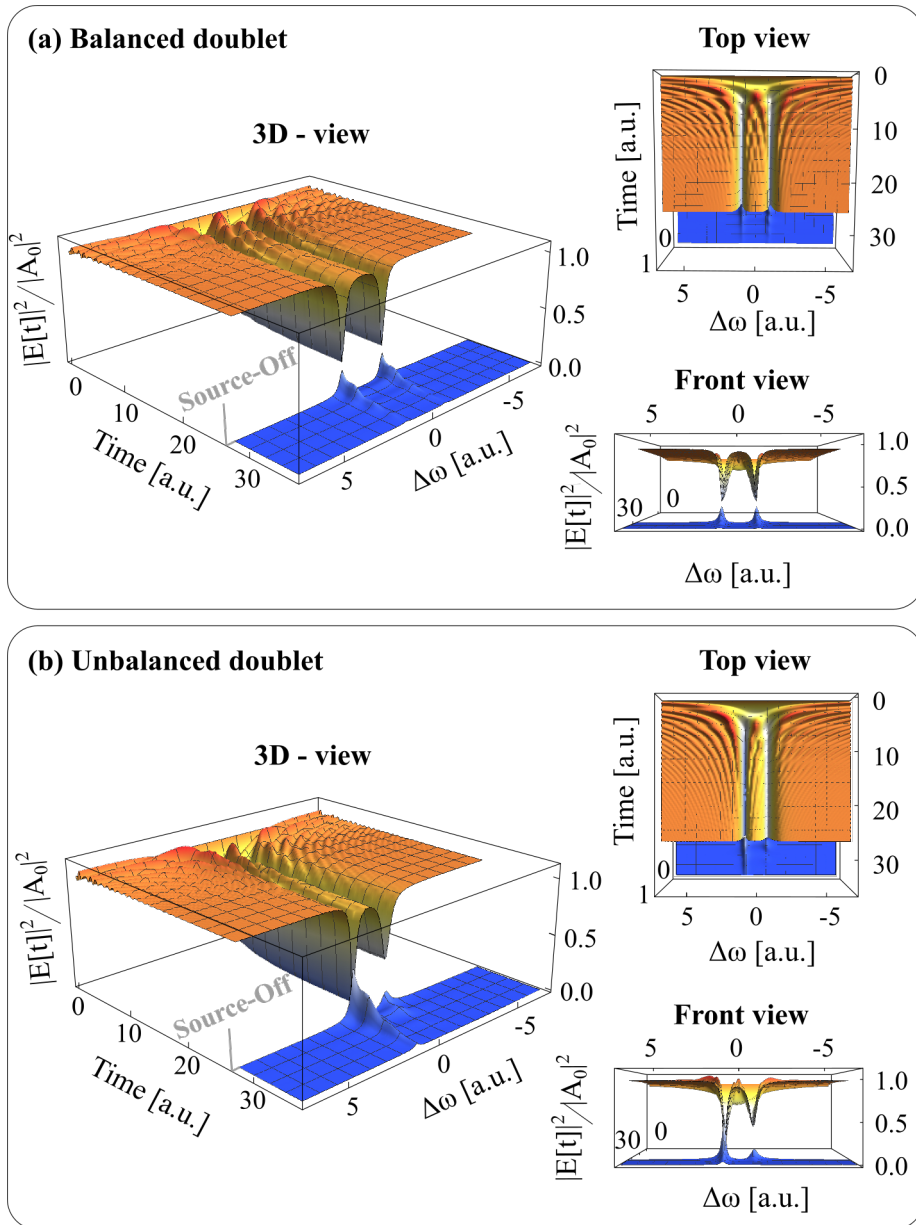


Figure 3.8: (a) and (b) Normalized electric field intensity as a function of time and frequency detuning for the balanced and unbalanced case respectively. The data are shown in three different views: a 3D prospective, top and front view.

3. Time response of Hermitian and non-Hermitian systems

contrary, in the case of non-Hermitian coefficients, there is a clear difference between the height of the peaks. Therefore, the dissipative terms induce a different energy distribution between the two eigenstates.

Chapter 4

Nonlinear response: the Bogoliubov like dispersion and the Thermo Optic Coefficient

In the previous chapters we have analyzed the spectral and temporal response in the linear regime. Here, we will consider the propagation of laser beams confined within a nonlinear material. Precisely, we will see how the typical pulse propagation equation of a single-mode channel waveguide is mathematically analogous to the Gross-Piatevskii equation of a diluted Bose-Einstein condensate [103]. This correspondence allows not only using the solution methods elaborated in the case of cold atoms, but also investigating behaviors that are exotic in the field of the nonlinear optics. We will study the propagation of a high pump power laser modulated by the presence of a weak signal. This process, known in nonlinear optics as a stimulated degenerate four wave mixing [104], finds a description in terms of the Bogoliubov's theory of cold boson atoms [103, 105]. As a result, a weak-power signal on top of a strong-power pump acquires a dispersion relation with peculiar collective features such as a sound-like shape at low detuning [27].

The parallelism between photons and cold atoms has extended the study of quantum fluid physics to nonlinear optics, introducing the field of quantum fluids of light [25]. This analogy is based essentially on the presence of: (a) a significant spatial confinement and/or weak diffraction combined with a strong degree of monochromaticity [26, 27]; (b) the presence of a third order nonlinearity, i.e. a Kerr material [26, 27]. When these conditions are satisfied, light interacts with matter giving rise to photon-like particles, which, unlike photons in vacuum, have a sizeable effective mass and mutual interaction. In particular, the effective mass is a result of point (a), while the interaction and, thus, the energy exchange between the photons is a consequence of point (b). Therefore, systems of many photons may exhibit a collective behaviour similar to that of quantum fluids of matter.

The study of the quantum fluid of light has experienced a great growth in recent years thanks to the progress of technology and, therefore, the advent of semiconductor microcavities. In fact, the improvement in light confinement and cavity field enhancement have made possible the study of strong light-matter interaction regimes [106]. This has led to the theoretical and experimental study of exciton polaritons, i.e. bosonic quasiparticles, which condense displaying long-range coherence at cryogenic temperatures [107, 108]. These exciton polariton condensates are characterized by Bogoliubov dispersion relations showing new features out of equilibrium [109, 110].

4. Nonlinear response: the Bogoliubov like dispersion and the Thermo Optic Coefficient

Taking as reference the work [27], we will study an alternative optical platform consisting of a single-mode channel waveguide made of a Kerr material. In this case, the dynamic of light propagation is governed by Schroedinger's nonlinear equation. In the absence of losses and exchanging the role of the time parameter and the propagation coordinate, it is mathematically identical to the Gross-Piteavski equation. Within this time-space mapping, the effective mass of photons corresponds to the group velocity dispersion of the system, while the Kerr nonlinearity gives rise to the mutual interaction. The nonlinear Schroedinger equation has been extensively studied and used to describe interesting phenomena such as the evolution of solitons or modulation instabilities. However, it presents, under the analogy with the cold atoms, new unresearched facets. In fact, although in the study of modulation instability the wave equation predicts spectra formally analogous to Bogoliubov's dispersion [104, 111, 112], such spectra were only used to obtain modulation-instability gain in nonlinear optical fibres [111, 113, 114, 115]. This means that no special attention has been paid to their study and measurements in terms of dispersion relation of the elementary excitations of a propagating quantum fluid of light [27].

In the following sections after a first theoretical introduction to nonlinear optics, we will see in detail the analogy between photons and cold atoms and then we will treat the process of nonlinear degenerate four wave mixing in Bogoliubov's perspective. We will solve the problem in the ideal case neglecting the losses of the waveguide and, then, considering both linear and nonlinear losses. We will study how the Bogoliubov spectrum can be acquired through an interferometric measurement. Finally, in the last section, we will see how the response of a waveguide/microresonator system is affected by the input power. Precisely, the increase of the power gives rise to a strong nonlinear response strictly connected to both the thermo optic and the Kerr coefficient. The typical transmission Lorentzian (seen in section 2) loses its perfect symmetry and assumes a peculiar triangular shape. This section allows introducing the main theoretical concepts to understand the experimental results reported in chapter 5 for the characterization of the *SiON* platform. In addition, since the nonlinear response depends on the energy inside the cavity, it opens future prospectives in studying unidirectional reflection devices. Indeed, forcing a different energy distribution between the counterpropagating modes could break the reciprocity theorem giving rise to a nonreciprocal transmission response.

4.1 Towards nonlinear optics

In the previous chapters, we have considered the propagation of light within materials that present a linear response. Actually, linearity is not a characteristic that only some materials exhibit a priori, but it is closely related to the intensity of the incident beam (I). To understand when and how the response of a medium can be defined linear or nonlinear, let us consider the polarization density vector \mathbf{P} . It is strictly connected to the characteristics of the material and describes its response to an applied electric field \mathbf{E} . Generally, at low power,

the relation between the applied electric field and the polarization vector is essentially linear. However, by increasing the input power, stronger electric fields must be considered, so that the simple linear relation between \mathbf{P} and \mathbf{E} no more holds. This behavior leads to describe \mathbf{P} via a power series of \mathbf{E} [104]:

$$\mathbf{P} = \mathbf{P}_L + \mathbf{P}_{NL} = \epsilon_0 \chi^1 \cdot \mathbf{E} + \epsilon_0 \chi^2 : \mathbf{E}\mathbf{E} + \epsilon_0 \chi^3 \vdots \mathbf{E}\mathbf{E}\mathbf{E} + \dots, \quad (4.1)$$

where ϵ_0 is the vacuum permittivity and $\chi^{(i)}$ is the i -th order susceptibility.

Since a material may exhibit distinct behavior for different directions of \mathbf{E} , the susceptibility is a tensor [116]. Precisely, $\chi^{(1)}$ is a two-rank tensor, $\chi^{(2)}$ ($\chi^{(3)}$) is a three (four)-rank tensor, and so on. However, when amorphous or isotropic materials are considered, susceptibility can be treated as a scalar quantity. From the physical point of view, $\chi^{(1)}$ takes into account the dispersion properties of a medium, and is, therefore, closely related to the permittivity (ϵ_r) seen in equation 2.51. The introduction of nonlinear terms leads to the violation of some fundamental properties such as the superposition principle, the non-interaction between photons (basic assumption in the Plank model), the constancy of the refractive index and the beam frequency. This means that light can interact with itself, exchanging momentum and energy, and therefore new electric fields at different frequencies can be generated. As a result, the equation which governs the electric field propagation changes with respect to that already seen (relation 2.51). In particular, by separating the linear and nonlinear contribution of \mathbf{P} , it is possible to reformulate the electric field propagation as [104]:

$$\nabla^2 \mathbf{E} - \mu_0 \epsilon_0 \epsilon_r \frac{\partial^2}{\partial t^2} \mathbf{E} = 4\pi \mu_0 \epsilon_0 \frac{\partial^2}{\partial t^2} \mathbf{P}_{NL}, \quad (4.2)$$

where the electric permittivity is $\epsilon_r = (1 + 4\pi\chi^{(1)})$, and \mathbf{P}_{NL} acts indeed like a source.

A further feature of the power series (equation 4.1) is that as the order of the nonlinear susceptibility increases, its value decreases. This sentence should not be taken literally, in fact, the different orders of susceptibility have different units of measurement and thus, they are not comparable (e.g. $\chi^{(2)} \approx 10^{-12} \text{m/V}$ and $\chi^{(3)} \approx 10^{-24} \text{m}^2/\text{V}^2$ [104]). However, from the experimental point of view, it can be seen that, with the same electric field, the nonlinear contribution to the polarization vector decreases as the order of susceptibility increases. As a result, processes related to the nonlinearity of the second-order require lower input powers than those of the third-order one. However, the even-order susceptibility and, in particular, the second-order one disappears in centrosymmetric materials. These satisfy the inversion symmetry and their properties are unaffected by spatial transformations: $\mathbf{r} \rightarrow -\mathbf{r}$. In the following sections, we will focus our attention on materials which show only the third-order susceptibility. These dielectrics are typically called Kerr media. Silicon is a centrosymmetric material, and thus, shows only odd-order susceptibilities. Nevertheless, processes generated by higher order susceptibilities, like $\chi^{(5)}$, are usually not considered due to the tremendous intensity required to their activation. For this reason Silicon falls in the Kerr media category.

4. Nonlinear response: the Bogoliubov like dispersion and the Thermo Optic Coefficient

At this point, it should be noted that the susceptibility is a complex quantity. In the linear case, the real part of permittivity is related to the dispersion of a medium, while the imaginary part is connected to losses in passive materials (one-photon absorption) and gain in active materials [117]. This also applies to the susceptibility of higher orders. In fact, if the real part is connected to the phenomena of interaction between photons, the imaginary part typically gives rise to losses of absorption in passive materials. This statement arises spontaneously by formulating the refractive index n and the absorption coefficient α as a function of the susceptibility [111]:

$$n = 1 + \frac{1}{2} \text{Re}[\chi^{(1)}]; \quad \alpha_0 = \frac{\omega}{cn} \text{Im}[\chi^{(1)}], \quad (4.3)$$

where c is the vacuum speed of light. Therefore, the introduction of $\chi^{(3)}$ gives rise to a change of both the refractive index and absorption coefficient as [111]:

$$\tilde{n} = n + n_2 |\mathbf{E}|^2; \quad \tilde{\alpha} = \alpha_0 + \alpha_2 |\mathbf{E}|^2, \quad (4.4)$$

where n_2 and α_2 are formulated as:

$$n_2 = \frac{3}{8n} \text{Re}[\chi^{(3)}]; \quad \alpha_2 = \frac{3\omega}{4cn} \text{Im}[\chi^{(3)}]. \quad (4.5)$$

The nonlinearity of the third order induces a change in the refraction index and a mechanism of losses dependent on intensity. This nonlinear loss is dominant at high optical intensities and is called Two Photon Absorption (TPA). From the physical point of view, this phenomenon consists in the absorption of two photons that have a total energy greater than the bandgap of the material [111]. In a semiconductor, an electron is excited from the valence band to the conduction one resulting in the generation of a free carrier (electron-hole pair) [118]. This process gives rise to free charges, so that TPA is connected by a further loss process called free carrier absorption (FCA) loss. The two absorbed photons do not necessarily have the same energy and both have insufficient energy to complete the transition on their own. Typically, TPA can be observed in the spectrum region where the material is transparent (e.g. Silicon is strongly affected by TPA at a wavelength of 1550 nm [119]).

4.2 Pulse propagation: the dissipative Gross-Pitaevskii equation

Let us consider the propagation of light along a Kerr nonlinear single-mode channel waveguide (see figure 4.1). Precisely, we deal with the propagation in the positive z -direction of a spectrally narrow beam of frequency Ω , linearly polarized along the x axis. The waveguide shows a dispersion law $\beta[\omega]$ and its core exhibits an instantaneous and spatially local Kerr nonlinearity (n_2), as well as the linear (α_0) and nonlinear TPA (α_2) loss at frequency Ω . In the slowly varying approximation, the complex electric field can be formulated as:

$$E[\mathbf{r}, t] = F[x, y]A[t, z]e^{-i\Omega t}e^{i\beta_0 z}, \quad (4.6)$$

where $F[x, y]$ is the normalized transverse distribution of the waveguide's fundamental mode, $\beta_0 = \beta[\Omega]$ is the propagation constant and $A[t, z]$ is the field amplitude. $A[t, z]$ is a slowly varying scalar function of time and z coordinate which satisfies the usual wave equation of nonlinear fiber optics [111]:

$$i \frac{\partial A}{\partial z} = \frac{\beta_2}{2} \frac{\partial^2 A}{\partial t^2} - \gamma |A|^2 A - \frac{i}{2} (\alpha_0 + \alpha_2 |A|^2) A, \quad (4.7)$$

where $\beta_2 = d^2\beta[\Omega]/d\omega^2$ is the group velocity dispersion and γ is the Kerr-nonlinearity coefficient. This nonlinear Schroedinger equation is formulated in the frame moving at the group velocity of the electric wave, i.e. $1/\beta_1 = 1/(d\beta[\Omega]/d\omega)$. The Kerr-nonlinearity coefficient takes into account the distribution of the mode inside the core and it is defined as: $\gamma = (\Omega n_2)/(c A_{eff})$. A_{eff} denotes the effective area of the transverse mode, namely [111, 116]:

$$\frac{\left(\int_{-\infty}^{\infty} \int_{-\infty}^{\infty} |F[x, y]|^2 dx dy \right)^2}{\int_{-\infty}^{\infty} \int_{-\infty}^{\infty} |F[x, y]|^4 dx dy}. \quad (4.8)$$

The equation 4.7 is of the Ginzburg-Landau type and it is well known in optics. It is used to model different nonlinear phenomena in one-dimensional optical waveguides such as the four wave mixing (FWM), self-phase modulation, the formation of temporal solitons or the Raman scattering.

Interestingly, neglecting the loss terms α_0 and α_2 , the equation 4.7 is formally analogous to the Gross-Pitaevskii equation of a quasi-one-dimensional dilute atomic Bose-Einstein condensate [27, 103]. Generally, this is used to model nonlinear phenomena in one-dimensional atomic Bose quantum fluids such as the formation of spatial solitons and shock waves, chaos effects, or nonlinear-tunneling superfluid like phenomena and matter-wave Anderson localization in the presence of inhomogeneities [27]. Precisely, the one-dimensional Gross-Pitaevskii equation can be formulated as:

$$i \hbar \frac{\partial \psi}{\partial t} = -\frac{\hbar^2}{2m} \frac{\partial^2 \psi}{\partial z^2} + g |\psi|^2 \psi, \quad (4.9)$$

written here with a null external time dependent potential. ψ is the macroscopic single-particle wavefunction of the atomic condensate, m is the atom mass, g



Figure 4.1: Sketch of a monochromatic beam propagating in positive z -direction along a channel waveguide. The dark (light) blue color denotes the core (cladding) of the waveguide.

4. Nonlinear response: the Bogoliubov like dispersion and the Thermo Optic Coefficient

denotes the atom-atom interaction constant in the zero-range-pseudopotential approximation. The mathematical analogy between the lossless equation 4.7 and 4.9 is based on the exchange of the role played by the spatial and temporal coordinates. In particular, the radiation-axis z of the propagation equation plays the role of the time t in the Gross-Pitaevskii equation. As a result, the following correspondences are obtained:

- the electric field complex amplitude is the analogous of the macroscopic single-particle wavefunction of the atomic condensate ($A[t, z] \rightarrow \psi[z, t]$);
- the opposite of the inverse of the group velocity dispersion corresponds to the atom mass ($-1/\beta_2 \rightarrow m$);
- the opposite of the Kerr-nonlinearity coefficient corresponds to the atom-atom interaction constant ($-\gamma \rightarrow g$);
- $A[t, z = 0]$ determines the initial condition on the solution of equation 4.7.

This parallelism between the two bosonic particles, photons and cold atoms, highlights some interesting aspects. Precisely, the confinement of light attributes an effective mass to photons and the nonlinearity of the material introduces, as mentioned in the previous section, an interaction between them. As a result, it is possible to apply both the language and the mathematical techniques of atomic bosons, specific of the field of quantum hydrodynamics.

4.3 A degenerate four wave mixing in the language of the Bogoliubov's theory

The FWM is a type of nonlinear Kerr effect which occurs when at least two fields with different frequencies propagate together along a third-order nonlinear medium [120]. This phenomenon was first observed in bulk materials [121]. Subsequently, the search of larger efficiency led to consider field confinement within silica fibres [122] or in waveguides on SOI platforms [123]. Since silicon is a Kerr material, it is an ideal platform for the study of FWM processes. These studies have enabled many applications such as signal amplification [116], wavelength conversion [124], light generation [120].

In the quantum picture, the FWM process is characterized by the annihilation of two (three) photons with the instantaneous generation of two (one) photons at different frequencies respect to the starting ones. This interaction shows up via different patterns; here we will consider one of the common scheme called degenerate four wave mixing (DFWM). In this case, as shown in figure 4.2, (a) two input photons of a pump laser at the same frequency ω_p are converted into a signal and idler photons at frequency ω_s and ω_i , respectively. Precisely, we will deal with a degenerate stimulated Four Wave Mixing (sDFWM). In fact, together with the input pump laser, also a stimulating laser is provided at the frequency of the signal (see figure 4.2 (b)). The presence of the signal laser boosts the generation rate of the idler improving the efficiency of the process.

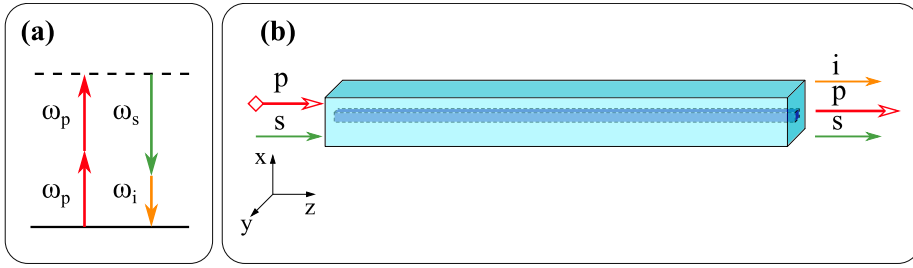


Figure 4.2: (a) Pattern of the DFWM in which two photons of frequency ω_p are converted via nonlinearity into a signal and idler of frequency ω_s and ω_i . Panel (b) shows the sketch of a sDFWM process where two monochromatic beam (p and s) propagates in the positive z -direction along the core of a channel waveguide. The dark (light) blue color indicates the core (cladding) of the waveguide.

The FWM phenomena are constrained by two conditions: the energy conservation and the quasi-phase matching. In the sDFWM, the pump and the signal wave interact via third-order nonlinearity generating an idler wave. This field exhibits an optical frequency determined by the energy conservation which is given by the following relation [120]:

$$\omega_i = 2\omega_p - \omega_s. \quad (4.10)$$

However, this condition is not sufficient to guarantee an efficient idler generation. Indeed, the efficiency of the interaction, and therefore, the exchange of energy between the three waves depends on their level of coherence. In particular, the waves generated in phase within the material add up constructively leading to a strong generation. This condition corresponds to the conservation of the momentum and is called phase matching. Generally, it is not automatically satisfied and, in the case of integrated circuits, it requires special design of the structures. The parameter used to quantify the lack of the momentum conservation is the phase mismatch. It is given by the following equation [120]:

$$\Delta\beta = \Delta\beta_L + \Delta\beta_{NL} = 2\beta_p - \beta_s - \beta_i + 2\gamma|A_p|^2, \quad (4.11)$$

where $\beta_{p,s,i}$ is the propagation constant of the pump, signal, idler and $|A_p|^2$ is the power of the pump beam. In particular, the lower the phase mismatch the greater the process efficiency. Thus, when the phase mismatch reduces to zero, the momentum conservation is fully satisfied.

The equations that govern the sDFWM process are obtained thanks to the equation 4.7, considering the field amplitude as the superposition of the three waves: pump, signal and idler ($A = A_p + A_s + A_i$). Assuming the power of the pump much greater than the powers of signal and idler ($|A_p|^2 \ll |A_{s,i}|^2$), the

4. Nonlinear response: the Bogoliubov like dispersion and the Thermo Optic Coefficient

sDFWM equations reduce to [120]:

$$\begin{cases} i \frac{\partial A_p}{\partial z} = \frac{1}{2} (\alpha_0 + \alpha_2 |A_p|^2) A_p - \gamma |A_p|^2 A_p, \\ i \frac{\partial A_s}{\partial z} = \frac{1}{2} (\alpha_0 + \alpha_2 |A_p|^2) A_s - 2\gamma |A_p|^2 A_s - \gamma A_i^* A_p^2 e^{-i\Delta\beta_L z}, \\ i \frac{\partial A_i}{\partial z} = \frac{1}{2} (\alpha_0 + \alpha_2 |A_p|^2) A_i - 2\gamma |A_p|^2 A_i - \gamma A_s^* A_p^2 e^{-i\Delta\beta_L z}. \end{cases} \quad (4.12)$$

It is possible to obtain the same equations using the analogy between photons and cold atoms. In particular, this process can be described by means of the Bogoliubov theory. In order to understand such parallelism, we open a short parenthesis on this theory. The Gross-Pitaevskii equation 4.9 presents, as a stationary solution, the condensate wave function of the ground state, of the type:

$$\psi[z, t] = \psi_0[z] e^{-i\mu \frac{t}{\hbar}}, \quad (4.13)$$

where μ is the chemical potential and the square modulus of the macroscopic function represents the particle density. In 1947 Bogoliubov introduced a way to determine the excited states of a condensate that consisted in using a linear combination of particle creation and annihilation operators [125]. This approach considers small deviation around the ground state as:

$$\psi[z, t] = (\psi_0[z] + u[z] e^{-i\omega t} + v[z]^* e^{i\omega t}) e^{-i\mu \frac{t}{\hbar}}, \quad (4.14)$$

where u and v are complex functions which, in the case of a uniform gas, take the form of plane waves, i.e. $u[z] = u e^{ikz}$ and $v[z] = v e^{ikz}$, where k is the excitation wavevector. Substituting the relation 4.14 in the Gross-Pitaevskii equation, considering an uniform gas and keeping terms linear in the complex functions (u and v), we obtain the following coupled equations [103]:

$$\hbar\omega \begin{pmatrix} u \\ v \end{pmatrix} = \begin{pmatrix} \frac{\hbar k^2}{2m} + \mu & \mu \\ -\mu & -\frac{\hbar^2 k^2}{2m} - \mu \end{pmatrix} \begin{pmatrix} u \\ v \end{pmatrix}. \quad (4.15)$$

Solving the eigenvalues problem, we derivate the excited states energies of the condensate as:

$$\omega = \pm \sqrt{\frac{\hbar^2 k^2}{2m} \left(\frac{\hbar^2 k^2}{2m} + 2\mu \right)}. \quad (4.16)$$

This relation is the well-known Bogoliubov spectrum. For greater momenta it assumes the free particle energy $\frac{\hbar^2 k^2}{2m}$ and thus follows a parabolic shape. While for low wavevectors equation 4.16 reduces to the typical phonon dispersion $\sqrt{\frac{u\hbar^2}{m}} k$, where the square root is the sound velocity in the gas.

In the optical case, the strong amplitude of the pump, i.e. A_p , represents the fundamental state. The small deviations around the pump are obtained by the low amplitude of the signal and idler (A_s and A_i). This allows taking advantage of the mathematical framework of the Bogoliubov theory to study the sDFWM process. As mentioned in the previous section, the analogy between the impulse propagation and the Gross-Pivtaevskii equation is based on the

exchange of the role between temporal and spatial coordinate. This, as we will see in detail, makes the spectrum of energies of the excited states (equation 4.16) to correspond to the wavevector of the signal and idler laser. From the physical point of view, we are therefore interested in the phase of the signal. As a result, it is useful for the analytical resolution of our problem, to exploit the Madelung representation [27] of the equation 4.7 by reformulating the amplitude of the field as:

$$A[t, z] = \sqrt{\rho[t, z]} e^{i\theta[t, z]}, \quad (4.17)$$

where $\rho[t, z]$ and $\theta[t, z]$ are real quantities. Specifically, ρ is connected to the instantaneous local power ($P[t, z] = \frac{1}{2} c \epsilon_0 n \rho[t, z]$) and θ corresponds to the instantaneous local phase of the beam. Substituting the amplitude field 4.17 in the pulse propagation equation 4.7 and separating the real and imaginary part we obtain the following coupled equations:

$$\begin{cases} \frac{\partial \rho}{\partial z} = \beta_2 \frac{\partial}{\partial t} \left(\rho \frac{\partial \theta}{\partial t} \right) - (\alpha_0 + \alpha_2 \rho) \rho \\ \frac{\partial \theta}{\partial z} = -\frac{\beta_2}{2\sqrt{\rho}} \frac{\partial^2 \sqrt{\rho}}{\partial t^2} + \frac{\beta_2}{2} \left(\frac{\partial \theta}{\partial t} \right)^2 + \gamma \rho \end{cases} \quad (4.18)$$

Within the analogy based on time-space mapping, the equation 4.18 corresponds to Euler's equation of quantum hydrodynamics for the density-like ($\rho[t, z]$) and velocity-like ($-\beta_2 \partial \theta[t, z] / \partial t$) fields [27]. The ground state of these coupled equations is determined by considering a monochromatic pump light beam at a frequency Ω . According to the slowly varying amplitude approximation, A_p does not depend on time (i.e. we consider a continuous CW laser beam) and it reduces as:

$$A[t, z] = A_0[z] = \sqrt{\rho_0[z]} e^{i\theta_0[z]}, \quad (4.19)$$

where $\rho_0[z]$ and $\theta_0[z]$ are solutions of the t-independent version of the system 4.18, i.e. [27]:

$$\begin{cases} \frac{\partial \rho_0}{\partial z} = -(\alpha_0 + \alpha_2 \rho_0) \rho_0, \\ \frac{\partial \theta_0}{\partial z} = \gamma \rho_0. \end{cases} \quad (4.20)$$

These equations provide an analytical solution for $\rho_0[z]$ and $\theta_0[z]$ as a function of the propagation z-coordinate along the waveguide of the type:

$$\rho[z] = \rho_0[0] \frac{e^{-\alpha_0 z}}{1 + \frac{\alpha_2 \rho_0[0]}{\alpha_0} (1 - e^{-\alpha_0 z})}, \quad (4.21)$$

$$\theta_0[z] = \theta_0[0] + \gamma \int_0^z \rho[z'] dz' = \theta_0[0] + \frac{1}{\alpha_2} \ln \left[1 + \frac{\alpha_2 \rho_0[0]}{\alpha_0} (1 - e^{-\alpha_0 z}) \right]. \quad (4.22)$$

These equations simply state that the power, in the presence of losses, decreases during the propagation along the waveguide, while the absorption coefficients modify the phase.

At this point, we derive the weak-amplitude deviations propagation equation from the t-independent and power-dependent solutions 4.21 and 4.22, within the Bogoliubov's theory of elementary excitation. Therefore, we introduce the

4. Nonlinear response: the Bogoliubov like dispersion and the Thermo Optic Coefficient

fluctuations with respect to the stationary states of power-dependent departures as:

$$\rho[t, z] = \rho_0[z] + \varrho[t, z], \quad (4.23)$$

$$\theta[t, z] = \theta_0[z] + \vartheta[t, z], \quad (4.24)$$

where $\varrho[t, z]$ and $-\beta_2 \partial \vartheta[t, z] / \partial t$ are real fluctuating fields which are assumed to be small. These functions can be Fourier expanded as [27]:

$$\varrho[t, z] = \sqrt{\rho_0[z]} \int_{-\infty}^{\infty} (a[\omega] f_+[\omega, z] e^{-i\omega t} + a^*[\omega] f_+^*[\omega, z] e^{i\omega t}) \frac{d\omega}{2\pi}, \quad (4.25)$$

$$\vartheta[t, z] = \frac{1}{2i\sqrt{\rho_0[z]}} \int_{-\infty}^{\infty} (a[\omega] f_-[\omega, z] e^{-i\omega t} + a^*[\omega] f_-^*[\omega, z] e^{i\omega t}) \frac{d\omega}{2\pi}, \quad (4.26)$$

where the $a[\omega]$ are chosen to be z -independent and with a dimension given by voltage times time. In this way, the $f_{\pm}[\omega, z]$ functions exhibit all the z -dependence of the fluctuations and are dimensionless. Inserting the equation 4.23 and 4.24 into the power-phase propagation equation 4.18, linearizing the corresponding system around $[\rho[t, z], -\beta_2 \partial \theta[t, z] / \partial t] = [\rho_0[z], 0]$, we obtain the following matrix differential equation for the Fourier amplitudes $f_{\pm}[\omega, z]$:

$$i \frac{\partial}{\partial z} \begin{pmatrix} f_+ \\ f_- \end{pmatrix} = - \begin{pmatrix} \frac{i}{2} (\alpha_0 + 3\alpha_2 \rho_0[z]) & \frac{\beta_2}{2} \omega^2 \\ \frac{\beta_2}{2} \omega^2 + 2\gamma \rho_0[z] & \frac{i}{2} (\alpha_0 + \alpha_2 \rho_0[z]) \end{pmatrix} \begin{pmatrix} f_+ \\ f_- \end{pmatrix}. \quad (4.27)$$

This equation is formally analogous to the the Bogoliubov-de Gennes matrix equation of dilute atomic Bose gases within Madelung's picture [27]. In particular, the opposite of the 2x2 matrix corresponds to the Bogoliubov-de Gennes matrix. Since this matrix is an even function of ω , its eigenlements have to be even too. It is worth noticing that in this case, ω is not directly connected to the signal or idler frequency. In fact, we are dealing with t -dependent departures from the steady profile, and this makes ω to be considered with respect to the central frequency of the monochromatic pump Ω . The linear and nonlinear losses enter as diagonal elements in the Bogoliubov-de Gennes matrix. In particular, α_0 , thanks to the minus sign on the right side of the equation 4.27, acts by decreasing the amplitude of the modulations during the propagation of the light beam along the waveguide. In addition, α_2 is connected to the beam power and brings a saturation contribution to the modulation amplitude. It is worth noticing that, by removing the minus preceding the 2x2 matrix of equation 4.27, we obtain the case of the modulation of a paraxial optical field propagating in an active medium [27, 104]. In fact, in this scenario, α_0 describes an amplification of the optical field modulation, while the nonlinear parameter α_2 depends on the intensity and acts exactly like a gain-saturation term in the laser medium.

4.3.1 Lossless waveguide

Let us consider the ideal case where the linear and nonlinear losses are neglected ($\alpha_0 = \alpha_2 = 0$). Here, light propagates spatially without loss of power. Consequently, the ground state of the equation 4.21 remains constant along the entire

length of the waveguide (L):

$$\rho[z] = \rho_0[0] = \rho_0 = \text{const.} \quad (4.28)$$

In addition, this causes the phase profile of the fundamental state (see equation 4.22) to grow linearly with the propagation distance:

$$\theta[z] = \theta_0[0] + \gamma\rho_0 z. \quad (4.29)$$

The greater the beam power or nonlinear index, the greater the phase variation. Neglecting the losses, the diagonal elements of the Bogoliubov-de Gennes matrix reduce to zero. This means that it is homogeneous and thus the Fourier $f_{\pm}[\omega, z]$ components of the power and phase fluctuations of the fluid of light, solution of the equation 4.27, are plane waves with an amplitude and a wavenumber dependent on ω :

$$f_{\pm}[\omega, z] = \tilde{f}_{\pm}[\omega] e^{ik[\omega]z}. \quad (4.30)$$

This is in agreement with the previous discussion of an uniform gas within the Bogoliubov's theory. Replacing the relation 4.30 in the differential equation 4.27, we obtain the following eigenvalue problem:

$$k[\omega] \begin{pmatrix} \tilde{f}_+ \\ \tilde{f}_- \end{pmatrix} = \begin{pmatrix} 0 & \frac{\beta_2}{2}\omega^2 \\ \frac{\beta_2}{2}\omega^2 + 2\gamma\rho_0 & 0 \end{pmatrix} \begin{pmatrix} \tilde{f}_+ \\ \tilde{f}_- \end{pmatrix}. \quad (4.31)$$

As we will see, the two eigenvalues $k[\omega]$ are strictly related to the wavevector of the signal and idler beam. They are the roots of the characteristic polynomial and are, by construction, symmetrical and opposite, corresponding to a positive (+) and negative (-) branch [27, 105]:

$$k[\omega] = \pm \sqrt{\frac{\beta_2}{2}\omega^2 \left(\frac{\beta_2}{2}\omega^2 + 2\gamma\rho_0 \right)}. \quad (4.32)$$

This relation is comparable, within the $t \rightarrow z$ mapping, to the Bogoliubov spectrum seen in equation 4.16. In fact, in this analogy, the frequency directly corresponds to the wavenumber. However, since the nonlinear parameter and the group velocity dispersion can assume both positive and negative value, here equation 4.32 may be complex. When the group velocity dispersion (β_2) and the Kerr nonlinearity (γ) are of the same sign equation 4.32 directly corresponds to the dispersion relation of the elementary excitation propagating on top of a homogeneous dilute Bose-Einstein condensate at rest [27]. Precisely, this happens when the waveguide exhibits a normal group velocity dispersion ($\beta_2 > 0$) and a self-focusing nonlinear parameter ($\gamma > 0$), or when it shows an anomalous group velocity dispersion ($\beta_2 < 0$) and a self-defocusing nonlinear parameter ($\gamma < 0$). As in the case of the Bogoliubov spectrum, we can identify two main trends. Precisely, depending on the ω frequency, the wave vector exhibits two asymptotic behaviors:

$$k[\omega] \approx \pm \begin{cases} v^{-1}|\omega|, & |\omega| \ll 1/\tau, \\ \frac{|\beta_2|}{2}\omega^2 + |\gamma|\rho_0, & |\omega| \gg 1/\tau, \end{cases}. \quad (4.33)$$

4. Nonlinear response: the Bogoliubov like dispersion and the Thermo Optic Coefficient

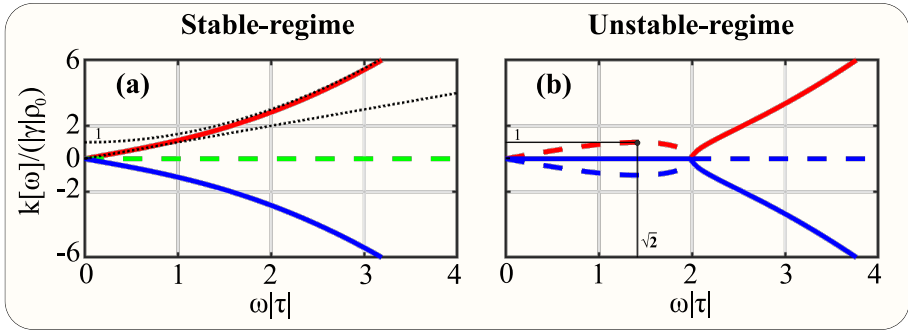


Figure 4.3: Real (plain curves) and imaginary (dashed curves) parts of the normalized Bogoliubov dispersion relation as a function of the adimensional quantity $\omega|\tau|$. The red (blue) color highlights the positive (negative) branch. Panel (a) shows the dynamically stable regime, when the group velocity dispersion and the nonlinear parameter have the same sign. The dotted lines display the two approximations of equation 4.33: the phonon-like at low- ω and particle-like at large- ω . Panel (b) shows the dynamically unstable regime, when the group velocity dispersion and the nonlinear parameter have different signs. The black thin lines highlight the identity of relation 4.38.

where the parameters are set as:

$$v^{-1} = \sqrt{\beta_2 \gamma \rho_0} \quad , \quad (4.34)$$

$$\tau = \sqrt{\frac{\beta_2}{\gamma \rho_0}} = \frac{|\beta_2|}{v^{-1}}. \quad (4.35)$$

For small ω the wavevector is linear and, therefore, presents a phonon-like dispersion [103, 105]. While for large ω it assumes the quadratic pattern showing the typical particle-like dispersion. Within the parallelism of photons and cold atoms, the speed of equation 4.34 is the analogue of the speed of sound and τ corresponds to the healing length [103]. Figure 4.3 (a) shows the adimensional ratio $k[\omega]/(|\gamma|\rho)$ as a function of the adimensional variable $\omega|\tau|$. In particular, the group velocity dispersion and the Kerr nonlinear coefficient have the same sign and the red (blue) solid line displays the positive (negative) branch. While the real (imaginary) part is plotted by solid (dashed) line. The black dotted line denotes the two approximations of equation 4.33, i.e. the phonon-like and particle-like dispersion.

Interestingly, the parallelism between photons and cold atoms allows introducing the concept of the superfluidity. The Landau's criterion states that at zero-temperature conservative Bose-Einstein condensate flowing with a velocity smaller than the Bogoliubov speed of sound is unaffected by the presence of a

weakly perturbing impurity. In this case, the velocity of equation 4.34 may be regarded as a direct optical equivalent of Landau's critical velocity for superfluidity. Such a critical velocity has been investigated in a different optical configuration where a collimated flat beam has been lunched through a cylindrical sample filled with methanol/graphene solution [126]. In that case, the effective mass of the photons originates from paraxial diffraction in the plane transverse to the propagation axis. This allows studying the Bogoliubov spectrum in the plane transverse to the propagation and then defining a Landau's critical velocity to compare with the velocity in the propagation direction. In this way, it is possible to directly investigate the suppressed drag force felt by moving impurity crossing the superfluid. In fact, by fixing a propagation velocity less than the Landau critical velocity, the fluid of light does not feel the impurity [26]. In contrast, our case is based on a one-dimensional geometry and, therefore, presents an effective mass originated from the group velocity dispersion of the material. This makes prohibitive such a direct investigation of the superfluid behavior.

When the group velocity dispersion β_2 and the nonlinear Kerr parameter γ have opposite sign, the wavevector of equation 4.32 is a complex function of ω . Figure 4.33 (b) shows the trend in the dimensionless units of the real (solid line) and imaginary (dashed line) part of the wavevector in this scenario. As in the panel (a), the red (blue) line displays the positive (negative) branch. Here, the following identities can be identified (see panel (b) of figure 4.33):

$$Re(k[\omega]) = 0 \quad \forall \quad |\omega| < 2/\tau, \quad (4.36)$$

$$Im(k[\omega]) = 0 \quad \forall \quad |\omega| > 2/\tau, \quad (4.37)$$

$$|Im(k[\pm\sqrt{2}/\tau])| = |\gamma|\rho_0. \quad (4.38)$$

This behavior is known in the nonlinear optics framework as sideband instability [104, 111]. It corresponds to the situation where light propagation along the waveguide is not robust against the formation of modulation instabilities [113, 114]. In fact, the deviations from the background pattern are reinforced by the nonlinearity of the material and can lead to the generation of sidebands and eventually to breakup the wave profile into a train of pulses. Within the analogy with the Gross-Pitaevskii equation, the presence of an imaginary part in Bogoliubov's dispersion spectrum makes the evolution of the fluid unstable [27, 103]. In particular, for frequencies such that $Im[k[\omega]] < 0$, the analogous Fourier amplitudes diverge as the time-like parameter z ($|f_{\pm}[\omega, z]| = ||\tilde{f}_{\pm}[\omega]|e^{-Im[k[\omega]]z}$) increases.

4.3.2 Estimation of the waveguide parameters

As we have seen in previous subsection, the effective mass is strictly connected to the group velocity dispersion of the system. While the interaction between photons is determined by the nonlinear properties of the material. Therefore, the waveguide design and the choice of material allow investigating both regimes: stable (same sign of β_2 and γ) and unstable (opposite sign of β_2 and γ). The parameters related to the confinement of the light within the single-mode waveguide

4. Nonlinear response: the Bogoliubov like dispersion and the Thermo Optic Coefficient

were determined through numerical simulations. These are based on the FEM engine by Comsol Multiphysics and controlled by the mathematical environment of Matlab. Regarding the non-linear parameters, these have been estimated by evaluating the different values present in the literature. We have made an exception in the case of the *SiON*. In fact, in this platform, the particular mixture of silane, ammonia and nitrous gasses, used during the manufacturing, strongly modifies the optical properties. For this reason, as we will see in chapter 5, we have characterized linearly and non-linearly the *SiON* platform grown through a chemical vapor deposition process by the FBK factory.

The simulation model is simply based on a two-dimensional waveguide cross-section. The structures analyzed are channel and rib waveguides with a rectangular core. We considered a cladding of *SiO₂* and different cores of *Si*, *Si₃N₄* and *SiON*. In addition, the study was extended to classical telecommunication optical fiber in *SiO₂*. For the different geometries, only the first mode, in the two polarizations, was computed. The simulations provide the effective index as a function of wavelength, which allows estimating the group velocity dispersion as [111]:

$$\beta_2 = -\frac{\lambda^2}{2\pi c} \frac{d\beta_1}{d\lambda}, \quad (4.39)$$

where β_1 is the inverse of the group velocity (v_g) and is defined as [111]:

$$\beta_1 = \frac{1}{v_g} = \frac{1}{c} \left(n_{eff} - \lambda \frac{dn_{eff}}{d\lambda} \right). \quad (4.40)$$

The effective area (A_{eff}) was estimated using the numerical mode profile through equation 4.8. The table 4.1 shows the values of a channel waveguide with a core of *Si* and *Si₃N₄*, used in the work [27] for a first estimation of the Bogoliubov's spectrum.

4.3.3 Lossy waveguide

Let us consider a realistic scenario with the presence of linear and non linear losses ($\alpha_0 \neq 0$ and $\alpha_2 \neq 0$). In this case, the dissipative Bogoliubov-de Gennes-type problem of equation 4.27, requires a numerical resolution. The general solution can be written in the matrix form as:

$$\begin{pmatrix} f_+[\omega, z] \\ f_-[\omega, z] \end{pmatrix} = e^{iK_{eff}[\omega, z]z} \begin{pmatrix} f_+[\omega, z] \\ f_-[\omega, z] \end{pmatrix}, \quad (4.41)$$

where $K_{eff}[\omega, z]$ is a 2x2 matrix which depends on ω and z and it is defined through:

$$e^{iK_{eff}[\omega, z]z} = Z \left\{ e^{i \int_0^z K[\omega, z'] dz'} \right\} = \lim_{N \rightarrow \infty} \prod_{n=N}^0 e^{iK[\omega, z_n] \delta z}. \quad (4.42)$$

Silicon (<i>Si</i>) waveguide	
Effective refractive index, n_0	$\approx \begin{cases} 1.8 & \text{(TM mode)} \\ 2.3 & \text{(TE mode)} \end{cases}$
Group velocity dispersion parameter, β_2	$\approx \begin{cases} 13.0 \text{ ps}^2 \cdot \text{m}^{-1} & \text{(TM mode)} \\ -1.3 \text{ ps}^2 \cdot \text{m}^{-1} & \text{(TE mode)} \end{cases}$
Kerr index, n_2	$\approx \frac{1}{2} c \epsilon_0 n_0 \cdot 10^{-18} \text{ m}^2 \cdot \text{V}^{-2}$
Effective mode Area, A_{eff}	$\approx 0.2 \mu\text{m}^2$
Kerr-nonlinearity coefficient, γ	$\approx \frac{1}{2} c \epsilon_0 n_0 \cdot 20.3 \text{ m}^{-1} \cdot \text{V}^{-2}$
One-photon loss coefficient, α_0	$\approx 3.5 \text{ dB} \cdot \text{cm}^{-1}$
Two-photon loss coefficient, α_2	$\approx 0.2 \gamma $
Silicon nitride (<i>Si₃N₄</i>) waveguide	
Effective refractive index, n_0	$\approx \begin{cases} 1.5 & \text{(TM mode)} \\ 1.6 & \text{(TE mode)} \end{cases}$
Group velocity dispersion parameter, β_2	$\approx \begin{cases} -0.6 \text{ ps}^2 \cdot \text{m}^{-1} & \text{(TM mode)} \\ 0.3 \text{ ps}^2 \cdot \text{m}^{-1} & \text{(TE mode)} \end{cases}$
Kerr index, n_2	$\approx \frac{1}{2} c \epsilon_0 n_0 \cdot 10^{-19} \text{ m}^2 \cdot \text{V}^{-2}$
Effective mode Area, A_{eff}	$\approx 2 \mu\text{m}^2$
Kerr-nonlinearity coefficient, γ	$\approx \frac{1}{2} c \epsilon_0 n_0 \cdot 20.3 \cdot 10^{-2} \text{ m}^{-1} \cdot \text{V}^{-2}$
One-photon loss coefficient, α_0	$\approx 0.2 \text{ dB} \cdot \text{cm}^{-1}$
Two-photon loss coefficient, α_2	$\rightarrow 0$

Table 4.1: Optical parameters at about $1.55 \mu\text{m}$ for channel waveguides whose cores are made of silicon and silicon nitride. These parameters were used in ref. [27].

In this equation, K is the 2x2 Bogoliubov-de Gennes matrix defined in equation 4.27 as:

$$K = \begin{pmatrix} \frac{i}{2}(\alpha_0 + 3\alpha_2\rho_0[z]) & \frac{\beta_2}{2}\omega^2 \\ \frac{\beta_2}{2}\omega^2 + 2\gamma\rho_0[z] & \frac{i}{2}(\alpha_0 + \alpha_2\rho_0[z]) \end{pmatrix}, \quad (4.43)$$

while $Z\{\dots\}$ is the equivalent of the chronological ordering for time-dependent quantum mechanical system. It appears because $K[\omega, z]K[\omega, z'] \neq K[\omega, z']K[\omega, z]$ for all $z \neq z'$. As shown in equation 4.42, Z can be defined through the infinite, reversely order product, where $z_n = n\delta z = n z/N$ ($n \in [0, N]$) [27]. The Bogoliubov dispersion relation corresponds to the local eigenvalues $k_{eff}[\omega, z]$ of the effective propagation matrix $K_{eff}[\omega, z]$. As usual, these can be determined from the numerical diagonalization of $K_{eff}[\omega, z]$.

The system of differential equations 4.27, admits an analytical solution even in the presence of linear and nonlinear losses. This is based on the assumption

4. Nonlinear response: the Bogoliubov like dispersion and the Thermo Optic Coefficient

of the validity of the adiabatic approximation. It is determined by reformulating the adiabatic theorem of quantum mechanics in the optical language [27]. This theorem states that in presence of a sufficiently slow evolution, a system starting in an eigenstate will remain as an instantaneous eigenstate through the evolution [127]. In our case this means that each eigenvector of the matrix 4.43 is a function of the spatial coordinate of propagation z that strictly follows the variations of its corresponding eigenvalue as a function of z . Since the presence of losses makes the evolution not cyclic ($\rho_0[L]\rho_0[0]$), i.e. $K[\omega, L] \neq K[\omega, 0]$, we have that a trivial choice of gauge for the eigenvector allows eliminating the phase factor typically introduced by applying the adiabatic theorem [128]. It is worth noticing that this factor corresponds, in the quantum field, to the well-know Berry-phase, which, for a closed path, cannot be deleted by the choice of gauge [128]. This introduces important physical consequences that led to the birth of quantum topology. Considering an adiabatic evolution we can write the solution of equation 4.27 as:

$$f_{\pm}[\omega, z] = \tilde{f}_{\pm}[\omega, z] e^{i \int_0^z k[\omega, z'] dz'} = \tilde{f}_{\pm}[\omega, z] e^{i \langle k[\omega, z] \rangle_z z}, \quad (4.44)$$

where the symbol $\langle \dots \rangle_z$ denotes $\langle a \rangle_z = \frac{1}{z} \int_0^z a dz'$. The amplitudes $\tilde{f}_{\pm}[\omega, z]$ and the wave number $k[\omega, z]$ along the z axis are eigenelements of the 2x2 K matrix:

$$k[\omega, z] \begin{pmatrix} \tilde{f}_{+}[\omega, z] \\ \tilde{f}_{-}[\omega, z] \end{pmatrix} = K[\omega, z] \begin{pmatrix} \tilde{f}_{+}[\omega, z] \\ \tilde{f}_{-}[\omega, z] \end{pmatrix}. \quad (4.45)$$

In this way, the equation 4.45 admits nontrivial solutions when $k[\omega, z]$ is a root of the characteristic polynomial:

$$k[\omega, z] = i \left(\frac{\alpha_0}{2} + \alpha_2 \rho_0[z] \right) \pm \sqrt{\frac{\beta_2}{2} \omega^2 \left(\frac{\beta_2}{2} \omega^2 + 2\gamma \rho_0[z] \right) - \frac{(\alpha_2 \rho_0[z])^2}{4}}. \quad (4.46)$$

This expression therefore allows determining the Bogoliubov dispersion $\langle k[\omega, z] \rangle_z$ of a beam that evolves adiabatically as appears in equation 4.44. As derived in detail in [27], this analytical result is valid if the following condition is satisfied:

$$\max_{z \in [0, L]} \frac{|\langle \tilde{f}_{\pm}[\omega, z] | \frac{\partial K}{\partial z} | \tilde{f}_{\mp}[\omega, z] \rangle|}{|k_{\mp}[\omega, z] - k_{\pm}[\omega, z]|} \ll \min_{z \in [0, L]} |k_{\mp}[\omega, z] - k_{\pm}[\omega, z]|, \quad (4.47)$$

where $k_{\pm}[\omega, z]$ denotes the \pm branch of the $k[\omega, z]$ in equation 4.46 and $|\tilde{f}_{\pm}[\omega, z]\rangle \propto {}^t(\tilde{f}_{+}, \pm[\omega, z] \tilde{f}_{-}, \pm[\omega, z])$ to the corresponding eigenvector, normalized to unity [27].

Let us now consider the Bogoliubov dispersion in a real case, using the parameters reported in table 4.1. We treat a beam of incident light at a wavelength of $1.55 \mu\text{m}$ with a maximum pump power of about 100 mW . This power refers to the beam right at the entrance of the waveguide (i.e. $z = 0^+$). Moreover, let us consider a value of the spatial propagation coordinate equal to $z = L$, since from an experimental point of view the signal is acquired at the

waveguide output. This point will be further justified in the next subsection where we will talk about the observable to measure. For Silicon (Silicon Nitride) we set a waveguide length of about 2 cm (20 cm). The difference of one order of magnitude between the two lengths is essentially due to the absence of the α_2 nonlinear losses, in the first telecom window, for the case of Silicon Nitride and to the lower linear losses (α_0) of Silicon Nitride with respect to Silicon (see table 4.1)

Figure 4.4, shows the wavevector as a function of ω , for a silicon (a)-(d) and a silicon nitride (e)-(h) waveguide. In particular, panels (a), (c), (e) and (g) ((b), (d), (f) and (h)) show the real (imaginary) part of k_{eff} . The black lines represent the numerical values from the exact solution of $Re[k_{eff}[\omega, L]]$ and $Im[k_{eff}[\omega, L]]$. While the red lines show the Bogoliubov's dispersion computed by using the adiabatic approximation $\langle k[\omega, z] \rangle_L$. As can be seen from figure 4.4, the adiabatic approximation is in good agreement with the exact solution of the eigenvalue problem. In addition, we numerically check from equations 4.27 and 4.45 that the adiabatic evolution constrain 4.47 is verified for a wide range of Bogoliubov angular frequencies ω . This allows using the following adiabatic identification:

$$k_{eff}[\omega, L] = \langle k[\omega, z] \rangle_L = \frac{1}{L} \int_0^L k[\omega, z] dz, \quad (4.48)$$

to describe quantitatively the Bogoliubov behavior of Si or Si_3N_4 represented in the figure 4.4.

In contrast to the phononic (linear) dispersion at low- ω of the stable case (β_2 and γ of same sign) and without losses ($\alpha = 0$ and $\alpha_2 = 0$), seen in figure 4.3 (a), the trend obtained for the real (imaginary) part in figures 4.4 (a), (c) and (e) ((b), (d) and (f)) shows a non-propagating behaviour. Indeed, the real part of k_{eff} is equal to zero and therefore, the Bogoliubov's law is dispersionless. This over-damped behavior for low frequencies, has been observed and described theoretically in the context of exciton-polariton quantum fluids in semiconductor microcavity [25, 109, 129, 130]. As shown in figures 4.4 (a), (b) and (e) the real part of the wavevector becomes different from zero for large- ω , exhibiting two symmetrical branches with respect to zero, when the imaginary part becomes independent from ω . Since the imaginary part is strictly connected to the intrinsic properties of the passive material, it always remains different from zero and positive. For small frequencies, $Im[k_{eff}[\omega, L]]$ symmetrically splits with respect to its large- ω value. The positiveness of the imaginary part, simply indicates that the Bogoliubov waves oscillating on top of the fluid of light, are exponentially damped by the losses, at any ω according to $e^{-Im[k_{eff}[\omega, L]]L}$. Moreover, the horizontal symmetry of the curves, refers directly to the \pm sign of the equation 4.46, in particular the upper (lower) part refers to the positive + (negative -) branch of the Bogoliubov dispersion. There is a quantitative difference between figure 4.4 (b) and (d). Precisely, the behaviour at low- ω is different in the two plots. From the equations 4.46, and 4.48, we get, in the second order of the limit

4. Nonlinear response: the Bogoliubov like dispersion and the Thermo Optic Coefficient

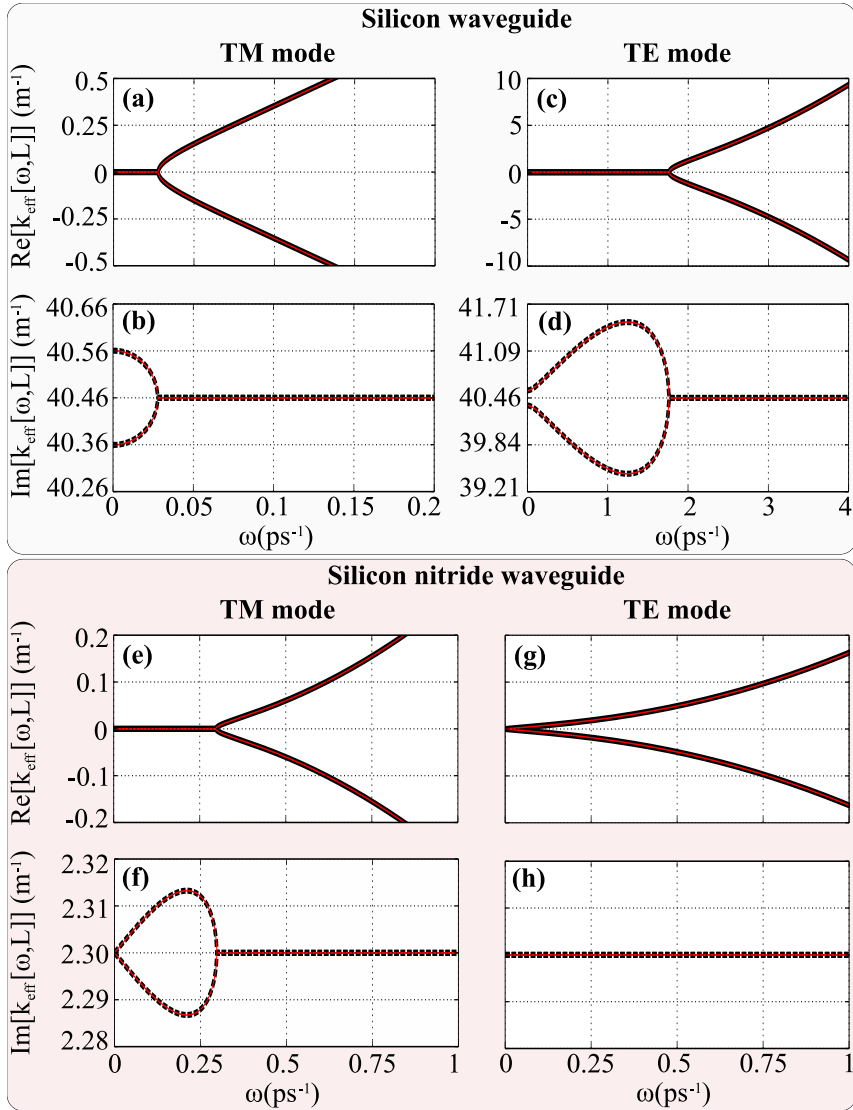


Figure 4.4: Real and imaginary part of the Bogoliubov dispersion relation for the two cases: 2 cm-long *Si* and 20 cm-long *Si₃N₄* waveguide. The black solid (dashed) lines show the real (imaginary) part obtained from the numerical diagonalization of $K_{\text{eff}}[\omega, L]$. The red curves show the adiabatic predictions. Panels (a), (b), (e) and (f) ((c), (d), (g) and (h)) represent the TM (TE) modes. The curves are obtained considering the parameters of table 4.1, with an input power of 100 mW. These images are taken from [27].

in which ω tends to zero ($\omega \rightarrow 0$), the following expression:

$$Im[k_{eff}[\omega \rightarrow 0, L]] \approx Im[k_{eff}[\omega, L]] \quad (4.49)$$

$$\mp sign[\beta_2] \frac{|\beta_2| \gamma}{\alpha_2} \omega^2, \quad (4.50)$$

where \mp refers to the \pm branch of the bogoliubov dispersion. In the case of TM mode of figure 4.4 (b), the β_2 is positive. As a result, $sign[\beta_2] = 1$ and then the imaginary part of the + (–) branch of the dispersion approaches quadratically its value at $\omega = 0$ from below (above). In the TE case of figure 4.4 (d), the group velocity dispersion is negative. Consequently, $sign[\beta_2] = -1$ and therefore the imaginary part shows an opposite trend. In addition, there is another quantitatively different trend between panel (f) and panels (b) and (d). Precisely, at $\omega = 0$, in figure 4.4 (f), the value of the imaginary part equals that of the large- ω , while in figures 4.4 (b) and (d) it does not. This different behavior is originated by the presence of the nonlinear TPA losses (α_2), which are negligible in Si_3N_4 but strongly present in Si . From equations 4.46 and 4.48 we find:

$$Im[k_{eff}[\omega = 0, L]] = Im[k_{eff}[|\omega| \rightarrow \infty, L]] \quad (4.51)$$

$$\pm \frac{\alpha_2}{2} \langle \rho_0[z] \rangle_L. \quad (4.52)$$

This relation verifies what has been stated above, in fact the two imaginary parts at $\omega = 0$ and $\omega \rightarrow \infty$ are equal when $\alpha_2 = 0$. Although Si has a higher nonlinear coefficient and a lower effective area with respect to Si_3N_4 , the higher linear losses combined with the presence of the nonlinear TPA process make the use of silicon prohibitive for the measurement of the sound-like dispersion at a wavelength of $1.55 \mu m$. This result, combined with an easier theoretical derivation, led us to neglect the nonlinear losses closely related to TPA, namely the FCA.

The Bogoliubov dispersion relation of figure 4.4 (g) (h) shows the case of Si_3N_4 for the TE mode. Here, the real part of the wavevector (panel (g)) looks like the stable result displayed in figure 4.3 (a). This spectrum, can be studied from a quantitative point of view, considering the equation 4.46 and the adiabatic identification 4.48 in the approximation where $\alpha_2 \rightarrow 0$. As reported in the table 4.1, the TE mode presents both γ and β_2 positive. As a result, the square root of Bogoliubov's dispersion is real for all ω and the ω -independent imaginary part of $k[\omega, z]$ is $\alpha_0/2$. Therefore, by means of the identification 4.48, the space average over the length $[0, L]$ of the first (second) row of $k[\omega, z]$ when $\alpha_2 \rightarrow 0$ corresponds to the imaginary (real) part of $k_{eff}[\omega, L]$. In particular, the imaginary part is given by:

$$Im[k_{eff}[\omega, L]] = \frac{\alpha_0}{2} \approx 2.3 m^{-1}, \quad (4.53)$$

4. Nonlinear response: the Bogoliubov like dispersion and the Thermo Optic Coefficient

while the real part is:

$$Re[k_{eff}[\omega, L]] = \pm \left\langle \sqrt{\frac{\beta_2}{2}\omega^2 \left(\frac{\beta_2}{2}\omega^2 + 2\gamma\rho_0[0]e^{-\alpha_0 z} \right)} \right\rangle_L \quad (4.54)$$

$$\approx \pm \begin{cases} \langle v^{-1}[z] \rangle_L |\omega|, & |\omega| \ll 1/\tau[L], \\ \frac{\beta_2}{2}\omega^2 + \gamma\langle\rho_0[0]e^{-\alpha_0 z}\rangle_L & |\omega| \gg 1/\tau[0], \end{cases} \quad (4.55)$$

where, we have defined the local, z -dependent, version of equation 4.33 for a $\rho_0[z]$ given by the no TPA losses limit of equation 4.21:

$$v^{-1}[z] = \sqrt{\beta_2\gamma\rho_0[0]e^{-\alpha_0 z}}, \quad (4.56)$$

$$\tau[z] = \sqrt{\frac{\beta_2}{\gamma\rho_0[0]e^{-\alpha_0 z}}} = \frac{\beta_2}{v^{-1}[z]}. \quad (4.57)$$

In this case, $1/\tau[L] \approx 0.16 \text{ ps}^{-1}$, $1/\tau[0] \approx 0.26 \text{ ps}^{-1}$,

$$\langle v^{-1}[z] \rangle_L = 2 \frac{z_{eff}[L/2]}{L} v^{-1}[0] \approx 6.25 \cdot 10^{-2} \text{ ps m}^{-1}, \quad (4.58)$$

and

$$\gamma\langle\rho_0[0]e^{-\alpha_0 z}\rangle_L = \frac{z_{eff}[L]}{L} \gamma\rho_0[0] \approx 1.32 \cdot 10^{-2} \text{ m}^{-1}, \quad (4.59)$$

where $z_{eff}[z] = (1 - e^{-\alpha_0 z})/\alpha_0 \leq z$ denotes the effective length of a portion of waveguide of length $z \in [0, L]$ [111]. Figure 4.4 (g) do not display the approximation of equation 4.55, for visibility sake.

4.3.4 Observable to measure

In the previous subsections, we have indicated the Bogoliubov's dispersion as $k[\omega]$, $\langle k[\omega, z] \rangle_z$ and $k_{eff}[\omega, z]$ in the lossless case, in adiabatic approximation and in generic evolution, respectively. It is determined by the wavevector behavior as a function of frequency. This quantity is strictly related to the phase of the components $f[\omega, z]$ of the fluctuations $\varrho[t, z]$ and $\vartheta[t, z]$ of the power and phase of the light beam in the waveguide. Thus, it is possible to extract the Bogoliubov's spectrum by the knowledge of the phase that the perturbation of the amplitude of the complex electric field accumulates during the propagation along the waveguide. This accumulated phase is measured at the waveguide output, i.e. $z = L$, as a function of the fluctuation's frequency ω . As we will see in the following, in the language of the sDFW process this quantity is nothing else than the phase of the weak-power signal (idler) beam as a function of the detuning between the frequency of the signal (idler) and the pump.

Let us define $\bar{A}[t, z]$ as the amplitude of the complex optical field in-air, i.e. $z \notin [0, L]$. It can be formulated in terms of a weakly deviation from the constant (time-independent) mean field ($\bar{A}_0[z]$) of the pump as:

$$\bar{A}[t, z] = \bar{A}_0[z] + e^{i\bar{\theta}_0[z]} \int_{-\infty}^{\infty} \bar{a}[\omega, z] e^{-i\omega t} \frac{d\omega}{2\pi}, \quad (4.60)$$

where

$$\bar{A}_0[z] = \sqrt{\bar{\rho}_0[z]} e^{i\bar{\theta}_0[z]} = \begin{cases} \sqrt{\rho_<} e^{i\theta_<}, & z < 0, \\ \sqrt{\rho_>} e^{i\theta_>}, & z > L. \end{cases} \quad (4.61)$$

The accumulated phase at the output of the waveguide is related the principal argument of the Fourier component $\bar{a}[\omega, z]$ as [27]:

$$\phi_L[\omega] = \text{Arg} \left[\frac{\bar{a}[\omega, L^+]}{\bar{a}[\omega, 0^-]} \right] + \Delta\theta \pmod{2\pi}, \quad (4.62)$$

where $\Delta\theta = \theta_> - \theta_<$, and the constants $\rho_<$ and $\theta_<$ ($\rho_>$ and $\theta_>$) correspond to the power and phase of the in-air beam of light before (after) the propagation along the nonlinear waveguide. The Bogoliubov dispersion relation enters in the equation 4.62 via the argument, therefore, through the relation linking the output Fourier component $\bar{a}[\omega, L^+]$ of the in-air perturbation $\bar{A}[t, z] - \bar{A}_0[z]$ to its input one $\bar{a}[\omega, 0^-]$. This relation may be deduced from matching the Poynting vector at the air-waveguide interfaces ($z = 0, L$). The conservation of the electromagnetic flux at the interface, within the slowly-varying-envelope approximation, reads as:

$$\bar{A}[t, 0^-] = \sqrt{n_0} A[t, 0], \quad (4.63)$$

$$\sqrt{n_0} A[t, L] e^{i\beta_0 L} = \bar{A}[t, L^+] e^{i\beta_0 L/n_0}. \quad (4.64)$$

Linearizing the Madelung representation 4.17 of the amplitude $A[t, z]$ of the complex electric field inside the waveguide ($z \in [0, L]$), according to equations 4.23 and 4.23 we obtain, using equation 4.25 and 4.26:

$$A[t, z] = A_0[z] + e^{i\theta_0[z]} \int_{-\infty}^{\infty} (a[\omega] u[\omega, z] e^{-i\omega t} + a^*[\omega] v^*[\omega, z] e^{i\omega t}) \frac{d\omega}{2\pi}. \quad (4.65)$$

Here, $u[\omega, z]$ and $v[\omega, z]$ are, within the cold atom context, the Bogoliubov quasi-particle amplitudes [103] and they are defined as [27]:

$$u[\omega, z] \pm v[\omega, z] = f_{\pm}[\omega, z]. \quad (4.66)$$

Considering this last equation, we can introduce the following normalization condition:

$$|u[\omega, z]|^2 - |v[\omega, z]|^2 = N[\omega, z], \quad (4.67)$$

where $N = \text{Re}(f_+^*[\omega, z] f_-[\omega, z])$. Finally, combining equations 4.19, 4.60, 4.61, 4.63, 4.64 and 4.67 we obtain the following identities for the power and phase:

$$\begin{aligned} \rho_< &= n_0 \rho_0[0], & \rho_> &= n_0 \rho_0[L], \\ \theta_< &= \theta_0[0], & \theta_> &= \theta_0[L] + (1 - 1/n_0) \beta_0 L, \\ \bar{a}[\omega, L^+] &= \frac{U[\omega]}{N[\omega, 0]} \bar{a}[\omega, 0^-] + \frac{V^*[\omega]}{N[\omega, 0]} \bar{a}^*[-\omega, 0^-], \end{aligned} \quad (4.68)$$

4. Nonlinear response: the Bogoliubov like dispersion and the Thermo Optic Coefficient

where we have defined:

$$U[\omega] = u[\omega, L]u^*[\omega, 0] - v^*[\omega, L]v[\omega, 0], \quad (4.69)$$

$$V[\omega] = v[\omega, L]u^*[\omega, 0] - u^*[\omega, L]v[\omega, 0]. \quad (4.70)$$

At this point, we have to fix the initial conditions of the nonlinear problem. Precisely, the input condition at $z = 0^-$ for the perturbation $\bar{A}[t, z] - \bar{A}_0[z]$ on top of $\bar{A}_0[z]$. Since we are dealing with a sDFWM process, we consider a single perturbation, oscillating at $+\omega$, injected into the waveguide, namely:

$$\bar{a}[\omega, 0^-] \neq 0 \quad \text{while} \quad \bar{a}[-\omega, 0^-] = 0. \quad (4.71)$$

This makes sense because, in our derivation, the frequencies of the signal and of the idler are defined with respect to the frequency of the pump Ω , e.g. $\omega_s = \Omega + \omega$. Therefore, using the energy conservation (see equation 4.10), we obtain that the idler has a frequency $\omega_i = \Omega - \omega$.

Lastly, making use of equation 4.68, the phase accumulated by the Bogoliubov fluctuations (see equation 4.62) reduces to:

$$\phi_L = \text{Arg}[U[\omega]] + \Delta\theta \pmod{2\pi}. \quad (4.72)$$

When $N[\omega, 0] > 0$ the last equation is strictly valid, while when $N[\omega, 0] < 0$ an extra phase shift of π appears in the $\Delta\theta$ terms.

4.3.5 Accumulated phase in lossless waveguide

In the absence of linear and nonlinear losses ($\alpha_0 = 0$ and $\alpha_2 = 0$), the non-dissipative Bogoliubov-de Gennes-type matrix of equation 4.27 makes $N = \pm 1$. Therefore, the Bogoliubov quasi-particle amplitudes obey the normalization condition $|u|^2 - |v|^2 = \pm 1$ [105], where the $+$ ($-$) sign refers to the positive (negative) branch of the Bogoliubov dispersion relation $k[\omega]$. In this scenario, treated in subsection 4.3.1, the Bogoliubov wavefunction reduces to:

$$u[\omega, z] = \tilde{u}[\omega]e^{ik[\omega]z}, \quad (4.73)$$

$$v[\omega, z] = \tilde{v}[\omega]e^{ik[\omega]z}, \quad (4.74)$$

and consequently equation 4.69 becomes:

$$U[\omega] = |\tilde{u}[\omega]|^2 e^{ik[\omega]L} - |\tilde{v}[\omega]|^2 e^{-ik^*[\omega]L}. \quad (4.75)$$

Let us consider, for the sake of simplicity, just the positive branch of the Bogoliubov's dispersion $k[\omega]$. In other words, we deal with the case where β_2 and γ have the same sign, precisely, they are both positive. Within these assumptions, the Bogoliubov weights $\tilde{u}[\omega]$ and $\tilde{v}[\omega]$ are real functions of ω and they satisfy the relation (see equation 4.30 and 4.66):

$$\tilde{u}[\omega] \pm \tilde{v}[\omega] = \left(\frac{\omega^2 \tau^2}{\omega^2 \tau^2 + 4} \right)^{\pm \frac{1}{4}} = \left(\frac{\sqrt{1 + (k[\omega]/(\gamma\rho_0))^2} - 1}{k[\omega]/(\gamma\rho)} \right)^{\pm \frac{1}{2}}, \quad (4.76)$$

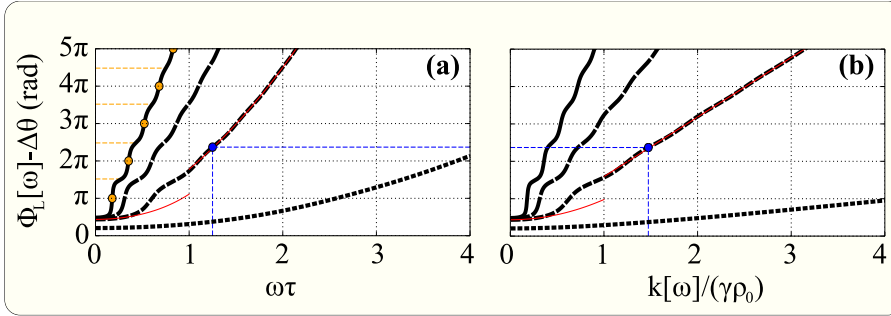


Figure 4.5: (a) and (b) Accumulated phase (ϕ_L) as a function of the frequency and of the normalized wavevector. These graphs show ϕ_L for the positive branch of the Bogoliubov fluctuations and for different values of the normalized length: $l = 0.75$ (black densely dashed curves), $l = 5$ (black dashed lines), $l = 10$ (black weakly dashed curves) and $l = 17.5$ (black solid lines). Panels (a) and (b) display the dynamically stable regime where $\beta_2, \gamma > 0$. Panel (b) allows extracting the wavenumber $k[\omega]$ of the Bogoliubov fluctuations as pictorially sketched with the blue dashed lines. The orange circular markers and the orange dashed lines, in panel (a), highlight the inflection points and plateaus given by equation 4.82 and 4.83, respectively. The red lines show the approximation (low- and large- ω .) of equations 4.77 and 4.84 for $l = 5$. These images are taken from ref. [27].

where τ is defined in equation 4.35. At this point, it is possible to obtain the accumulated phase ϕ_L using the definition of equation 4.72 and considering equations 4.75, 4.76, and the Bogoliubov dispersion's relation 4.32. In this way, we get the graphs of figure 4.5 (a) and (b) which show the behavior of $\phi_L - \Delta\theta$ as a function of the adimensional units $\omega\tau$ and $k[\omega]/(\rho_0)$, respectively.

To analyze the behavior of the accumulated phase, figure 4.5 shows several curves for different values of the l parameter, which represents the length of the waveguide in units of the “nonlinear” length ($1/(\gamma\rho_0)$). This definition takes into account two crucial parameters for measuring the sound-like regime, namely ρ_0 and L . In fact, an increase of the background power (ρ_0) increases the derivative with respect to the $k[\omega]$ wave vector in the low- ω (see equation 4.34). From the physical point of view, the increase of the power can be seen as a boost of the interaction between the different photons. While lengthening the waveguide increases the phase accumulation (i.e. $\phi_L \propto k[\omega]L$). Interestingly, in the low- ω regime ($|\omega|\tau \ll 1$), where the sonic behavior appears, the equation 4.72 can be Taylor expanded as [27]:

$$\phi_L[\omega] - \Delta\theta = 2 \arctan \left[\frac{l}{1 + \sqrt{1 + l^2}} \right] + \frac{l(3 + 2l^2)}{6(1 + l^2)} \left(\frac{k[\omega]}{\gamma\rho_0} \right)^2 + \dots \quad (4.77)$$

Considering the limit $l \ll 1$, and $l \gg 1$, this approximation can be straightfor-

4. Nonlinear response: the Bogoliubov like dispersion and the Thermo Optic Coefficient

wardly reduced to:

$$\phi_L[\omega] - \Delta\theta \approx l + \frac{l}{2} \left(\frac{k[\omega]}{\gamma\rho_0} \right)^2 + \dots \quad \text{for } l \ll 1 \quad (4.78)$$

$$\phi_L[\omega] - \Delta\theta \approx \frac{\pi}{2} + \frac{l}{3} \left(\frac{k[\omega]}{\gamma\rho_0} \right)^2 + \dots \quad \text{for } l \gg 1 \quad (4.79)$$

These approximations are the most satisfying as the second term is much smaller than the first one in each right-hand side, i.e. as $|\omega|\tau \ll 1/\sqrt{l}$. As a result, equations 4.78 and 4.79 are valid when $|\omega|\tau \ll 1 \ll 1/\sqrt{l}$ and $|\omega|\tau \ll 1/\sqrt{l} \ll 1$, respectively [27]. Most importantly, equations 4.77, 4.78 and 4.79, show that the low- ω Bogoliubov dispersion relation, i.e $k[\omega] \approx v^{-1}|\omega|$ (see equation 4.33) may be extracted from the accumulated phase $\phi_L - \Delta\theta$ by Taylor expanding the latter at least at the second order in $|\omega|\tau \ll 1$. As shown in figure 4.5, increasing the l parameter, the accumulated phase exhibits smooth staircase features. This can be explained, observing that for frequencies $\omega \geq 0$ such that:

$$\text{Arg} [U [\omega^\mp]] = \pi^\mp, \quad (4.80)$$

$$\text{Arg} [U [\omega]] = 0, \quad (4.81)$$

the graph $\phi_L - \delta\theta$ presents inflection points of values:

$$[\phi_L - \Delta\theta]_n = n\pi, \quad (4.82)$$

where $n \in \mathbb{N}$. While the accumulated phase smoothly varies between two successive inflections points as:

$$[\phi_L - \Delta\theta]_{n'} = 2n'\pi \mp 2\arctan \left[\frac{l}{1 - \sqrt{1+l^2}} \right] \approx \begin{cases} 2n'\pi \mp \pi/2 & l \gg 1, \\ 2n'\pi \mp \pi/2 & l \ll 1, \end{cases} \quad (4.83)$$

where also $n' \in \mathbb{N}$. In Figure 4.5, the orange circular markers and the orange dashed lines highlight the inflection points and the plateaus of equation 4.82 and 4.83, respectively. When $l \gg 1$, the inflection points of equation 4.82 are very distinct with respect to the points of equation 4.83 (plateau). In this way, as shown in figure, for $l = 17.5$ the phase assumes the staircase structure. On the contrary, when $l \ll 1$, the values of the inflection points (equation 4.82) and those of equation 4.83, almost coincide, i.e. $[\phi_L - \Delta\theta]_{n'} - [\phi_L - \Delta\theta]_n \rightarrow 0$. In fact, the staircase structures disappear, as shown in figure 4.5 by the $l = 0.75$ curves.

Let us consider now the particle-like behaviour, which occurs in the limit of $|\omega|\tau \gg 1$. We have seen that in this case, the Bogoliubov dispersion relation reduces to equation 4.33, i.e. $k[\omega]/(\gamma\rho) \approx |\beta_2|/(2\gamma\rho_0)\omega^2 + 1 = \omega^2\tau^2/2 + 1$. From equation 4.76, we have the zeroth-order approximations $\tilde{u}[\omega] \approx 1$ and $\tilde{v}[\omega] \approx 0$, which lead to the following relation:

$$\phi_L - \Delta\theta \approx k[\omega]L = \frac{k[\omega]}{\gamma\rho_0} l. \quad (4.84)$$

This last approximation, is strictly valid when the right-hand side is large, i.e. $|\omega|\tau \gg 1/\sqrt{l}$. From equation 4.84 is straightforward to extract the Bogoliubov dispersion relation for large- ω . As shown in figure 4.5, in this limit, the dispersion is mostly particelike and the plateau features are negligible. It is worth noticing that at low- ω , the plateaus are very pronounced, but when the plateau structure is smoothened out, the shape of ϕ_L recovers the Bogoliubov dispersion $k[\omega]$ for almost all the frequencies, except those close to $\omega = 0$, where the first plateau remains. This is highlighted by the red curves of figure 4.5. They are obtained for $l = 5$ in the case of low- ω and large- ω by using equation 4.83 and 4.84, respectively.

4.3.6 Accumulated phase in lossy waveguide

In the realistic case with negligible linear and nonlinear losses ($\alpha_0 \neq 0$ and $\alpha_2 \neq 0$), studied in the subsection 4.3.3, the Bogoliubov wavefunctions read:

$$u[\omega, z] = \tilde{u}[\omega, z]e^{ik_{eff}[\omega, z]z}, \quad (4.85)$$

$$v[\omega, z] = \tilde{v}[\omega, z]e^{ik_{eff}[\omega, z]z}. \quad (4.86)$$

Consequently, the equation 4.69 reduces to:

$$U[\omega] = \tilde{u}[\omega, L]\tilde{u}^*[\omega, 0]e^{ik_{eff}[\omega, L]L} - \tilde{v}^*[\omega, L]\tilde{v}[\omega, 0]e^{-ik_{eff}^*[\omega, L]L}. \quad (4.87)$$

In the previous subsection 4.3.3, we have seen that for Si_3N_4 , the TE mode has an interesting low frequency phonon-like behavior. Let us consider this scenario, recalling that β_2 and γ are both positive. For simplicity we focus our study on the positive branch (+) of the Bogoliubov's dispersion law ($k_{eff}[\omega, z]$). Since the adiabatic approximation reproduces the trend of the exact solution (see subsection 4.3.3), also in this section we identify $k_{eff}[\omega, z]$ with $\langle k[\omega, z] \rangle$. In this case, $Re[k_{eff}[\omega, z]]$ is positive and \tilde{u} and \tilde{v} are real quantities which satisfy the following relation:

$$\tilde{u}[\omega, z] \pm \tilde{v}[\omega, z] = \sqrt{N[\omega, z]} \left(\frac{\omega^2 \tau[z]^2}{\omega^2 \tau[z]^2 + 4} \right)^{\pm \frac{1}{4}}, \quad (4.88)$$

where the local time parameter $\tau[z]$ is defined in the equation 4.57 and $N[\omega, z]$ is positive. Figure 4.6 shows the plot of the accumulated phase $\phi_L[\omega] - \Delta\theta$ obtained using equation 4.53, 4.54, 4.72, 4.87 and 4.88. In particular, panel (a) ((b)) displays the accumulated phase as a function of ω ($Re[k_{eff}[\omega, L]]$). Contrary to the graph shown in figure 4.5 for the lossless case, here, figure 4.6 does not show a staircase structure. This can be explained by the fact that the normalized length l is very small. In fact, as we will estimate in the following, it is of the order of 10^{-3} .

In the low- ω region, i.e. $|\omega| \ll 1/\tau[L] \approx 0.16 ps^{-1}$, $Re[k_{eff}[\omega, L]] \ll 1.10 \cdot 10^{-2} m^{-1}$ is sound-like and it can be approximated by the first row of equation

4. Nonlinear response: the Bogoliubov like dispersion and the Thermo Optic Coefficient

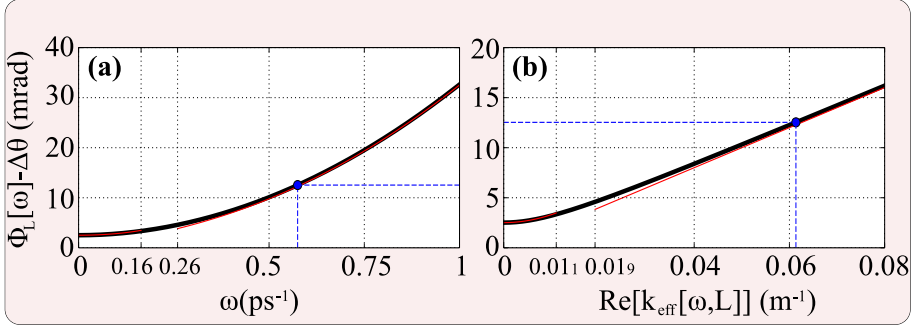


Figure 4.6: (a) and (b) Accumulated phase as a function of the frequency ω and the real part of the effective wavenumber $Re[k_{eff}[\omega, L]]$. These graphs show the phase for the TE mode in a 20 cm-long waveguide with a Si_3N_4 core and characteristic parameters given in table 4.1. The incident power is set at 100 mW as in figure 4.4. The red curves display the $|\omega| \ll 1/\tau[L] \approx 0.16$ ps $^{-1}$ and $|\omega| \gg 1/\tau[0] \approx 0.26$ ps $^{-1}$ approximations of equation 4.90 and 4.93. Precisely, $Re[k_{eff}[\omega, L]] \ll 1.10 \cdot 10^{-2}$ m is approximately phonon-like and $Re[k_{eff}[\omega, L]] \gg 1.92 \cdot 10^{-2}$, m $^{-1}$ is asymptotically particle-like, given by the first and second row of equation 4.55. The blue dashed lines and the blue points allow comparing the two figures. These graphs are taken from ref. [27].

4.55. Here, the accumulated phase obeys a Taylor expansion similar to equation 4.77:

$$\begin{aligned} \phi_L[\omega] - \Delta\theta &= 2 \arctan \left[\frac{l}{1 + \sqrt{1 + l^2}} \right] \\ &+ \frac{l(3 + 2l^2)}{6(1 + l^2)} \left(\frac{Re[k_{eff}[\omega, L]]}{\zeta[\alpha_0] \gamma \langle \rho_0[0] e^{-\alpha_0 z} \rangle_L} \right)^2 + \dots \end{aligned} \quad (4.89)$$

$$\approx 2.51 \cdot 10^{-3} + 7.951 Re^2[k_{eff}[\omega, L]] + \dots \quad (4.90)$$

where, we have defined the parameter ζ and the normalized length l as:

$$\zeta[\alpha_0] = \frac{1}{\cosh^2[\alpha_0 L/4]} \approx 0.95, \quad (4.91)$$

$$l = \zeta[\alpha_0] \gamma \langle \rho_0[0] e^{-\alpha_0 z} \rangle_L L \approx 2.51 \cdot 10^{-3}, \quad (4.92)$$

while $Re[k_{eff}[\omega, L]]$ is expressed in m $^{-1}$. The ζ parameter is equal to 1 when $\alpha_0 = 0$ and the expansion 4.89 reduces to that of the lossless case (equation 4.77). The red lines, in figure 4.6 at low- ω , show the approximation given by equation 4.90.

For large- ω , i.e. $|\omega| \gg 1/\tau[0] \approx 0.26$ ps $^{-1}$, the regime where $Re[k_{eff}[\omega, L]] \gg 1.92 \cdot 10^{-2}$ m $^{-1}$ is particle-like and it can be approximately given by the second row of equation 4.54. In this case, in analogy to the lossless case of subsection 4.3.3),

we have $\tilde{v}[\omega, z] \approx 0$ and $\tilde{u}[\omega, z] \approx \sqrt{N[\omega, z]}$. Consequently, the accumulated phase reduces to:

$$\phi_L[\omega] - \Delta\theta \approx \text{Re}[k_{eff}[\omega, L]]L = 0.20 \text{Re}[k_{eff}[\omega, L]], \quad (4.93)$$

where $\text{Re}[k_{eff}[\omega, L]]$ is expressed in m^{-1} too. Figure 4.6 displays, through the red lines, the asymptotic behavior predicted by equation 4.93 at large- ω .

4.3.7 Experimental extrapolation of the accumulated phase

We have seen in the previous subsections that the measurement of the Bogoliubov's dispersion relation is related to the measurement of the accumulated phase seen in equation 4.62. We are, therefore, interested in the phase acquired by the beam propagating along the nonlinear waveguide. This quantity can be measured through an interferometry experiment. Since Bogoliubov's dispersion arises from the reformulation of a sDFWM process, a pump and probe experiment is necessary. The system must be excited by a high-power pump with a frequency of Ω and a weak probe beam, which, within the sDFWM process, corresponds to the signal with a frequency of $\Omega + \Delta\omega$ (with $\Delta\omega$ greater or less than 0). As mentioned in the theoretical derivation, the peculiar Bogoliubov relation is encoded in the probe. Therefore, the interferometer must have a particular filtering system able to extrapolate the weak probe intensity from the pump power. In this way, it is possible to formulate the phase difference as:

$$\phi_L = \left[\frac{A_p[\Delta\omega, L^+]}{A_p[\Delta\omega, 0^-]} \right] \pmod{2\pi}, \quad (4.94)$$

where A_p is the probe amplitude. This notation is identical to that seen in equation 4.62 for the simple reason that the two quantities are exactly equal. Indeed, the weak-power signal on top of the strong-power pump corresponds to the weak-amplitude fluctuation superimposing upon the steady profile $\bar{A}_0[z]$ in equation 4.60 [27]. This can be proved by using the following definition in the equation 4.60:

$$\bar{a}[\omega, z] = 2\pi\delta[\omega - \Delta\omega]A_p[\omega, z]e^{-i\bar{\theta}_0[z]}, \quad (4.95)$$

$$A_p[\omega, z] = \tilde{A}_p[\omega, z]e^{i\Delta\beta_p[\omega]z}. \quad (4.96)$$

In this way, we obtain the following decomposition of the total field amplitude:

$$\bar{A}[t, z] = \bar{A}_0[z] + \tilde{A}_p[\Delta\omega, z]e^{-i\Delta\omega t}e^{i\Delta\beta_p[\Delta\omega]z} \quad (4.97)$$

in terms of a pump and a probe with frequency (wavevector) Ω and $\Omega + \Delta\omega$ (β_0/n_0 and $\beta_0 + \Delta\beta_p[\Delta\omega]$), respectively.

In the same way, the Bogoliubov wave on top of the stationary mean field $A_0[z]$ in equation 4.65 corresponds to the linear superposition of the signal and idler at frequency (wavevector) $\Omega + \Delta\omega$ and $\Omega - \Delta\omega$ ($\beta_0 + \Delta\beta_s[\Delta\omega]$ and $\beta_0 + \Delta\beta_i[\Delta\omega]$):

$$A[t, z] = A_0[z] + \tilde{A}_s[\Delta\omega, z]e^{-i\Delta\omega t}e^{i\Delta\beta_s[\Delta\omega]z} + \tilde{A}_i[\Delta\omega, z]e^{-i\Delta\omega t}e^{i\Delta\beta_i[\Delta\omega]z} \quad (4.98)$$

4. Nonlinear response: the Bogoliubov like dispersion and the Thermo Optic Coefficient

where, in this case, the signal and idler amplitudes ($\tilde{A}_s[\Delta\omega, z]$ and $\tilde{A}_i[\Delta\omega, z]$) are defined through the following relation:

$$\begin{pmatrix} a[\omega]u[\omega, z] \\ a^*[\omega]v^*[\omega, z] \end{pmatrix} = 2\pi\delta[\omega - \Delta\omega] \begin{pmatrix} A_s[\omega, z] \\ A_i[\omega, z] \end{pmatrix} e^{-i\bar{\theta}_0[z]} \quad (4.99)$$

$$A_{s,i}[\omega, z] = \tilde{A}_{s,i}[\omega, z]e^{i\Delta\beta_{s,i}[\omega]z}. \quad (4.100)$$

Summarizing, by measuring the accumulated phase of the signal within a sDFWM process, it is possible to extrapolate the Bogoliubov dispersion relation. It is worth noticing that in the pump and probe interferometry experiment we measure the phase $\phi_L[\Delta\omega]$ as a function of the detuning between the pump and signal frequency. This detuning directly corresponds to the ω frequency of Bogoliubov fluctuations from the δ peak in the definition 4.99.

To conclude, we have seen that the confinement of the light and the non-linearity of the material introduce an effective mass and interaction between photons. This allows exploiting a parallelism between boson cold atoms and photons, based, in our case, on the analogy between the impulse propagation and the Gross-Pitaevskii equation. Thanks to the space-time mapping, the phase of the stimulating signal, within a nonlinear sDFW process, can be traced back to the Bogoliubov's energy spectrum. From this point of view, we have investigated the case of Kerr-type waveguides, made of two materials Si and Si_3N_4 , in the ideal case without losses and in the real case with linear and non-linear losses. We have thus estimated the trend of the accumulated phase, strictly connecting it to the Bogoliubov spectrum. In this way, we have seen how the case of Si_3N_4 makes possible a first validation of the theory and how the massive presence of losses makes the measurement prohibitive in the case of Si . These results are based on a first estimation, and future developments plan to extend these derivations to the case of different platforms, in order to increase the variation of the observable ϕ_L . In particular, we are taking into account the possibility of exploiting waveguides formed by a material with a high nonlinear index, such as Chalcogenide [131]. In addition, we are also considering the use of silicon optical fibers. Although these present a low nonlinear index (i.e. $\approx 2.7 \cdot 10^{-20} m^2/W$), the low linear losses (i.e. $\approx 1.8 \cdot 10^{-6} dB/cm$) allow extending the length of the sample considerably and then, increasing the accumulated phase. It is worth noticing that our one-dimensional results in time domain are conceptually very general and can be extended to the generalized three-dimensional Schroedinger nonlinear equation.

4.4 Nonlinear response in a microresonator

As we have seen in the previous sections, by increasing the power of the incident beam, the relation between the polarization vector and the electric field is no longer linear. In particular, in the case of a microresonator made of an amorphous Kerr material, the electric field displays two predominant contributions: the Kerr nonlinearity and the thermo-optic effect.

For the sake of completeness, in this section, we will see how the presence of a nonlinear term modifies the stationary response of a waveguide/microresonator system. In particular, we will introduce the thermo-optic coefficient of the medium, and we will see how it gives rise to a shift in the resonance frequency. We will see how the variation of the index introduced by the thermo-optic coefficient has the same dependence on the power as in the case of the Kerr nonlinear coefficient. In addition, the high power transmission will be treated in detail, focusing on the bistable behaviour of the system.

4.4.1 Thermo-optic coefficient

The thermal effects on integrated optical circuits have been widely studied, not only because they induce unavoidable operational problems, but mainly because they allow a controlled variation of the refractive index and, therefore, the introduction of new processes. For example, in *Si* waveguides the thermo-optic effect permits to realize modulators [132], filters and switches [133]. In the case of microresonators the resonance condition is extremely sensitive to temperature variations. Therefore, a temperature dependent control of the resonance spectral position can be used to develop microresonator-based switches and routers [134]. Typically, this kind of control, so-called active, can be achieved by placing metal wires over the resonators: heating the wires by the Joule effect creates an appreciable temperature variation in the resonator. Another thermal effect originates from the absorption losses, in particular, by the photon absorption through defects, or by the nonlinear absorption such as the TPA and the consequent FCA. This is known as all-optics thermal effect and falls into the classification of nonlinear processes.

Let's start by considering the modulation of the refractive index as a consequence of the heating of a material. The temperature change of a medium leads necessarily to a variation in the real part of the refractive index:

$$n[T_1] = n[T_0] + \left. \frac{dn}{dT} \right|_{T_0} (T_1 - T_0), \quad (4.101)$$

where T_0 (T_1) is the starting (final) temperature of the material, while $\frac{dn}{dT}$ represents the thermo-optic coefficient. In the case of interference phenomena, such as the fringes produced in a waveguide by the Fabry-Perot of the facets or by the response of an interferometer, this temperature variation translates into

4. Nonlinear response: the Bogoliubov like dispersion and the Thermo Optic Coefficient

a shift of the fringes in the spectral domain:

$$\Delta\lambda = \lambda_1 - \lambda_2 = \left. \frac{d\lambda}{dn} \frac{dn}{dT} \right|_{T_0} \Delta T, \quad (4.102)$$

where $\Delta T = T_1 - T_0$. This shift is particularly evident in the case of high-Q microresonators. Indeed, the sharpness of the resonance increases the sensitivity to temperature variation. The resonance condition of the microresonators allows writing the last equation as:

$$\Delta\lambda \approx \left. \frac{\lambda_0}{n_{eff}} \frac{dn_{eff}}{dT} \right|_{T_0} \Delta T, \quad (4.103)$$

where n_{eff} is the effective index of the material and λ_0 is the wavelength of the resonance at T_0 . As we will see in chapter 5, this dependence permits to experimentally estimate the thermo-optic coefficient of *SiON*. The possibility to vary the spectral position of the resonance by means of a temperature variation, permits not just a control of the system, but also to correct afterwards possible fabrication errors.

As we have mentioned, the temperature variation can be activated by pumping the resonance with a high-power laser. In such a way, the high power stored into the resonator and the linear absorption of the material transform part of this power in heat. This results in a temperature gradient. Thus, it is possible to obtain a resonance shift induced exclusively by an optical effect. The wavelength variation can be written by considering the total absorbed power (P_{abs}):

$$\Delta\lambda \approx \left. \frac{\lambda_0}{n_{eff}} \frac{dn_{eff}}{dT} \right|_{T_0} R_{th} P_{abs}, \quad (4.104)$$

where R_{th} takes into account the thermal resistance of the material and it is measured in K/W . Thus, the temperature increase can be connected to the power lost by the resonator. As we have seen in section 3, this quantity is given by the derivative with respect to the time of the energy stored inside the resonator (see equation 3.18). In this way, we can reformulate the absorbed power as $P_{abs} = 2(\Gamma + \gamma)\xi$. Precisely, ξ is proportional to the square modulus of the amplitude field inside the resonator α , and, then, to the incident power P_{in} . Therefore, relation 4.104 can be reformulated considering the transmitted intensity 2.13 as:

$$\begin{aligned} \Delta\lambda &\approx \left. \frac{\lambda_0}{n_{eff}} \frac{dn_{eff}}{dT} \right|_{T_0} R_{th} (1 - |t|^2) P_{in} \\ &\approx \left. \frac{\lambda_0}{n_{eff}} \frac{dn_{eff}}{dT} \right|_{T_0} R_{th} \frac{4\Gamma\gamma}{\Delta\omega^2 + (\gamma + \Gamma)^2} P_{in}. \end{aligned} \quad (4.105)$$

It is worth noting that γ does not only take into account absorption losses but also those related to the bending or to the surface scattering. Typically, these

sources of losses, in standard devices, bring a negligible contribution with respect to the absorption one. However, they strongly depend on the characteristics of the system, such as the curvature radius and the index contrast between the core and the cladding. In addition this formulation of the absorbed power neglects the nonlinear terms related to TPA or FCA. Indeed, in the case of a Kerr media these terms introduce further absorption losses and can be considered as other loss rates.

At this point, it should be remarked that the refractive index variation resulting from the thermo-optic coefficient is strictly related to the intensity of the electric field. In fact, considering the definition of effective area (see equation 4.8), one can reformulate the power as $\frac{1}{2}\epsilon_0 c |E_{in}|^2$. This allows the modulation of the refractive index introduced by the thermal coefficient and the Kerr nonlinear modulation to have the same dependence on the intensity (see equation 4.4). Therefore, if these coefficients have the same sign, they give an indiscernible and inseparable contribution. However, they do have a property that distinguishes them: the response time. In fact, the thermo-optic effect has a characteristic time in the order of μs , i.e. much greater than that of TPA or Kerr which is in the order of ps [135]. Indeed, the requests of more performing optical switches has led to the exploitation of the Kerr nonlinearity [136, 137]. This different response time is the basis for the study of self-pulsing in microresonators and of stochastic signals generation [138].

4.4.2 Nonlinearity and transmission response

Let us see how the presence of the thermo-optic coefficient induces a change in the waveguide/microresonator response. In this case, we will focus on the stationary regime, considering a single mode microresonator. In addition, since the thermo-optic coefficient and the nonlinear term have the same dependence on the incident field intensity, the following results extend to the Kerr case under proper assumptions. The temporal mode equation (see relation 3.1 in chapter 3) can be extended in order to consider the nonlinear contribution. In this way, the amplitude of the resonant field assumes a temporal dependence given by:

$$\frac{d\alpha}{dt} = (i(\omega_0 - \omega_{in}) - \gamma - \Gamma) \alpha + i\sqrt{2\Gamma} E_{in} - i\gamma k |\alpha|^2 \alpha, \quad (4.106)$$

where we have added to equation 3.1 a nonlinear term proportional to the product between the intrinsic coefficient and the field intensity inside the resonator ($i\gamma k |\alpha|^2 \alpha$). Here, k is a real parameter which takes into account the strength of the thermo-optic coefficient. Moreover, this latter determines the positivity or negativity of k . As we have seen in the previous subsection, the shift induced by the thermo-optic effect is strictly connected to the absorbed power. This explains the product with γ , which in our model considers the losses of the microresonator. As mentioned, in this formulation we have considered that all the power loss is absorbed by the material. However it is possible to extend our model to a general case just using an effective \tilde{k} parameter which takes into account both contributions: the thermo-optic coefficient and the fraction of the

4. Nonlinear response: the Bogoliubov like dispersion and the Thermo Optic Coefficient

absorbed field. Since the Kerr nonlinearity depends on the field intensity inside the microresonator, equation 4.106 can be modified to consider such nonlinearity just removing the intrinsic coefficient γ . In this way, the last term of the temporal equation reduces to $i k |\alpha|^2 \alpha$.

There is no analytical solution to equation 4.106, but we can solve it numerically. Thus, once the value of α has been determined, one can formulate the transmission amplitude simply using the equation 3.2 of chapter 3 as follows:

$$t = 1 + i \frac{\sqrt{2\Gamma} \alpha}{E_{in}}. \quad (4.107)$$

In order to consider scans of the laser with different powers, let us define $\omega_{in} = (\omega_{in}^0 + v_{sc} t)$, where $v_{sc}(t)$ denotes the speed (increasing time) of the scan. Here, we consider a quasi-stationary condition assuming that the time of the scan is much greater than the characteristic time of the thermo-optic effect. Moreover, let us deal with materials which exhibit a positive thermo-optic coefficient and, therefore, a positive nonlinear coefficient ($k > 0$), e.g. *Si*, *Si₃N₄*, *SiON*. Figure 4.7 (a) shows several scans performed by increasing the wavelength (from blue to red), fixing an intrinsic and an extrinsic coefficient, and the same nonlinear term k for different incident power values. Obviously, at low power, we obtain the same symmetrical Lorentzian seen in the stationary regime in figure 2.5 of section 2.2. Increasing the power, i.e. the input field ($P_{in} \propto |E_{in}|^2$), the resonance loses its symmetry and assumes a triangular shape. This can be explained physically in the following way: as the laser incidence wavelength

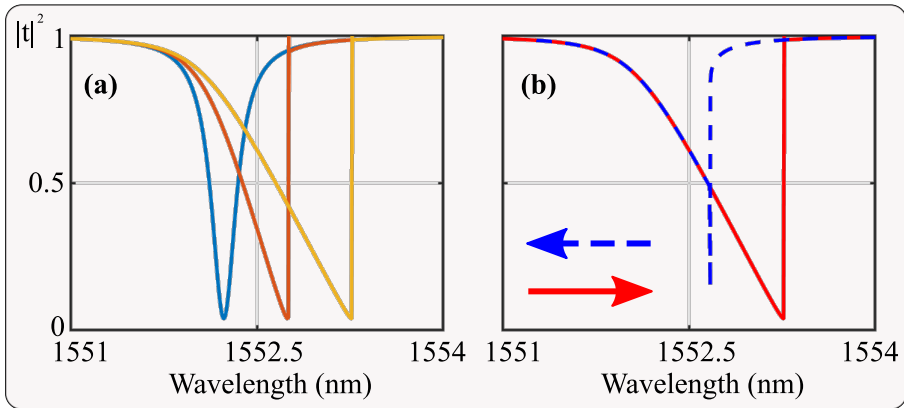


Figure 4.7: (a) and (b) Transmitted intensity as a function of the incident wavelength. Panel (a) shows three scans performed by increasing the incident wavelength with three different powers: blue ($10^{-3} a.u.$), light brown ($0.6 a.u.$) and orange ($1.2 a.u.$) line. Panel (b) displays the bistability of the system. Precisely, the red (blue) line denotes a scan increasing (decreasing) the incident wavelength. The red solid and blue dashed arrow highlight the scan direction.

approaches the resonance, the power stored inside the cavity increases and, consequently, the temperature of the material increases which, in turn, induces a resonance red shift as described by equation 4.104. In this way, as the laser wavelength increases, the transmission decreases smoother with respect to the low power case. Once the temperature increase reaches its maximum value, the resonance position of the resonator does no longer increase. Therefore, a further increase of the laser wavelength brings the laser on the low absorption side of the resonance. In this situation, the stored power decreases and, thus, also the nonlinear coefficient decreases causing a sharp blue shift of the resonance position. This induces the resonance to abruptly step back to its cold position, making the transmission sharply jump to 1. The effect of the nonlinear term can therefore be seen as a positive feedback on the stored optical power.

The triangular shape described in figure 4.7 (a) represents a first evidence of the presence of the nonlinear term. Another peculiar characteristic of the nonlinear response is the bistability [139]. Figure 4.7 (b) shows with the red solid line (blue dashed line) the scan around the resonance for a fixed power, varying the wavelength towards the red (blue). As can be seen in panel (b), depending on the scanning direction (i.e. in our case $v_{scan} < 0$ and $v_{scan} > 0$), the system displays different responses. Therefore, the transmission assumes two different values for the same wavelength. This results from the fact that the nonlinear term acts as a positive feedback for blue to red scans, while it acts as a negative feedback for an opposite scanning direction.

It is worth noticing that in the case of the thermo-optic nonlinear term ($ik\gamma|\alpha|^2\alpha$) the transmitted intensity does not change by changing the intrinsic with the extrinsic coefficient (i.e. by passing from an over- to an under-coupling regime). Figures 4.8 (a) and (b) show the transmitted response and the field intensity inside the microresonator as a function of the incident wavelength for a nonlinear term given by ($ik\gamma|\alpha|^2\alpha$). Figures 4.8 (c) and (d) display the same quantities but for a nonlinear term of the Kerr type ($ik|\alpha|^2\alpha$). In these cases, we consider a frequency scan from blue to red and we determine the over-coupling regime (red line) by exchanging the value of the extrinsic and intrinsic coefficients of the under-coupling (dashed blue line). In addition, in order to allow the comparison between panels on different rows, we set an input field to get the same intensity ($|\alpha|^2$) inside the microresonator in the under-coupling regime for the two nonlinear terms. As shown in panel (a), the over- and under-coupling regimes exhibit the same transmission response and the same wavelength shift. This is confirmed by equation 4.105, which is unaffected by changing the intrinsic with the extrinsic coefficient. On the other hand, the two intensities inside the microresonator are different (see panel (b)). Indeed, as mentioned in chapter 3, in the over-coupling case, we couple more light inside the cavity. The same transmission response is explained by the fact that in the over-coupling regime we couple more field inside the microresonator but we lose less power, while in the under-coupling regime, we couple less field but we lose more power. As a result, it is not possible to distinguish between the two regimes. On the contrary, if we consider just the Kerr nonlinear term (i.e. removing the γ coefficient from the nonlinear term namely, $ik|\alpha|^2\alpha$), the wavelength shift

4. Nonlinear response: the Bogoliubov like dispersion and the Thermo Optic Coefficient

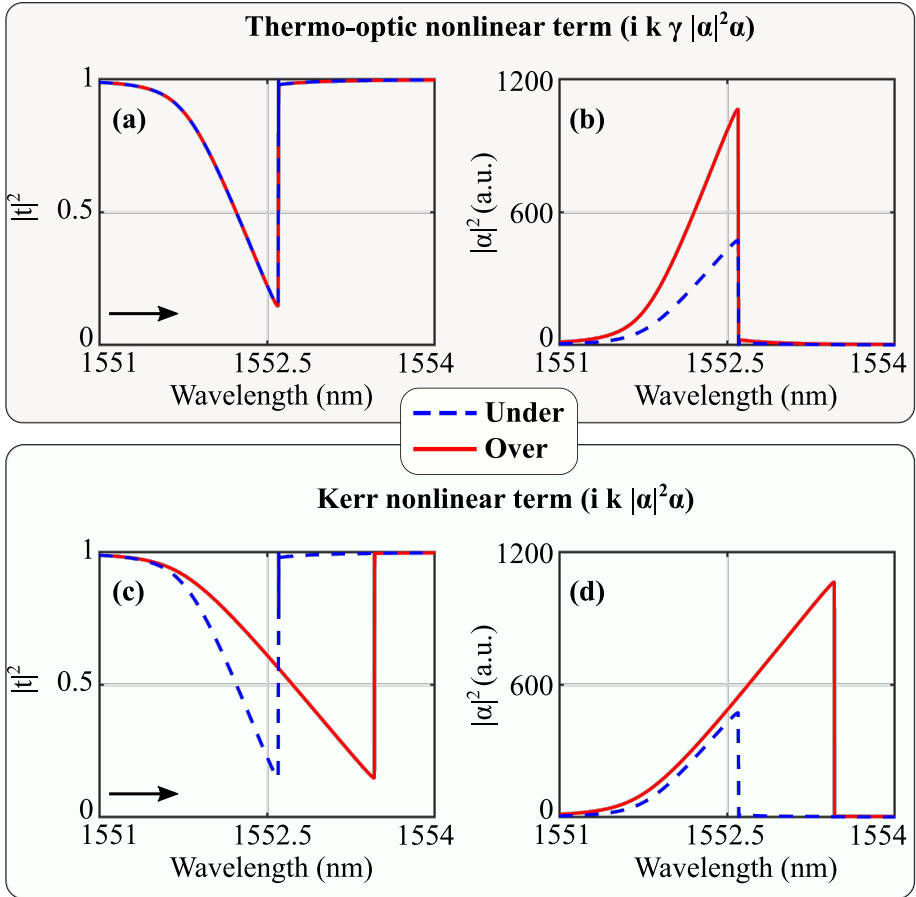


Figure 4.8: (a) and (b) Transmitted and field intensity inside the microresonator as a function of the incident wavelength for an under- (dashed blue lines) and an over-coupling (solid red lines) regime. These graphs are obtained using equations 4.106 and 4.107, considering a thermo optic nonlinear term ($i \gamma k |\alpha|^2 \alpha$). Panels (c) and (d) show the same quantities computed by using a nonlinear term of the Kerr type: $i k |\alpha|^2 \alpha$. The black arrows highlight the wavelength scan direction from blue to red.

depends just on the intensity inside the microresonator. In this way, as shown in figure 4.8 (c), the two different regimes give rise to a distinct shift and, therefore, to a different transmission response.

This dependence of the nonlinear term with respect to the power inside the resonator opens new possibilities of study on the taiji microresonator seen in chapter 2.2. In fact, the different distributions of energy among the counter-propagating modes, can be exploited in order to break the Lorentz reciprocity

theorem and, then, to induce different transmission for the two-excitation directions. From the intuitive point of view, as seen in figure 2.18, the presence of the S gives rise to a different internal energy inside the microresonator. Thus, this difference can give rise to distinct cycles of hysteresis for excitations from left to right or from right to left. The same reasoning can be applied to boost nonlinear phenomena in structures composed by two microresonators coupled with two bus waveguides in the add-drop configuration. In these systems, also called photonic molecules, the possibility to tune the coupling parameters allows defining an Hermitian and a non-Hermitian coefficient (β_{12} and β_{21}) in a deterministic way. Therefore, the energy stored in the system under a proper coupling permits to enhance nonlinear phenomena as recently demonstrated for a sFWM process in [140].

Part II

Experiments and Results

Chapter 5

Complex field characterization in integrated Hermitian and non-Hermitian optical devices

In this chapter, taking as reference the work [141], we will describe the optical setup realized to measure simultaneously the transmitted intensity and the phase of an optical signal. In the theoretical part, we have seen that the phase measurements complement the information given by the intensity measurements. In fact, the amplitude of the propagating field is fully characterized when one has the measurements of both the phase and the intensity of the electric field. In addition, we have seen that the evolution of the phase within a nonlinear optical process can be used to analyze the physics of cold atoms on optical platforms.

Interferometry is the most widely used method for extrapolating the phase of a signal. Progresses in fabrication techniques make possible to integrate different interferometers in photonics circuits. This allows a fast and simple analysis of the designed device and this does not require a special optical setup to perform the measurements. On the contrary, it requires a greater effort in the design of the optical circuit. Moreover, in a pump and probe experiment, the presence of the pump can make prohibitive the use of a simple integrated interferometer scheme to extrapolate the phase of the probe. In our case, the need to perform different measurements on different integrated systems has led to built an optical setup able to fully characterize the response of any photonics chip. This setup is based on a fully-automatized free-space Mach-Zehnder interferometer, which allows to conduct degenerate pump and probe experiments. Slightly detuned pump and probe signals can be distinguished without any optical filter thanks to a Lock-in amplifier. Such filtering technique does not depend on wavelength and it makes the setup a versatile platform for any pump and probe experiment even if the probe has the same wavelength of the pump. This is crucial in measuring the Bogoliubov's spectrum because, as we have seen in section 4, the peculiar sound-like dispersion appears at small detunings between the frequencies of the pump and the probe.

In this chapter, we will discuss also few representative experimental results. The versatility of the setup makes our Mach-Zehnder interferometer an useful tool in the characterization of integrated circuits. We will start by reporting the measurements of resonators coupled to a bus waveguide. In particular, the knowledge of both the transmission intensity and the phase allows defining the coupling regime and estimating the intrinsic (γ) and the extrinsic (Γ) coefficient. Then, we will discuss the experimental measurements of a wedge microresonator vertically coupled to a bus waveguide. Here, the surface wall-roughness gives rise

5. Complex field characterization in integrated Hermitian and non-Hermitian optical devices

to doublets in the transmission spectrum. Therefore, we will see how the use of the phasor diagram and the complex inverse, introduced in the theoretical part (see section 2.2), allows analyzing the backscattering. Finally, we will present the measurements performed on multi-modal microrisnators where the interaction between two radial families gives rise to a Fano interference. This will permit to apply complex visualization techniques and then to analyze the reactive coupling coefficient Δ .

5.1 The optical setup

In this section, we will describe the main characteristics of the Mach-Zehnder interferometer. Figures 5.1 shows the sketch of the optical setup. To simplify the description, three different parts are highlighted by colored squares and letters: the in-fiber optical preparation (a), the free space interferometer (b) and the detection (c1-c2) stages.

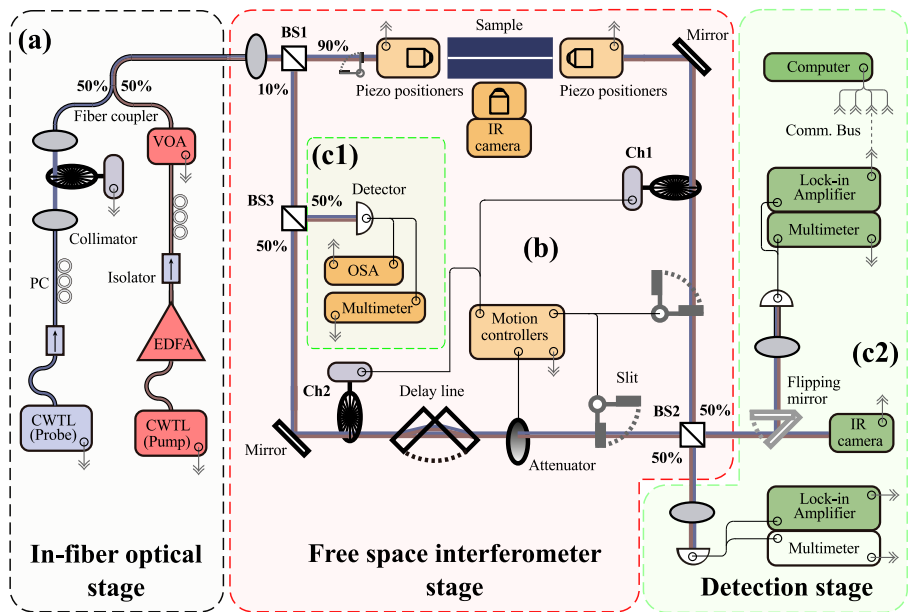


Figure 5.1: Sketch of the experimental setup: the black, red and green dashed borders (i.e. (a), (b) and (c1-c2)) highlight the in fiber optical preparation, the free space interferometer stage and the detection stage, respectively. CWTL: Continuous Wave Tunable Laser, EDFA: Erbium Doped Fiber Amplifier, VOA: Variable Optical Attenuator, PC: Polarization Controller, BS*i*: Beam Splitter *i*-th, IR: Infrared Camera, Ch1 (Ch2): Chopper Wheel of the sample (reference) arm.

5.1.1 In-fiber optical preparation stage

In this stage, the pump and probe signals are manipulated to enter into the Mach-Zehnder interferometer. Here, the light is guided by single mode fibers. Both pump and probe signals are generated by a Continuous Wave Tunable Laser (CWTL) operating in the infrared (IR) range from 1490 nm to 1610 nm , with a maximum power of about 10 mW . The pump beam is amplified by an Erbium Doped Fiber Amplifier (working wavelengths $1535\text{ nm} - 1565\text{ nm}$) resulting in a power signal spanning from 0.20 W to 5 W . Both signals pass through an isolator and a polarizer (PC). This prevents laser damage by means of backscattered pulses and allows fixing the polarization, Transverse Electric (TE) or Transverse Magnetic (TM). The versatility of the system permits to work with different probe CWTL laser also in the second telecom window at about $1.3\text{ }\mu\text{m}$. The probe is modulated in intensity through a chopper wheel. This introduces an optical amplitude modulation with a frequency from a few Hz to 1.2 kHz . As we will see in the detection stage (c2), this modulation allows using a Lock-in amplifier to acquire the signal. The pump laser passes through a Variable Optical Attenuator (VOA), provided with remote control, and, then, it is coupled to the modulated probe via an integrated 2×1 (50/50) fiber optic coupler.

5.1.2 Free space interferometer stage

The pump and probe signals coupled in fiber are guided to a collimator that represents the starting point of the interference stage. In this part, the signals are manipulated in free space through the Mach-Zehnder interferometer shown in the photograph 5.2. A 90/10 cube beam splitter (BS1 in figure 5.1 or 5.2) splits the beam into two arms. We indicate as the sample arm, the path followed by the light that reaches the device under test. While we label the other path as reference arm. The first beam splitter is not a classic 50/50 but a 90/10; this choice has been made in order to partially compensate the losses caused by the coupling with the sample. In this way, 90 percent of the signal continues and is coupled to the sample through an objective. At the output of the sample, the beam is again collected by another objective and collimated towards the first mirror. Both objectives are placed on a piezo translational stage that allows controlling the displacement in the three spatial directions (x-y-z). This is necessary in order to optimize the coupling and to control its temporal evolution. Indeed, to minimize the coupling losses, an active control of the alignment is also present: simultaneous movement of the objectives and acquisition of the transmitted probe power allow to maximize the signal output and to find the best configuration for the measurement. The characteristics of the objectives are chosen according to the input waveguide cross-section of the integrated circuit. A system consisting of an IR camera and zoom lenses allows a direct observation of the sample from the top. In this way, the scattered light allows reaching a first effective coupling of the device under test. A neutral filter controlled by a stepper motor is placed before the input objective. It enables to reduce the input

5. Complex field characterization in integrated Hermitian and non-Hermitian optical devices

power by 20 *dB* and, therefore, it makes possible to switch from high power (i.e. nonlinear regime) to low power (i.e. linear regime) without changing the settings of the source.

The light traveling in the reference arm passes through another 50/50 beam splitter cube (see BS3 in figure 5.1 or 5.2). Thus, the 50 percent of the beam travels unperturbed along the reference arm, while the remaining 50 percent passes through a power control stage (see the green dashed border (c1) in figure 5.1). We will explain this part in the following subsection. In order to balance the different intensities between the two arms, a mechanical slit is placed after the BS3. This allows obtaining a remote fine tuning of the intensity and, thus, compensating the different losses. To balance also the different optical path lengths between the two arms, it is possible to place two different types of delay line inside them. The first consists of two glasses positioned to form a V-shape. In this way, exploiting the remote control of the distance between the two glasses, it is possible to balance the different dispersions between the two arms without

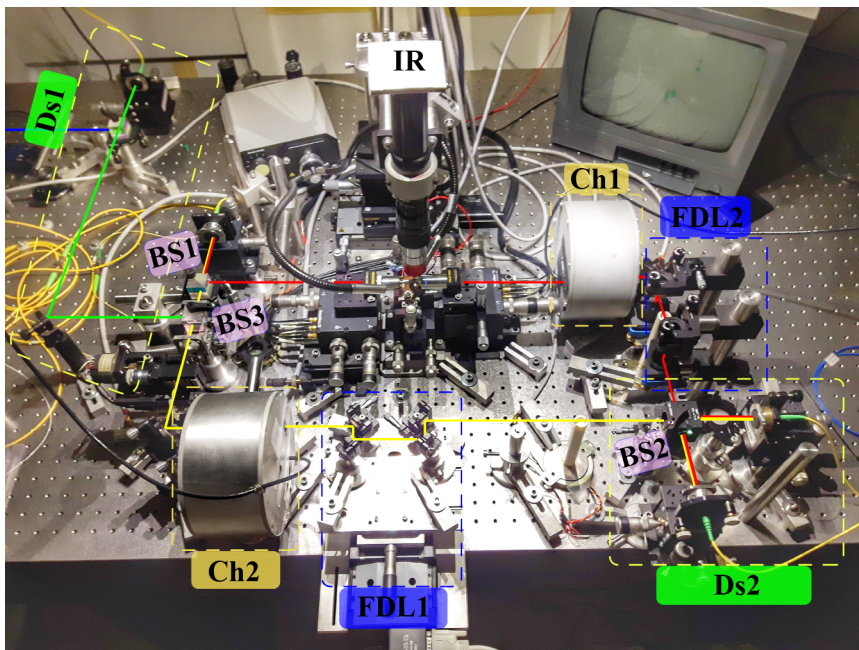


Figure 5.2: Photograph of the free space interferometer stage. Precisely, DS_{*i*}: *i*-th Detection stage, BS_{*i*}: *i*-th Beam Splitter, IR: Infrared Camera, Ch1 (Ch2): Chopper Wheel of the sample (reference) arm, FDL_{*i*}: *i*-th Free space Delay Line. The red (yellow) line is the optical path followed by the light in the sample (reference) arm. The green and blue lines display the optical path to the detection stage 1 (Ds1).

changing the line of the optical beam. The second system consists of a free space delay line composed by four mirrors placed to form a rectangle shape (see FDL1 in figure 5.2). By varying the distance between the two upper and lower mirrors, it is possible to increase or decrease the space traveled by the light. Generally, the delay perceived by the light when traveling along the sample arm depends on the wavelength due to the dispersion of the involved medium. Therefore, the same delay can be reproduced just inserting into the reference arm the same material with the same dimension. Unfortunately, this solution is not feasible. However, by combining both delay lines it is possible to obtain an excellent balance in a reasonable wavelength range in order to study the response of the device under test. For some media, the balancing of the two arms requires the installation of a delay line in both arms. Therefore, as indicated by the label FDL2 in figure 5.2, we have realized another free space delay line. This is composed by four mirrors fixed in order to increase the optical path by raising and lowering the light beam.

In addition, a chopper wheel and an open/closed shutter are placed on each arm. These allow modulating the amplitude of the laser beam and then defining the two different acquisition modes as we will see in the description of the detection stage. The chopper wheels are boxed in a cage to limit the air flow inside the arms (see Ch1-Ch2 in figure 5.2). Finally, the two beams are recombined at the last beam splitter (BS2) where the interference takes place.

5.1.3 Detection stage

The detection can be divided into two parts: a first one to control the power during the signal processing (panel (c1) (DS1 rectangle) of figure 5.1 (5.2)) and a second one (panel (c2) (DS1 rectangle) of figure 5.1 (5.2)) to acquire the final measurements.

The 50/50 beam splitter cube (BS3) placed at the beginning of the reference arm, allows guiding 50 percent of the beam in the control stage. Here, the light is collimated in a single mode fiber which makes possible to continuously measure the power and acquire a wavelength spectrum with a multimeter and an Optical Spectrum Analyzer (OSA), respectively. In this way, any power fluctuations or variations in the spectral position of the pump are monitored during the acquisition of the phase.

Once the signal from each of the two arms is recombined by the last beam splitter cube (BS2), it enters the final detection part. In this stage, the light is divided into two collection arms and is collimated in two single mode fibers. Thus, the signal intensity is acquired by means of two Germanium photodetectors. Their electrical signals are then sent to both a multimeter and a Lock-in amplifier. At this point, the *DC* signal of the pump is simply measured by the multimeter. At the same time, the modulated probe is filtered by the *DC* component thanks to the Lock-in amplifier. The analog output of the Lock-in amplifier is then sent to an oscilloscope (Picoscope) and an acquisition card (DAQ). In the collection arm, just before the collimator, a flipping mirror can send the optical signal to an IR camera (see panel (c2) of figure 5.1). This allows viewing the shape of the

5. Complex field characterization in integrated Hermitian and non-Hermitian optical devices

beams in both arms. In addition, the camera permits verifying the overlap of the beams coming from the reference and sample arm. This is necessary to optimize the interference and thus to reduce the error in the phase measurement.

5.1.4 Acquisition modes and Isolation

The optical setup can work in two different data acquisition modes, namely *normal* and *choppered*. In both modes, the detection stage provides four different intensity measurements. These are defined by the position of the mechanical shutters (chopper wheels) for the *normal* (*choppered*) configuration. In particular, we can identify the following cases:

- both arms are closed: the intensity measure of the background noise (I_B) is acquired. This measure can be disabled in the *normal* mode to increase the speed of the acquisition;
- both arms are open: the intensity measure of the interference (I) is acquired;
- the arm of the sample is open while the reference one is closed: the intensity transmitted by the sample (I_S) is measured;
- the arm of the sample is closed while the reference one is open: the intensity of the reference arm (I_0) is acquired;

From these four quantities, it is possible to obtain the phase difference accumulated by the light in the two different optical paths. In fact, the typical interference relation between two monochromatic and coherent beams is:

$$I = I_0 + I_S + 2\sqrt{I_0 I_S} \cos[\Delta\phi], \quad (5.1)$$

where $\Delta\phi$ is the phase difference between the field amplitude of the sample and the reference arm. By reformulating the previous equation, it is trivial to obtain the phase difference as a function of the three intensities:

$$\Delta\phi = \arccos\left[\frac{I - I_0 - I_S}{2\sqrt{I_0 I_S}}\right]. \quad (5.2)$$

This equation shows that an interferometer characterized by the same intensity for the two arms minimizes the experimental error on $\Delta\phi$. In addition, the accuracy of the measurement depends on the slope of the *arccosine* function. Indeed, it is possible to increase the accuracy of the data, unbalancing the optical path of the two arms to work at around $\pi/2$. On the contrary, the larger slope of the *arccosine* function at the border of its domain (i.e. -1 and 1) brings to a lower accuracy of the extracted phase values when $\Delta\phi$ is about 0 or π .

In *normal* configuration, the two chopper wheels inside the interferometer remain open and they do not play any role in the measurement. In this case, as shown in figure 5.3 (a), the four different intensities are acquired thanks to three scans of the probe repeated in the four different positions of the movable

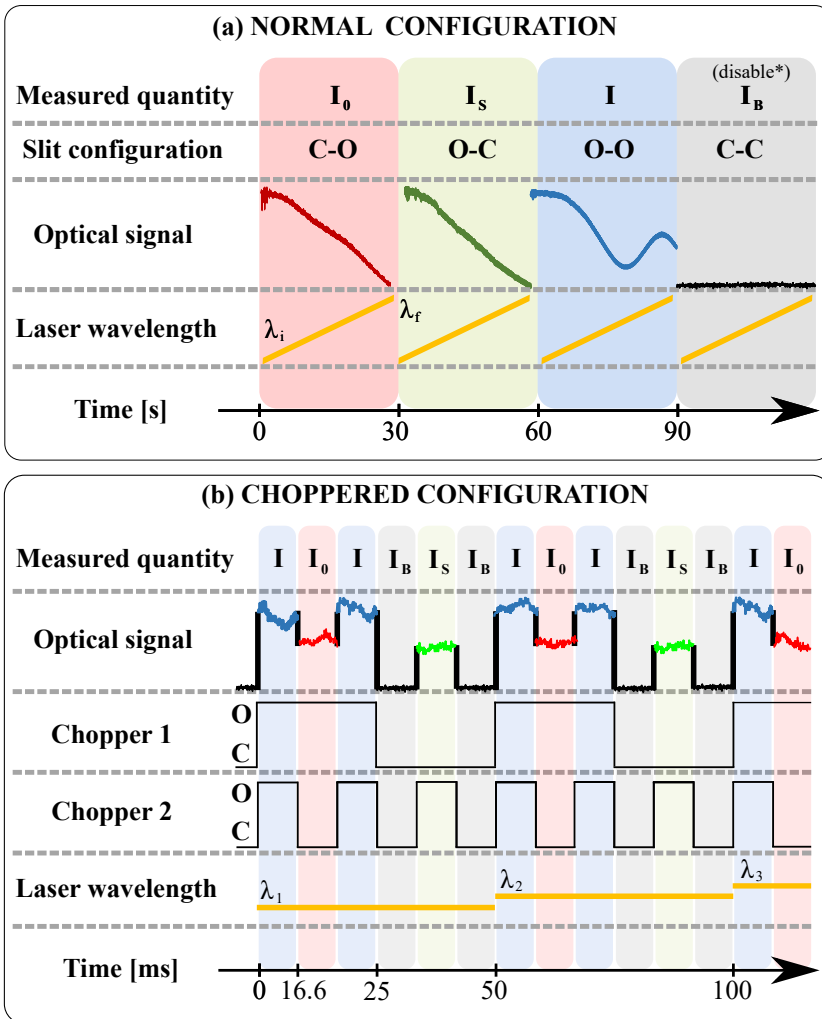


Figure 5.3: Sketch of the *normal* and *chopped* acquisition (a) and (b), respectively. In the *normal* acquisition (a) the four different intensities I_0 , I_S , I and I_B are measured along four identical scans of the laser wavelength by setting the movable shutter in the closed-open (C-O), open-closed (O-C), open-open (O-O) and closed-closed (C-C) position. In the *chopped* acquisition, the two chopper wheels provide two different intensity modulations of the reference and sample arm (Chopper 1 at 20 Hz and Chopper 2 at 60 Hz). The modulation of the optical signal so obtained contains the information of the four intensities. Thus, repeating the wavelength step scan (precisely one every period of Chopper 1) allows extrapolating the phase and the transmitted intensity spectrum.

5. Complex field characterization in integrated Hermitian and non-Hermitian optical devices

shutters (closed-open (C-O), open-closed (O-C), open-open (O-O), closed-closed (C-C)). As previously mentioned, the background noise measure can be disabled to decrease the acquisition time. In fact, typically, the closed-closed intensity measurement is performed only in the early stages of the experiment to fix the background noise.

In the *choppered* acquisition method, the two movable shutters remain in the open-open position and the two wheels are driven at multiple frequencies (see figure 5.3 (b)). The choice of the frequency of the two choppers is limited by the modulation frequency of the probe. In our case, fixing an input signal modulation of 1 kHz , we find two ideal frequency combinations: 20 Hz and 60 Hz , or 60 Hz and 180 Hz . This measurement method allows acquiring the four intensities for a given wavelength while slowly scanning the wavelength of the probe. In figure 5.3 (b) are shown the evolution of the two chopper wheels and the intensity measured as a function of time. At the end of each Chopper 1 period, the laser source changes the wavelength. Since the Chopper 2 has a frequency equal to one third of that of Chopper 1, within a Chopper 1 period, two sets of interference and background intensity data are measured, while just one set of the reference and sample intensity data is acquired.

The sample and the type of experiment determine the choice of the acquisition mode. In fact, both methods have advantages and limitations. In *normal* mode, we can quickly scan a wide range of wavelengths. Indeed, it is possible to get in less than 3 min a scan at a speed of 100 nm/s with 1 pm resolution. However, wavelength and power accuracy are not assured, as the laser response may vary within the four repeated scans. Such an effect becomes detrimental when unstable lasers are used or when sharp spectral features (i.e. narrow resonances) are studied because they are highly influenced by wavelength variations. In these cases, the measurement in the *choppered* mode is a better procedure. In fact, the quasi-simultaneity of the four intensities measurement is ensured within a period of the chopper ($\approx 50\text{ ms}$ ($\approx 17\text{ ms}$) in the case of 20 Hz and 60 Hz (60 Hz and 180 Hz)), increasing the accuracy in wavelength and power measurement. The quasi-simultaneity of the measurement also reduces the influence of the external environment (mainly temperature and air flux) on the acquired data. The limitation of the *choppered* method is related to the acquisition time of the full spectrum. It can be 20 times longer than the time taken to measure in *normal* mode with the same range and resolution. Typically, the *normal* acquisition mode is used to obtain a long scan. While to study small parts of the spectrum, such as resonances, we use the *choppered* acquisition.

The optical setup is enclosed in a polystyrene box as shown in figure 5.4 (a). This allows isolating the Mach-Zehnder from external noise sources, such as temperature variation or the presence of air flux. Insulation is essential in the interferometry measurement, where even small variations in room temperature lead to an appreciable variation of the phase. In addition, the chopper wheel used to modulate the intensity of the probe is placed outside the box. This minimizes the vibration noise and, therefore, decreases the error on the phase measurements.

Figure 5.4 (b) shows the phase measurement performed with the box open

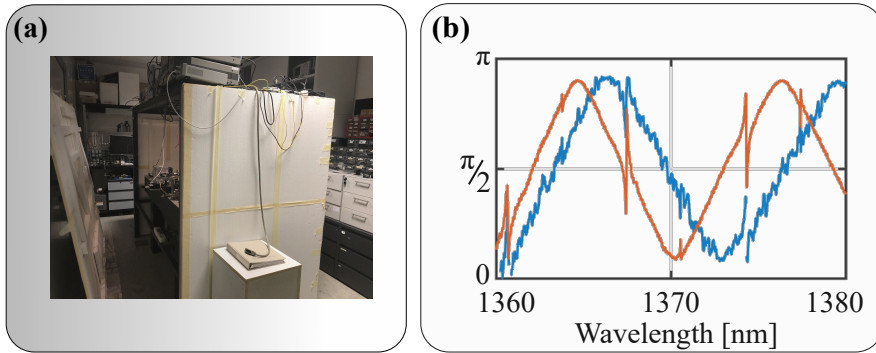


Figure 5.4: (a) Photograph of the polystyrene box that encloses the Free space Mach-Zehnder interferometer. Panel (b): phase response measured on a microring resonator. Precisely, the red and blue dots show the phase as a function of the incident frequency measured when the box is closed and open respectively. The set measured in the isolated condition exhibits less noise with respect to the open condition and thus, evidences even the presence of weak resonances at 1364 nm and 1377 nm .

(blue dots) and with the box closed (red dots). The measurement shows the phase of a microresonator coupled to a bus waveguide as a function of the wavelength. When the system is not insulated, the measurement has large fluctuations in the signal compared to the insulated scenario. This results in less visibility of the phase variation close to the resonances that characterize the transmission spectrum of the waveguide/microresonator system, particularly at 1364 nm and 1377 nm . Around these wavelengths, the phase shows the peculiar response of a resonator coupled to a waveguide in the under-coupling regime, seen in section 2.2. Comparing the two sets of data, it is evident that the acquisition with the box open does not allow appreciating the real phase jump of the resonance. The oscillation that presents a longer period is related to the dispersion of the sample material (i.e. silicon oxy nitride $SiON$). While the shift in wavelength between the two curves is given by the different temperature and air condition before and after the opening of the insulated box.

It is possible to perform the measurements keeping the optical system physically insulated thanks to the remote control of the essential components of the setup. In fact, a Lab View code allows acquiring the data automatically introducing different control processes during the measurement, such as the self-alignment with the sample, the movement of the shutters, the balance of the optical path and intensity between the two arms, etc. Figure 5.5 shows a screen shot of the front page of the Labview control program. Precisely (a) shows the setting parameters, while (b) shows the graphs of the measured intensities in the *normal* mode. This computer driven measurement allows an exact and repeatable experimental parameter selection, providing stable operating conditions.

5. Complex field characterization in integrated Hermitian and non-Hermitian optical devices

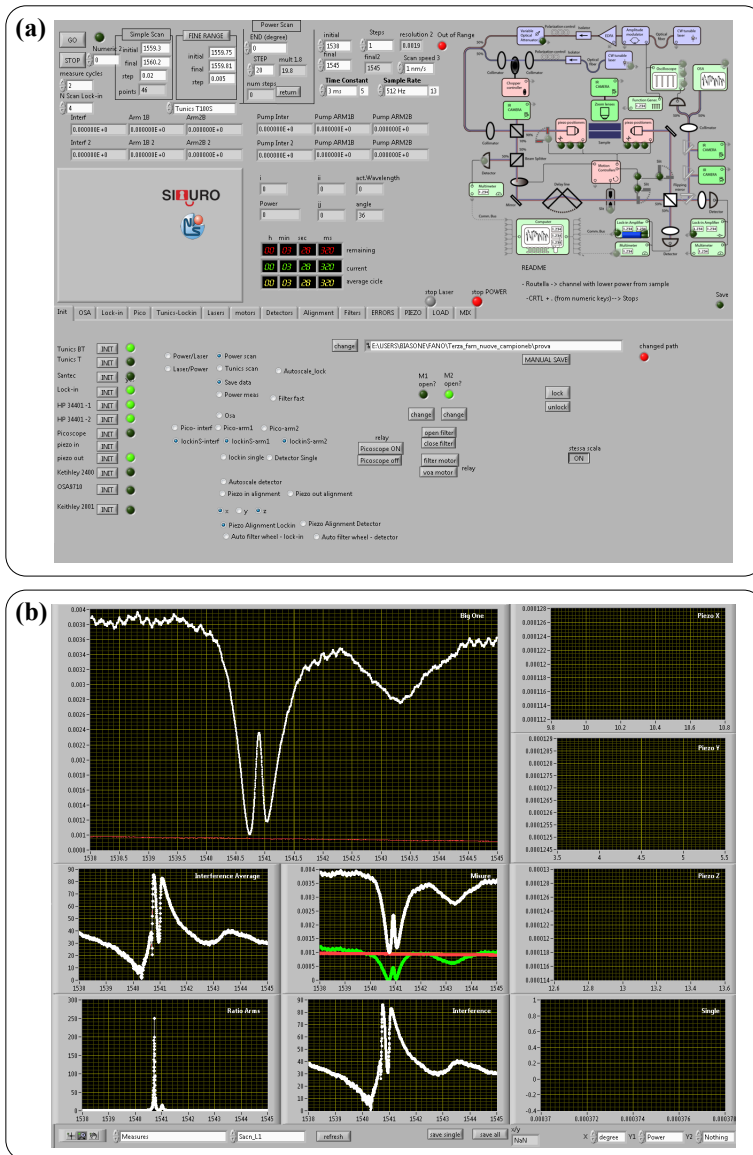


Figure 5.5: Front panel of the Labview code built to control the phase measurements. Panel (a) shows the main page where the fundamental parameters are set and the measured cycle is designed. Panel (b) displays the page where the measurements from the *normal* acquisition are monitored in real time (after each scan).

5.1.5 Characterization of the optical setup

We test the interferometer on different integrated devices under distinct power regimes [141]. In particular, considering only the probe laser, we first measure the response of a Silicon OxyNitride (SiON) waveguide which exhibits a cross section of $2.5 \mu\text{m} \times 250 \text{nm}$ and a length of 6mm . More details on the sample fabrication are reported in [142]. Using a low power probe of 5mW , the three different intensities are acquired by varying the wavelength in a range ranging from 1510nm to 1580nm . Figure 5.6 (a) shows the experimental measurements of the intensities of: the reference arm (I_0), the sample arm (I_S) and the interference (I). The slow variation of the three signals and the long wavelength range justify the use of the *normal* acquisition mode. Indeed, no fast features have to be detected. The phase difference is straightforward reconstructed through equation 5.2, and it is plotted in figure 5.6 (b). Accordingly with the *arccos* function it oscillates between 0 and π . It is worth noticing that the estimated phase does not touch the two limits because the two beams are not perfectly overlapped on the last beam splitter. The blue line of figure 5.6 (b) shows the fit by using a simple analytical model reported in appendix A. This simulates the real Mach-Zhender interferometer taking into account the different dispersion relations of the elements which compose the optical setup (i.e. the lens of the objectives, the glass of the delay line and the beam splitters) and the material of the sample under test (i.e. *SiON*). The slightly deviation between the fit and

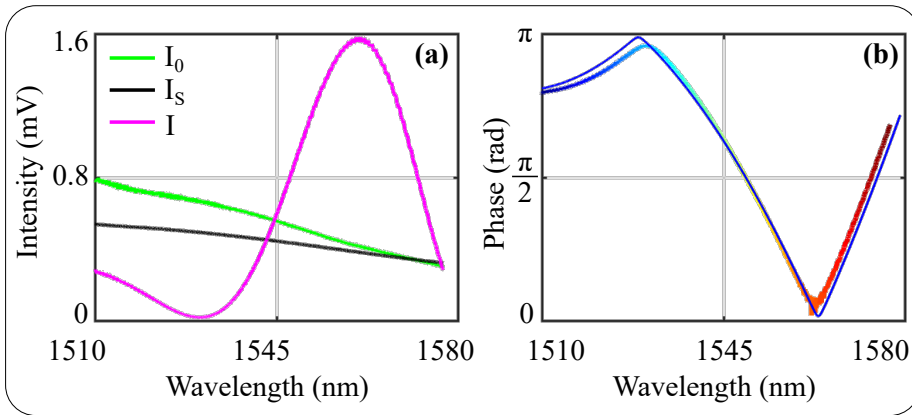


Figure 5.6: (a) Experimental intensity measured in the *normal* acquisition mode for the three different configurations of the mechanical shutters: C-O (I_0), O-C (I_S) and O-O (I). This graph is obtained using only the probe laser and varying the wavelength between 1510nm and 1580nm at 1nm/s . Panel (b) shows the phase as a function of the wavelength computed from the intensities of panel (a) by using the equation 5.2. The blue line is the fit with the simple analytical model reported in appendix A.

5. Complex field characterization in integrated Hermitian and non-Hermitian optical devices

the experimental data is mainly due to the inexact estimation of the dispersion and thickness of the glass composing the delay line.

Moreover the *choppered* acquisition method is tested, measuring the response of optical resonators. The phase computed by means of classical characterization models allows verifying the accuracy of the measurements as we will see in detail in the following sections. In addition, we have performed pump and probe experiments that demonstrate the ability of the setup to filter the probe from the pump, by verifying the possibility of filtering the probe even when it has the same wavelength of the pump. The *SiON* waveguide is analyzed in the high power regime. Using the *normal* acquisition mode the probe is scanned, as before, in the wavelength range of $(1510 - 1570) \text{ nm}$, fixing a pump laser at a wavelength of 1550 nm . Figure 5.7 (a), (b) and (c) shows the three intensities measurements of the probe as a function of the wavelength for different values of the pump power. This latter is obtained by fixing the EDFA output power at 2 W and tuning it by the remote VOA until 0 W . Figure 5.7 (d) shows the output power as a function of the input one. Precisely, it is measured at the output of the last beam splitter (BS2), while the input power is acquired at the detection stage (c1). The difference of the value between the EDFA and the input power of figure 5.7 (d) is justified by the propagation losses through the path to reach the detection stage (23 dB). Figure 5.7 (e) shows the phase computed through the three intensities of panels (a), (b) and (c) by using equation 5.2. The color code allows relating the different graphs. The different curves of the phase in panel (e) display a regular trend also around the wavelength of the pump laser. Indeed, around 1550 nm no signature of the pump appears (see magenta vertical dashed lines in figures 5.7 (a),(b),(c) and (e)). This means that the filtering system based on the Lock-in amplifier works even at high pump powers (in our case, 2 W at the EDFA correspond to 200 mW at the sample stage [141]). This paves the way for the study of what we have seen in chapter 4, namely the phase evolution of the probe within a DFWM experiment in the peculiar sound-like dispersion. On the other hand the shift between the phase curves at different pump powers suggests that a power dependent phenomenon is occurring. By looking at the three intensities of panels (a), (b) and (c) this variation can not be related to an instability of the system. In fact, both the intensities of the reference and sample arms are barely influenced by the increasing of the pump power. On the contrary, the intensity of the interference shows a noticeable power dependence. This is due to the variation of the effective index by means of the thermo-optic effect [141]. Also in this case the experimental phases at the *arccos* domain limits do not reach 0 and π for the same alignment reason as explained before. In addition, as mentioned in the acquisition subsection, the noise of the phase at the two theoretical limits is due to the high sensitivity of the *arccos* function to small perturbations, which causes a decrease of the accuracy of the phase value.

Finally, time stability tests of the phase measurement have been performed. The acquisition mode is set, and the output phase of *SiON* waveguide is measured. In low power conditions, a phase drift of about 0.25 degree/min is observed and an average noise of about 1 degree is estimated. Nonetheless, most of the

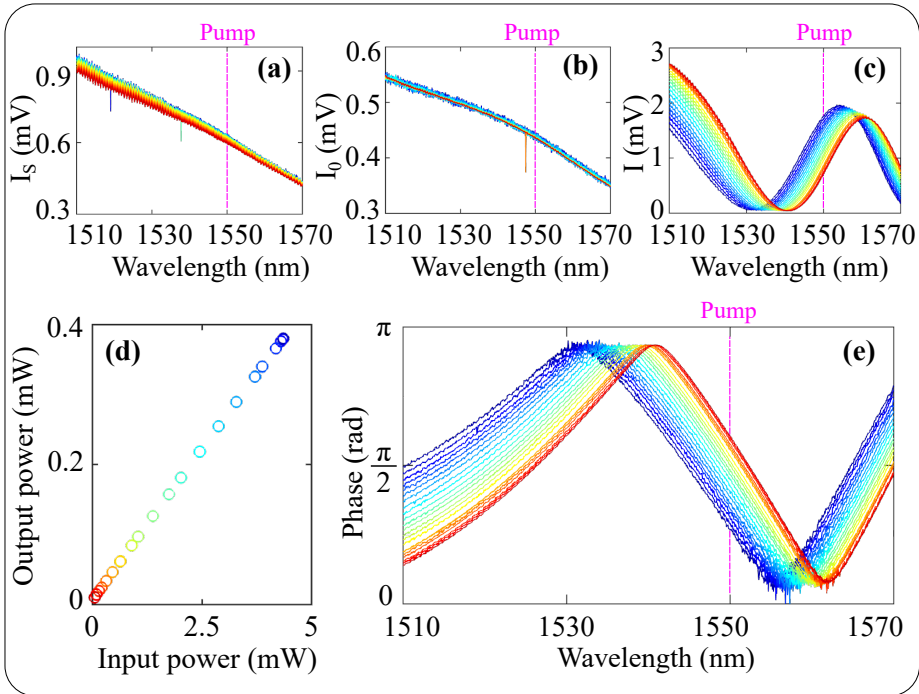


Figure 5.7: (a), (b) and (c) Experimental measurements of the intensity as a function of the probe wavelength for the three configurations of the mechanical shutters: O-C (I_s), C-O (I_0) and O-O (I) respectively. These are measured in the pump and probe configuration using the *normal* acquisition mode. Panel (d) shows the output power as a function of the input one. Panel (e) displays the phase as a function of the wavelength computed using equation 5.2. In panels (a), (b), (c) and (e), the magenta dashed vertical lines highlight the wavelength of the pump laser. The rainbow color code allows comparing the different graphs.

measurements require less than 5 minutes to be carried out, with related phase drift of about 1 degree . Conversely, the average noise shows remarkably low values, even when compared to other systems equipped with stabilizing reference laser [143]. Time stability has been tested even in the presence of the pump laser. Also in this case, the resolution of about 1 degree is observed along the whole measurement and a constant average drift of about $1\text{ degree}/\text{min}$ is extrapolated. Here, the most marked drift is due to the thermal response of the sample when a high power beam is injected. Indeed, a lengthening of the waveguide due to thermal expansion of about 0.3% per hour is sufficient to explain such a large drift [141]. The installation of the air delay line, introduced after the work in ref. [141], and the application of a more rigorous insulation of the setup allows reducing the average noise to about 0.5 degree .

5.2 Characterization of the *SiON* platform

In this section, taking as reference the work ref. [144], we will deal with the characterization of integrated waveguides in *SiON* and, specifically, with the measurement of the thermo-optic coefficient and of the nonlinear refractive index n_2 . Such characterization not only represents a test of the optical setup, but also allows fixing the parameters related to the on-chip *SiON* platform. As we will see in the following, the *SiON* platform has been used to obtain the bus guides of the resonator studied in the case of backscattering and interaction between two co-propagating modes. In addition, the taiji resonator is also made with integrated waveguide based on the *SiON*. The knowledge of the nonlinear refractive index also permits to verify if this material can be used to investigate the Bogoliubov spectrum of a quantum fluid of light.

The Silicon photonics is one of the most promising technological platform for development of chip-scale densely integrated devices [116, 145, 146]. However, in the case of pure Silicon (*Si*) the presence of TPA and, consequently, of free-carriers issue at telecom windows, as well as the band-to-band absorption below a wavelength $\approx 1 \mu m$, limits the use of Silicon in many applications [147, 148]. An example is the dispersion spectrum of the luminous fluid oscillation seen in chapter 4, where with a silicon platform, the presence of nonlinear TPA losses suppresses the sound-like dispersion. The demand for transparent Si-based circuits has led to study alternative platforms such as silicon Nitride (Si_3N_4), doped silica oxides or oxynitrides [149, 150, 151]. The *SiON* has found interest in the scientific community because of the relatively high index contrast and broadband transparency. In addition, the lack of two-photon absorption and, then, of the free-carrier losses at telecom wavelength and the ability to fabricate waveguides with low linear losses make the *SiON* an ideal platform for on chip nonlinear optics and for the realization of integrated quantum lightwave circuits [144].

5.2.1 Samples and Experimental setups

The sample studied is a racetrack resonator integrated in the All-Pass configuration. A racetrack resonator is characterized by a straight part which is used to lengthen the coupling section with the bus waveguide. Figure 5.8 (a) shows the sketch of the device. It has a radius of curvature R of $50 \mu m$ and a cross section of $1.2 \times 0.55 \mu m^2$ (see figure 5.8 (b)). The cross section makes the waveguides single mode at wavelengths around $1550 nm$ for both TE and TM polarizations. The coupling is achieved by fixing the gap between the waveguide and the resonator at $g = 1.05 \mu m$, and setting the length of the straight part of the racetrack to $L = 20 \mu m$. As one can see in figure 5.8 (b), the sample is fabricated from a deposition of *SiON* on top of $5 \mu m$ of thermal Silica SiO_2 grown on a 6-inch *Si* wafer. The details of the *SiON* growth such as the mixture of silane, ammonia and nitrous gasses and the chamber temperature of the parallel-plate plasma enhanced chemical vapor deposition (PECVD), are reported in ref. [144]. As shown in figure 5.8 (b), the light is confined between a

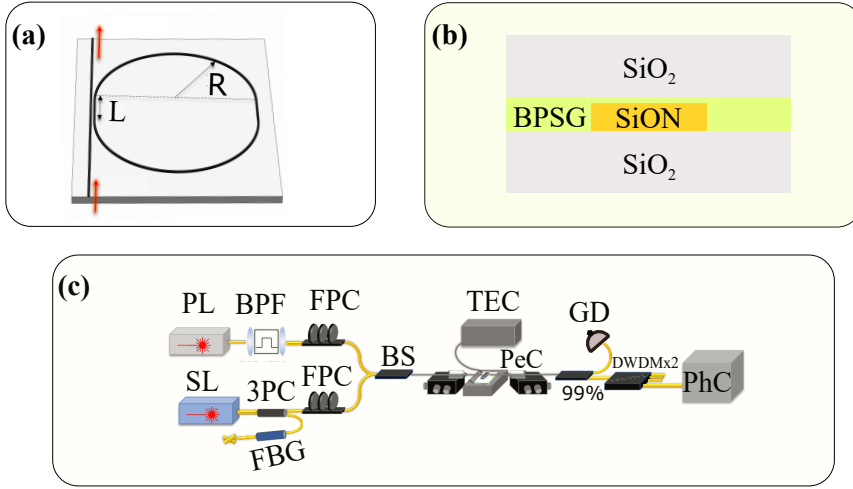


Figure 5.8: (a) Sketch of the top view of a racetrack microresonator coupled to a bus waveguide. L denotes the length of the straight part of the racetrack while R indicates the radius of curvature. Panel (b) and (c): sketch of the waveguide cross section and of the optical setup used to define the thermo-optic and n_2 coefficient. Precisely, in (c) the abbreviations have the following meanings: PL: Pump Laser, IL: Idler Laser, BPF: Band-pass Filter, FPC: Fiber Polarization Controller, 3PC: Three Port Circulator, FBG: Fiber Bragg Grating, BS: Beam-Splitter, TEC: Temperature Controller, PeC: Peltier Cell, AS: Alignment Stage, GD: Germanium Detector, DWDM: Dense Wavelength Division Multiplexing, PhC: Photon Counter.

lower thermal oxide cladding and an upper one, consisting by a double stack of 400 nm Borophosphosilicate glass (BPSG) and $2\ \mu\text{m}$ thick SiO_x .

To study this racetrack resonator three different optical setups have been used. The first one is a simple characterization, thermally controlled, setup for measuring passive waveguides. In this case, the source is a C-band tunable Continuous Wave Laser (CW). It is connected through a single mode fiber to a polarization controller, which is butt-coupled to the chip by a tapered lensed fiber. The coupling between the fiber and the sample in both excitation and collection phase is ensured by piezometric translation stages. The sample holder is composed by a Peltier cell that allows systematically heating or cooling the device under test. The transmitted intensity of the sample is then measured by means of a Germanium detector.

The second setup is the Mach-Zehnder interferometer seen in the previous section. It allows defining univocally the quality factors of the resonances. In fact, the measurement of the transmission intensity and of the phase makes possible to characterize the coupling regime. The third experimental setup, instead, is used to determine the nonlinear coefficient n_2 . It is shown in figure

5. Complex field characterization in integrated Hermitian and non-Hermitian optical devices

5.8 (c) and it allows performing an experiment of stimulate Four Wave Mixing (sFWM). This setup consists of two CW tunable sources: a pump and an idler laser. They are combined by an integrated 2×1 (50/50) fiber optic coupler and injected into the sample through the input facet. The idler signal is used to stimulate the nonlinear process. The peculiarity of this setup is the possibility to filter the background spontaneous emission to a level below -110 dB. The generated signal inside the resonator is filtered from the co-propagating pump and idler beams by using two cascaded Dense Wavelength Division Multiplexing (DWDM) modules, and directed to a photon counter (ID Quantique ID220) operating in Free Running mode, with a detection efficiency of 5% and a dead time of 40 μ s. The DWDM modules achieve a signal isolation of more than 100 dB [144].

5.2.2 Estimation of the thermo-optic coefficient

By keeping the sample at a constant temperature, the spectra of the transmitted intensities are measured by varying the incident power. The scans are performed by tuning the wavelength from blue to red (i.e. increasing the wavelength). Figure 5.9 (a) shows the transmitted intensity as a function of the incident wavelength for three different values of the power. Precisely, the blue dots indicate the cold response (i.e. low power, 0.78 mW) while the red and yellow points denote the response at 52.5 mW and 105.0 mW. Increasing the power, the resonance loses its symmetry and exhibits a triangular shape as seen in chapter 4. This response is a first evidence of a nonlinear behavior of the material. Figure 5.9 (b) shows the shift of the resonant wavelength with respect to the cold Lorentzian. As can be seen, the increase in power introduces a linear shift of the resonance towards the red (see fit in panel (b)). This is a signal that the thermo optic coefficient can be positive. However, as we have explained in chapter 4, this measure shows an overall nonlinear contribution, also linked to the nonlinear term n_2 . The contribution of the thermo-optic coefficient can be decoupled from the nonlinear Kerr effect by considering the response of the waveguide/microresonator system at low power but with different temperatures. Indeed, the thermo-optic coefficient is measured by estimating the shift of the resonance $\Delta\lambda$ as a function of the temperature variation ΔT , fixing a reference temperature of $T = 28^\circ\text{C}$. As explained in section 4, the variation of the temperature produces a change in the effective index by a quantity $\Delta n_{eff}[\Delta T]$. In this way, considering equation 4.103, we can connect the shift of the resonant wavelength with respect to the reference resonance λ_0 (at $T = 28^\circ\text{C}$) as:

$$\Delta\lambda[\Delta T] = \frac{\Delta n_{eff}[\Delta T]}{n_{eff}[\lambda_0]} \lambda_0. \quad (5.3)$$

The quantities λ_0 and $\Delta\lambda[\Delta T]$ can be extrapolated from the experimental measurements. In fact, using the optical setup of thermal characterization, it is possible to vary the temperature and trace the spectra of the resonator as a function of the wavelength. As mentioned, the different temperatures are set by an external Peltier cell placed under the sample. Figure 5.9 (c) shows the

transmitted intensity as a function of the wavelength for different values of the temperature. Here, the temperature increase causes a red-shift to the resonance dip and the Lorentzian maintains its symmetry. Figure 5.9 (d) shows that the $\Delta\lambda$ shift is, in the range of temperatures investigated, linear as a function of temperature.

On the contrary, it is more complex to accurately determine the cold effective index $n_{eff}[\lambda_0]$. This has been demonstrated in [152], where the extrapolation of n_{eff} for a resonator with a short Free-spectral range (FSR) is rather difficult. In our case, the FSR is about 3.7 nm , so the effective index is derived from FEM simulations using Comsol Multiphysics. Finite element simulations are also necessary to decouple the thermal contributions of the cladding. In fact, the guided mode also extends into the cladding of the material and therefore, the measured amount of $\Delta n_{eff}/\Delta T$ is not directly the thermal-optical coefficient of *SiON*. It contains information on thermo-optic properties of both: the core and

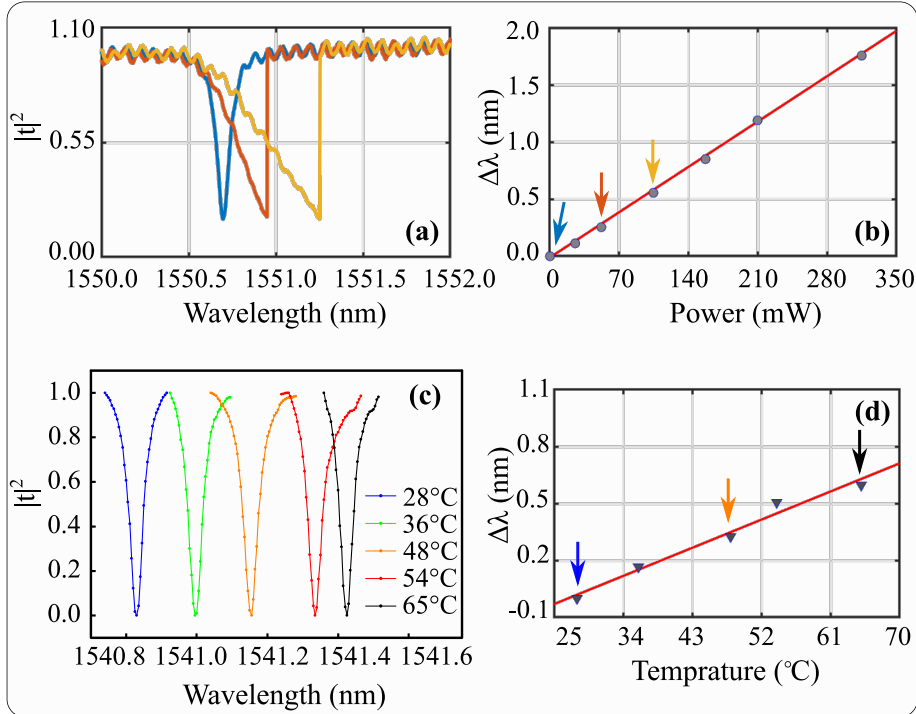


Figure 5.9: Panels (a) and (c) show the transmitted intensity as a function of the incident wavelength for different values of the power and temperature, respectively. Panels (b) and (d): shift of the resonance wavelength as a function of power and temperature. The red lines display the linear fit. The arrows allow relating the different panels on the same row.

5. Complex field characterization in integrated Hermitian and non-Hermitian optical devices

the cladding material. In addition, FEM simulations also allow neglecting the impact of the photo-elastic effect on the shift of the effective index. The variation of the temperature introduces an accumulation of stress/strain on the waveguide that also gives rise to a resonant shift [144]. In the experimental investigated range of temperatures (28-65 °C) the stress-optical effect can be safely neglected, since the simulations results show that it contributes to less than 2 % of the total effective index shift. In this way, we determine a thermo-optic coefficient $\frac{dn}{dT} = (1.84 \pm 0.17) \cdot 10^{-5} K^{-1}$, which is close to the one of stoichiometric Silicon Nitride ($2.5 \cdot 10^{-5} K^{-1}$).

5.2.3 Estimation of the nonlinear refractive index n_2

The nonlinear refractive index, was determined by the efficiency of the sFWM process η . This quantity is well known in nonlinear optics and it is defined as the ratio between the power of the converted signal (P_s) and the one of the stimulating idler (P_i) [120]. In the case of a single mode resonator, starting from the temporal equation 3.1 and assuming a classical undepleted pump and idler approximation, it can be shown that η depends on the power enhancement factors $|FE[\omega_j]|^2$ (where $j = p, s, i$ labels the pump, signal and idler frequency respectively) and the nonlinear coefficient J_{nl} [116]:

$$\eta = J_{nl} p P_p |FE[\omega_p]|^4 |FE[\omega_s]|^2 |FE[\omega_i]|^2, \quad (5.4)$$

p is the perimeter of the resonator and P_p is the power of the pump in the waveguide. In this way, the nonlinear refractive index is obtained by reformulating the following definition of the nonlinear coefficient [111, 116]:

$$J_{nl} = \frac{\omega_p n_2 n_g^2}{c n_{SiON}^2 A_{eff}}, \quad (5.5)$$

where n_g is the group index, c is the speed of light in vacuum, n_{SiON} is the bulk *SiON* refractive index and A_{eff} is the effective area of the mode, defined in equation 4.8. At this point, it is worth noticing that the group index can be extracted from the simple measurement of the Free spectral range of the resonance through the known relation $n_g = \frac{\lambda^2}{p FSR}$. While the effective area can be estimated from FEM numerical simulations. Therefore, the only parameter to be determined is the power enhancement factor. It depends on the characteristic parameters of the resonator and can be formulated as [153]:

$$|FE[\delta]|^2 = \frac{1}{\omega_0 \tau_{rt} Q_{ext}} \frac{1}{\delta^2 - \left(\frac{1}{2Q_{tot}}\right)^2}, \quad (5.6)$$

where $\tau_{rt} = L n_g / c$ is the round trip time of light within the cavity, $\delta = \frac{\omega_0 - \omega_s}{\omega_0}$ is the normalized detuning, Q_{ext} and Q_{tot} are the total and the extrinsic quality factors. To understand the presence of normalized detuning, we note that the sFWM process is done by tuning the frequency of the pump and the idler in two resonances orders of the resonators and monitoring the signal generated at

the frequency $\omega_s = 2\omega_p - \omega_i$. Since the group velocity dispersion of the used waveguides is non-zero at the pump frequency, the converted signal frequency ω_s does not match perfectly with the eigenfrequency ω_{0s} of the resonator, but has indeed the normalized detuning δ . Thus, the Q_{ext} , Q_{int} and the sum of the two Q_{tot} must be determined by the resonator response measures.

From the equation 5.6 we can see that the coupling regime is of fundamental importance for estimating the enhancement factor. For this reason, the information carried by the phase is crucial in order to uniquely determine the intrinsic and extrinsic quality factor. In fact, as seen in section 2.2 of the theoretical part, just from the spectrum of the transmitted field intensity it is possible to obtain only the resonance line-width and the extinction ratio. These are not

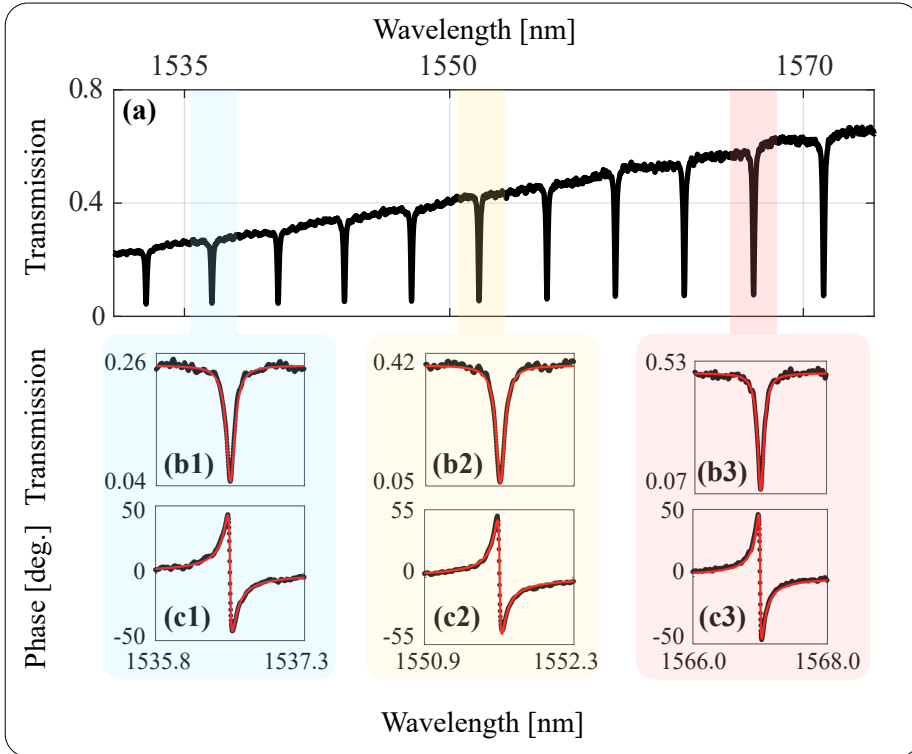


Figure 5.10: (a) Normalized transmitted intensity of the racetrack resonator as a function of the wavelength for TM. The light blue, light yellow and light red rectangles highlight respectively the signal, pump and idler resonance orders involved in the sFWM. Panels (b1-b3) and (c1-c3) represent the transmitted intensity and phase as a function of wavelength for these three resonances. The black dots correspond to the measured data while the red line displays the fit with the theoretical model.

5. Complex field characterization in integrated Hermitian and non-Hermitian optical devices

affected by an exchange between the intrinsic and extrinsic coefficient. Using the Mach-Zehnder interferometer, the intrinsic and extrinsic coefficients have been estimated for the two polarizations TE and TM. Figure 5.10, shows the normalized intensity as a function of the wavelength with the polarizer set to TM. The black dots represent the experimental data. In particular, the panel (a) shows the spectrum acquired with the *normal* acquisition mode in a range of wavelengths ranging from 1530 nm to 1575 nm. The resonance condition gives rise to a set of Lorentzians. As one can see from the transmission spectrum, the linear losses increase as the wavelength decreases. These have been estimated from measurements of the transmitted intensity of waveguides with different lengths, while the coupling losses have been estimated with the cut-back technique. The variation of the linear losses connected to the variation of the effective index as a function wavelength, leads to the change of the coupling regime among the different Lorentzians. In figures 5.10 (b1-b3) and (c1-c3) are shown the zoom of the intensity and the relative phase spectrum for the three resonances involved in the sFWM process. From the phase behavior of panels (c1-c3) it is easy to see that the resonator is in an under-coupling regime in all three resonances. In fact, as we have seen in the theoretical part, the phase shift on resonance is equal to 0. The experimental values of transmission and phase, have been estimated using the equation 2.12. In order to reduce the mutual dependency of the parameters shared among the module and the argument of the transmission amplitude we have simultaneously fit the phase and the transmitted intensity. This allows determining the intrinsic and extrinsic coefficient and, therefore, the values of Q_{int} and Q_{ext} . In summary, the estimation of these parameters permit to find a nonlinear refractive index for the *SiON* equal to $n_2 = 6 \pm 1 \cdot 10^{-16} cm^2 W^{-1}$ for the TE polarization and $n_2 = 8 \pm 1 \cdot 10^{-16} cm^2 W^{-1}$ for the TM. All parameters used are reported in the table 5.1.

To conclude, the nonlinear refractive index of *SiON* lies between the nonlinear refractive index of Silica ($n_2 = 2.36 \cdot 10^{-16} cm^2 W^{-1}$) and the one of stoichiometric silicon nitride ($n_2 = 2.4 \cdot 10^{-15} cm^2 W^{-1}$). It is worth noticing that this estimation was also obtained considering nonlinear contributions due to cladding. In fact, as we have already discussed, the mode extends into cladding. However, as detailed in ref. [144], this issue represents a minor correction in the final estimation that does not go beyond the experimental error. Actually, the accuracy of the experimental estimation is mainly limited by the resolution of the measure of the detuning δ . The nonlinear coefficient (n_2) and the linear losses estimated make this particular platform unsuitable for the investigation of the Bogoloubov dispersion relation.

Parameter	Pump (TE)	Idler (TE)	Signal (TE)
λ_0 (nm)	1551.940 ± 0.001	1567.045 ± 0.001	1537.145 ± 0.001
$Q_{tot} \times 10^4$	3.00 ± 0.04	2.60 ± 0.04	2.71 ± 0.05
$Q_{ext} \times 10^4$	7.17 ± 0.04	6.53 ± 0.05	8.58 ± 0.07
$\delta \times 10^{-5}$	≈ 0	≈ 0	1.02 ± 0.05
$\tau_{rt}(ps)$		2.14 ± 0.05	
$ FE ^2$	19.4 ± 0.7	16.1 ± 0.7	8.4 ± 0.4

Parameter	TE polarization
P_s (dBm)	-93.80 ± 0.03
P_p (dBm)	0.5 ± 0.2
P_i (dBm)	-0.6 ± 0.2
Loss (dB cm^{-1})	4 ± 0.5 at λ_s 2.0 ± 0.5 at λ_i, λ_p
C.Loss (dB/cm)	3.0 ± 0.2
A_{eff} (μm^2)	0.99
J_{nl} (1/(mW)) \S	0.25 ± 0.04
n_2 cm^2/W	$(6 \pm 1) \cdot 10^{-16}$

Parameter	Pump (TM)	Idler (TM)	Signal (TM)
λ_0 (nm)	1551.590 ± 0.001	1566.960 ± 0.001	1536.540 ± 0.001
$Q_{tot} \times 10^4$	1.50 ± 0.02	1.33 ± 0.01	1.58 ± 0.01
$Q_{ext} \times 10^4$	3.58 ± 0.02	3.19 ± 0.01	4.30 ± 0.02
$\delta \times 10^{-5}$	≈ 0	1.96 ± 0.06	
$\tau_{rt}(ps)$		2.10 ± 0.05	
$ FE ^2$	9.8 ± 0.3	8.8 ± 0.2	6.1 ± 0.1

Parameter	TM polarization
P_s (dBm)	-98.43 ± 0.08
P_p (dBm)	5.5 ± 0.2
P_i (dBm)	-3.3 ± 0.2
Loss (dB cm^{-1})	4 ± 0.5 at λ_s 2.0 ± 0.5 at λ_i, λ_p
C.Loss (dB/cm)	3.0 ± 0.2
A_{eff} (μm^2)	1.58
J_{nl} (1/(mW)) \S	0.21 ± 0.03
n_2 cm^2/W	$(8 \pm 1) \cdot 10^{-16}$

Table 5.1: List of the main parameters extrapolated from the characterization process for TE and TM polarization. Precisely, the first and second (upper) table report the estimated parameters for the TE polarization. While the third and fourth (lower) table show the same coefficients for the TM polarization.

5.3 Backscattering measurements

In this section, we will discuss the results obtained from the measures of the backscattering doublets. We will compare the analytical model introduced in chapter 2 and verify the presence of Hermitian and non-Hermitian coupling. Using the techniques of data representation, such as the parametric phasor graph and the complex inverse, we will explain the experimental measurements for the four cases: single Lorentzian, balanced, unbalanced and hidden doublet.

5.3.1 Samples and Experimental setting

As anticipated in the simulation part of chapter 2, the experimental samples are disk-shaped wedge microdisk resonators made using standard silicon microfabrication tools. In particular, the microdisks are multi-modal with a thickness of 400 nm and a diameter of $50\text{ }\mu\text{m}$. These are manufactured in Si_xN_y and are excited through a single mode SiON bus waveguide using a vertical coupling geometry. In contrast to the typical in-plane coupling shown in figure 5.11 (a), in the vertical scheme the resonator and the waveguide lay in different planes as shown in panel (b). This allows achieving a shallow angle wedge, while keeping the excitation waveguide intact, and using different materials for the optical components. Such an optical design permits reaching a high quality factor of about $2 \cdot 10^5$ in a monolithic-integrated optical system [142]. The devices were fabricated using plasma-enhanced CVD techniques to grow the materials on

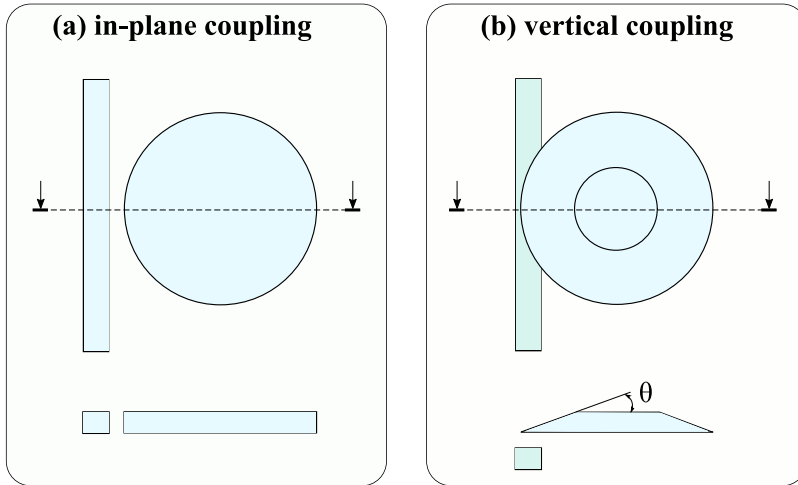


Figure 5.11: (a) Sketch of the in plane coupling of a waveguide/microdisk system. Panel (b) shows the sketch of the vertical coupling scheme for a waveguide/wedge-microdisk system. The angle of the wedge is denoted with θ . In both panels the upper sketch shows the top view, while the lower one displays the cross section.

top of crystalline *Si* wafer. The wet etch and the adhesion properties of the photoresist give rise to a sharp angle wedge of about $\theta = 7^\circ$. Details of the chip's fabrication and the first characterization measures are reported in ref. [142].

The measurements of the transmission and phase spectra were made by placing the sample inside the Mach-Zehnder interferometer. This is set in a nearly balanced condition by using the delay system made of glass and the mechanical slit as optical attenuator. Since we have focused our attention on the single backscattering doublets, the measurement has been obtained using the *choppered* acquisition mode and using only the probe laser. The laser intensity is chosen to be weak enough to stay in the linear regime. The laser scan was measured using the Lock-in amplifier in order to decrease the signal-to-noise ratio. In this way, the probe is modulated in amplitude at a frequency of 1 kHz , while the chopper wheel in the sample (reference) arm rotated at a frequency of 20 Hz (60 Hz). The stability and systematicity of the measurements are ensured by closing the interferometer inside a box and remotely controlling it through the LabView platform.

5.3.2 Result discussion

As reported in [142], in the wedge samples at about $1.3\ \mu\text{m}$ the fundamental mode splits into a doublet. It is observed a relatively small splitting of the doublets compared to the free spectral range of the microdisk resonator and to the distance to other family of modes. This clearly indicates that the split must originate from the coupling of counter-propagating modes with an opposite angular momentum in the microdisk. For the sake of completeness and comparison, we also re-report the measurements of the single mode racetrack microresonator shown in the previous section (see figure 5.10). This allows verifying the methods of complex analysis explained in the theoretical part (subsection 2.3.3).

Figure 5.12 shows the measured data in the three different representations: transmitted intensity and phase as a function of wavelength (first column, panels (a1-d1)), the respective parametric phasor diagram (second column, panels (a2-d2)) and the complex reverse (third column, panels (a3-d3)). The experimental data are shown by the rainbow color code so that each color corresponds to a certain wavelength value. This allows comparing the different representations of data along the same row. The panels in the first row (a1)-(a3), show the measurement performed on the single mode racetrack microresonator seen in the previous section. Precisely, they show the TM polarization response of the waveguide/microresonator system reported in figure 5.10 within the blue light column. The presence of a negligible side-wall roughness leads a typical single Lorentzian-shaped resonant feature. On the contrary, the wedge microresonator exhibits clear double resonant peaks in transmission and a double-step jumps in the phase-shift. The three rows in figure 5.12 (b)–(d) show three examples of transmission and phase-shift spectra in different wavelength ranges, where the mode splitting for different azimuthal modes displays different features. While the doublets observed for high/ultra-high quality-factor and single mode

5. Complex field characterization in integrated Hermitian and non-Hermitian optical devices

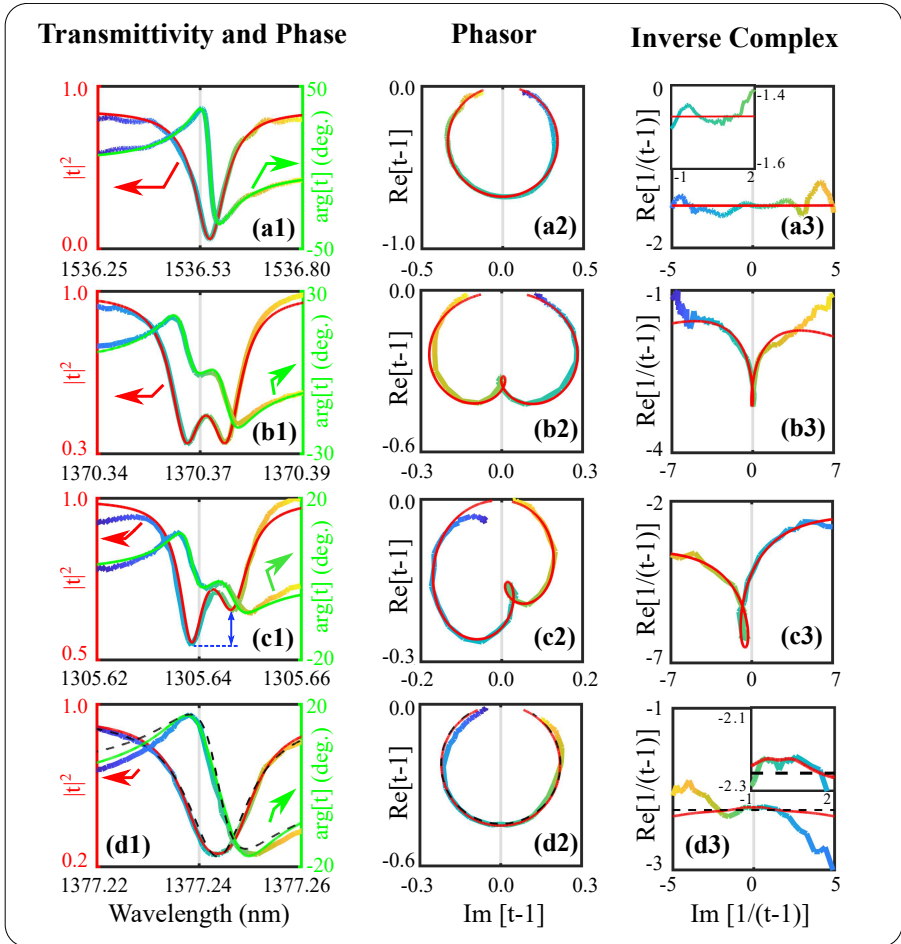


Figure 5.12: (a) Experimental spectra of the transmitted intensity and phase for a single mode microresonator with a negligible surface roughness [144]. Panels: (b-d) experimental spectra for the wedge microresonator in different frequency ranges showing a balanced (b), an unbalanced (c), and a hidden (d) doublet. The different columns represent the transmitted intensity and phase as a function of the signal wavelength (a1-d1), the phasor representation (a2-d2) and the inverse complex representation (a3-d3). The colour code (rainbow curves) represents the data as a function of the wavelength (the colour allows to relate the different panels on the same row). The red and green lines refer to the theoretical fits based on the analytical model of section 2.2. The black-dashed lines of panels (d1-d3) show the fit with the single mode transmission response of equation 2.12. On panel (c1) we specifically show the intensity unbalance by the arrow and the dashed line.

microresonators [11, 14, 15] consist of a pair of balanced peaks of equal intensity, in most cases we observe unbalanced doublets formed by a pair of peaks of appreciably different heights (see, e.g., figure 5.12 (c1)). To obtain a balanced doublet (see panel (b1)) we have to increase the temperature of the sample. As a consequence, a slightly unbalanced doublet at room temperature is red shifted and it changes casually to a balanced configuration [16]. In addition, by using the phase sensitive set-up, we also evidence cases where no frequency-split in transmission is visible (figure 5.12 (d1)). We have named this situation in chapter 2 as hidden doublet. Summarizing, we do observe all the different cases introduced in the theoretical model: balanced (b), unbalanced (c) and hidden (d) doublets.

The intensity and phase information are condensed in the phasor and complex inverse representation of panels (a2)-(d2) and (a3)-(d3) respectively. In the ideal resonator/waveguide system with no backscattering shown in figure ref (a1)-(a3), only a single forward propagating mode is excited. In this case, in agreement with the theoretical part, the phasor graph represents the typical Lorentzian in transmission with his peculiar phase-shift into a perfect circle (see figure 5.12 (a2)). The diameter of the circle is smaller than unity and, therefore, the system is in the under-coupling regime. In the presence of resonance splitting, the circle in the phasor representation is significantly deformed. A balanced doublet corresponds to a pair of symmetric lobes as shown in figure 5.12 (b2). When the doublet is not balanced, one can see, as in figure (c2), that the two lobes acquire different sizes as a result of the asymmetry in the transmission and phase-shift of the split modes. Typically, the grade of unbalance is denoted as the difference between the peak depths. The knowledge of both transmitted intensity and phase allows defining a different figure of merit. Indeed, the ratio between the areas of the lobes in the phasor diagram can be taken as a quantitative measure of the unbalance.

The two-dimensional nature of the phasor diagram allows using the inverse complex representation. In figure 5.12 (a3), we confirm that in the case of single resonance the complex inversion yields a straight line within the experimental errors (panels (a3)). As explained in chapter 2, in this complex inversion representation, even a very small perturbation of the circle in the phasor diagram gives rise to a sizeable deformation of its inverse (figure 5.12 (b3) and (d3)). More interesting is the case of the hidden doublet. In this case, the side-wall roughnesses cause a resonance split which yields an indiscernible perturbation of the symmetric Lorentzian in transmission or of the perfect circle in the phasor representation. On the contrary, it produces a noticeable peak in the single line of the inverse complex (see figure 5.12 (d3)).

Our simple analytical model, seen in section 2.2, can reproduce the experimental behavior. Both the acquired transmitted intensity and the transmission phase-shift spectrum have been fitted simultaneously to remove the mutual dependency of the same parameters among the different equations. The red and green lines display a theoretical fit based on the analytical model of section 2.2. The quality of the fit can be appreciated on the phasor diagram of panels (a2-d2) which shows both the information encoded in the real and complex parts. The

5. Complex field characterization in integrated Hermitian and non-Hermitian optical devices

small differences between the fit and the data out of the resonance region is likely due to the weak Fabry-Perot cavity effect at the facets of the bus waveguide, an effect that is more visible far from the resonance region.

The experimental data of figure 5.12 (a) require a zero value of the intra-cavity coupling coefficient: they match with a typical Lorentzian ($|h| = |n| = 0$ and $\Gamma/\gamma = 0.58$). The measurements of figure 5.12 (b) exhibit a balanced doublet which can be reproduced by the second case of the classification seen in subsection 2.3.6: $|n|/|h| = 2 \cdot 10^{-2}$, $\Delta\Theta = -270$ degrees and $\phi = -90$ degrees with $\Gamma/\gamma = 0.54$. The data of figure 5.12 (c) show a certain degree of unbalance, as highlighted by the blue arrow in the transmission spectrum (see panel (c1)). This behavior falls in the third case of our classification and requires the simultaneous presence of Hermitian and non-Hermitian parts, $|n|/|h| = 0.13$, $\Delta\Theta = -193.63$ degrees and $\phi = -13.64$ degrees with $\Gamma/\gamma = 0.24$.

In the case of the figure 5.12 (d1) the presence of the doublet is hidden. The transmittivity could have been fitted also by a single resonance model with $|h| = |n| = 0$ (i.e. equation 2.12), see black-dashed line. Even though the phasor diagram in figure 5.12 (d2) shows the same fit uncertainty for the two cases, the ambiguity is resolved by the complex inverse representation, as shown in panel (d3). In this diagram, the small difference between the perfect circle of a single resonance and the experimental data is clear. The hidden doublet corresponds to the following intra-cavity coupling parameters: $|n|/|h| = 0.16$, $\Delta\Theta = -270$ degrees and $\phi = -90$ degrees with $\Gamma/\gamma = 0.37$. This experimental configuration falls into the second case of our classification and the small contribution of the intra-cavity coefficients introduces a clear peak on top of the straight line in the complex inverse representation.

To conclude we provide experiments, numerical simulations and an analytical model which show that the unbalance can be generated inside the microresonator due to the stochastic nature of inherent roughness. Generally, in the ideal case, the stochastic nature of the roughness leads to a simple statistical approach which ignores the non-Hermitian behavior of the back-coupling. Therefore, just the presence of scatterers placed in the evanescent field of a resonator, can introduce a geometrical-induced non-Hermitian coupling, as already shown in [52, 154, 155, 156]. In fact, by carefully adjusting the scatterers position it is possible to control the degree of splitting and achieve the counterintuitive features of non-Hermitian physics [52]. This perturbation can lead to an asymmetric backscattering and an unidirectional emission in the extreme case at a so-called exceptional point. The optical chirality is ensured by the dissipative nature of the back-coupling and does not require the break of the Lorentz reciprocity. However, we show that the repeated backscattering processes induced by several scatterers on the surface could turn the light back by crossing loss paths. As a result, a dissipative non-Hermitian coefficient should be considered also in the case of the stochastic roughness. In the scenario of a multi-mode resonator, additional couplings and loss channels are enabled. These paths could mediate the energy exchange between counter-propagating modes, increasing the non conservative effect [16]. As we have explained in section 2.2, this interplay between the stochastic roughness and the inter-modal dissipative coupling is

strictly related to the reflection of the waveguide/microresonator system and could exhibit a collective non-symmetrical behavior. In other words, the idea is that the symmetrical losses, depending on the propagation direction of the beam, could be differently distributed between conservative (back-reflections) and dissipative couplings.

5.4 The inter-modal interaction measurements

In this section, we will report the measurements of multi-mode resonators coupled through a single mode bus waveguide. As we have explained in section 2.5, the interplay of resonant modes could give rise to an asymmetric Fano line shape in the transmitted spectrum. The ingredients for achieving this asymmetrical response are the presence of broad and narrow resonances, which do mutually exchange energy. We will see that this phenomenon could be studied in microresonators where their radial modes interact through a vertically coupled bus waveguide. Precisely, we will show that the transmittance can be complemented by studying its asymmetrical phase. In such a way, the intermodal interaction can be analyzed. Moreover, the optical response acquires one more dimension with the possibility to condensate it either in a polar plot or in an inverse complex representation. As we will see in the following, these tools allow confirming the theoretical prediction of a reactive inter-mode coupling [40, 84], analogous to an off-diagonal Lamb shift in atomic physics.

5.4.1 Sample and Experimental setting

The samples analyzed are thin microdisk resonators vertically coupled to a single mode waveguide. Precisely, they are Si_xN_y microdisk resonators (400 nm-thick, 40 μm -diameter on a SiO_2 substrate) vertically coupled to buried SiO_xN_y waveguides. This particular coupling scheme, already seen in the previous section (see figure 5.11 (b)), allows exploiting two independent free parameters: the lateral and vertical position of the bus waveguide. In contrast to the traditional in-plane coupling (see figure 5.11 (a)) where only the lateral position of the bus waveguide can be tuned. Typically, in the in-plane coupling configuration, just the first radial modes family exhibits an efficient coupling. The vertical coupling scheme allows freely tuning the two gap parameters and thus exciting efficiently even radial families of different order. Thus, it is possible to design a microrisonator/waveguide system in order to have two or more different radial mode families close to the critical coupling condition and, therefore, visible in transmission spectra [84]. More details on the sample fabrication are reported in ref. [142].

The transmission intensity and phase have been measured as a function of the incident frequency by placing the microdisk resonator into the sample arm of the free space Mach-Zehnder interferometer. The interferometer has been set in a nearly balanced condition by using the optical attenuator and the glass delay line. A single probe laser has been used to cover a range of wavelengths spanning

5. Complex field characterization in integrated Hermitian and non-Hermitian optical devices

the third telecom window. Precisely, the CWTL used operates in the range from 1490 nm to 1610 nm , with a fixed power of 5 mW . This power has been chosen to guarantee the linear regime during the measurement. The polarization was fixed in the in-fiber stage and analyzed at the detection stage. The power stability of the CWTL laser together with the accuracy of the insulated optical set-up allows using the *normal* acquisition mode. Therefore, the laser has been swept at 1 nm/s and the transmission spectra of the different arms of the Mach-Zehnder were recorded with a Germanium (*Ge*) detector. In addition, also in this case, the measurements have been carried out using the Lock-in Amplifier to reduce the signal to noise ratio.

5.4.2 Result discussion

The interaction between the excited modes in the resonator, mediated by the single mode bus waveguide, strongly modifies the transmission spectrum. Figure 5.13 shows the experimental transmission and phase spectra for a wide range of frequencies. Instead of a conventional symmetric Lorentzian, as in the case of a single mode microresonator (see figure 5.12 (a1)), two features are observed. They correspond to the coupling of the bus waveguide with the two radial family modes of the microresonator. The different group and effective index of the two modes yield slightly different free spectral ranges (FSRs) of the first (narrow features) and second (broader features) resonances. Therefore, by changing the frequency we observe a different detuning among the resonances [84] and, according to the theory (see section 2.5.1), doublets with different lineshapes are observed in the transmitted intensity.

As mentioned in chapter 2, the phase of the transmitted field allows to understand the coupling regimes of the two radial modes. In figure 5.13(a)-(d) the first and second radial mode families are in under and over coupling regime, respectively. Indeed, we observe a 2π shift for the over coupled resonance and a small phase shift for the under coupled one. This is also observed in the parametric phasor diagram. Figure 5.13(b) highlights the coupling regime of the modes. The second radial mode family exhibits a bigger circle with respect to the first one. Its circumference passes through negative values indicating the over coupling regime. In fact, as we have explained in the theoretical part, its diameter is greater than one. Increasing the incident frequency, as shown in figure 5.13(e)-(i), the second radial mode family changes its coupling regime to an under coupling one. The first radial mode family remains in under coupling regime over all the scanned frequency range and, consequently, its representative loop does not assume negative values (figure 5.13(b), (e), and (h)). Therefore, the diameter associated with its loops is always less than one.

The experimental phase, transmission and real part of the inverse complex are fitted by the analytical model seen in section 2.5.1 with a single set of parameters. Since the phase (transmission) is given by the argument (square modulus) of the transmitted amplitude, a simultaneous fit of them allows to reduce the mutual dependency among the share parameters. As we have seen in the section 2.5.1, the real part of the inverse complex permits to remove the Δ

coefficient and to highlight its role. The data are in good agreement with the theoretical model (see red curves in figure 5.13(a)-(i)). The phasor diagrams show a small difference between the analytical prediction and the experimental data (see figure 5.13(b),(e) and (h)). In figure 5.13(h), the difference between the fit and the data out of the resonance region is likely due to the presence of a third radial mode family which slightly perturbed the shape of the doublet [84].

Figure 5.14 shows the fit parameters. As in the case of the work in ref. [84],

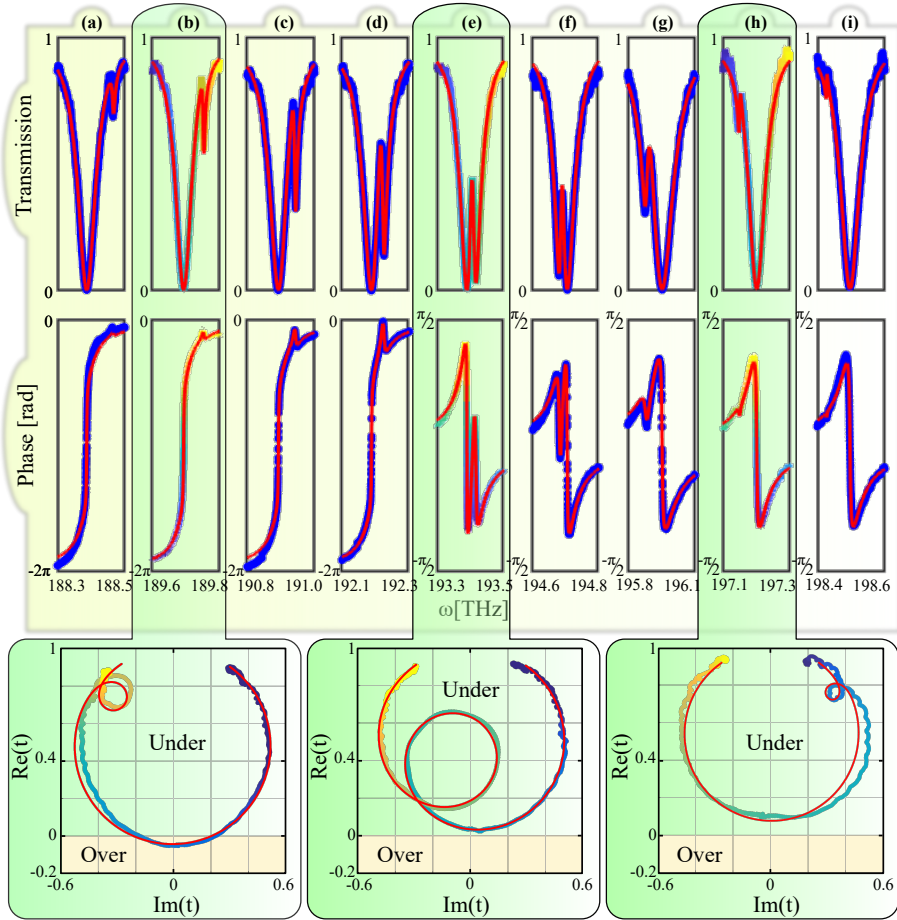


Figure 5.13: (Top) Transmittance and phase spectra as a function of the incident frequency for each doublet considered. Panels (b), (e) and (h) include the parametric phasor diagram of the transmission and phase spectra for the respective doublets. The rainbow and blue curves display the experimental data, while the red lines are the fits with the model of section 2.5.1. As always, the colored scale has been chosen to permit the connection with the phasor diagrams.

5. Complex field characterization in integrated Hermitian and non-Hermitian optical devices

the off-diagonal reactive coupling is necessary to reproduce the experimental data. However, the fitting procedure produces three possible solutions with comparable intrinsic and extrinsic coefficients (see figure 5.14(p1)-(p2),(n1)-(n2) and (f1)-(f2)) but different sign of the overall frequency shift Δ (see figure 5.14(p3),(n3) and (f3)). In particular, figure 5.14(p) (figure 5.14(n)) is obtained by constraining in the fit a positive (negative) reactive inter-mode coupling coefficient. Figure 5.14(f) is obtained with a totally free fit and displays both positive and negative overall frequency shift. The sign change takes place when one resonance crosses the other (see figure 5.13(e)-(f)). To quantify the goodness of the fit we define for the i -th spectrum, the coefficient K as the square root of the ratio between the residual sum of squares (RSS) and the total sum of squares (TSS): $K = \sqrt{(RSS/TSS)}$. Therefore, a value of K close to zero means that the theoretical model is in agreement with the experimental data, while high values of K indicate discordance between the theory and the experiment. To compare the three different cases of the fit we introduce \bar{K} as an average of

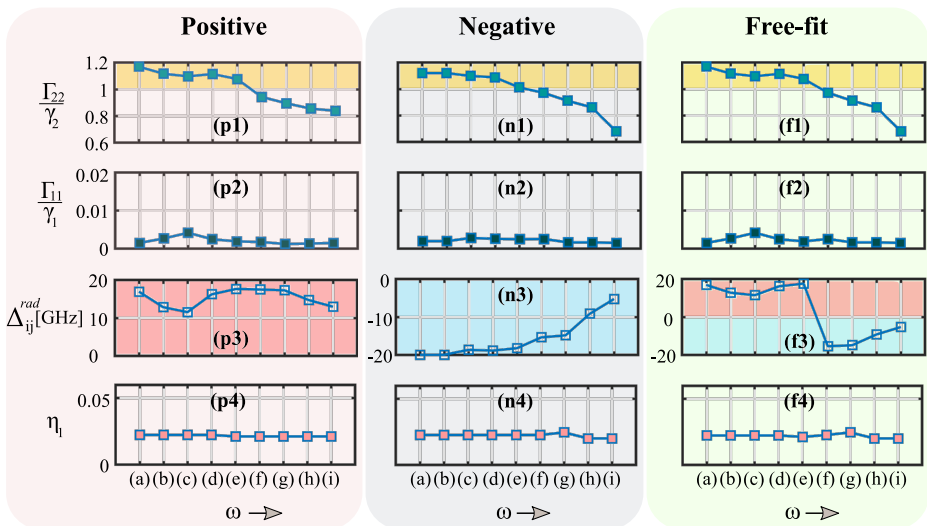


Figure 5.14: Parameters of the theoretical model obtained by fitting the transmission, the phase and the real part of the inverse complex with a single set of parameters. The fit has been performed independently for each resonance order identified by the same letters used in the different panels of figure 5.13; here the panels are highlighted with the following labels: (p) positive, (n) negative overall frequency shift and (f) free fit process which exhibits both positive and negative Δ coefficients. Precisely, panels (p1), (n1) and (f1) ((p2), (n2) and (f2)) show the ratio between the extrinsic and intrinsic coefficient of the second (first) radial mode family. Panels (p3), (n3) and (f3) display the off-diagonal inter-mode coupling parameter Δ_{ij} . Panels (p4), (n4) and (f4) report the relative weight η_1 .

K obtained for the 9 different spectra. In this way, we derivate $\bar{K}_P = 0.049$, $\bar{K}_N = 0.047$ and $\bar{K}_F = 0.048$ for the positive-, negative- and free-fit, respectively. These values are comparable and it is not possible to exclude any of the three fitting solutions.

A priori, the theoretical model allows both sign of the Δ parameter. As we have seen in section 2.5.1, its symmetric behaviour requires a change of sign when one resonance crosses the other. In our case, the two radial mode families swap the relative frequency position along the spectra, and the doublet (e) of figure 5.13 can be considered almost the mirror image of the doublet (f). In fact, the fit procedure naturally shows a change of sign of the Δ coefficient passing from doublet (e) to (f) (see figure 5.13). In this case, the equal goodness of the three fits does not allow choosing a particular set of the fitting parameters. However no sign swapt was observed in our simulation seen in section 2.5.3, therefore we can neglect the third column of Figure 5.14, but both positive or negative overall frequency shift can be a possible solution.

To conclude, the knowledge of the phase permits to introduce the inverse complex representation and a multi-fit process which allows to reduce the mutual dependency of the fit parameters and to isolate the inter-mode coupling coefficient. We confirm that the presence of this reactive coupling is essential in order to reproduce the experimental data. However, the fit process leaves the sign of the Lamb shift (i.e. Δ) undetermined and shows possible solutions consisting in a swap of the sign when the resonances frequencies of the two modes cross. By using a simple model, where two single mode ring resonators are coupled through a bus waveguide, we performed numerical simulations of the system. These confirmed the presence of either a positive or negative reactive coupling Δ , excluding any possible change of sign attributed to the crossing of the resonant frequencies. The sign of Δ strongly depends on the details of the physical system under study.

5.4.3 A curious inter-modal interaction

The vertical coupling between the microdisk resonator and the bus waveguide allows obtaining different coupling regimes between the two radial mode families. A special case is when both modes of different radial order are in over-coupling regime. Here, the knowledge of the phase can lead to the detection of a family hidden by the inter-modal interaction.

Figure 5.15 shows the measurement of the transmitted intensity and phase as a function of the incident frequency. The rainbow color shows the experimental data while the red lines display the fit with the analytical model of section 2.5.1. In this peculiar doublet, the feature of the first radial family disappears in the transmission spectrum (see the left side of the quasi-Lorentzian in panel (a)). However, in figure 5.15 (b), the phase spectrum allows observing the presence of two modes. In fact, the two different radial orders lead to a double phase jump of 2π in the system response. This is highlighted by condensing the knowledge of transmission intensity and phase in a parametric phasor diagram. As shown in figure 5.15 (c), the two circumferences associated to the two lobes pass through

5. Complex field characterization in integrated Hermitian and non-Hermitian optical devices

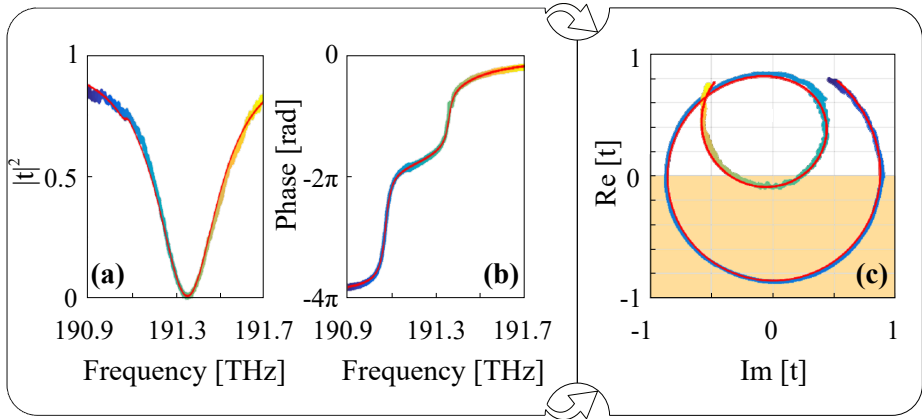


Figure 5.15: (a) and (b) Transmitted intensity and phase as a function of the incident frequency. The rainbow color displays the experimental data and allows relating the three graphs. Panel (c): parametric phasor plot which condensates the informations of panels (a) and (b). The red lines show the experimental fit with the model of section 2.5.1.

negative values. This means, as explained in the chapter 2, that the diameter associated to the two lobes is greater than one and therefore, that the two families are indeed in the over-coupling regime.

Interestingly, the analytical model can reproduce the experimental behavior. In fact, there is a good agreement between the experimental data and the red lines of figure 5.15.

Chapter 6

Unidirectional reflection and time characterization

In this chapter, we will describe the experimental apparatus and then report the measures obtained for the taiji microresonator and the temporal evolution. We will then see the measurements of the transmitted and reflected intensity in the case of an integrated microresonator consisting of a racetrack with an S-shaped waveguide contained within it. We will prove that, as we have seen in chapter 2, this design, working on an exceptional point, allows obtaining an unidirectional reflection device.

In addition, we will discuss the measurement of the time-dependent transmission response of an integrated waveguide/microresonator system with high Q . Using the model of section 3.1, we will see how an excitation given by a rectangular pulse of duration Δt allows estimating the characteristic parameters of the sample, i.e. the intrinsic and extrinsic coefficients. The optical system used to measure the temporal response of an integrated microresonator will be extended to the case of a macroscopic cavity of the Fabry-Perot type. In particular, we will see the values experimentally obtained for the Q factor in a macroscopic cavity exciting the first and second order modes.

6.1 Transmitted and reflected intensity response

In this section, we will report the description of the optical setup and the experimental results of the taiji microresonator. We will see how the introduction of the S-shaped waveguide in the cavity strongly changes the response of the optical system [63]. Indeed, as seen in the theoretical section 2.3.9, this feature allows the microresonator working on an EP. The orientation of the S-shape permits to select the propagation direction of the cavity guided mode and, therefore, to force the energy exchange to CCW or CW mode.

6.1.1 Samples and Experimental setup

The samples studied are taiji microresonators coupled to a bus waveguide. The fabrication of these devices has been made on the same chip used for the racetrack microresonators analyzed to characterize the nonlinear coefficient of $SiON$ (seen section 5.2). Therefore, the taiji microresonator/bus waveguide system is composed by a single mode channel waveguide of $SiON$ placed on top of a $5.15 \mu m$ thermal SiO_2 layer grown on a 6-inch Si wafer. Precisely, the width of the waveguide is about $1.2 \mu m$ and the height is about $0.57 \mu m$. A micrograph of the top view and a scanning electron microscopy (SEM) image of

6. Unidirectional reflection and time characterization

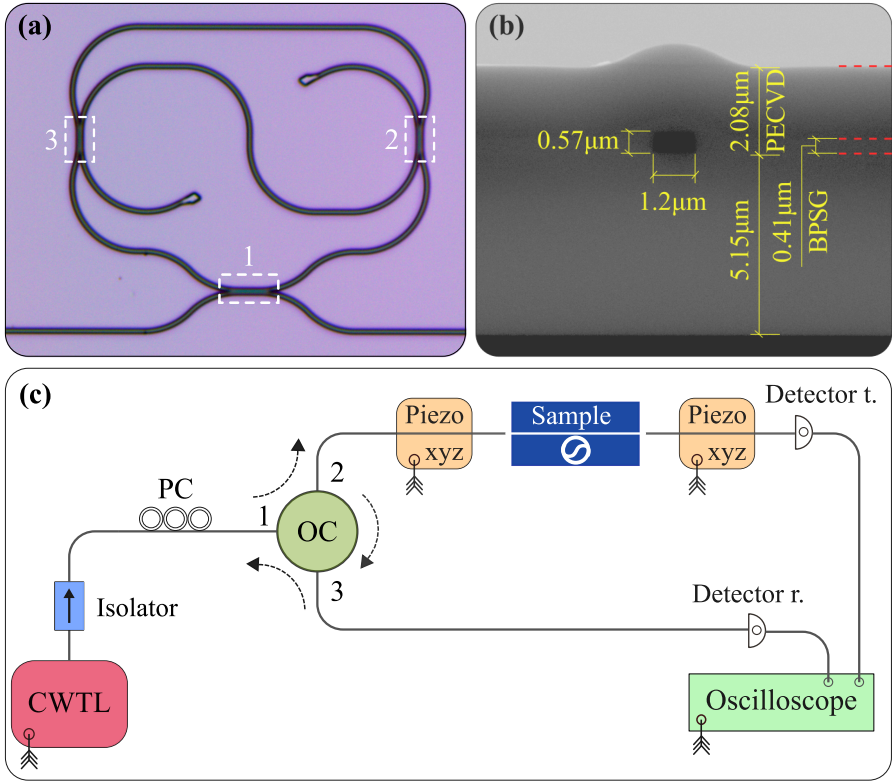


Figure 6.1: (a) and (b) Optical micrograph of the top view and SEM image of the cross section of the integrated taiji microresonator. In panel (a), the white dashed rectangles highlight the three coupling regions, precisely, 1 indicates the coupling with the bus waveguide, while 2 and 3 denote the ones with the S. The red dashed lines of panel (b) highlight the different layers of deposition. Panel (c): sketch of the experimental set-up. CWTL: Continuous Wave Tunable Laser, PC: Polarization Controller, OC: Optical Circulator, Detector r. (t.): reflection (transmission). The symbol “ \lll ” indicates the remote control via computer.

the cross section of the taiji microresonator is shown in figure 6.1 (a) and (b), respectively. As shown in figure 6.1 (a) the taiji system consists of a racetrack resonator coupled to a bus waveguide. The three coupling regions are numbered and highlighted by white dotted rectangles. The coupling is done by directional couplers with a proper coupling length. In particular, in our case, the coupling lengths are $l_{c1} = 18.81 \mu\text{m}$, and $l_{c2} = l_{c3} = 10.28 \mu\text{m}$, respectively. The gaps between the waveguides are $g_1 = 0.86 \mu\text{m}$ and $g_2 = g_3 = 0.8 \mu\text{m}$. In this vision, the coupling is not point-like but based on a directional coupler. Here, the power is exchanged periodically between the two interacting waveguides as a function

of position along the propagation direction. As can be seen from the micrograph of figure 6.1 (a), the ends of the S waveguide are progressively widened. This peculiar geometry is known as mode killer [157], and allows suppressing the mode propagation. Precisely, in our case, it permits to avoid back-reflections at the ends of the S and, most importantly, it allows introducing a significant contribution to the radiation modes (defined as E_e in the theoretical model, section 2.2) at the S-shape branch end. As can be seen in panel (b), the light is confined between the lower thermal oxide cladding and the higher one, consisting of a double stack of 410 nm Borophosphosilicate glass (BPSG) and a $2.08\ \mu\text{m}$ thick PECVD SiO_x layer. More details on the fabrication and growth of the waveguides can be found in ref. [144].

The optical setup was obtained by adapting a linear characterization apparatus to the simultaneous measurement of both the transmitted and reflected intensities. The sketch of the optical setup is shown in figure 6.1 (c). The light is guided in the different elements via single mode fibers. The source is a CWTL that allows tuning the wavelength in a range spanning from 1490 nm to 1610 nm with an output power between 0.1 mW and 10 mW . The laser light is guided to an isolator and then to a polarization control. In this way, it is possible to fix the polarization of the excitation beam and prevent backscattered light from entering the laser cavity. At the output of the polarizer, the light is sent to a fiber circulator, which allows selecting the guided mode according to the direction of propagation. Precisely, the light is rotated in the lensed tapered fiber, which is the input excitation of our optical system. The lensed tapered fiber is placed on a $x - y - z$ translation stage consisting of a piezo with a nanometric control. This allows achieving an optimal coupling with the sample and monitoring the position of the fiber during the acquisition of the measurements. The light reflected from the sample is guided by the same lensed tapered fiber within the circular. This sends the optical signal to a Ge detector (Detector r. in figure 6.1 (c)). While the light transmitted from the sample is collected by another lensed tapered fiber placed on another $x - y - z$ translation stage with a nanometric precision. The beam thus collected, is then sent to a another Ge detector (Detector t. in figure 6.1 (c)). The two Ge detector outputs are connected to an oscilloscope (picoscope) that allows monitoring the signal intensity. In particular, the picoscope is remotely controlled by a PC so that, it is possible to simultaneously measure the transmitted and reflected intensity of the sample.

6.1.2 Result discussion

The coupling and propagation losses of the waveguides are reported in the table 5.1 of section 5.2. As mentioned, the propagation losses have been characterized by using particular waveguides with different lengths thanks to the Lambert-Beer's law. The coupling losses have been estimated using the cut-back technique. The light polarization has been set in order to analyze the TE polarization. The laser power was set to about 5 mW to guarantee a response in the linear regime. As seen in the previous section, in a microresonator system, this regime is

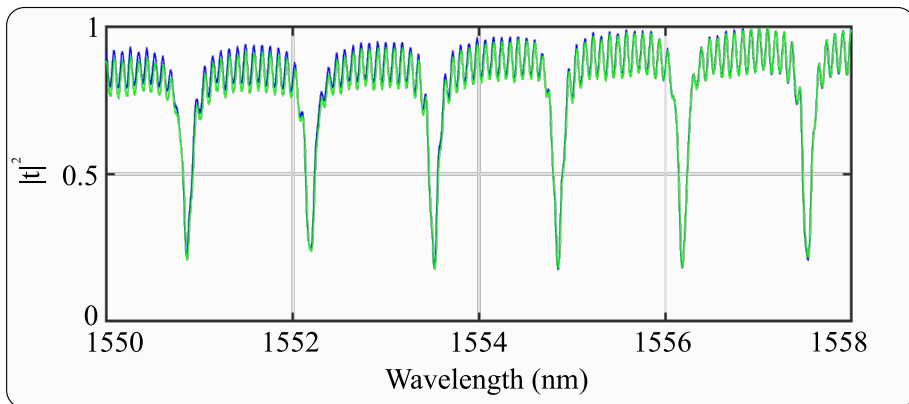


Figure 6.2: Transmitted intensity as a function of the incident wavelength. The blue (green) data show the waveguide/microresonator response injecting the light from left (right) to right (left).

characterized by the symmetry of the Lorentzian in the transmission spectrum. The spectra of reflected and transmitted intensity as a function of wavelength were measured simultaneously. This was possible by triggering the oscilloscope through the laser's sync signal. This signal is generated by the piezo of the laser, which allows lengthening the cavity and, therefore, changing the wavelength of the incident beam. Thus, for each wavelength, the values of the reflected and transmitted intensity are measured by the two different Ge detectors. Since the reflection has a lower intensity than the transmission, the detector that monitors its response (Detector r. in figure 6.1) has a gain of 20 dB higher than the transmission one. The system was first excited from left to right and then, by rotating its orientation, from right to left.

In agreement with the theory of chapter 2, the transmission intensity exhibits the same trend in both excitation directions. As shown in the long spectrum of figure 6.2, the transmitted intensities obtained injecting the light from left (blue data) and from right (green data) are almost completely overlapping.

Let us consider the simultaneous acquisition of transmission and reflection response. The figure 6.3 shows the transmitted and reflected intensity in the two directions of excitation. Precisely, panel (a) reports the transmission while panels (b) and (c) report the reflection spectra when the input is fed from right and left respectively. The blue points are the experimental measurements. The transmitted intensity shows symmetric Lorentzians within a fast oscillation due to the Fabry-Perot formed by bus waveguide facets. The reflected intensity exhibits visible peaks for light incident from left, while when the light is incident from right it shows the typical Fabry-Perot oscillations. Therefore, as mentioned in section 2.3.9, the system works as a unidirectional reflection device. The different heights of the peaks in the panel 6.3 (b) can be interpreted as interferences

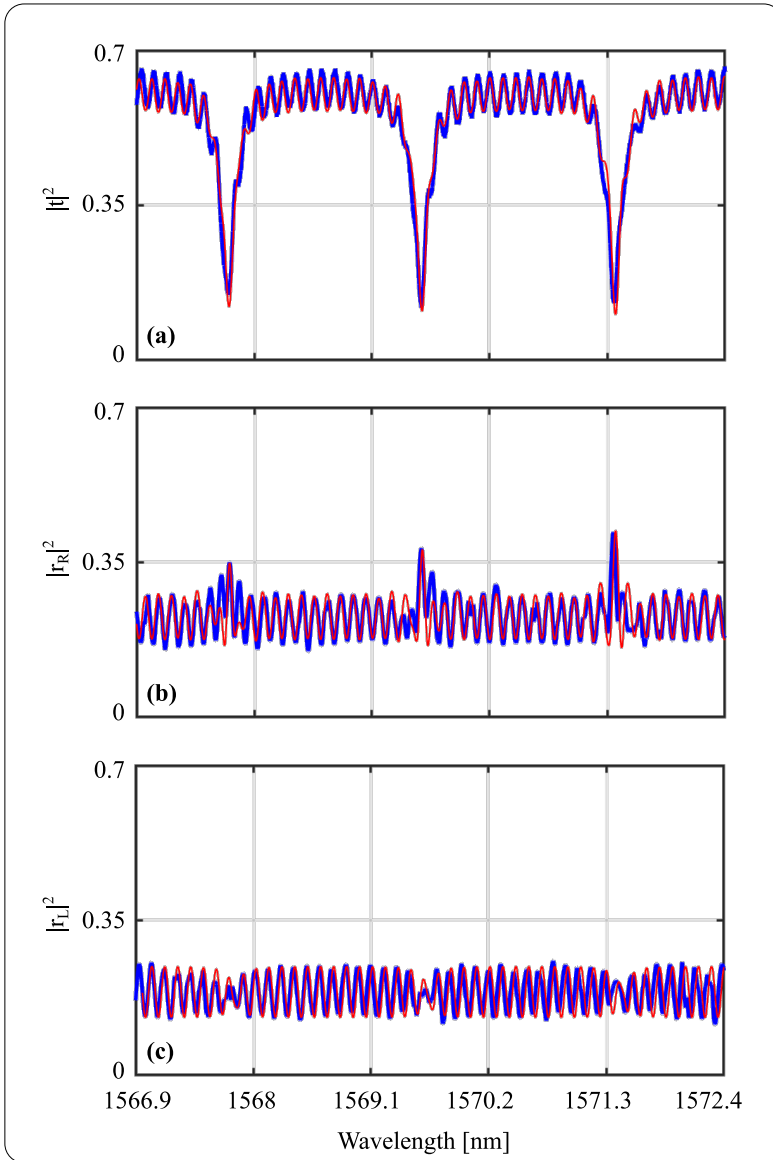


Figure 6.3: (a) Transmitted intensity as a function of the incident wavelength. Panels (b) and (c) show reflected intensity spectra for an incident beam from left and right respectively. The blue points are the experimental measurements while the red lines are the fit with the theoretical model (equations 2.36, 2.37 and 2.38).

6. Unidirectional reflection and time characterization

between the reflected field at the end of the waveguide and the reflected field inside the taiji microresonator.

The red lines show the fits with the theoretical model reported in section 2.3.11. In particular, the three curves have been fit using the expression for the transmission 2.36 and reflection 2.37, 2.38 amplitude. As can be seen in figure 6.3, these accurately reproduce the experimental behavior. Interestingly, the model captures the features related to the interference between the fields reflected by the facets and inside the taiji microresonator. As done for the backscattering and Fano interaction, a simultaneous fit process has been exploited to reproduce the experimental data. Also in this case, the simultaneous fit of the three spectra allows reducing the mutual dependency of the shared terms between the different equations. The parameters fixed in the fit procedure are the geometric dimensions of the taiji microresonator/waveguide. They are determined by the mask design and verified through SEM images. The free parameters used in the fit process are: the reflection coefficients of the input and output facets, the linear losses of the material, the coupling coefficients related to the microresonator/bus waveguide and the S-shape embedded into the cavity, a correction of the effective refractive index of the medium and a wavelength shift between the t_R and r_L . The correction of the effective index is just added to the results of Comsol Multiphysics. Precisely, we have extrapolated the effective refractive index as a function of wavelength by simulating the cross-section of the waveguide using the bulk refractive index estimated form FBK by an ellipsometry technique. On the other hand, the wavelength shift is necessary because t_R exhibits a slightly shift in wavelength with respect to the r_L . This shift is strictly connected to the laser source and it is due to the fact that t_R and r_L are measured at different times. In addition, we have introduced two distinct normalization processes to

Fit parameters	Values
Reflection amplitudes: $\rho_R = \rho_L$	0.2181 ± 0.0003
Losses: α	$(69.84 \pm 0.03) m^{-1}$
Coupling coefficient waveguide/taiji: t_1	0.95890 ± 0.00018
Coupling coefficients S-branch: $t_2 = t_3$	0.92058 ± 0.00067
Correction of the effective refractive index	-0.130510 ± 0.000003
Offset wavelength between t_L and r_R	$(-0.04453 \pm 0.00016) nm$

Fixed Parameters	Values
Distance taiji from facet L: l_L	$0.00329 m$
Length of the bus waveguide: $l_L + l_R$	$0.00591 m$
Length: $z_1 = z_3$	$0.000202 m$
Length: z_2	$0.000391 m$
Length: z_4	$0.000611 m$

Table 6.1: Parameters used in the fit process of the experimental data show in figure 6.3.

take into account the different offset and gain of the two *Ge* detectors used to measure the transmission and reflection response [63]. The free fit and the fixed parameters are reported in table 6.1.

In order to quantify the difference between the two reflection intensities, in figure 6.4 are drawn the values of the fit functions at the resonant wavelengths (λ_i). Precisely, the red squares show the transmitted intensity, the upward light blue triangles denote the reflected intensity for light incident from right, while the downward blue triangles are the reflected intensity for light incident from left. Both r_L and r_R coefficients take into account also the reflection of the facets and, therefore, they consider an inseparable contribution of the Fabry-Perot. Consequently, the values of the reflected intensities for light incident from left do not reduce to zero as in the case of an isolated taiji microresonator. However, comparing the upward with the downward triangles, one can see that the r_L is significantly lower than r_R for all the resonant wavelengths across the spectrum. Specifically, the average values of the resonant r_R and r_L intensities are 0.376 and 0.184, respectively. Therefore, the average value of the $|r_R(\lambda_i)|^2$ is about twice the average value of $|r_L(\lambda_i)|^2$. This is highlighted in figure 6.4 by the difference between the light blue and the blue dashed lines.

To conclude, we have seen that the introduction of an S-shaped waveguide in the cavity makes it possible to obtain a unidirectional reflection device. This represents, as seen in the theoretical section, an extreme case of the backscattering

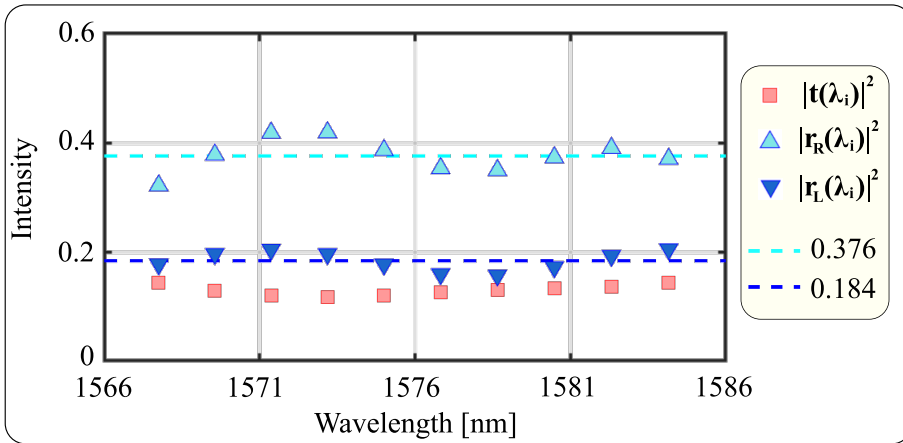


Figure 6.4: Intensity as a function of the wavelength computed with the equations 2.36, 2.37 and 2.38 using the parameters of table 6.1 at the resonant wavelengths (λ_i). Precisely, the red squares are the transmitted intensities, the upward light blue triangles are the reflected intensities for light incident from right and the downward blue triangles are the reflected intensities for light incident from left. The light blue and blue dashed lines denote the average of the resonant values for the $|r_R(\lambda_i)|^2$ and the $|r_L(\lambda_i)|^2$, respectively.

when one of the two β coefficients assumes a null value. We realized this particular cavity on a *Si* wafer and characterized its transmission and reflection response. We have seen that the analytical model, reported in section 2.2, reproduces not only the simulation outcomes but also the experimental measurements. In accordance with the Lorentz reciprocity theorem, the transmitted intensity for and input fed from right and from left is the same. On the contrary, the reflection exhibits a different behavior in the two directions of excitation. Precisely, it shows evident peaks in one direction and spurious reflections in the other. The taiji microresonator/waveguide system can be improved by decreasing the oscillations of the Fabry-Perot. This is possible by using different types of coupling with the chip, such as grating coupler, index matched liquid or inverse coupling [158]. In this way, the intrinsic properties of taiji can be isolated and the transmission and reflection is reduced to the ideal case seen in the subsection 2.3.9.

6.2 Time response measurements of an integrated microresonator

In this section, we will show the experimental measurements of the temporal response of a microresonator [95]. In particular, we will see how the intensity, as a function of time, allows estimating its intrinsic and extrinsic coefficients. In this way, we will determine the light storage capacity of the system by estimating the quality factor Q . In addition, the peculiar trend of the time response will permit defining the coupling regime of the microresonator/waveguide system.

6.2.1 Sample and Experimental setup

The sample studied is a Si_3N_4 ultra-high-quality factor racetrack microresonator monolithically integrated on a silicon chip. The system is based on a strip-loaded configuration and operates at both near-infrared and third-telecom wavelengths. In particular, the racetrack resonator has a bending radius of $350\ \mu m$, furthermore the strip-loaded design benefits from the absence of physically etched lateral boundaries to show minute light scattering. More details on the fabrication processes are reported in ref. [159].

Figure 6.5 shows the experimental setup used to measure the time response of an integrated optical cavity. The source is a continuum wave tunable laser diode (CWTL) operating in the near infrared range ($1061 - 1064\ nm$) with a maximum power of about $50\ mW$. Precisely, it is a distributed feedback Bragg laser diode and its emission can be tuned in frequency by changing either the laser temperature or the diode supply current. The diode is driven by a laser controller which allows setting the temperature with a resolution of $0.1\ ^\circ C$ and the supply current up to $0.01\ mA$. An optical fiber guides the beam to an electro-optical-modulator (EOM), which pulses the laser beam. This device is based on a Mach-Zehnder interferometer in which the arms are made of an optical crystal of Lithium-Niobate. Therefore, the refractive index changes as a function of the applied electric field and the output signal is characterized by

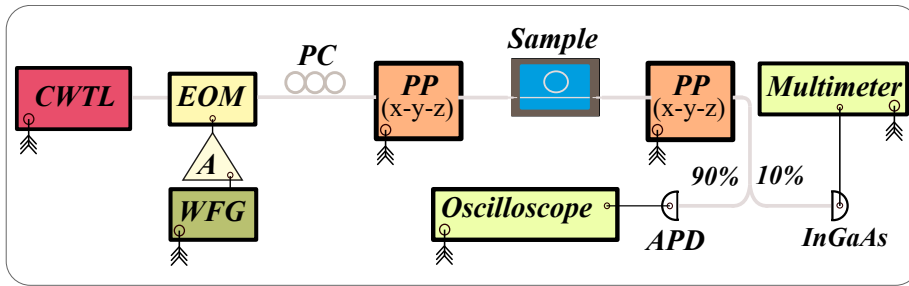


Figure 6.5: Sketch of the experimental optical setup. CWTL continuous wave tunable laser; EOM electro-optical-modulator; A amplifier; WFG wave front generator; PC polarization controller; PP piezo-positioners; APD silicon avalanche photo diode detector. The symbol “<<<” indicates the remote control via computer.

interference fringes [160]. The modulator is controlled via a waveform generator (WFG). This operates by sending patterns of bits that are sequences of zeros and ones, to a programmable amplifier that drives the optical modulator. Gain and bias of the amplifier are set in order to associate zeros to minimum possible optical output power, and ones to maximum power. The patterns can be as long as 2000 *bits*, while the bit rate can be varied between 50 *MHz* and 3.2 *GHz*. After the modulator a polarizer controller (PC) controls the polarization of the light. The light pulses are then coupled to the sample via a tapered fiber mounted on a $x - y - z$ piezo-positioners stage (PP). At the end of the sample another lensed tapered fiber mounted on another PP collects the transmitted light signal and transfers it to the detector. This consists of an *InGaAs* detector or a silicon avalanche photodiode (APD). The *InGaAs* detector has a much higher sensitivity compared to the APD, however it is much slower and, therefore, it is unsuitable for time resolved measurements. This detector is used to set the light polarization and to optimize the coupling between the lensed tapered fibers and the sample. While the APD is used to measure the time dependent response of the system. The APD is used with the internal gain set to about 100 and no additional electronic amplification.

6.2.2 Result discussion

A first transmission response of the waveguide/microresonator system is acquired by means of the *InGaAs* detector tuning the temperature. This allows verifying that the racetrack microresonator is single mode in the wavelength region of interest. Once the resonance to be characterized has been chosen, a detail scan around it is performed by controlling the laser current. In this way, the transmitted intensity exhibits a good resolution as shown in figure 6.6 (a). At this point, fixing the laser frequency it is possible to measure the time-dependent

6. Unidirectional reflection and time characterization

intensity (figure 6.6 (b)). Here, a rectangular pulse of duration 20 ns is used. Specifically, the green and blue curves represent the data measured when two different laser frequencies are used. The green (blue) line shows the system response out (on) resonance. In order to make the picture clearer, the green data and its fit are time shifted by about 1.5 ns . The racetrack resonator exhibits a time dependent response that is typical of resonators in the under-coupling regime. In fact, as we have seen in the theoretical part (subsection 3.2.1), in the under-coupling regime the round-trip losses become equal to the coupled power before the power inside the microresonator is high enough to observe the destructive interference. Therefore, the stationary state is reached without observing a zero value of the transmission intensity. In addition, at 20 ns , when the source is turned off, the peak before the exponential decay is lower than the peak formed at time zero during the resonator charging. This is typical of the

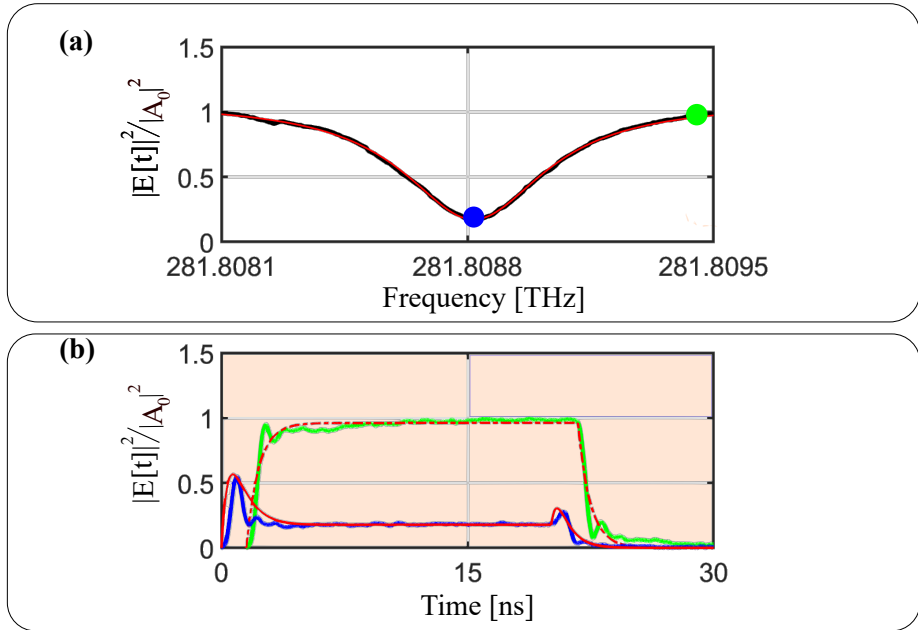


Figure 6.6: (a) and (b) Experimental normalized transmission spectra as a function of the incident frequency and time, respectively. The green (blue) data displays the system response out (on) resonance as indicated by the points in panel (a). The red solid-line of panel (a) shows the fit with the Lorentzian equation 2.12. The red dashed-line of panel (b) displays the fit with the typical expression of a RC filter, while the red solid-line shows the plot of the time response using the fit parameter obtained in the frequency spectra. The green data and its fit are shifted in time of about 1.5 ns in order to make the picture clearer.

under-coupling regime, where the power trapped in the micro-resonator is lower than the source's one.

The experimental data of figure 6.6 (a) have been fitted using equation 2.12. A quality factor $Q \approx (5.763 \pm 0.005) \times 10^5$ is estimated by the resonance width. As one can see in figure 6.6 (b), the field far from the resonance frequency (green line) is not perfectly steep as in the theoretical model of section 3.1. This behavior is related to the response times of the EOM and APD detector, which introduce two additional time constants, with the EOM one being negligible (10 GHz BW). As a result, the system exhibits a smooth response. The response time of the experimental set-up can be estimated by fitting the signal out of resonance with the convolution between the step function of equation 3.11 and an exponential ($\frac{\Theta(t)e^{-\frac{t}{\tau}}}{\tau}$). This convolution assumes the typical expression of a RC filter, where the time constant τ is connected to the time response of the EOM and of the APD detector [161]. The same reasoning can be applied to the transmitted signal on resonance which is given by the convolution between equation 3.14 and the exponential response ($\frac{\Theta(t)e^{-\frac{t}{\tau}}}{\tau}$). This convolution is plotted in figure 6.6 (b) by using the parameters obtained from the fit of the signal transmission on resonance ($\Gamma = (5.32 \pm 0.03) \times 10^8 \text{ Hz}$, $\gamma = (10.0 \pm 0.1) \times 10^8 \text{ Hz}$, $f_0 = 281.80882 \text{ THz}$) and the one of the out of resonance transmitted signal ($\tau = (750 \pm 10) \text{ ps}$). The model matches the time and the frequency response of the system and allows estimating a quality factor of about $Q \approx (5.77 \pm 0.01) \times 10^5$ at f_0 by using equation 3.20. This value matches the one estimated from the transmission line-shape (figure 6.6 (a)).

As in the analytical model of section 3.1, the step features observed in the FDTD simulation are not visible in Figure 6.6 (b). This is due to the small round-trip time. For the microresonator studied here ($R = 350 \mu\text{m}$, $n_{eff} = 2$), the round-trip time is 10 ps . Thus, the time resolution to see the steps is beyond our detector resolution. In ref. [162], a 2.2 km long optical fiber resonator is used and the steps due to the $10 \mu\text{s}$ round-trip time are visible in the exponential decay.

To conclude, we have analyzed the response of an integrated microresonator excited by a rectangular light pulse. In particular, it has been shown that the knowledge of the intensity of the time dependent electric field response permits, through its particular evolution, to understand the coupling regime of the system. The simple model capable of capturing the physics of a waveguide/microresonator system, presented in section 3.1, allows uniquely extrapolating from the measurements the experimental intrinsic and the extrinsic damping rates. In this way, both the coupling regime and the quality factor of a Si_3N_4 racetrack microresonator monolithically integrated on a silicon chip have been estimated.

6.3 From integrated devices to macroscopic cavities

The optical set-up used to measure the response of an integrated microresonator (see figure 6.5) has been modified to perform a cavity ring down (CRD) spectroscopy measurement on a macroscopic cavity. The sample studied has been designed by the Airbus space and defense division and is a Fabry-Perot optical stabilizing reference cavity for space applications. This is used in two main experiments: the first involves the creation of an optical clock while the second one is about laser stabilization in the LISA mission [163]. This cavity has been realized with an ultra-low-expansion glass and has an extremely high quality factor. Since in both applications, the cavity must be launched into space, it is important to know how the glass of the cavity reacts to ionizing radiation from the sun.

Typically, exposure to radiation can degrade optical mirrors and thus drastically decrease the quality factor. In fact, as reported in literature [164, 165], when mirrors are subjected to ionizing radiation, they can undergo different phenomena such as appearance of dark spots, refractive index variation due to density changes, fractures and dielectric breakdown. To investigate the action of ionizing radiation, Airbus has agreed a collaboration with FBK to simulate solar ionizing radiation by using the Research Laboratory of Proton Therapy Center at Trento. In this project, our laboratory (NanoLab) was responsible for measuring the quality factor before and after irradiation in order to determine the damage caused to mirrors by proton bombardment.

6.3.1 Sample and Experimental setup

In this thesis, we cannot reveal the material and characteristics of the mirrors used by Airbus. However, to give an idea of the size of the whole system, we can report that the distance between two mirrors of the Fabry-Perot cavity is about 5 *cm*.

The first part of our optical setup, consisting of the excitation source (CWTL) and the EOM (seen in figure 6.5) remains unchanged. On the contrary, the laser/sample coupling changes radically. In fact, the main difference between the integrated circuit and the Fabry-Perot cavity lies in the excitation of the system. In the case of an integrated microresonator, the transmission response is measured by injecting light into the input facet of the bus waveguide. The design of the microresonator/waveguide determines a priori the light transmission modes and the coupling regime. Therefore, from an experimental point of view it is prohibitive to choose a propagation mode inside the cavity simply by moving the lensed tapered fiber. Even in the case of a Fabry-Perot cavity, the design of the structure, i.e. the radius of curvature of the mirrors, the coating and the distance between them, fixes the transmission optical response. However, the lack of a bus waveguide allows varying the characteristics of the incident beam a posteriori and, therefore, to efficiently excite different cavity modes.

The lensed tapered fibers and translation stages are replaced by an optical system consisting of a collimator and two biconvex lenses (L1 and L2). As shown

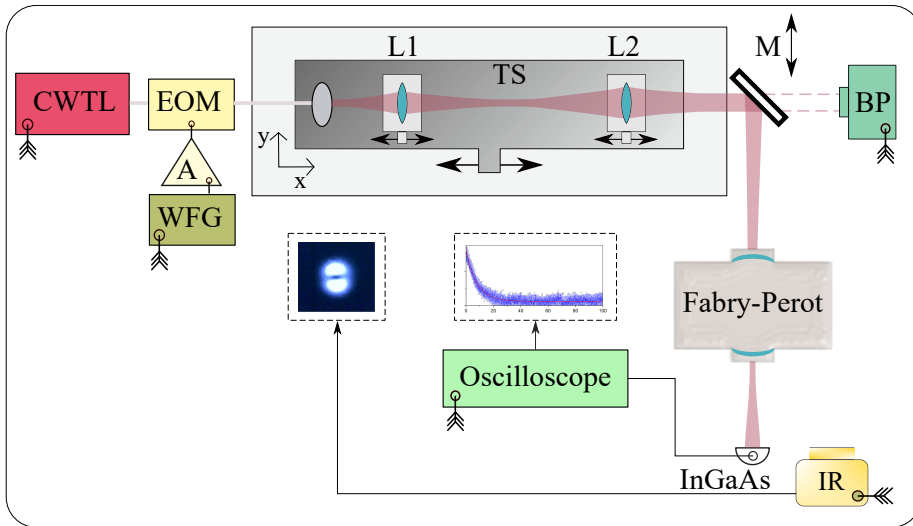


Figure 6.7: Sketch of the experimental optical setup. CWTL: continuous wave tunable laser; EOM: electro-optical-modulator; A: amplifier; WFG: wave front generator; Ln: n-th biconvex lens; TS: translation stage; M: mirror; BP: beam profiler; IR: infrared camera. The black arrows highlight the free movement direction. The symbol “≪≪≪” indicates the remote control via computer.

in figure 6.7, this system is placed on a mechanical translation stage (TS) that allows the movement along the x coordinate. In this way, it is possible to vary the distance between the excitation system and the mirror (M) which guides the beam to the entrance of the cavity. Moreover, since also each one of the two lenses are placed on a translation stage, it is possible to vary the relative distance between them (see black arrows of figure 6.7). This particular system allows not only varying the waist of the incident beam, but also its position. In fact, simply by translating the entire optical system, consisting of the collimator and the two lenses, it is possible to change the position of the waist inside the cavity. It is worth noticing that the excitation mirror (M) can be removed from the optical line to use a beam profile (BP). This allows characterizing the incident beam profile in the three spatial coordinates and, then, verifying the size and position of the waist. The output response of the cavity can be measured through an *InGaAs* detector or can be mapped in two dimensions by using an IR camera. In this case, it is not necessary to use an APD. In fact, as we will see in the next subsections, the high quality factor of the system permits to measure the time response of the cavity simply using an *InGaAs* detector. The signal thus measured is sent to an oscilloscope that records its trend (see figure 6.7).

6.3.2 Excitation of the TEM00 mode

As mentioned in the previous section, the excitation of the Fabry-Perot cavity needs a particular profile of the incident beam. Precisely, the aim of this project is the quality factor estimation for the fundamental mode, i.e. Transverse Electro Magnetic 00 (TEM00). The modal analysis of the confocal Fabry-Perot cavity shows that a waist of about $229 \mu m$, is required to excite the TEM00 mode. Since the mirrors are symmetrical, the proper excitation of the fundamental mode is obtained by placing this waist in the center of the cavity. This ensures that the spatial profile of the mode during the repeated transmission and reflection processes perfectly overlaps on the input and output mirror.

The biconvex lenses (L1 and L2) and their position on the translation stage were determined by using the ABCD matrix method. This allows representing the paraxial optical components when the aberrations introduced by the optical focusing elements are negligible [166]. The shape of the beam coming out of the collimator was measured as a function of distance, using the beam profile. In this way, it is possible to fix the waist of the incident beam and then, the initial conditions of the resolution via the ABCD matrix method. The figures 6.8 (a) and (b) show the beam intensity along the y and z coordinate respectively at $x = 1 \text{ cm}$ from the collimator. The blue points are the experimental data while the red lines are the fit with a Gaussian function ($A e^{-\frac{(x-b)^2}{2\sigma^2}}$). The fit parameters obtained for panels (a) ((b)) are: $A = 98.94 \pm 0.18 \text{ a.u.}$ ($A = 97.01 \pm 0.05 \text{ a.u.}$), $b = (-86.68 \pm 0.2) \mu m$ ($b = (-294.51 \pm 0.07) \mu m$) and $\sigma = (97.52 \pm 0.2) \mu m^2$ ($\sigma = (-107.39 \pm 0.07) \mu m^2$). The Gaussian shape can approximate the intensity profile of the beam coming out from the collimator. From different intensity profile measurements as a function of the distance (x), we estimated a minimum beam waist (w_0) at the collimator of about $= 209 \mu m$.

It is well known that a Gaussian profile at a given x position can be described by using the complex parameter q :

$$q[x] = \frac{1}{\frac{1}{R[x]} - i \frac{\lambda}{\pi w^2[x]}}, \quad (6.1)$$

where $R[x]$ ($w[x]$) is the x-dependent radius of curvature of the wavefront (the beam waist), while λ is the wavelength. In this way, the beam propagation through different optical elements, such as curved lenses and mirrors, can be described by changing its parameters with the ABCD matrix as [166]:

$$q'[x] = \frac{Aq + B}{Cq + D}. \quad (6.2)$$

In addition, the new minimum beam waist position is given by solving $BD + ACq^2 = 0$ [166]. The evolution of q as a function of the x coordinate allows uniquely describing the propagation of the Gaussian beam through the optical system. In our case, the ABCD matrix is determined by the propagation of light through the two biconvex lenses and can be expressed as:

$$\begin{pmatrix} A & B \\ C & D \end{pmatrix} = \begin{pmatrix} 1 & d_2 \\ 0 & 1 \end{pmatrix} \begin{pmatrix} 1 & 0 \\ -\frac{1}{f_2} & 1 \end{pmatrix} \begin{pmatrix} 1 & d_1 \\ 0 & 1 \end{pmatrix} \begin{pmatrix} 1 & 0 \\ -\frac{1}{f_1} & 1 \end{pmatrix} \begin{pmatrix} 1 & d_0 \\ 0 & 1 \end{pmatrix}, \quad (6.3)$$

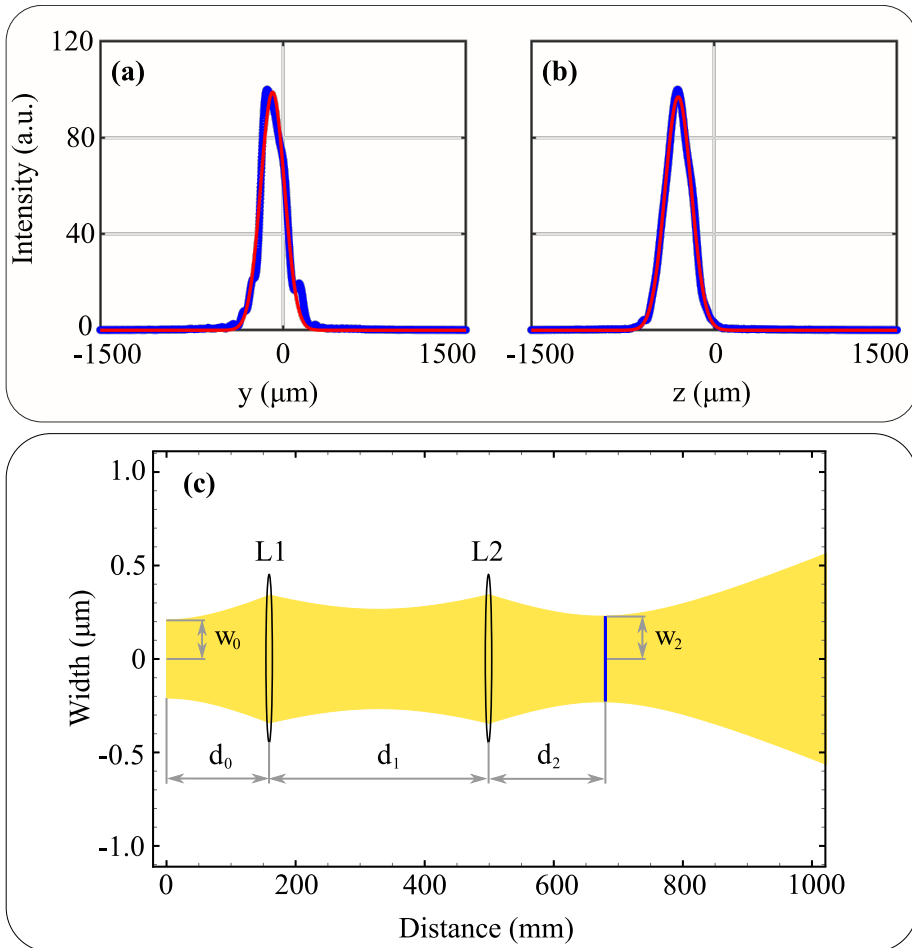


Figure 6.8: (a) and (b) Intensity profile in the y and z coordinates respectively. The blue points are the experimental values while the red lines are the fit with a Gaussian function. Panel (c): width of the Gaussian beam as a function of the distance computed via the ABCD matrix method. $L1$ and $L2$ are the two lenses of the optical system, w_i is the i -th minimum beam waist and d_j is the j -th distance. Precisely, the focal lengths of the lenses $L1$ and $L2$ are $f_1 = 160\text{ mm}$ and $f_2 = 180\text{ mm}$, respectively, while the distances from the collimator to the lens ($L1$) and between $L1$ and $L2$ are $d_0 = f_1$, $d_1 = f_1 + f_2$. Consequently, the distance between $L2$ and the waist (w_1) is $d_2 = f_2$ and $w_2 = 229\text{ }\mu\text{m}$.

where d_0 is the distance between the minimum beam waist (w_0), i.e. the collimator, and the first lens of focal f_1 . While d_1 is the distance between the two biconvex lenses and d_2 is the one between the lens of focal f_2 and the final

minimum beam waist w_2 . By exploiting the matrix product, we can reformulate the ABCD matrix as:

$$\begin{pmatrix} \frac{f_1-d_1}{f_1} + d_2 \left(\frac{d_1-f_1-f_2}{f_1 f_2} \right) & d_0 \left(d_2 \left(\frac{d_1-f_1-f_2}{f_1 f_2} \right) + \frac{f_1-d_1}{f_1} \right) + \frac{d_2(f_2-d_1)+d_1 f_2}{f_2} \\ \frac{d_1-f_1-f_2}{f_1 f_2} & d_0 \left(\frac{d_1-f_1-f_2}{f_1 f_2} \right) - \frac{d_1}{f_2} + 1 \end{pmatrix} \quad (6.4)$$

The figure 6.8 (c) shows the Gaussian beam evolution obtained solving equation 6.2 with the matrix elements of 6.4. Precisely, a particular solution obtained by fixing $d_0 = f_1$ and $d_1 = f_1 + f_2$ is reported. This results in a distance, $d_2 = f_2$ and in a final minimum waist, $w_2 = w_0 \frac{f_2}{f_1}$. Taking advantage of this solution and knowing that the excitation of a TEM00 mode requires a beam waist of about $229 \mu m$, we have chosen two lenses (L1 and L2) with focal lengths $f_1 = 160 mm$ and $f_2 = 180 mm$.

6.3.3 Result and discussion

Once the distances between the lenses of the excitation system have been set, the mirror (M) is aligned so that the light is impinged perpendicular into the cavity. This has been achieved by fixing the *InGaAs* detector to the output of the cavity and monitoring the transmission response. In this case, the controller of the laser is set to scan continuously over a range larger than the free spectral range of the cavity. Subsequently, the laser wavelength is tuned manually where the signal transmission is maximum. In addition, the input mirror is re-adjusted to maximize the output signal.

The detector is replaced by the infrared camera. This allows verifying the mode pattern and, therefore, better adapting the distance between the lenses and the position of the translation stage. At the end of this procedure, only the circular TEM00 mode spot is mapped in 2D by the camera. At this point, it is possible to measure, by mounting again the *InGaAs* detector at the output of the cavity, the decay time of the CRD. The typical mono-exponential discharge pattern is acquired several times. In order to verify the optical setup and to test its versatility, the second TEM01 mode is also measured. With the IR camera mounted at the output of the cavity, the wavelength of the laser is varied in order to maximize the typical two-lobe pattern of the TEM01 mode. Then, by changing the distance between the lenses and the translation stage position, the mode coupling is maximized.

As we have seen in the previous section, the decay time measurement is affected by the response time of the detector and EOM. Therefore, we make sure that the input laser is shut-down at a higher speed than the typical discharge decay constant. This is possible by simply measuring with the *InGaAs* detector the response of the optical system before entering the cavity.

Figure 6.9 shows the results obtained from CRD measurements before and after exposure to the proton beam. In particular, panels (a) and (b) display the measurement of the intensity transmitted as a function of time for the TEM00 and TEM01 modes before the proton bombardment. As can be seen, when the laser source is shut-down, the cavity discharge is characterized by the typical

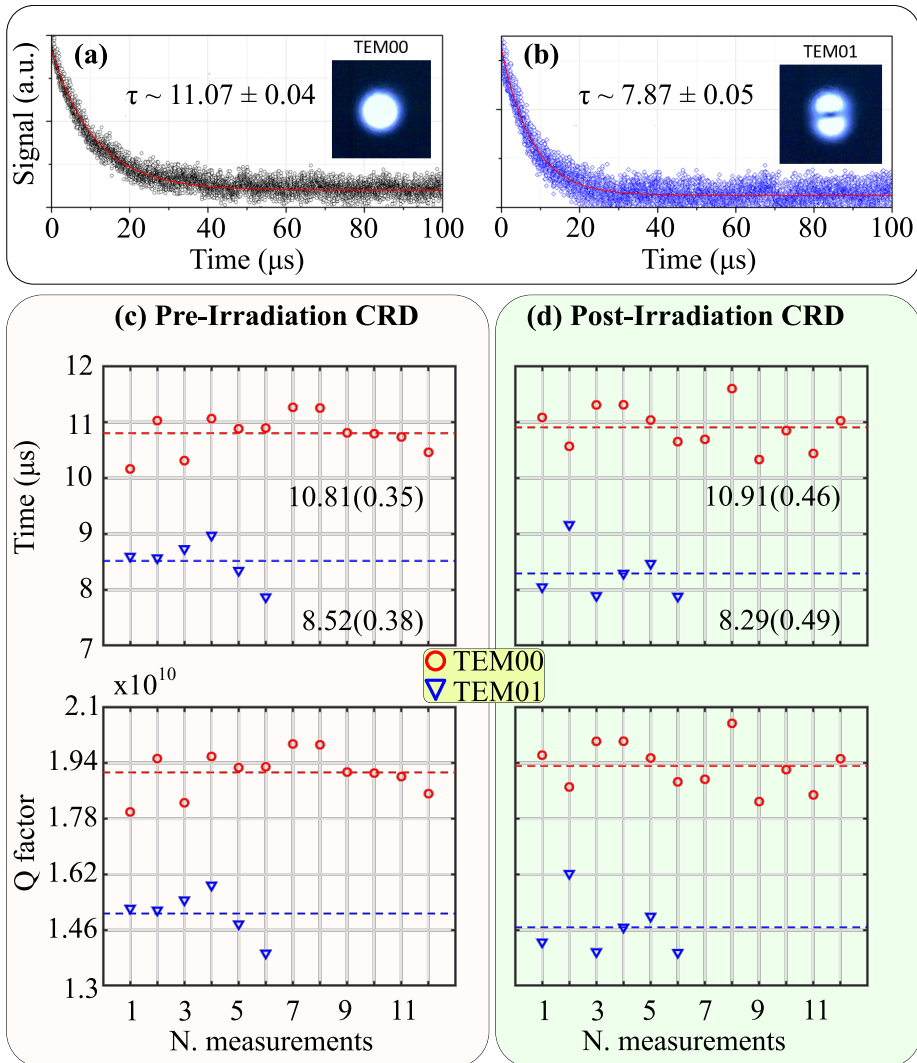


Figure 6.9: (a) and (b) Transmitted intensity as a function of time of the Fabry-Perot cavity for the TEM00 and TEM01 modes, respectively. When the laser is shut-down, the cavity discharges the trapped power following the typical mono-exponential pattern. The inset pictures display the IR camera images. Panels (c) and (d): fit results for the time constant before and after the proton bombardment for TEM00 (red circles) and TEM01 (blue down-pointing triangles). Precisely, the upper (lower) graph shows the time constant (Q factor).

exponential pattern. The blue dots represent the experimental measurements,

6. Unidirectional reflection and time characterization

while the red line shows the fit with an exponential function like $e^{-\frac{\omega}{Q}t}$, where ω is the incident frequency of the laser and Q is the quality factor. In this way, one can define the decay time constant as $\tau = Q/\omega$. The exponential discharge function can be easily obtained by exploiting the definition via energy stored of the quality factor [95] (see equation 3.15). From the fit of panels (a) and (b), time constants of $(11.07 \pm 0.04) \mu m$ and $(7.87 \pm 0.05) \mu m$ are estimated for the TEM00 and the TEM01 modes. This corresponds to a quality factor of $(1.9598 \pm 0.0071) \cdot 10^{10}$ and $(1.3933 \pm 0.0088) \cdot 10^{10}$ respectively. Here, is worth to point out that the time constant of both modes is much higher than the time constant estimated by the time measurement of the beam before entering the cavity ($165 ns$). For this reason, it is not necessary to use the APD as in the case of the integrated microresonator.

The images in the inset of panels (a) and (b) show the IR camera image for TEM00 and TEM01 mode, respectively. As anticipated, the fundamental mode is characterized by a single circular spot, while the TEM01 mode exhibits two lobes. Figures 6.9 (c) and (d) show the time constants and quality factors estimated by the fit procedure for different CRD measurements. Precisely, the two panels show the results before and after exposure to the proton beam. As can be seen, the quality factor before and after remains unchanged within the experimental error and therefore we can say that the mirrors are not affected by radiation exposure.

To conclude, it has been seen that the optical setup built for the time measurement of an integrated circuit can be exploited also for a macroscopic cavity. The free space measurement has made it necessary to introduce an optical system consisting of two biconvex lenses and a collimator. This allows varying the characteristics of the incident beam and, therefore, excite the TEM00 and TEM01 modes. The discharge is characterized by the typical exponential decay from which the quality factor can be estimated. Therefore, the time constant permits to understand that the exposure to the proton beam does not influence the mirrors designed by the Airbus space and defense agency.

Chapter 7

Conclusion

This thesis explored fundamental concepts of linear optics focusing on the modal interaction within waveguide/microresonator systems. In addition, it investigated a nonlinear process of sDFWM in a channel waveguide exploiting the analogy between photons and cold boson atoms. The backscattering phenomenon is addressed within the λ three-level framework making use of graphic methods based on the phasor diagram and the inverse complex representation. The interaction between counterpropagating modes is studied considering the presence of conservative and dissipative coupling coefficients, namely Hermitian and non-Hermitian terms. Precisely, the model of chapter 2 along with the experimental results of chapter 5 show that the stochastic nature of the surface wall roughness can give rise to an unbalanced doublet, i.e. a different height in the depth of the split peaks. This is evident in a multimodal microresonator, where additional couplings and loss channels could mediate the energy exchange increasing the non-Hermitian nature. The unbalanced exchange of energy between the two modes with opposite angular momenta can generate a different reflection by swapping the injection of the light between the input and the output ports. This effect lies at the heart of the realization of an unidirectional reflection device and it finds an explanation in the physics of the exceptional points. Such a counterintuitive behavior is proved by introducing an S-shape waveguide inside the microresonator and then forcing, as a function of the S orientation, the exchange of energy to CW or CCW mode. Finally, the knowledge acquired in the analysis of the backscattering phenomenon is used to model the Fano lineshape, considering a system composed by a two-mode microresonator coupled to a single mode bus waveguide. The versatility of our optical setup based on a Free-space Mach-Zhender interferometer allows measuring both the transmitted intensity and the phase. This paves the way to investigate the theoretical model introduced in ref. [84]. The presence of an off-diagonal coefficient analogous to the Lamb shift in atomic physics is confirmed, but the reliability of different fit parameters leaves its sign an open question. In all these studied phenomena, a theoretical model is provided along with a first numerical validation, and a final comparison with the experimental outcomes.

Chapter 2 analyses the field propagation in the frequency domain focusing on the stationary regime. The time response is studied in chapter 3, where is reported a simple theoretical model able to describe the temporal evolution of a field propagating in a waveguide/microresonator system. Numerical simulations with a FDTD software verify the predictions of the analytical model. Precisely, the response of a microresonator to a rectangular pulse of light has been analyzed in detail. This allows understanding the time evolution of the light propagating in the three different coupling regimes: over-, critical, under-coupling. Because

7. Conclusion

of the coupling, a different interference between the light propagating along the waveguide and that circulating into the microresonator occurs. This interference defines both the intensity and the phase of the output field. Consequently, the regime of the system can be understood by looking at the intensity of the time dependent electric field response. In addition, the fundamental coupling parameters such as the intrinsic and the extrinsic coefficients are connected to the quality factor allowing a complete characterization of the microresonator. In chapter 6, an experiment demonstrates the validity of the theoretical analysis in the case of the under-coupling regime. Here, the quality factor and the coupling regime are estimated for a Si_3N_4 racetrack resonator monolithically integrated on a Si chip. Finally, the experimental setup is extended to measure the time response of a free space cavity of the Fabry-Perot type. The exponential decay of this macroscopic cavity allows to characterize the TEM00 and TEM01 modes by using the definition of the quality factor via the stored energy. In addition, it permits to demonstrate that the mirrors designed by the Airbus space and defense agency are not affected by the exposure to a proton beam.

Chapter 4 deals with the propagation of a high-power laser along a channel waveguide, which exhibits a third-order susceptibility. Exploiting the analogy between the pulse propagation equation and the Gross-Pitaevskii equation of a Bose Einstein condensate, a sDFWM process is reformulated in the language of the Bogoliubov theory. This parallelism between photons and cold atoms finds its base in the mapping between the propagation coordinate and the time ($z \xleftrightarrow{\text{mapped}} t$). Consequently, the confinement of light gives rise to an effective mass of the photons connected to the group velocity dispersion of the structure. At the same time, the nonlinearity of the material generates an interaction between the photons related to the Kerr nonlinear parameter. This does not only pave the way to study the peculiar physics of cold atom on optical platforms, but also permits to introduce phenomena that are exotic in classical optics. Indeed, this chapter demonstrates that the phase of the signal and idler in a sDFWM process behaves as the Bogoliubov dispersion relation. Precisely, we show that a low-power signal propagating concurrently with an high-power pump assumes a phonon-like dispersion for small detuning between the frequencies of the pump and the signal, while the classical parabolic dispersion relation is recovered for large detuning. Since the effective mass and the interaction of the photons are strictly connected to the system under study, the design of the waveguide structures and the choice of the materials allow analyzing different scenarios. Here, we show the theoretical derivation and a possible way to extrapolate the phase by means of interferometry measurements. Unfortunately, this process is under investigation and does not find an experimental validation in this thesis. Although, the novel optical setup based on a free space Mach-Zhender interferometer, reported in chapter 5, is completed and allows performing pump and probe experiments, the optimum design of the waveguide is not yet available. For the sake of completeness, the last part of chapter 4 reports the response of a waveguide/microresonator system to a high-power laser. Precisely it shows how the thermo optic coefficient and the Kerr nonlinearity modify the transmission

response. A simple model based on the introduction of a nonlinear term in the usual temporal equation allows understanding the asymmetrical behavior reported in the characterization of the SiON platform in chapter 5.

In conclusion, in this work we have seen that a detailed description of a fundamental phenomenon, such as the backscattering of light due to the surface wall roughness, allows introducing versatile complex visualization techniques, which can be easily extended to analyze more complex phenomena as for example the Fano interference. Most importantly, this detailed explanation allows discovering new unintuitive behaviors, which can be used in new devices. In fact, the accurate knowledge of the exchange of energy between the counter-propagating modes inside a microresonator allows designing devices that, working on an exceptional point, behave like unidirectional reflection systems. These fundamental analyses of the response of non-Hermitian devices are a step toward the investigation of more complex structures, which can link the topological to the non-Hermitian physics. An example can be a particular matrix of taiji microresonators or an array of microresonators properly perturbed in order to obtain a peculiar unbalance between the counter-propagating modes. Here, the introduction of optical nonlinearity and/or gain can induce new behaviors and, therefore, the develop of novel applications.

Appendices

Appendix A

A simple model of a Mach-Zhender interferometer

The response of a Mach-Zhender interferometer can be modeled simply considering the propagation of two laser beams along the reference and the sample arms. This allows explaining the oscillating pattern of the interference seen in the characterization of the optical setup for the *SiON* waveguides (chapter 5). Considering the sketch of figure A.1, let us write the field taking into account the contributions of the different materials, which compose the sample and the reference arms. Precisely, at the last beam splitter (*BS2*) the wave propagating along the sample arm can be formulated as:

$$A_S = A_0 bs_1 bs_2 e^{-\frac{2i\pi c}{\lambda} t + \frac{4i\pi n_{bs}[\lambda]L_{bs}}{\lambda} + \frac{4i\pi n_{ob}[\lambda]L_{ob}}{\lambda} + \frac{2i\pi L_{as}}{\lambda}} \tau_S[\lambda], \quad (\text{A.1})$$

where A_0 is the amplitude of the probe beam while bs_1 and bs_2 are coefficients connected to the beam splitter *BS1* and *BS2* respectively. They consider the fraction of light which propagates along the two arms and, therefore, for a 50×50 beam splitter they reduce to $1/\sqrt{2}$. The first exponential argument ($-\frac{i2\pi c}{\lambda} t$) takes into account the oscillating part of the electric field where λ is the

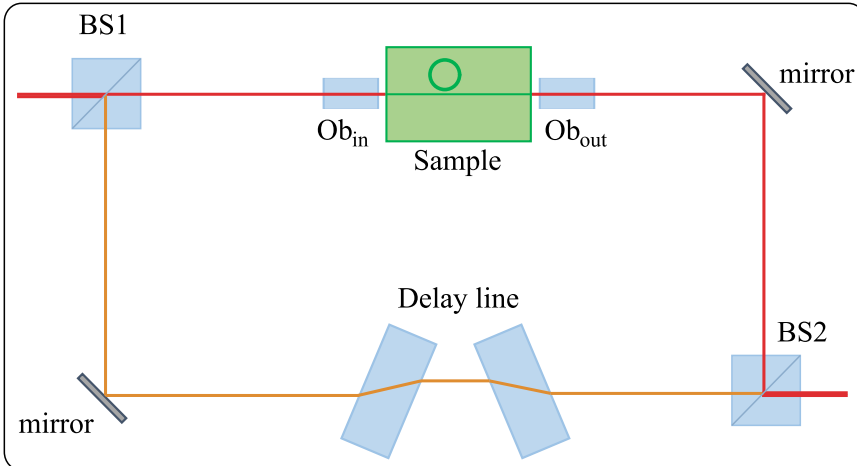


Figure A.1: Schematic representation of a Mach-Zhender interferometer. The red (orange) lines display the optical path of the sample (reference) arm. The label ob_{in} (ob_{out}) stands for input (output) objective.

A. A simple model of a Mach-Zhender interferometer

wavelength of the probe. While the second term considers the contribution to the phase of the beam splitters and reads as $\frac{i4\pi n_{bs}[\lambda]L_{bs}}{\lambda}$. Here, L_{bs} is the length of the beam splitter while n_{bs} is its effective index. It is worth noticing that we assume the same length and the same dispersion for the two beam splitters. The contribution of the two objectives is given by the third term of the argument, i.e. $i\frac{4\pi n_{op}[\lambda]}{\lambda}L_{ob}$. In this formulation, L_{ob} is the length of the objective lenses while n_{ob} is its wavelength dependent effective index. To simplify the description in this case we consider two identical objectives for the input and output coupling with the sample. The last term of the exponential takes into account the total air path traveled by the beam along the sample arm. The phase variation induced by the sample is enclosed in the wavelength dependent τ_S factor. For a simple waveguide in the linear regime, it can be formulated as:

$$\tau_S[\lambda] = e^{i\beta[\lambda]L_w - \alpha L_w}, \quad (\text{A.2})$$

where $\beta[\lambda]$ is the propagation constant and α (L_w) represents the linear losses (length) of the waveguide. In addition, it is possible to consider the fast oscillations induced by the Fabry-Perot cavity formed by reflections at the two facets of the waveguide by reformulating the τ_S coefficient as:

$$\tau_S[\lambda] = \frac{t^2 e^{i\beta[\lambda]L_w - \alpha L_w}}{1 - r^2 e^{2(i\beta[\lambda]L_w - \alpha L_w)}}, \quad (\text{A.3})$$

where we assume the same transmittivity (t) and reflectivity (r) of the two sample facets. It is worth noticing that by changing $\tau_S[\lambda]$ it is possible to deal with the response of different devices. For example, using the transmission amplitude seen in chapter 2 by means of equation 2.46, one can integrate in this simple model the response of a waveguide/microresonator system.

In the same way, considering the sketch of figure A.1, we can reformulate the wave propagating along the reference arm as:

$$A_R = A_0 bs'_1 bs'_2 e^{-\frac{2i\pi c}{\lambda}t + \frac{4i\pi n_{bs}[\lambda]L_{bs}}{\lambda} + \frac{2i\pi n_{dl}[\lambda]L_{dl}}{\lambda} - L_{dl}\alpha_{dl} + \frac{2i\pi L_{ar}}{\lambda}}, \quad (\text{A.4})$$

where we add to the exponential argument the contribution of the delay line. Precisely, using a delay line of glass we introduce an effective index dependent on the wavelength ($n_{dl}[\lambda]$) and a possible loss term ($\alpha_{dl} L_{dl}$). On the contrary, using an air delay line, the only contribution is due to the additional path traveled in air by the beam and the arguments reduces to $\frac{i2\pi L_{dl}}{\lambda}$. The bs'_1 and bs'_2 are the fraction coefficients of the BS1 and BS2, and they are connected via the energy conservation to bs_1 and bs_2 .

Once the two beams are formulated taking into account the different contribution along their individual arms, the intensities related to the three mechanical shutters configurations can be found in the form: $I_S = |A_S|^2$, $I_0 = |A_R|^2$ and $I = |A_S + A_R|^2$. Neglecting the Fabry-Perot of the sample facets, considering a delay line in air and two beam splitters 50 x 50, the interference reduces to:

$$I[\lambda] = 4 A_0^2 bs_1^2 bs_2^2 \cos \left[\frac{\pi (L_{as} - L_{ar} - L_{dl} + 2n_{ob}[\lambda]L_{ob} + n_s[\lambda]L_s)}{\lambda} \right]^2 \quad (\text{A.5})$$

It is worth noticing that the phase contribution of the beam splitters cancels in the interference because it is present in both arms traveled by the beam. In the last equation, we can identify two contributions: a geometrical one connected to the free space interferometer ($L_{as} - L_{ar} - L_{dt}$) and one related to the sample response and the objective lenses ($2n_{ob}[\lambda]L_{ob} + n_s[\lambda]L_s$). In this derivation we consider only one output of the last beam splitter (BS2). The other response changes just the interference, that, due to the energy conservation, is shifted by $\pi/2$. Moreover, in order to simplify the description, the third beam splitter is neglected in this derivation. Obviously, one can consider this contribution adding another fraction term (bs_3) and a phase accumulation ($e^{\frac{2i\pi n_{bs3}[\lambda]L_{bs3}}{\lambda}}$) on the reference arm.

Therefore, at this point the phase difference between the two arms can be calculated by using the usual interferometric equation 5.2. Figures A.2 (a) and (b) show the results of this simple model for the three intensities: I_0 , I_S and I as a function of the probe wavelength. Precisely, panel (a) displays the response of the Mach-Zhender to a waveguide, which exhibits a Fabry-Perot modulation due to the facets. While panel (b) shows the response for a waveguide/resonator system obtained considering a τ given by equation 2.42. In this last case we consider also a weak amplitude modulation due to the facets of the sample. As shown in panel (a) the Fabry-Perot of the waveguide gives rise to a fast oscillation of the sample arm intensity. This introduces the same modulation on the intensity of the interference. On the other hand in figure A.2 (b), the response of the waveguide/microresonator system gives rise to a set of Lorentzians in the transmission spectra that introduces some features in the interference. The phase is computed using equation 5.2 by exploiting the intensities of panel (a) and (b) and thus it is plotted in panel (c) and (d) respectively. As mentioned in chapter 5, the phase is folded each time it reaches the theoretical limits of the *arccosine* function (0 and π). The corresponding unfolded representation can be easily obtained with post processing of the phase signal. Anyway, the sharp variation of the phases induced by the resonances can be easily identified inside panel (c) at the resonant wavelength of the resonator.

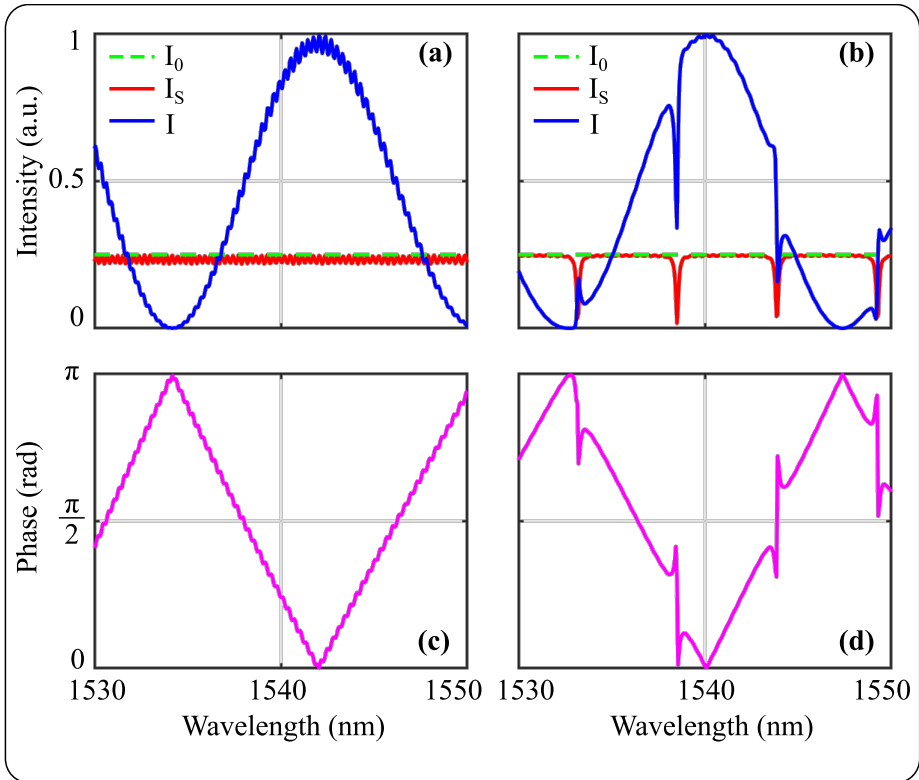


Figure A.2: (a) and (b) Intensity of the sample arm (I_S), reference arm (I_0) and interference (I) as a function of the wavelength computed by the theoretical model. Precisely, panel (a) shows the case of a single mode waveguide which exhibits a Fabry-Perot oscillation due to its facets. While panel (b) displays the case of a waveguide/microresonator system simulated by considering τ_S given by equation 2.42. Panel (c) and (d) show the phase computed by equation 5.2 considering the intensities of figures (a) and (b) respectively.

Bibliography

- [1] J. Kerry and K. J. Vahala. “Optical microcavities”. In: *Nature* vol. 424 (2003), pp. 839–846.
- [2] F. Vollmer and L. Yang. “Label-free detection with high-Q microcavities: a review of biosensing mechanisms for integrated devices”. In: *Nanophotonics* vol. 1, no. 1 (2012), pp. 267–291.
- [3] A. Samusenko, D. Gandolfi, G. Pucker, T. Chalyan, R. Guider, M. Ghulinyan, and L. Pavesi. “A SiON Microring Resonator-Based Platform for Biosensing at 850 nm”. In: *Journal of lightwave technology* vol. 34 (2016).
- [4] J. Müller, F. Merget, S. S. Azadeh, J. Hauck, S. R. Garcia, B. Shen, and J. Witzens. “Optical Peaking Enhancement in High-Speed Ring Modulators”. In: *Nature Photonics* vol. 4 (2014).
- [5] S. Amiri and A. Afroozeh. *Ring Resonator Systems to Perform Optical Communication Enhancement Using Soliton*. Springer, 2015.
- [6] T. Udem, R. Holzwarth, and T. W. Hänsch. “Optical frequency metrology”. In: *Nature* vol. 416, no. 9 (2002), pp. 233–237.
- [7] S. B. Papp, K. Beha, P. Del’Haye, F. Quinlan, H. Lee, K. J. Vahala, and S. A. Diddams. “Microresonator frequency comb optical clock”. In: *Optica* vol. 1, no. 1 (2014), pp. 10–14.
- [8] J. E. Heebner and R. W. Boyd. “SLOW AND STOPPED LIGHT ‘Slow’ and ‘fast’ light in resonator-coupled waveguides”. In: *Journal of Modern Optics* vol. 49, no. 14-15 (2002), pp. 2629–2636.
- [9] P. D. Haye, A. Schliesser, O. Arcizet, T. Wilken, R. Holzwarth, and T. J. Kippenberg. “Optical frequency comb generation from a monolithic microresonator”. In: *Nature* vol. 450 (2007), pp. 1214–1217.
- [10] J. W. Silverstone, R. Santagati, D. Bonneau, M. J. Strain, M. Sorel, J. L. O’Brien, and M. G. Thompson. “Qubit entanglement between ring-resonator photon-pair sources on a silicon chip”. In: *Nature Communications* vol. 6, no. 7948 (2015), pp. 1214–1217.
- [11] T. J. Kippenberg, S. M. Spillane, and K. J. Vahala. “Modal coupling in traveling-wave resonators”. In: *Opt. Lett.* Vol. 27, no. 19 (2002), pp. 1669–1671.
- [12] A. Li, T. V. Vaerenbergh, P. D. Heyn, P. Bienstman, and W. Bogaerts. “Backscattering in silicon microring resonators: a quantitative analysis”. In: *Laser Photonics Rev.* Vol. 10, no. 3 (2016).

- [13] M. Borselli, T. J. Johnson, and O. Painter. “Beyond the Rayleigh scattering limit in high-Q silicon microdisks: theory and experiment”. In: *Opt. Express* vol. 13, no. 5 (2005), pp. 1515–1530.
- [14] Q. Li, Z. Zhang, J. Wang, M. Qiu, and Y. Su. “Fast light in silicon ring resonator with resonance-splitting”. In: *Opt. Express* vol. 17, no. 2 (Jan. 2009), pp. 933–940.
- [15] Z. Zhang, M. Dainese, L. Wosinski, and M. Qiu. “Resonance-splitting and enhanced notch depth in SOI ring resonators with mutual mode coupling”. In: *Opt. Express* vol. 16, no. 7 (2008), pp. 4621–4630.
- [16] S. Biasi, F. Ramiro-Manzano, F. Turri, P. Larré, M. Ghulinyan, I. Carusotto, and L. Pavesi. “Hermitian and Non-Hermitian Mode Coupling in a Microdisk Resonator Due to Stochastic Surface Roughness Scattering”. In: *IEEE Photonics Journal* vol. 11, no. 2 (Apr. 2019), pp. 1–14.
- [17] L. D. Bino, J. M. Silver, S. L. Stebbings, and P. Del’Haye. “Symmetry Breaking of Counter-Propagating Light in a Nonlinear Resonator”. In: *Scientific Reports* vol. 7 (2017).
- [18] R. El-Ganainy, M. Khajavikhan, D. N. Christodoulides, and S. K. Ozdemir. “The dawn of non-Hermitian optics”. In: *Communications Physics* vol. 2, no. 1 (2019), p. 37.
- [19] M. A. Miri and A. Alù. “Exceptional points in optics and photonics”. In: *Science* vol. 363, no. 6422 (2019).
- [20] O. Yasutomo, T. Kenta, O. Tomoki, A. Alberto, J. Zhetao, K. Boubacar, N. Masaya, A. Yasuhiko, and I. Satoshi. “Active topological photonics”. In: vol. 9 (2020). 3, p. 547.
- [21] H. Ramezani, T. Kottos, R. El-Ganainy, and D. N. Christodoulides. “Unidirectional nonlinear \mathcal{PT} -symmetric optical structures”. In: *Phys. Rev. A* vol. 82 (4 Oct. 2010), p. 043803.
- [22] B. Peng, c. K. Özdemir, M. Liertzer, W. Chen, J. Kramer, H. Yilmaz, J. Wiersig, S. Rotter, and L. Yang. “Chiral modes and directional lasing at exceptional points”. In: *Proceedings of the National Academy of Sciences* vol. 113, no. 25 (2016), pp. 6845–6850.
- [23] M. A. Bandres, S. Wittek, G. Harari, M. Parto, J. Ren, M. Segev, D. N. Christodoulides, and M. Khajavikhan. “Topological insulator laser: Experiments”. In: *Science* vol. 359, no. 6381 (2018).
- [24] B. Midya, H. Zhao, and L. Feng. “Non-Hermitian photonics promises exceptional topology of light”. In: *Nature Communications* vol. 9, no. 1 (2018), p. 2674.
- [25] I. Carusotto and C. Ciuti. “Quantum fluids of light”. In: *Rev. Mod. Phys.* Vol. 85 (1 2013), pp. 299–366.
- [26] I. Carusotto. “Superfluid light in bulk nonlinear media”. In: *Proceedings of the Royal Society A: Mathematical, Physical and Engineering Sciences* vol. 470, no. 2169 (2014), p. 20140320.

-
- [27] P.-E. Larré, S. Biasi, F. Ramiro-Manzano, L. Pavesi, and I. Carusotto. “Pump-and-probe optical transmission phase shift as a quantitative probe of the Bogoliubov dispersion relation in a nonlinear channel waveguide”. In: *Eur. Phys. J. D* vol. 71, no. 6 (2017), p. 146.
- [28] A. Amo, J. Lefrère, S. Pigeon, C. Adrados, C. Ciuti, I. Carusotto, R. Houdré, E. Giacobino, and A. Bramati. “Superfluidity of polaritons in semiconductor microcavities”. In: *Nature Physics* vol. 5, no. 11 (2009), pp. 805–810.
- [29] G. Grosso, G. Nardin, F. Morier-Genoud, Y. Léger, and B. Deveaud-Plédran. “Soliton Instabilities and Vortex Street Formation in a Polariton Quantum Fluid”. In: *Phys. Rev. Lett.* Vol. 107 (24 2011), p. 245301.
- [30] E. Noether. “Invariant Variation Problems”. In: *Gott. Nachr.* Vol. 1918 (1918), pp. 235–257.
- [31] R. M. Marino. “Noether's theorem in classical mechanics revisited”. In: *European Journal of Physics* vol. 28, no. 1 (Oct. 2006), pp. 37–43.
- [32] R. Loudon. *The Quantum Theory of Light*. Vol. 42. Jan. 2000.
- [33] R. El-Ganainy, K. G. Makris, M. Khajavikhan, Z. H. Musslimani, S. Rotter, and D. N. Christodoulides. “Non-Hermitian physics and PT symmetry”. In: *Nature Physics* vol. 14 (Jan. 2018). Review Article, 11 EP.
- [34] S. K. Özdemir, S. Rotter, F. Nori, and L. Yang. “Parity-time symmetry and exceptional points in photonics”. In: *Nature Materials* (2019).
- [35] M. Berry. “Physics of Nonhermitian Degeneracies”. In: *Czechoslovak Journal of Physics* vol. 54, no. 10 (Oct. 2004), pp. 1039–1047.
- [36] C. M. Bender and S. Boettcher. “Real Spectra in Non-Hermitian Hamiltonians Having PT Symmetry”. In: *Phys. Rev. Lett.* Vol. 80 (24 June 1998), pp. 5243–5246.
- [37] Z. Lin, H. Ramezani, T. Eichelkraut, T. Kottos, H. Cao, and D. N. Christodoulides. “Unidirectional Invisibility Induced by PT -Symmetric Periodic Structures”. In: *Phys. Rev. Lett.* Vol. 106 (21 May 2011), p. 213901.
- [38] L. Feng, Y.-L. Xu, W. S. Fegadolli, M.-H. Lu, J. E. B. Oliveira, V. R. Almeida, Y.-F. Chen, and A. Scherer. “Experimental demonstration of a unidirectional reflectionless parity-time metamaterial at optical frequencies”. In: *Nature Materials* vol. 12 (Nov. 2012), 108 EP –.
- [39] L. Feng, X. Zhu, S. Yang, H. Zhu, P. Zhang, X. Yin, Y. Wang, and X. Zhang. “Demonstration of a large-scale optical exceptional point structure”. In: *Opt. Express* vol. 22, no. 2 (Jan. 2014), pp. 1760–1767.
- [40] A Guo, G. Salamo, D Duchesne, R. Morandotti, M. Volatier, V Aimez, G A Siviloglou, and D N Christodoulides. “Observation of PT -Symmetry Breaking in Complex Optical Potentials”. In: *Physical review letters* vol. 103 (Aug. 2009), p. 093902.

- [41] J. Wiersig. “Chiral and nonorthogonal eigenstate pairs in open quantum systems with weak backscattering between counterpropagating traveling waves”. In: *Physical Review A* vol. 89 (Dec. 2013).
- [42] H. Hodaei, M. A. Miri, M. Heinrich, D. N. Christodoulides, and M. Khajavikhan. “Parity-time-symmetric microring lasers”. In: *Science* vol. 346, no. 6212 (2014), pp. 975–978.
- [43] S. Wonjoo, W. Zheng, and F. Shanhui. “Temporal coupled-mode theory and the presence of non-orthogonal modes in lossless multimode cavities”. In: *IEEE Journal of Quantum Electronics* vol. 40, no. 10 (Oct. 2004), pp. 1511–1518.
- [44] M. Berry, R. Bhandari, and S. Klein. “Black plastic sandwiches demonstrating biaxial optical anisotropy”. In: *European Journal of Physics* vol. 20, no. 1 (Jan. 1999), pp. 1–14.
- [45] C. M. Bender. “PT-symmetric quantum theory”. In: *Journal of Physics: Conference Series* vol. 631 (2015), p. 012002.
- [46] M. Azadeh. *Light Coupling and Passive Optical Devices*. In: *Fiber Optics Engineering. Optical Networks*. Springer, Boston, Ma, 2009.
- [47] C. L. Zou, F. J. Shu, F. W. Sun, Z. J. Gong, Z. F. Han, and G. C. Guo. “Theory of free space coupling to high-Q whispering gallery modes”. In: *Opt. Express* vol. 21, no. 8 (2013), pp. 9982–9995.
- [48] X. Ji, F. A. S. Barbosa, S. P. Roberts, A. Dutt, J. Cardenas, Y. Okawachi, A. Bryant, A. L. Gaeta, and M. Lipson. “Ultra-low-loss on-chip resonators with sub-milliwatt parametric oscillation threshold”. In: *Optica* vol. 4, no. 6 (2017), pp. 619–624.
- [49] J. Heebner, R. Grover, and T. Ibrahim. *Optical microresonators: theory, fabrication, and applications*. eng. Springer series in optical sciences 138. OCLC: 255604479. London: Springer, 2008.
- [50] L. L. Sánchez-Soto, J. J. Monzón, and G. Leuchs. “The many facets of the Fabry–Perot”. In: *European Journal of Physics* vol. 37, no. 6 (Sept. 2016), p. 064001.
- [51] T. Needham. *Visual Complex Analysis*. Oxford University press Inc., 1997, New York.
- [52] J. Wiersig. “Structure of whispering-gallery modes in optical microdisks perturbed by nanoparticles”. In: *Phys. Rev. A* vol. 84 (6 2011), p. 063828.
- [53] W. Chen, S. Kaya Özdemir, G. Zhao, J. Wiersig, and L. Yang. “Exceptional points enhance sensing in an optical microcavity”. In: *Nature* vol. 548 (Aug. 2017), 192 EP –.
- [54] J. Wiersig. “Enhancing the Sensitivity of Frequency and Energy Splitting Detection by Using Exceptional Points: Application to Microcavity Sensors for Single-Particle Detection”. In: *Phys. Rev. Lett.* Vol. 112 (20 May 2014), p. 203901.

-
- [55] J. L. Miller. “Exceptional points make for exceptional sensors”. In: *Physics Today* vol. 70, no. 10 (2017), pp. 23–26.
- [56] Y. H. Ja. “A spectacles-shaped optical fibre ring resonator with two couplers”. In: *Optical and Quantum Electronics* vol. 23, no. 3 (1991), pp. 379–389.
- [57] S. Kharitonov and C. S. Brés. “Isolator-free unidirectional thulium-doped fiber laser”. In: *Light: Science & Applications* vol. 4, no. 10 (2015), e340–e340.
- [58] S. Kharitonov and C. Brés. “Dual-emission band all-fiber laser based on theta cavity with thulium- and holmium-doped fibers”. In: (2017), pp. 1–3.
- [59] J. P. Hohimer, G. A. Vawter, and D. C. Craft. “Unidirectional operation in a semiconductor ring diode laser”. In: *Applied Physics Letters* vol. 62, no. 11 (1993), pp. 1185–1187.
- [60] S. Kharitonov and C. S. Brés. “Isolator-free unidirectional thulium-doped fiber laser”. In: *Light: Science & Applications* vol. 4 (2015). Original Article, p 340 EP.
- [61] L. Zhou, T. Ye, and J. Chen. “Coherent interference induced transparency in self-coupled optical waveguide-based resonators”. In: *Opt. Lett.* Vol. 36, no. 1 (2011), pp. 13–15.
- [62] Z. Xu, Y. Luo, Q. Sun, C. Mou, Y. Li, P. P. Shum, and D. Liu. “Light velocity control in monolithic microfiber bridged ring resonator”. In: *Optica* vol. 4, no. 8 (2017), pp. 945–950.
- [63] A. Calabrese, F. Ramiro-Manzano, H. Price, M. Bernard, S. Biasi, M. Ghulinyan, I. Carusotto, and L. Pavesi. “Unidirectional reflection from an integrated “taiji” microresonator”. In: *preparation* ().
- [64] C. Allegra. ““Study of a “taiji” microresonator as an asymmetric and/or nonreciprocal optical device”. In: *M. Sc. Thesis, University of Trento* (2015).
- [65] P. Grellu. *Nonlinear Optical Cavity Dynamics: From Microresonators to Fiber Lasers*. eng. Wiley-VCH, 2016.
- [66] C. Castellán, R. Franchi, S. Biasi, M. Bernard, M. Ghulinyan, and L. Pavesi. “Field-Induced Nonlinearities in Silicon Waveguides Embedded in Lateral p-n Junctions”. In: *Frontiers in Physics* vol. 7 (2019), p. 104.
- [67] Z. Ahmed. “Schrödinger transmission through one-dimensional complex potentials”. In: *Physical Review A - PHYS REV A* vol. 64 (Sept. 2001).
- [68] S. A. R. Horsley, M. Artoni, and G. C. La Rocca. “Spatial Kramers-Kronig relations and the reflection of waves”. In: *Nature Photonics* vol. 9 (June 2015), 436 EP.
- [69] A. Mostafazadeh. “Spectral Singularities of Complex Scattering Potentials and Infinite Reflection and Transmission Coefficients at Real Energies”. In: *Phys. Rev. Lett.* Vol. 102 (22 June 2009), p. 220402.

A. A simple model of a Mach-Zhender interferometer

- [70] J. Jackson. *Classical Electrodynamics, 3rd Ed.* Wiley India Pvt. Limited, 2007.
- [71] Z. Daniel. *Handbook of Differential Equations*. Oct. 1997, pp. 153–157.
- [72] R. Newton. *Scattering theory of waves and particles*. Texts and monographs in physics. Springer-Verlag, 1982.
- [73] F. Siegfried. *Practical Quantum Mechanics*. 1974, Problem 39.
- [74] J. Lekner. “Reflectionless eigenstates of the sech² potential”. In: *American Journal of Physics* vol. 75, no. 12 (2007), pp. 1151–1157.
- [75] P. S. Epstein. “Reflection of waves in an inhomogeneous absorbing medium”. In: *Proceedings of the National Academy of Sciences of the United States of America* vol. 16, no. 10 (Oct. 1930), pp. 627–637.
- [76] S. Biasi, F. Ramiro-Manzano, M. Ghulinyan, I. Carusotto, and L. Pavesi. “From the Backscattering to the reactive coupling”. In: *OSA Advanced Photonics Congress (AP) 2019 (IPR, Networks, NOMA, SPPCom, PVLED)*. Optical Society of America, 2019, ITh2C.5.
- [77] M. F. Limonov, M. V. Rybin, A. N. Poddubny, and Y. S. Kivshar. “Fano resonances in photonics”. In: *Nature Photonics* vol. 11 (2017). Review Article, 543 EP –.
- [78] B. Peng, S. K. Özdemir, W. Chen, F. Nori, and L. Yang. “What is and what is not electromagnetically induced transparency in whispering-gallery microcavities”. In: *Nature Communications* vol. 5 (2014). Article, 5082 EP –.
- [79] I. S. Sinev, I. S. Mukhin, A. P. Slobozhanyuk, A. N. Poddubny, A. E. Miroshnichenko, A. K. Samusev, and Y. S. Kivshar. “Mapping plasmonic topological states at the nanoscale”. In: *Nanoscale* vol. 7 (28 2015), pp. 11904–11908.
- [80] A. P. Vinogradov, Y. E. Lozovik, A. M. Merzlikin, A. V. Dorofeenko, I. Vitebskiy, A. Figotin, A. B. Granovsky, and A. A. Lisyansky. “Inverse Borrmann effect in photonic crystals”. In: *Phys. Rev. B* vol. 80 (23 2009), p. 235106.
- [81] Y. Yu, W. Xue, E. Semenova, K. Yvind, and J. Mork. “Demonstration of a self-pulsing photonic crystal Fano laser”. In: *Nature Photonics* vol. 11 (2016), 81 EP –.
- [82] L. Stern, M. Grajower, and U. Levy. “Fano resonances and all-optical switching in a resonantly coupled plasmonic-atomic system”. In: *Nature Communications* vol. 5 (2014). Article, 4865 EP –.
- [83] C. Wu, A. B. Khanikaev, R. Adato, N. Arju, A. A. Yanik, H. Altug, and G. Shvets. “Fano-resonant asymmetric metamaterials for ultrasensitive spectroscopy and identification of molecular monolayers”. In: *Nature Materials* vol. 11 (2011). Article, 69 EP –.

-
- [84] M. Ghulinyan, F. R. Manzano, N. Prtljaga, M. Bernard, L. Pavesi, G. Pucker, and I. Carusotto. “Intermode reactive coupling induced by waveguide-resonator interaction”. In: *Phys. Rev. A* vol. 90 (5 2014), p. 053811.
- [85] M. Bernard, F. R. Manzano, L. Pavesi, G. Pucker, I. Carusotto, and M. Ghulinyan. “Complete crossing of Fano resonances in an optical microcavity via nonlinear tuning”. In: *Photon. Res.* Vol. 5, no. 3 (2017), pp. 168–175.
- [86] K. Krupa, A. Tonello, B. M. Shalaby, M. Fabert, A. Barthélémy, G. Millot, S. Wabnitz, and V. Couderc. “Spatial beam self-cleaning in multimode fibres”. In: *Nature Photonics* vol. 11 (2017), 237 EP –.
- [87] T. Ozawa, H. M. Price, N. Goldman, O. Zilberberg, and I. Carusotto. “Synthetic dimensions in integrated photonics: From optical isolation to four-dimensional quantum Hall physics”. In: *Phys. Rev. A* vol. 93 (4 2016), p. 043827.
- [88] T. Ozawa, H. M. Price, A. Amo, N. Goldman, M. Hafezi, L. Lu, M. C. Rechtsman, D. Schuster, J. Simon, O. Zilberberg, and I. Carusotto. “Topological photonics”. In: *Rev. Mod. Phys.* Vol. 91 (1 2019), p. 015006.
- [89] S. Fan, W. Suh, and J. D. Joannopoulos. “Temporal coupled-mode theory for the Fano resonance in optical resonators”. In: *J. Opt. Soc. Am. A* vol. 20, no. 3 (2003), pp. 569–572.
- [90] D. Walls and G. Milburn. *Quantum Optics*. Springer, 1994.
- [91] B. E. Little, S. T. Chu, H. A. Haus, J. Foresi, and J. Laine. “Microring resonator channel dropping filters”. In: *Journal of Lightwave Technology* vol. 15, no. 6 (1997), pp. 998–1005.
- [92] M. A. Popović, C. Manolatou, and M. R. Watts. “Coupling-induced resonance frequency shifts in coupled dielectric multi-cavity filters”. In: *Opt. Express* vol. 14, no. 3 (2006), pp. 1208–1222.
- [93] M. Pöllinger, D. O’Shea, F. Warken, and A. Rauschenbeutel. “Ultra-high- Q Tunable Whispering-Gallery-Mode Microresonator”. In: *Phys. Rev. Lett.* Vol. 103 (5 2009), p. 053901.
- [94] M. H. P. Pfeiffer, J. Liu, M. Geiselmann, and T. J. Kippenberg. “Coupling Ideality of Integrated Planar High- Q Microresonators”. In: *Phys. Rev. Applied* vol. 7 (2 2017), p. 024026.
- [95] S. Biasi, P. Guillemé, A. Volpini, G. Fontana, and L. Pavesi. “Time Response of a Microring Resonator to a Rectangular Pulse in Different Coupling Regimes”. In: *J. Lightwave Technol.* Vol. 37, no. 19 (2019), pp. 5091–5099.
- [96] D. G. Duffy. *Green’s function with applications*. Chapman and Hall CRC, 2018.
- [97] C. B. Hitz, J. J. Ewing, and J. Hecht. *Introduction to Laser Technology*. Wiley-IEEE Press, 2012.

- [98] B. Jin, J. Yuan, K. Wang, X. Sang, B. Yan, Q. Wu, F. Li, X. Zhou, G. Zhou, C. Yu, C. Lu, H. Yaw Tam, and P. K. A. Wai. “A comprehensive theoretical model for on-chip microring-based photonic fractional differentiators”. In: *Scientific Reports* vol. 5 (2015). Article, 14216 EP –.
- [99] L. C. Andrews. *Special functions of mathematics for engineers*. 1000 20th St. Bellingham WA 98225-6705 USA: Bellingham, Wash. SPIE Press monograph, 1998.
- [100] A. Taflove and S. C. Hagness. *Computational electrodynamics: the finite-difference time-domain method*. eng. 3rd ed. Artech House antennas and propagation library. OCLC: 838516123. Boston, Mass.: Artech House, 2010.
- [101] A. Taflove, A. Oskooi, and S. G. Johnson, eds. *Advances in FDTD computational electrodynamics: photonics and nanotechnology*. eng. OCLC: 811964793. Boston: Artech House, 2013.
- [102] A. F. Oskooi, D. Roundy, M. Ibanescu, P. Bermel, J. Joannopoulos, and S. G. Johnson. “Meep: A flexible free-software package for electromagnetic simulations by the FDTD method”. en. In: *Computer Physics Communications* vol. 181, no. 3 (Mar. 2010), pp. 687–702.
- [103] L. P. Pitaevskii and S. Stringari. *Bose-Einstein Condensation and Superfluidity*. Oxford: Oxford University Press, 2016.
- [104] R. W. Boyd. *Nonlinear Optics, Third Edition*. 3rd. USA: Academic Press, Inc., 2008.
- [105] Y. Castin. “Bose-Einstein Condensates in Atomic Gases: Simple Theoretical Results”. In: *Coherent atomic matter waves* (2001), 1–136.
- [106] C. Weisbuch, M. Nishioka, A. Ishikawa, and Y. Arakawa. “Observation of the coupled exciton-photon mode splitting in a semiconductor quantum microcavity”. In: *Phys. Rev. Lett.* Vol. 69 (23 1992), pp. 3314–3317.
- [107] M. Kasprzak J. and Richard, S. Kundermann, A. Baas, P. Jeambrun, J. M. J. Keeling, F. M. Marchetti, M. H. Szymańska, R. André, J. L. Staehli, V. Savona, P. B. Littlewood, B. Deveaud, and L. S. Dang. “Bose-Einstein condensation of exciton polaritons”. In: *Nature* vol. 443, no. 7110 (2006), pp. 409–414.
- [108] H. Deng, G. S. Solomon, R. Hey, K. H. Ploog, and Y. Yamamoto. “Spatial Coherence of a Polariton Condensate”. In: *Phys. Rev. Lett.* Vol. 99 (12 2007), p. 126403.
- [109] P.-E. Larré, N. Pavloff, and A. M. Kamchatnov. “Polarization hydrodynamics in a one-dimensional polariton condensate”. In: *Phys. Rev. B* vol. 88 (22 2013), p. 224503.
- [110] V. Kohnle, Y. Léger, M. Wouters, M. Richard, M. T. Portella-Oberli, and B. Deveaud-Plédran. “From Single Particle to Superfluid Excitations in a Dissipative Polariton Gas”. In: *Phys. Rev. Lett.* Vol. 106 (25 2011), p. 255302.

-
- [111] G. P. Agrawal. *Nonlinear fiber optics*. Academic press, 2007.
- [112] N. N. Rosanov. *Spatial Hysteresis and Optical Patterns*. Springer, New York, 2002.
- [113] V. Zakharov and L. Ostrovsky. “Modulation instability: The beginning”. In: *Physica D: Nonlinear Phenomena* vol. 238, no. 5 (Mar. 2009), pp. 540–548.
- [114] S. K. Turitsyn, A. M. Rubenchik, and M. P. Fedoruk. “On the theory of the modulation instability in optical fiber amplifiers”. In: *Opt. Lett.* Vol. 35, no. 16 (2010), pp. 2684–2686.
- [115] M. Conforti, A. Mussot, A. Kudlinski, and S. Trillo. “Modulational instability in dispersion oscillating fiber ring cavities”. In: *Opt. Lett.* Vol. 39, no. 14 (2014), pp. 4200–4203.
- [116] M. Borghi, C. Castellan, S. Signorini, A. Trenti, and L. Pavesi. “Nonlinear silicon photonics”. In: *Journal of Optics* vol. 19, no. 9 (2017).
- [117] J. Leuthold, C. Koos, and W. Freude. “Nonlinear silicon photonics”. In: *Nature Photonics* vol. 4, no. 8 (2010), pp. 535–544.
- [118] S. Xinzhu, T. En-Kuang, and B. Ozdal. “Applications of two-photon absorption in silicon”. In: *Journal of Optoelectronics and Advanced Materials* vol. 11 (Jan. 2009), pp. 15–25.
- [119] F. R. Ahmad, Y. W. Tseng, M. A. Kats, and F. Rana. “Energy limits imposed by two-photon absorption for pulse amplification in high-power semiconductor optical amplifiers”. In: *Opt. Lett.* Vol. 33, no. 10 (2008), pp. 1041–1043.
- [120] S. Manna, M. Bernard, S. Biasi, F. R. Manzano, M. Mancinelli, M. Ghulinyan, G. Pucker, and L. Pavesi. “Stimulated degenerate four-wave mixing in Si nanocrystal waveguides”. In: *Journal of Optics* vol. 18, no. 7 (2016), p. 075801.
- [121] P. D. Maker and R. W. Terhune. “Study of Optical Effects Due to an Induced Polarization Third Order in the Electric Field Strength”. In: *Phys. Rev.* Vol. 137 (3A 1965), A801–A818.
- [122] R. H. Stolen, J. E. Bjorkholm, and A. Ashkin. “Phase-matched three-wave mixing in silica fiber optical waveguides”. In: *Applied Physics Letters* vol. 24, no. 7 (1974), pp. 308–310.
- [123] H. Fukuda, K. Yamada, T. Shoji, M. Takahashi, T. Tsuchizawa, T. Watanabe, J. ichi Takahashi, and S. ichi Itabashi. “Four-wave mixing in silicon wire waveguides”. In: *Opt. Express* vol. 13, no. 12 (2005), pp. 4629–4637.
- [124] S. Stefano. “Intermodal four wave mixing for heralded single photon sources in silicon”. In: *Ph.D. Thesis, University of Trento* (2019).
- [125] N. N. Bogolyubov. “On the theory of superfluidity”. In: *J. Phys.(USSR)* vol. 11 (1947). *Izv. Akad. Nauk Ser. Fiz.*11,77(1947)], pp. 23–32.

- [126] D. Vocke, T. Roger, F. Marino, E. M. Wright, I. Carusotto, M. Clerici, and D. Faccio. “Experimental characterization of nonlocal photon fluids”. In: *Optica* vol. 2, no. 5 (2015), pp. 484–490.
- [127] A. Messiah. *Quantum Mechanics*. New York: Dover Publications, 1999.
- [128] X. di, M. C. Chang, and Q. Niu. “Berry Phase Effects on Electronic Properties”. In: *Reviews of Modern Physics* vol. 82 (July 2009).
- [129] P.-E. Larré, N. Pavloff, and A. M. Kamchatnov. “Wave pattern induced by a localized obstacle in the flow of a one-dimensional polariton condensate”. In: *Phys. Rev. B* vol. 86 (16 2012), p. 165304.
- [130] M. Wouters and I. Carusotto. “Excitations in a Nonequilibrium Bose-Einstein Condensate of Exciton Polaritons”. In: *Phys. Rev. Lett.* Vol. 99 (14 2007), p. 140402.
- [131] B. J. Eggleton, B. Luther-Davies, and K. Richardson. “Chalcogenide photonics”. In: *Nature Photonics* vol. 5, no. 3 (2011), pp. 141–148.
- [132] G. T. Reed, G. Mashanovich, F. Y. Gardes, and D. J. Thomson. “Silicon optical modulators”. In: *Nature Photonics* vol. 4, no. 8 (2010), pp. 518–526.
- [133] F. G. Della Corte, G. Cocorullo, M. Iodice, and I. Rendina. “Temperature dependence of the thermo-optic coefficient of InP, GaAs, and SiC from room temperature to 600 K at the wavelength of 1.5 μm ”. In: *Applied Physics Letters* vol. 77, no. 11 (2000), pp. 1614–1616.
- [134] F. Testa, S. Tondini, F. Gambini, P. Velha, A. Bianchi, C. Kopp, M. Hofbauer, C. L. Manganelli, N. Zecevic, S. Faralli, G. Pares, R. Enne, A. Serrano, B. Goll, G. Fontana, A. Chalyan, J. Lee, P. Pintus, G. Chiaretti, H. Zimmermann, L. Pavesi, C. J. Oton, and S. Stracca. “Integrated Reconfigurable Silicon Photonics Switch Matrix in IRIS Project: Technological Achievements and Experimental Results”. In: *Journal of Lightwave Technology* vol. 37, no. 2 (2019), pp. 345–355.
- [135] M. W. Geis, S. J. Spector, R. C. Williamson, and T. M. Lyszczarz. “Submicrosecond submilliwatt silicon-on-insulator thermo-optic switch”. In: *IEEE Photonics Technology Letters* vol. 16, no. 11 (2004), pp. 2514–2516.
- [136] T. Liang, L. Nunes, T. Sakamoto, K. Sasagawa, T. Kawanishi, M. Tsuchiya, G. Priem, D. V. Thourhout, P. Dumon, R. Baets, and H. Tsang. “Ultrafast all-optical switching by cross-absorption modulation in silicon wire waveguides”. In: *Opt. Express* vol. 13, no. 19 (2005), pp. 7298–7303.
- [137] J. S. Pelc, K. Rivoire, S. Vo, C. Santori, D. A. Fattal, and R. G. Beausoleil. “Picosecond all-optical switching in hydrogenated amorphous silicon microring resonators”. In: *Opt. Express* vol. 22, no. 4 (2014), pp. 3797–3810.
- [138] J. Petráček, Y. Eksioğlu, and A. Sterkhova. “Simulation of self-pulsing in Kerr-nonlinear coupled ring resonators”. In: *Optics Communications* vol. 318 (2014), pp. 147–151.

-
- [139] F. Ramiro-Manzano, N. Prtljaga, L. Pavesi, G. Pucker, and M. Ghulinyan. “Thermo-optical bistability with Si nanocrystals in a whispering gallery mode resonator.” In: *Optics letters* vol. 38 18 (2013), pp. 3562–5.
- [140] M. Borghi, A. Trenti, and L. Pavesi. “Four Wave Mixing control in a photonic molecule made by silicon microring resonators”. In: *Scientific Reports* vol. 9, no. 1 (2019), p. 408.
- [141] F. Turri, S. Biasi, F. R. Manzano, and L. Pavesi. “A Free-Space Interferometer for Phase-Delay Measurements in Integrated Optical Devices in Degenerate Pump-and-Probe Experiments”. In: *IEEE Transactions on Instrumentation and Measurement* vol. 67, no. 12 (2018), pp. 2863–2871.
- [142] F. Ramiro-Manzano, N. Prtljaga, L. Pavesi, G. Pucker, and M. Ghulinyan. “A fully integrated high-Q Whispering-Gallery Wedge Resonator”. In: *Opt. Express* vol. 20, no. 20 (2012), pp. 22934–22942.
- [143] S. Mas, J. Matres, J. Marti, and C. J. Oton. “Accurate Chromatic Dispersion Characterization of Photonic Integrated Circuits”. In: *IEEE Photonics Journal* vol. 4, no. 3 (2012), pp. 825–831.
- [144] A. Trenti, M. Borghi, S. Biasi, M. Ghulinyan, F. Ramiro-Manzano, G. Pucker, and L. Pavesi. “Thermo-optic coefficient and nonlinear refractive index of silicon oxynitride waveguides”. In: *AIP Advances* vol. 8, no. 2 (2018), p. 025311.
- [145] S. Paesani, A. A. Gentile, R. Santagati, J. Wang, N. Wiebe, D. P. Tew, J. L. O’Brien, and M. G. Thompson. “Experimental Bayesian Quantum Phase Estimation on a Silicon Photonic Chip”. In: *Physical Review Letters* vol. 118, no. 10 (2017), p. 100503.
- [146] Y. Shen, N. C. Harris, S. Skirlo, D. Englund, and M. Soljačić. “Deep learning with coherent nanophotonic circuits”. In: *Photonics Society Summer Topical Meeting Series (SUM), 2017 IEEE*. IEEE. 2017, pp. 189–190.
- [147] M Mancinelli, A Trenti, S Piccione, G Fontana, J. S. Dam, P. Tidemand-Lichtenberg, C. Pedersen, and L Pavesi. “Mid-infrared coincidence measurements on twin photons at room temperature”. In: *Nature Communications* vol. 8 (2017), p. 15184.
- [148] A. D. Ludlow, M. M. Boyd, J. Ye, E. Peik, and P. O. Schmidt. “Optical atomic clocks”. In: *Reviews of Modern Physics* vol. 87, no. 2 (2015), p. 637.
- [149] A. Gondarenko, J. S. Levy, and M. Lipson. “High confinement micron-scale silicon nitride high Q ring resonator”. In: *Optics express* vol. 17, no. 14 (2009), pp. 11366–11370.
- [150] M. Kues, C. Reimer, P. Roztocky, L. R. Cortés, S. Sciara, B. Wetzel, Y. Zhang, A. Cino, S. T. Chu, B. E. Little, et al. “On-chip generation of high-dimensional entangled quantum states and their coherent control”. In: *Nature* vol. 546, no. 7660 (2017), pp. 622–626.

- [151] M. Fadel, M. Bülters, M. Niemand, E. Voges, and P. M. Krummrich. “Low-loss and low-birefringence high-contrast silicon-oxynitride waveguides for optical communication”. In: *Journal of Lightwave Technology* vol. 27, no. 6 (2009), pp. 698–705.
- [152] S. Dwivedi, A. Ruocco, M. Vanslebrouck, T. Spuesens, P. Bienstman, P. Dumon, T. Van Vaerenbergh, and W. Bogaerts. “Experimental extraction of effective refractive index and thermo-optic coefficients of silicon-on-insulator waveguides using interferometers”. In: *Journal of Lightwave Technology* vol. 33, no. 21 (2015), pp. 4471–4477.
- [153] T. J. A. Kippenberg. *Nonlinear optics in ultra-high-Q whispering-gallery optical microcavities*. California Institute of Technology, 2004.
- [154] B. Peng, cS. K. Özdemir, M. Liertzer, W. Chen, J. Kramer, H. Yilmaz, J. Wiersig, S. Rotter, and L. Yang. “Chiral modes and directional lasing at exceptional points”. In: *Proceedings of the National Academy of Sciences* vol. 113, no. 25 (2016), pp. 6845–6850.
- [155] A. Mazzei, S. Götzinger, L. de S. Menezes, G. Zumofen, O. Benson, and V. Sandoghdar. “Controlled Coupling of Counterpropagating Whispering-Gallery Modes by a Single Rayleigh Scatterer: A Classical Problem in a Quantum Optical Light”. In: *Phys. Rev. Lett.* Vol. 99 (17 2007), p. 173603.
- [156] M. Kim, K. Kwon, J. Shim, Y. Jung, and K. Yu. “Partially directional microdisk laser with two Rayleigh scatterers”. In: *Opt. Lett.* Vol. 39, no. 8 (2014), pp. 2423–2426.
- [157] S. Chen, Q. Yan, Q. Xu, Z. Fan, and J. Liu. “Optical waveguide propagation loss measurement using multiple reflections method”. In: *Optics Communications* vol. 256, no. 1 (2005), pp. 68–72.
- [158] G. Ren, S. Chen, Y. Cheng, and Y. Zhai. “Study on inverse taper based mode transformer for low loss coupling between silicon wire waveguide and lensed fiber”. In: *Optics Communications* vol. 284, no. 19 (2011), pp. 4782–4788.
- [159] L. Stefan, M. Bernard, R. Guider, G. Pucker, L. Pavesi, and M. Ghulinyan. “Ultra-high-Q thin-silicon nitride strip-loaded ring resonators”. In: *Opt. Lett.* Vol. 40, no. 14 (2015), pp. 3316–3319.
- [160] E. L. Wooten, K. M. Kissa, A. Yi-Yan, E. J. Murphy, D. A. Lafaw, P. F. Hallemeier, D. Maack, D. V. Attanasio, D. J. Fritz, G. J. McBrien, and D. E. Bossi. “A review of lithium niobate modulators for fiber-optic communications systems”. In: *IEEE Journal of Selected Topics in Quantum Electronics* vol. 6, no. 1 (2000), pp. 69–82.
- [161] W. H. P. Horowitz. *Art of Electronics*. New York, NY, USA: Cambridge Univ. Press, 1989.
- [162] P. B. Tarsa, P. Rabinowitz, and K. K. Lehmann. “Evanescent field absorption in a passive optical fiber resonator using continuous-wave cavity ring-down spectroscopy”. In: *Chemical Physics Letters* vol. 383, no. 3 (2004), pp. 297–303.

-
- [163] J. I. Thorpe. “LISA long-arm interferometry”. In: *Classical and Quantum Gravity* vol. 27, no. 8 (2010), p. 084008.
- [164] T. P. Appourchaux, G. Gourmelon, and B. Johlander. “Effect of gamma-ray irradiations on optical filter glass”. In: *Optical Engineering* vol. 33, no. 5 (1994), pp. 1659–1668.
- [165] P. N. Grillo and W. J. Rosenberg. “Proton radiation damage in optical filter glass”. In: *Appl. Opt.* Vol. 28, no. 20 (1989), pp. 4473–4477.
- [166] A. Yariv. *Optical Electronics*. Saunders College Publishing, Usa, 1991.